VALIDATION OF 3-D ICE ACCRETION DOCUMENTATION AND REPLICATION METHOD INCLUDING PRESSURE-SENSITIVE PAINT

BY

MARIANNE CATHLEEN MONASTERO

THESIS

Submitted in partial fulfillment of the requirements
for the degree of Master of Science in Aerospace Engineering
in the Graduate College of the
University of Illinois at Urbana-Champaign, 2013

Urbana, Illinois

Advisor:

Professor Michael B. Bragg

Abstract

Accurate representation of ice accretions is important to the study and understanding of aircraft icing. For research and certification purposes, replicas of ice accretions generated from icing wind tunnels are fabricated to perform aerodynamic tests in dry-air wind tunnels. The currently employed replication method consists of creating molds from original ice accretions and producing castings from the molds for wind tunnel testing. While this method reproduces the geometric features and aerodynamic effects of the original ice accretions well in the replicated ice shapes, it has several limitations. This method cannot scale the ice shapes to sizes other than the original and does not produce a digital record of the ice shape. Both of these capabilities are desirable in iced-aerodynamics research. To address these needs, NASA developed a methodology to obtain a digital record of ice accretions through the implementation of a laser scanner system. The resulting scan can be used in conjunction with rapid-prototype methods to generate ice shapes for wind tunnel testing. This work is a validation of the 3-D ice accretion measurement methodology where the ice shapes generated by both the currently-used and newly-developed methods from the same initial ice accretion are compared using force balance-derived aerodynamic performance, surface and wake pressures, and pressure-sensitive paint (PSP) data.

The 3-D features of the tested ice shapes necessitated the use of a technique capable of obtaining high resolution data. The PSP technique allowed pressure coefficient data to be obtained over a larger area and at a greater resolution than is possible by only using the surface pressure tap method. The results discussed show the capability of the PSP technique, as implemented in the 3ft by 4ft subsonic wind tunnel at the University of Illinois, to resolve aerodynamic differences between ice shapes made from both the current and newly developed ice accretion replication methods. The same trends were observed in the PSP data as were found in the aerodynamic performance and pressure tap data, and the newly developed 3-D ice accretion measurement methodology produced ice shapes which aerodynamically agreed well with ice shapes generated from the mold and casting method.

To my family: Mom, Dad, Allison, and Michelle

Acknowledgements

I would like to thank and acknowledge the many people who supported me throughout my thesis work and graduate studies at the University of Illinois. First, I want to thank my advisor, Professor Michael Bragg, for his guidance and insight, and for enabling me to undertake this project. I want to also acknowledge the FAA and Dr. Jim Riley for their sponsorship of the overall project through Cooperative Agreement Number 10-G-004 of which this research is a part. A thank you is also due to Professor Greg Elliott for answering my questions about pressure-sensitive paint at the onset of the project and for allowing me to borrow much of his optical equipment during testing. Dr. Andy Broeren, Dr. Sam Lee, and Gene Addy from the Icing Branch at NASA Glen Research Center worked closely with me in many aspects of the wind tunnel test and data analysis. They helped me fit my piece of the project into the work as a whole and collaborated with me to acquire the aerodynamic performance data. An immense thank you is due to Greg Milner, Lee Booher, Stephen Mathine, and Dave Foley from the UIUC Aerospace Engineering Research Machine Shop for ensuring that every facet of the mold and casting process went smoothly. They fabricated the components necessary to create the molds and castings and allowed those of us working on the project to invade the shop for most of a semester. Dave especially lent his valued expertise in mold and casting making and in instrumentation of all the many pressure taps.

Jeff Diebold supported much of this work by assisting with model and ice shape installation, modifying the tunnel code to accommodate this specific test, teaching me initially how to run the tunnel, and always being willing to discuss my project and share his aerodynamics knowledge. Thank you also to Dr. Brian Woodard for his tremendous guidance and humor during the writing process and for helping with various aspects of the project. Thank you to Dr. Phil Ansell for sharing his aerodynamics expertise and Brent Pomeroy for giving me access to his library of textbooks and helping me decipher grad school. Thanks also to Ruben Hortensius and Gustavo Fujiwara for being fantastic people

with whom to share work-space. Thanks for giving our office so much personality and for making my time there both fun and instructive.

I want to recognize some of my incredible friends: Nick Wengrenovich for his many years of friendship and for sharing his positive outlook on life, and Joanie Stupik and Justine Fortier for their never-ending support, encouragement, and laughter throughout our time in graduate school. Thank you from the bottom of my heart for your friendship. Lastly and most importantly, I want to acknowledge my family: my parents, Joan and Nick, and my sisters, Allison and Michelle. Thank you for always being there for me, for supporting me through all that I do, and for being my first and best teachers. Thank you for your love, your understanding, and your belief in me.

Table of Contents

Nomenclature

A_{ss}	Cross-sectional area of settling section
A_{ts}	Cross-sectional area of test section
C_A	Axial force coefficient
$C_{D,d}$	Drag coefficient
$C_{L,\ell}$	Lift coefficient
$C_{M,m}$	Moment coefficient
C_N	Normal force coefficient
F_A	Axial force acting on model
F_N	Normal force acting on model
V_A	Scaled axial force voltage output from force balance
V_M	Scaled moment voltage output from force balance
V_N	Scaled normal force voltage output from force balance
$c_{\ell,max}$	Maximum lift coefficient
$c_{\ell,\alpha}$	Lift slope
$c_{d,min}$	Minimum drag coefficient
c_p	Pressure coefficient
k_{nr}	Rate of deactivation due to non-radiative emission
k_q	Rate of deactivation due to quenching
k_r	Rate of deactivation due to radiative emission
x_{offset}	Quarter-chord point offset from balance center in x-direction
y_{offset}	Quarter-chord point offset from balance center in y-direction
$[Q]$	Concentration of quenching particles
‘	Per segment between pressure taps
b	Span
C	Area of wind tunnel test section
h	Tunnel height
k/c	Horn height non-dimensionalized by chord
K_1	Constant for wind tunnel corrections
Re	Reynolds number
s/c	Horn location non-dimensionalized by chord
t	Airfoil thickness
x	Direction parallel to chord
x/c	Direction parallel to chord non-dimensionalized by chord
y	Direction perpendicular to chord
z/b	Spanwise direction non-dimensionalized by span
A	Stern-Volmer slope
B	Stern-Volmer intercept

D	Drag
I	Intensity of emitted light
L	Lift
M	Moment
M	Mach number
P, p	Static pressure
R	Specific gas constant for air
S	Planform area
T	Temperature
U	Velocity
U	Uncertainty
c	Chord
q	Dynamic pressure
u	Velocity in pane

Greek Symbols

α	Angle of attack
α_{stall}	Angle of attack at stall
ϵ	Velocity increment correction
θ	Horn angle in relation to chord line
μ	Viscosity coefficient
ν	Wavelength
ρ	Density
σ	Streamline curvature correction factor
τ	Lifetime
Φ	Quantum yield of luminescence

Acronyms

CAD	Computer-aided design
CCD	Charge-coupled device
ESP	Electronically scanned pressure
FAA	Federal Aviation Administration
FAR	FAA Federal Aviation Regulation
IRT	NASA Glenn Icing Research Tunnel
ISSI	Innovative Scientific Solutions, Inc.
NACA	National Advisory Committee for Aeronautics
NASA	National Aeronautics and Space Administration
ONERA	Office National d'Etudes et de Recherches Aérospatiales
PSP	Pressure-sensitive paint
RMS	Root mean square
RPM	Rapid-prototype method

rpm	Revolutions per minute
SLA	Stererolithography
SLD	Supercooled large droplet
TsAGI	Central Aero-Hydrodynamic Institute
UIUC	University of Illinois at Urbana-Champaign
UV	Ultra-violet

Subscripts

0	Vacuum or freezing condition
ref	Reference condition
S	Signal luminophore
R	Reference luminophore
ss	Settling section
ts	Test section
amb	Ambient
∞	Freestream
1	Plane downstream of wake
w	Wake plane
total, o	Stagnation
sb	Solid blockage
wb	Wake blockage
u	Uncorrected
cor	Corrected
c/4	Quarter-chord point

Chapter 1

Introduction

1.1 Icing

The pursuit of a more complete understanding of aircraft icing is necessary for safe aircraft operation through icing conditions. Studying the process of ice formation on aircraft surfaces and the aerodynamic effects associated with ice accretion enables improved design, enhanced certification procedures, and more accurate computational prediction tools. Much of the past icing research has focused on ice formation and iced-aerodynamics of airfoils. Currently, airfoil icing is reasonably well understood, so the icing research focus is progressing towards improving the understanding of swept-wing icing.[1,2] The work reported here is part of the research necessary to build upon the current understanding of airfoil icing in order to study swept-wing icing.

1.1.1 Airfoil Icing

Iced-airfoil aerodynamics can be divided into the four main classifications defined by Bragg et al.[3] These classifications, roughness, horn, streamwise, and spanwise-ridge ice, are based on ice-shape geometry and resulting flowfield. A brief description of the definition and aerodynamic penalties of each ice shape type follows.

1.1.1.1 Roughness Ice

Roughness ice is formed during the beginning stages of ice accretion in either glaze or rime conditions, and is characterized by small-scale ice features that do not greatly alter the airfoil contour.[3] Roughness ice tends to consist of three zones: a smooth zone, rough zone, and feather region, as were defined by Anderson and Shin.[4] Figure 1.1 shows these regions. The smooth zone exists at the airfoil leading edge encompassing the stagnation point. Further downstream is the rough zone on both upper and lower surfaces, followed by

the feather region. The roughness features in the rough and feather zones are larger than the boundary layer height for typical flight Reynolds numbers and are the beginnings of significant ice shapes.[3] Each isolated roughness element, for low roughness density, acts as a flow obstacle over which the flow separates. This increases skin friction on the surface, which can lead to earlier transition and trailing-edge separation. Roughness ice is associated with increased drag, decreased maximum lift, and lower stall angle of attack. Bragg et al.[3] state that the specifics of the roughness' height, density, and chordwise location determine the extent of the aerodynamic penalties. The location of roughness most detrimental to performance is at the location of minimum pressure where the clean pressure peak occurs. The presence of roughness at this location causes a significant amount of energy to be extracted from the boundary layer, which results in lost lift and increased drag.

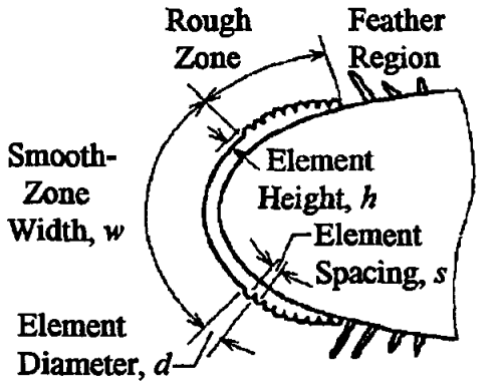

Figure 1.1: Typical ice roughness geometry.[4]

1.1.1.2 Horn Ice

Horn ice is formed during glaze ice conditions, where water droplets do not freeze directly on impact with the surface but flow along the chord for a distance before freezing.[5] This behavior yields a buildup of ice slightly downstream from the airfoil leading edge which protrudes into the flow. A simplified horn ice shape can be viewed in Figure 1.2. Horn ice shapes are characterized by their height (k/c), angle to the chord line (θ), and location along the chord (s/c). The aerodynamics of an airfoil with a horn ice shape are dominated by the presence of a separation bubble behind the horn.[3] The flow separates off the horn tip due to the severe adverse pressure gradient there and forms a separation bubble similar to the long separation bubbles described by Tani.[6] The separated shear layer transitions to turbulent

flow at some point after separation. The increased mixing and momentum associated with transition enable the shear layer to reattach to the airfoil surface.[3] Upstream of the reattachment line, the flow within the bubble is reversed. The separation bubble has an effect on the airfoil pressure distribution, as seen in Figure 1.3, where the separated flow is indicated by a pressure plateau, followed by region of steep pressure recovery. At higher angles of attack, the pressure decreases at the model trailing edge, which indicates increased pressure drag in comparison to the clean case with no ice accretion. Stall of an airfoil with a horn ice shape has characteristics of thin-airfoil stall.[5] Anderson[7] describes thin-airfoil stall as occurring as the growth of a separation bubble over the chord to the trailing edge with angle of attack increases, at which point the flow separates and the airfoil stalls.

Variations in flow behavior along the span of an airfoil with a three-dimensional horn shape or two-dimensional horn shape with added roughness, produce cellular-type structures that are evident in surface oil flow visualization. Bragg et al.[3] describe how these cells do not seem to correlate to the geometric features of the ice shape. Jacobs and Bragg[8] discuss how these features are due to a spanwise instability that produces spanwise vortices and are the result of roughness features on the horn ice shape. Figure 1.4 shows the surface oil flow visualization results from a test by Jacobs and Bragg,[8] where spanwise cells are visible behind a two-dimensional ice shape with added roughness. The cells do not exist for cases without roughness.

Overall, Bragg et al.[3] summarize that the gross shape (height (k/c), angle (θ), and location (s/c)) of the horn ice shape, not the roughness details, determines the aerodynamic effect. Horn ice shapes cause the most severe aerodynamic penalties.[5] They reduce the maximum lift and the stall angle of attack and increase drag due to the flowfield changes from the separation bubble. Additionally, since the horn tip sets the separation point, the aerodynamics of a horn ice shape are effectively independent of Reynolds number.[5]

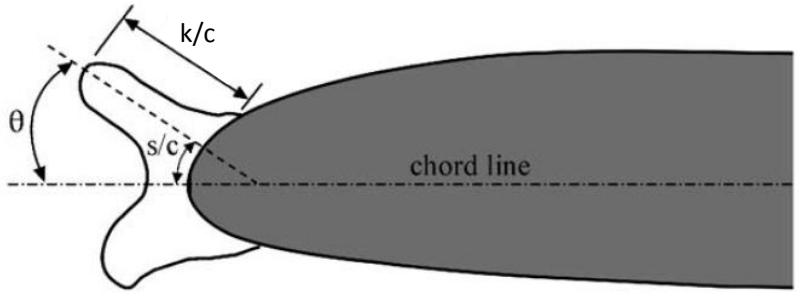

Figure 1.2: Horn ice shape geometry, adapted from Bragg et al.[3]

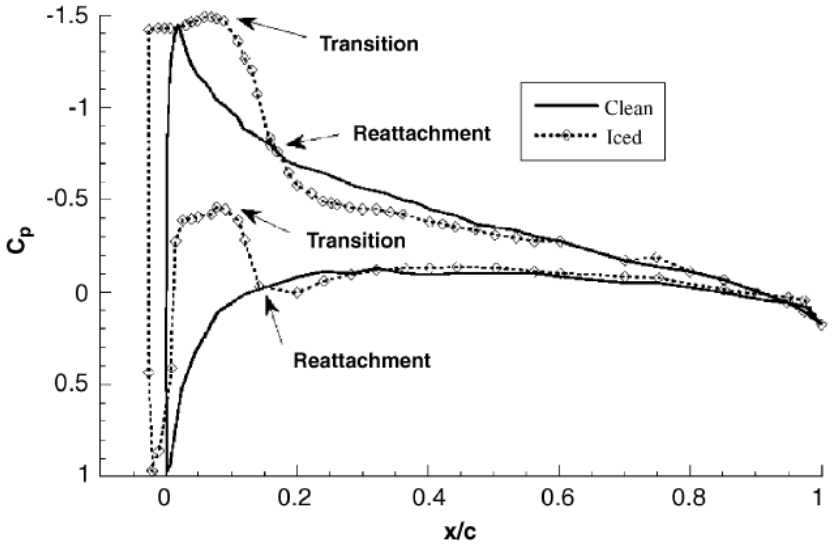

Figure 1.3: Surface pressure distribution for a simulated horn ice shape compared to the clean pressure distribution.[3]

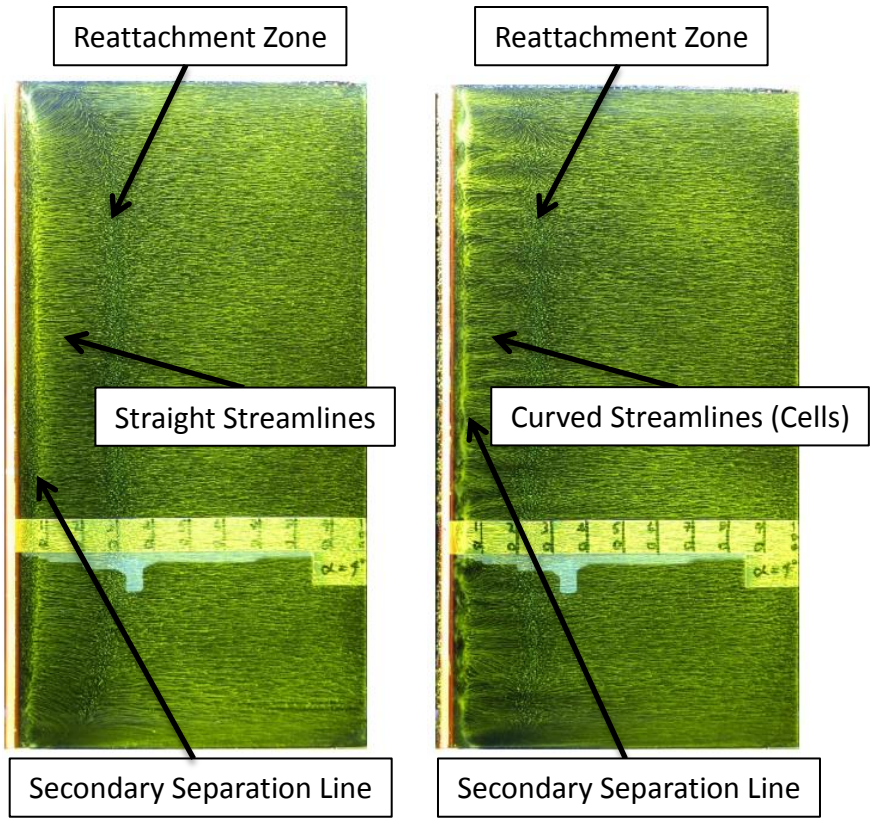

Figure 1.4: Surface oil flow visualization comparison between a) 2-D ice shape and b) 2-D ice shape with added roughness.[8]

1.1.1.3 Streamwise Ice

Bragg et al.[3] define streamwise ice as ice that forms during rime conditions and generally follows the airfoil contour. Rime conditions occur at temperatures where the impinging water droplets freeze on the surface at impact. The aerodynamic effects of streamwise ice shapes are generally not as drastic as those from horn shapes. Typically, streamwise ice extends forward of the leading edge, sometimes forming a horn-like extension into the flow. Figure 1.5 shows the geometry of a representative streamwise shape. The streamwise-ice flowfield is distinguished from that of the horn by a smaller separation region with a varying separation point. The flow over the airfoil remains attached until near the ice/airfoil junction, where an adverse pressure gradient causes separation. Since the separation region is small, the aerodynamic effects of the bubble are not as severe as those from a horn ice shape separation bubble. This means the roughness of the ice shape has more of an effect, leading to trailing-edge separation having a greater aerodynamic impact.[3]

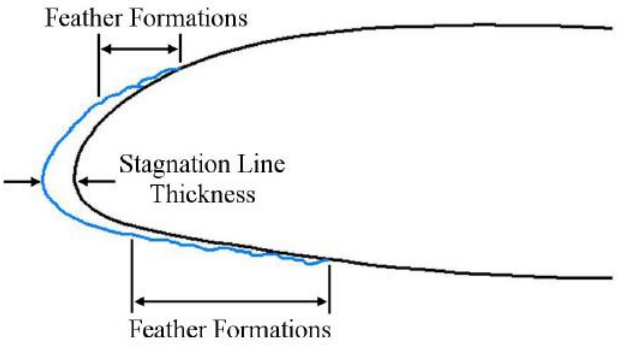

Figure 1.5: Streamwise ice geometry.[9]

1.1.1.4 Spanwise-Ridge Ice

Spanwise-ridge ice forms further downstream from the leading edge and is often the result of a heating device that is not operating at 100% evaporating efficiency. This type of ice shape may also form if the incoming droplet diameters have a large enough momentum to reach the surface behind a leading-edge ice protection system.[10] Conditions where these larger droplets, or supercooled large droplets (SLD), form are dangerous since ice protection systems are not as effective. For smaller droplet sizes, once the water passes a heating device operating below 100% evaporating efficiency, freezing can occur behind the de-icer, resulting in a spanwise-ridge ice accretion. Similar to the separation bubble that forms from a horn ice shape, a separation bubble will form from the spanwise-ridge shape and will dominate the flow behavior.[3] Bragg et al.[3] describe how the spanwise-ridge ice acts as a flow obstacle to the flow on the airfoil. By the time the flow reaches the ridge, the boundary layer is usually turbulent. The flow separates ahead of the ridge, due to the adverse pressure gradient, and forms a bubble upstream of the ice. The flow also separates off of the ridge tip, forming a second separation bubble downstream of the ice. These two bubbles greatly affect the aerodynamics of the flow over the airfoil. The aerodynamics of a spanwise-ridge shape are especially sensitive to ridge height, location, geometric shape, and spanwise variation.[3] Figure 1.6 shows a representative geometry of a spanwise-ridge ice shape formed behind a leading-edge ice protection system. Figure 1.6a is a photograph taken upstream of the model looking towards the leading edge and Figure 1.6b is a trace of the same shape.

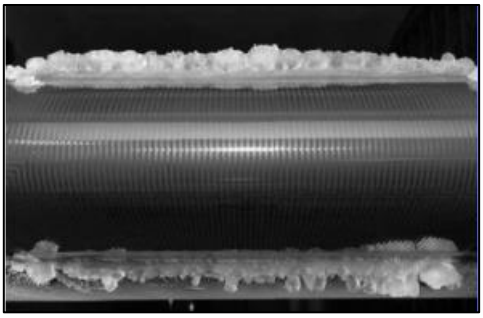

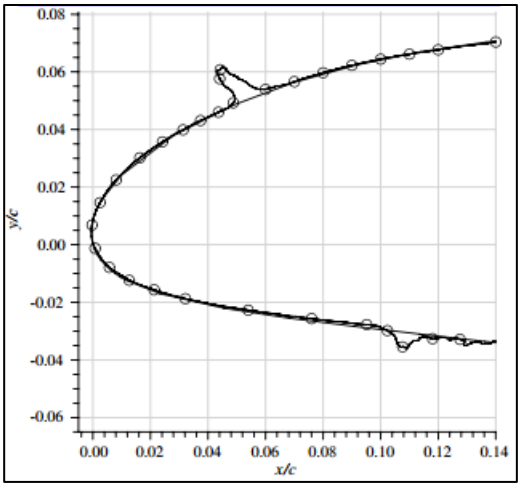

a) b)

Figure 1.6: Spanwise ridge ice shape example, a) photograph and b) tracing, adapted from Broeren et al.[11]

1.1.2 Swept-Wing Icing and the Need for 3-D Ice Accretion Measurement

To date, a number of swept-wing research programs have studied swept-wing icing. Broeren et al.[1] describe past and present work. Most previous work has focused on understanding icing physics, developing computational tools, and testing at low Reynolds numbers on small-scale models. Broeren et al.[1] explain the need for further swept-wing icing study and summarize the joint research collaboration between NASA (National Aeronautics and Space Administration), FAA (Federal Aviation Administration), ONERA (Office National d'Etudes et de Recherches Aérospatiales), UIUC (University of Illinois at Urbana-Champaign), and Boeing to accomplish this. The overall goal of this swept-wing icing research program is to develop experimental and computational swept-wing ice simulation methods, and to further understand swept-wing ice formation and aerodynamics. The work described here is a part of one of the phases of this swept-wing icing research program.

An essential capability is the ability to accurately record swept-wing ice accretions. NASA previously developed three main processes for recording ice shapes: two-dimensional cross-sectional traces, qualitative photographs, and molds and castings. The trace method yields good information about the general shape of a two-dimensional ice accretion but has large uncertainties based partly on the particular tracing method employed by the person performing the trace. A full three-dimensional understanding is impossible to obtain from traces. Qualitative photographs yield much less information than the traces, yet do provide

some three-dimensional knowledge. The mold and casting method is another technique often used by NASA to record ice shapes, and is capable of recording three-dimensional features along a model span. It involves making a mold of an accreted ice shape, and then creating castings from a master mold. The castings can be tested in a dry-air wind tunnel. While the mold and casting method can record three-dimensional features, it is expensive in both materials and time and does not produce a digital record of the ice shape. Therefore, NASA worked to develop a new method of recording ice shapes that could record complex shapes, document shapes digitally, and enable fabrication of shapes for testing. The present work is a part of the validation of the new technique developed by NASA in comparison to the currently accepted mold and casting method.

Once the validation of the new method is complete, the developed process will be used in further phases of the swept-wing icing project. Ultimately this involves the testing of artificially iced models in the ONERA F1 pressurized tunnel. The ice shapes used in this future test will be generated in the NASA Glenn Research Center Icing Research Tunnel (IRT) and recorded using the developed method. Both the replicas of those ice shapes and simulated shapes will be tested in order to determine the degree to which swept-wing ice shapes must be replicated in order to obtain comparable aerodynamic penalties. Ice shape simulations are simplified shapes based on the geometry of initial ice accretions, whereas ice shape replicas possess the three-dimensionality and small-scale features of the original ice accretion. Examples of simulations are two-dimensional extrusions of the ice shape geometry or the representation of a horn by a simple rectangle. Both the mold and casting and 3-D laser scanner and rapid-prototype techniques produce ice shape replicas. In addition to providing results concerning necessary simulation fidelity for swept-wing ice shape testing, the experimental data that will result from the future F1 tunnel test will also provide validations for three-dimensional icing codes. This will aid in the improvement of certification procedures to more accurately, efficiently, and safely certify aircraft for flight in icing conditions.

1.1.3 Ice Shape Documentation

Ice shape documentation is important for the experimental study of icing. Busch[5] discusses how icing tunnels are not ideal for aerodynamic testing due to their high turbulence

levels, making it necessary for experiments to be performed in other, dry-air wind tunnels. This necessitates the use of ice-shape representations that accurately replicate the flowfield effects and aerodynamics of the original ice accretions. Therefore, methods of recording and simulating the original ice accretions must be used to obtain these representations for use in dry-air wind tunnels. The method that has been used extensively by NASA Glenn Research Center in the Icing Research Tunnel (IRT) is the mold and casting method, mentioned briefly above. This is currently the highest fidelity method of recording ice shapes. With the focus now on swept-wing icing, a more complete documentation of ice shapes is needed. For this reason, NASA developed a 3-D ice accretion measurement methodology to replace the mold and casting technique.[28]

The other widely used means of documenting ice shapes is through 2-D traces. An ice tracing is obtained by hand tracing an ice accretion in the IRT at a spanwise location. An "ice knife," or heated metal sheet with the model leading-edge contour cut out from one side, is used to melt the ice at the spanwise location where the trace will be drawn. Once the ice is melted, a cardboard template with the model leading-edge contour cut out from one side is placed in the slot where the ice knife melted the ice. A pencil is then used to carefully draw the two-dimensional geometry of the ice on the cardboard template. This method has been used extensively to understand icing and to provide geometries for computational work.

Ice shape simulation uses simplified geometries based on the original ice accretions to attempt to reproduce the aerodynamics, with varying degrees of fidelity. The simplest simulation is through geometric representation. Mimicking a horn ice shape with a rectangular extrusion of a height, angle, and location similar to the original accretion, or representing a spanwise-ridge shape with a flow obstacle such as a quarter-round geometry, are examples of simplified geometric representation. Two-dimensional extrusions of an ice tracing have a higher fidelity, but do not replicate any three-dimensional effects. Adding distributed roughness elements to these representations helps retain some three-dimensional and roughness effects. Busch[5] discusses the specific simulation schemes most applicable to each ice shape classification and analyzes the aerodynamic differences between simulations and castings.

1.1.3.1 Current Method: Mold and Casting

In the 1980s, Reehorst and Richter[12] developed the mold and casting method as it is currently employed. This method replaced an older method that used wax and plaster and supplemented the two-dimensional ice tracings described previously. The mold and casting method employs molds made from ice accretions in an icing wind tunnel to make castings to be used in aerodynamic dry-air wind tunnel tests. The benefit of this method is its ability to capture three-dimensional features and small roughness details that are unable to be documented by the other previously available methods. The mold and casting process is time consuming due to curing and casting preparation time. Each mold or casting needs from a few hours to overnight to cure. Due to the freezing temperatures required during mold curing to prevent the ice accretion from melting, the specific mold material capable of curing at those temperatures is extremely stiff. Because of this, the mold is destroyed after one casting is made, and another more flexible and durable mold must be made. This adds another step to the process. Each casting must then be cut to size and is usually instrumented with pressure taps in order to be used in dry-air wind tunnel testing. Additionally, the larger the model, the greater the amount of costly molding and casting material is required. The greatest drawback is that these molds and castings are the only documentation of the ice shapes. Possessing a digital copy of the ice shape would be beneficial for record-keeping, comparison, scaling, computation, cost, and ease-of-use purposes.

1.1.3.2 New Method: 3-D laser scanner and rapid-prototyping methods

In response to the need for a more capable and robust ice accretion recording and measurement process, NASA investigated using a 3-D laser scanning system and rapid-prototype methods to record ice accretions and to generate ice shapes for testing.[28] Lee et al.[28] describe the development process of this system in detail. A 3-D laser scanner is used to scan an ice accretion. The chosen scanner, the Romer Absolute system, is arm-based and proved to be the most effective at scanning shapes, ease-of-use, and operating in the cold temperatures of the IRT. The scanner is used in conjunction with software that is able to fill in holes and gaps in the data to create “water-tight” surfaces, which are completely enclosed, in order to put the data in a form that can be used by rapid-prototype methods.[1] The holes for the pressure taps can be added in the software, and are created during the rapid-prototype

process. Initial testing with this process resulted in the ability to scale an ice shape scan to a smaller size and produce small-scale rapid-prototype shapes.[28] Qualitatively, Lee et al.[28] show the good agreement between full, 1/3, and 1/5 scale shapes. This agreement can be seen in Figure 1.7, where the smaller scale shapes visually to a good job of replicating the features on the full scale shape. Broeren et al.[1] include trace data from the castings and scan data at the same spanwise location. They conclude there seems to be good agreement between the methods.

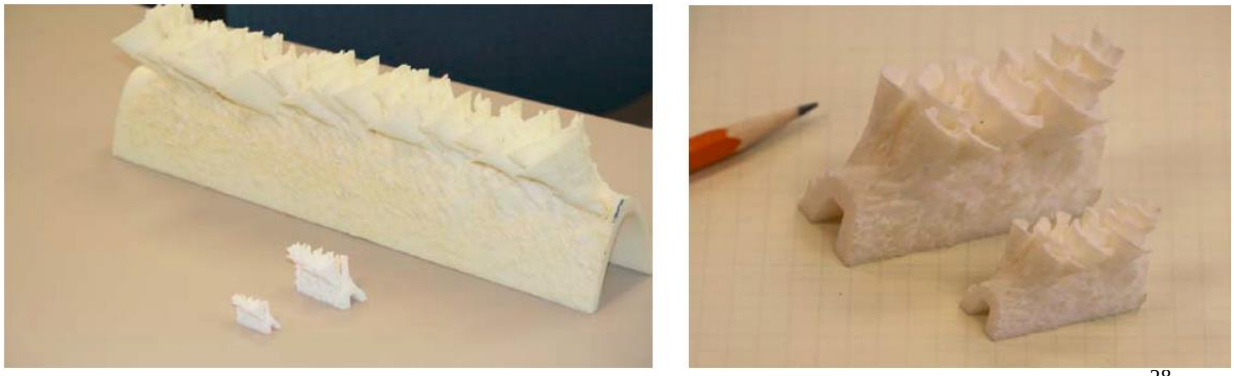

Figure 1.7: Full, 1/3, and 1/5 scale ice shapes made from the 3-D laser scanner method.[28]

1.2 Pressure-Sensitive Paint

The pressure-sensitive paint (PSP) method is a technique that was first developed in the 1980s and is becoming an accepted method for wind tunnel testing. It is based on photophysical properties that relate emitted intensity from excited paint particles to pressure. A PSP that is applied to an aerodynamic surface can yield pressure data over the entire painted area. This is a great increase in resolution compared to the amount of data that can be measured using discrete pressure taps. The highly three-dimensional flow of a swept wing cannot be well documented using a reasonable number of taps. For this reason, PSP was investigated as a means of obtaining three-dimensional pressure data over the model surface. A first step in this process was to use this method on the airfoil model to see if the PSP could resolve differences between the shapes made from the old and new methods. The effects of the three-dimensional features of the ice on the flowfield could be investigated using PSP.

1.2.1 Pressure-Sensitive Paint Background and Basics

1.2.1.1 Basic Theory

The pressure sensitive paint (PSP) technique uses the photophysical processes associated with excited electrons returning to their ground states in order to relate the intensity of luminescing particles, or luminophores, to pressure. Luminescent materials are defined as being "capable of absorbing energy and reemitting visible light."[13] PSP consists of two main components: the luminescing luminophores and the binder in which those luminophores are suspended.

When luminescing particles in PSP are excited using a high-energy excitation source, such as a lamp or laser, the particles absorb the radiative energy from the photon so that the electrons in the paint transition to higher energy levels. In order for these electrons to return to the ground state, the particles must lose the energy they gained through excitation. There are multiple ways this energy can be released, though the two most pertinent to PSP are fluorescence and external conversion through oxygen quenching. Fluorescence is a loss of energy through the emission of photons, and is a specific type of luminescence. Another type of luminescence is phosphorescence, which occurs over a longer time period and involves energy conversions from different energy levels than fluorescence. External conversion is the loss of energy through electron encounters with environmental entities. Oxygen quenching, or the external conversion of excited electrons due to collisions with oxygen molecules, is a competing process to fluorescence in PSP. In order to return to a ground state, the excited particle must lose a specific amount of energy. The greater amount of this energy lost to oxygen collisions in oxygen quenching, the smaller the amount of energy given off through fluorescence and vice versa. In other words, the greater the number of oxygen molecules able to interact with the excited particles, the fewer the photons given off as fluorescence. Since the number of oxygen molecules present is directly proportional to static pressure, the intensity of light emitted by fluorescing particles can also be related to pressure. These reactions form the basis for PSP.

A relationship between the local intensity of the emitted protons from PSP and the local pressure is derived from the Stern-Volmer equation. The Stern-Volmer equation, Eq. 1.1, states the intensity changes between systems with and without a quenching molecule.

$$\frac{\Phi_0}{\Phi} = \frac{I_0}{I} = 1 + \frac{k_q}{k_r + k_{nr}}[Q] \quad (1.1)$$

Φ is the quantum yield of luminescence and is equal to the rate of luminescence over the rate of excitation. I is the intensity of the emitted light. The three temperature-dependent constants, k_q, k_r, and k_{nr} are the rates associated with deactivation due to quenching (k_q), radiative emission (k_r), and non-radiative deactivation (k_{nr}). $[Q]$ is the concentration of the quenching molecules. The subscript 0 denotes the non-quenching reference state where no quenching molecules are present. According to Henry's Law, the partial pressure of oxygen is proportional to the concentration of oxygen. Therefore, $[Q]$ is proportional to the pressure, p. In most aerodynamic applications, it is not feasible to reach a state where no oxygen is present. Therefore, a different reference condition is used. The ratio of the Stern-Volmer equation at this reference state to the state of interest is the form of the equation used in aerodynamic testing. The reference condition is the "wind-off" condition where the wind tunnel velocity is zero. This is in comparison to the "wind-on" condition when the wind tunnel is running at some speed. The pressures over a model in the "wind-on" condition can be determined through the Stern-Volmer equation and known pressures at the "wind-off" condition with Eq. 1.2.

$$\frac{I_{ref}}{I} = \frac{\tau_{ref}}{\tau} = A(T) + B(T)\frac{p}{p_{ref}} \quad (1.2)$$

The coefficients A and B are both temperature dependent since they consist of the k terms, all of which depend on temperature. A more detailed derivation can be found in Liu and Sullivan.[14]

1.2.1.2 History

The development of pressure-sensitive paint (PSP) technology for aerodynamic applications began in the 1980s in the United States at the University of Washington and independently in the Soviet Union at the Central Aero-Hydrodynamic Institute (TsAGI). However, the effect of oxygen quenching on luminescence has been known since 1935 with the work done by H. Kautsky and H. Hirsch.[15] It was not until 1980 that oxygen quenching and fluorescence were used for flow visualization by Peterson and Fitzgerald.[16] Following this, luminescent coatings were used in biomedical and chemical applications before being used for aerodynamic testing.[14] Since then, a substantial amount of research has been done

and progress made in the pressure-sensitive paint area. Once the concept of PSP was proven, most of the research has involved improving the accuracy of the method. Important areas are in temperature effect compensation, image registration, image resection, and increased paint response. A number of methods have been developed to address these concerns and will be described briefly in the next section. Currently PSP is well beyond the proof of concept stage and has begun to be used as an integral flow diagnostic in aerodynamic testing.

1.2.1.3 PSP Methods

There are two main PSP methods: intensity-based and lifetime-based. Intensity-based, or radiometric, PSP uses imaged intensity values to determine surface pressures. Lifetime methods use the decay of luminescent intensity to determine pressure.

The single channel radiometric PSP method is straightforward. Much of the initial PSP research and proof-of-concept was performed with this technique. The "single channel" refers to the sole type of luminophore particles embedded in the paint binder. This is in contrast to other paints that contain multiple fluorescing particles. The single channel method employs the Stern-Volmer relation (Eq. 1.2) as its scientific basis. Two sets of images are used in this method: the wind-off and wind-on intensity images. Since the pressure at the reference wind-off condition is known, the wind-on static pressure over the surface can be calculated. The ratio between the wind-off and wind-on images theoretically removes luminophore concentration, paint thickness, and illumination spatial variation effects. It cannot, however, account for any temperature changes during data acquisition or spatially across the model. Temperature affects the emitted intensity of the paint similarly to how absolute pressure affects the emitted intensity.

Pressure sensitive paints containing multiple luminophores aim to remove the temperature dependence of the paints. A binary paint contains two luminophores: the first, the signal probe, is sensitive to both pressure and temperature, and the second, the reference probe, is only sensitive to temperature. If the temperature dependence of both luminophores is the same, then a ratio of the intensity from the signal probe to the intensity of the reference probe during the wind-on condition will remove the temperature dependence. A paint that is independent of temperature effects is called an ideal paint.[17] While the ratio of the signal-probe intensity to the reference-probe intensity theoretically removes temperature

dependence, it does not remove luminophore concentration effects. Therefore, wind-off signal and reference images must also be acquired. Paint thickness and illumination effects are removed in the ratio of the signal to reference intensities. To apply this binary PSP concept, a ratio of the ratios is taken. This ratio of ratios is expressed in Eq. 1.3. Binary paints are designed to behave as close to an ideal paint as possible. Of course, the temperature dependence of the two luminophores is not exactly the same, so binary paints are not perfectly ideal. Further research is being performed to minimize temperature effects.

$$\frac{I_{S_0}/I_{R_0}}{I_S/I_R} = A(T) + B(T)\frac{p}{p_{ref}} \tag{1.3}$$

Theoretically, lifetime PSP methods are not limited by some of the drawbacks from which intensity (radiometric) methods suffer. The lifetime of the paint luminophores' luminescence is not a function of paint thickness, luminophore concentration, or illumination intensity. This comes with the additional benefit of not requiring a wind-off image, in comparison to most radiometric methods. However, lifetime PSP results are still susceptible to temperature effects, especially at lower speeds and dynamic pressures where the signal to noise ratio is small. At higher speeds and dynamic pressures, the increased signal from the paint is significantly greater than the noise due to temperature. The benefits of the lifetime PSP method are best applied at higher speeds and dynamic pressures.

Lifetime, τ, is defined as the time it takes the emitted intensity from the paint luminophores to decrease by a factor of e when the decay signal can be fit with an exponential function. This method uses intensity images taken from multiple "gates," or time intervals, in the emission signal during and after an excitation pulse. Figure 1.8 shows typical excitation and emission signals over time with two gates specified.[18] During gate 1 in this figure, the camera acquires the first image, which encompasses the time before the excitation pulse until the beginning of signal decay. During gate 2, the camera acquires the second, which encompasses the end of the signal decay. Using the Stern-Volmer equation, the ratio of the integrated intensity over each of the gates can be used to determine a calibration between this ratio and pressure. Temperature effects can be accounted for using a method similar to the binary radiometric method, where a reference probe is used to remove the temperature dependency of the paint.[19]

The main benefit of using a lifetime method, especially at low speeds, is its independence from illumination effects that are the result of model deformation within the intensity field of the excitation source. However, some work has shown that the lifetime method is still susceptible to large amounts of noise that can be removed through a ratio with the wind-off condition, making the lifetime method no more beneficial than the intensity methods.[18] Crafton et al.[19] explain the noise inherent in lifetime PSP is a result of incomplete chemical processes that leave two types of fluorescing molecules in the paint. Since the lifetimes of these two probes are different and the probes are not distributed evenly within the binder, noise is present in the data.[19] Calculating the ratio of the wind-on lifetime with the wind-off lifetime would remove the dependence on the probe concentration, though this removes the main benefit of the lifetime method. In conclusion, Crafton et al.[19] recommend carefully implemented binary PSP methods for testing at low speeds. Higher-velocity flows yield higher signal-to-noise ratios, and can therefore benefit from lifetime PSP techniques.

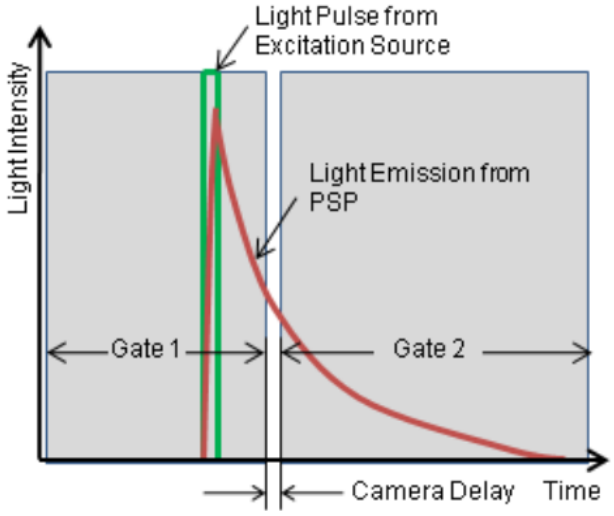

Figure 1.8: PSP excitation and emission decay with two gates for lifetime PSP method.[20]

1.2.2 PSP at Low Speeds

The difficulties of using the PSP method at speeds in the low-subsonic range stem from smaller pressure variations from the reference condition than are seen at high-subsonic or supersonic speeds. These small variations in pressure yield small variations in intensity and small signal-to-noise ratios.[21] For this reason, PSP experiments at low speeds are susceptible to errors that further decrease the signal-to-noise ratio. While these same errors may exist in high-speed PSP data, the associated noise is much smaller than the signal.[22]

Bell[21] lists that the major errors in low-speed PSP are random error from photon shot noise mostly, bias error from emitted intensity variations from temperature effects, and model deformation under aerodynamic loading. Despite the difficulties associated with low-speed PSP testing, careful experimental set-up with the correct equipment can yield good results. Lifetime or multi-luminophore PSP methods can also be successfully employed to reduce errors at low speed to obtain accurate, quantitative pressure data.

Bell[21] applied both single-channel and binary PSP to a NACA 0012 swept-airfoil model at NASA Ames Research Center and performed experiments at flow speeds as low as 17 m/s (55.77 ft/s). Using a careful experimental set-up and data processing scheme, errors of 0.0046 psi (31.7 Pa) for the binary case and 0.0033 psi (22.8 Pa) for the single-channel case were obtained. The single-channel case included ensuring the tunnel reached a thermal equilibrium by running for an hour before image acquisition and averaging enough images to reduce random error while keeping bias error low as well. It can be seen from the published data in Figure 1.9 that there is more spanwise pressure variation than is expected from a swept airfoil. This variation is visible especially towards the leading edge, where the lower pressure region has a smaller chordwise extent at the lower and upper model extremes of the model than at mid-span. The paper states that the model motion was small between the wind-on and wind-off conditions, meaning that a change in excitation illumination due to model deformation is most likely not the cause of this spanwise variation. It is therefore probable that temperature changes are the cause. This is supported in the data presented in Figure 1.10, where a binary paint was used for the same flow conditions. Here, there is less spanwise variation due to the removal of temperature effects. The tradeoff here was an increase in random noise. It should be noted that the CCD (charge-coupled device) array in the camera used by Bell[21] had a full-well capacity of 330,000 electrons/pixel. This is a very sensitive camera that will reduce error.

Crafton et al.[22] recently published an overview paper focusing on the use of PSP at low speeds, common errors associated with those speeds, and the evolution of the method in that flow regime. The discussed error sources that produce significant errors in PSP experiments are: temporal and spatial temperature variations, temporal and spatial illumination changes, model displacement and deformation, sedimentation, photo-degradation of the paint, stray light, and camera shot noise. For low-speed flows,

illumination errors due to model motion and temperature errors are the most detrimental. Crafton et al.[22] document the movement from proof-of-concept work using single-luminophore PSP to bi-luminophore PSP that can minimize temperature and illumination affects. They state that an ideal binary paint is most effective, if used in conjunction with careful experimental set-up. They tested models with PSP at Mach numbers of Mach 0.3 and as low as Mach 0.05 and deviations between the pressure tap and PSP data as small as 50 Pa (0.0073 psi) in small tunnels and 100 Pa (0.0145 psi) in large tunnels.[22]

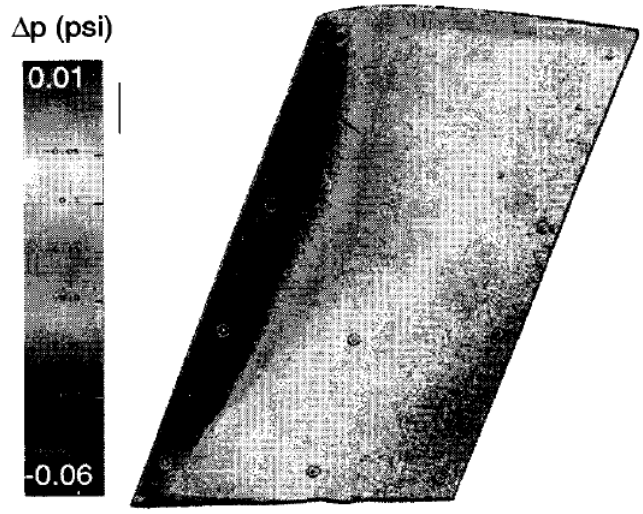

Figure 1.9: Single luminophore PSP data from Bell.[21]

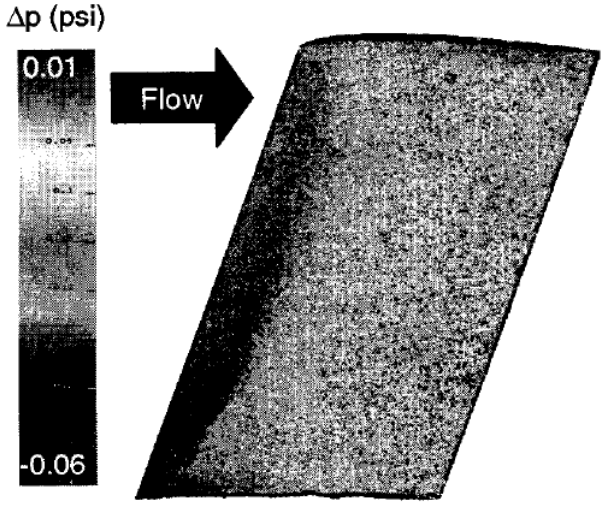

Figure 1.10: Binary PSP data from Bell.[21]

1.2.3 PSP and Icing Research Background

Some work in icing has been performed using PSP as a flow diagnostic. Bencic[23] developed a PSP technique to apply the paint directly to an ice accreted model in the IRT. The paint was applied and cured at sub-freezing temperatures, and PSP data acquired in the icing tunnel for two GLC 305 airfoils. It was concluded that PSP could successfully be applied to ice accreted models and that there was excellent agreement between the PSP and pressure tap data. It was also found that the PSP results differed between the iced region of the tested airfoils and the clean aluminum model section downstream of the ice. Ferrigno et al.[24] also studied icing using a PSP technique on a NACA 0012 model with simulated rime and glaze ice shapes. It was concluded during that work that PSP is a potentially beneficial technique to obtain pressure data over a surface. This work was performed at low speeds of $M \approx 0.2$, proving further that PSP results can be obtained in flows with small pressure gradients. A short study was performed in the UIUC 2ft by 2ft subsonic wind tunnel on a NACA 0012 model with and without an ice shape using binary PSP. This work is recorded by Crafton et al.[22] Figure 1.11 shows the published data from this test, where the PSP results qualitatively yield information about the separated flow region behind the ice shape. Diebold et al.[25] studied the pressure field of a swept wing, based on the Common Research Model,[26] using a radiometric PSP method at low speeds ($M \approx 0.18$). The presence and growth of a leading-edge vortex was clearly seen in the results shown in Figure 1.12, providing additional, though mostly qualitative, information about the aerodynamic penalties due to an ice shape that could not be obtained with pressure taps only. This is especially true for a swept wing, where the chordwise pressure distribution is not constant along the span. Diebold et al.[25] concluded that PSP was a useful technique for enabling further understanding of a three-dimensional flowfield.

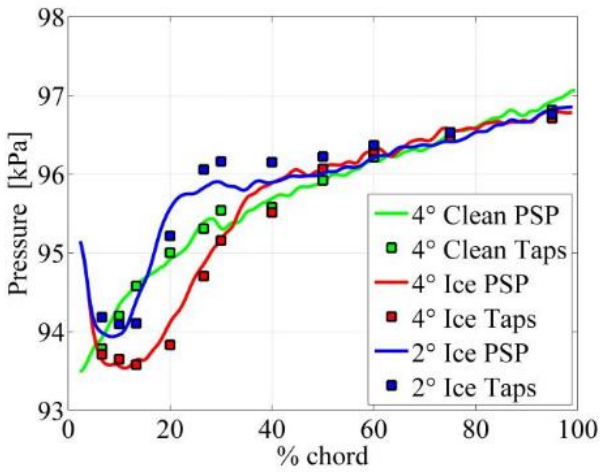

Figure 1.11: Comparison of PSP and pressure tap data for a clean NACA 0012 model and simulated ice using Binary FIB PSP.[22]

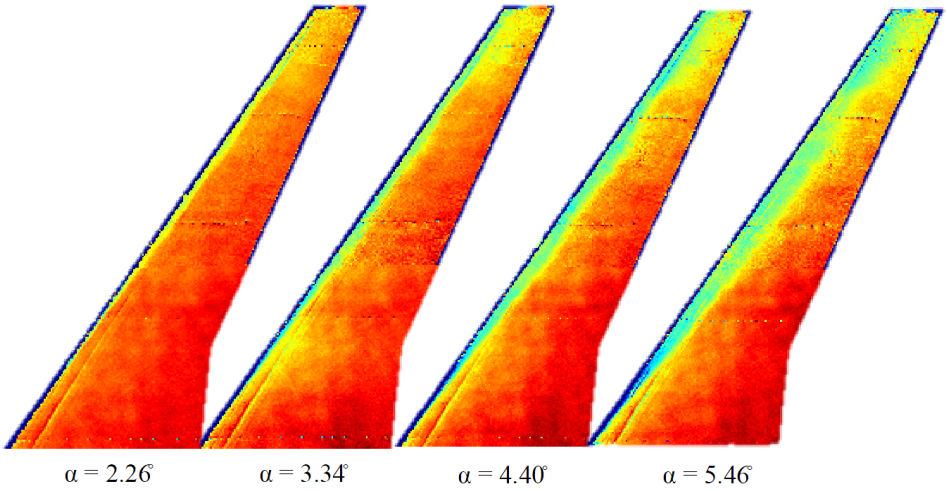

Figure 1.12: PSP data for a swept wing with simulated horn ice shape over an angle of attack range.[25]

1.3 Motivation

This work was performed in support of the validation of the three-dimensional ice accretion measurement methodology recently developed by NASA. The successful validation of this method with the currently-employed mold and casting process will enable future testing of large-scale ice shapes for the joint swept-wing icing project. The overall project seeks to improve the understanding of all aspects of icing on swept-wings and to obtain high-fidelity experimental icing data. This specific project seeks to aerodynamically

demonstrate that ice shapes from the new technique can reasonably replicate the performance of shapes from the mold and casting technique.

The second goal was to further implement the PSP method in the UIUC Aerodynamics Research Lab. A desired objective was to demonstrate the lab's ability to use PSP as a viable tool for subsonic testing of swept wings to gain high resolution pressure data in three-dimensional flows, through initial testing on an airfoil model. This method has the potential to provide important data on a swept-wing model which are unable to be obtained from discrete pressure taps. The iced-airfoil flowfields studied in this test allow evaluation of the PSP method in a well-understood flowfield. The focus of this study is to jointly validate the newly developed ice shape replication method with the use of the PSP method.

1.4 Objectives and Approach

The objectives of this study are:

- Determine whether ice shapes documented using a 3-D laser scanner and constructed using rapid-protype processes can accurately reproduce the ice-airfoil aerodynamics of ice shapes generated from the accepted NASA mold and casting process.
- Understand how any flowfield differences explain or relate to the discrepancies between aerodynamic data for the two sets of ice shapes.
- Determine how a pressure sensitive paint (PSP) method can be applied to these models to contribute to further understanding their flowfields, as well as how this contribution compares to more traditional surface pressure and flow visualization methods.

These objectives were pursued through experimental aerodynamic testing and comparison of both castings and rapid-prototype shapes on a NACA 23012 airfoil model. This validation test uses an airfoil model since iced-airfoil flowfields and aerodynamics are well understood. Documenting airfoil ice shapes with the newly developed method is a simpler first step than scanning swept-wing ice shapes. Additionally, the two-dimensional model allows the PSP technique to be further understood. That knowledge can then be applied to swept-wing models with more complex flows.

The wind tunnel comparison tests include force balance measurements, discrete surface pressure measurements from pressure taps, wake surveys with total pressure probes, surface oil flow visualization, and pressure-sensitive paint (PSP). This variety of experimental techniques allows aerodynamic and flowfield differences between the ice-shapes made from the current mold and casting method and the new 3-D laser scanner technique to be well understood.

This thesis is divided into three main chapters. The first chapter, the Introduction, describes the background necessary to understand the context and motivation of this work. The next chapter, the Experimental Methodology, describes in detail the experimental methods employed to validate the 3-D ice accretion measurement methodology and the facilities in which the tests took place. The last main chapter is the Results and Discussion, where the results from these tests are presented and analyzed. Following that, a Conclusions, Summary, and Recommendations section summarizes the work. Suggestions for future work are also made. The thesis includes appendices with specific descriptions of the PSP post-processing method, the mold and casting method, and measurement uncertainty analysis.

Chapter 2

Experimental Methodology

The experimental equipment used and test procedures followed during the course of this work are described in the proceeding chapter. These descriptions include details of the ice shape acquisition methods, the wind tunnel testing facilities, the employed experimental techniques, and the data post-processing techniques.

2.1 Ice Shape Acquisition

The ice accretions used in this study were generated in the NASA Glenn Research Center Icing Research Tunnel (IRT). After each run, the ice accretion was first documented with a digital scan using the 3-D laser scanner and second by making a mold. The molds from this test were sent to the University of Illinois at Urbana-Champaign (UIUC) to make the cast ice shapes used during dry air testing. The digital scans were processed by NASA and used with rapid-prototype processes to make the rapid-prototype ice shapes that are compared to the casting ice shapes as an objective of this work.

2.1.1 NASA Icing Research Tunnel (IRT) Test

The IRT is a closed-return, atmospheric, refrigerated tunnel used for icing research purposes. The airspeed within the 6ft by 9ft test section can vary between 50 and 350 knots and the temperature can be controlled down to -25 degrees Celsius within +/- 0.5 degrees. Upstream of the test section are spray bars that create an icing cloud within the tunnel of supercooled water droplets with median volume diameters between 15 and 50 microns. The icing cloud is about 4.5ft by 6ft centered in the IRT and its water content can be varied from 0.2 to 2.5 g/m^3. Models are mounted on a turntable in the test section floor.[27]

Ice accretions for twelve different icing conditions were generated during testing on a NACA 23012 aluminum model with a chord of 18 inches that spanned the 6ft height of the

test section. The conditions were chosen in order to generate ice shapes that correspond to the four classifications defined by Bragg et al.[3] as roughness, horn, streamwise, and spanwise ridge. Additionally, the conditions are the same as those used in the tests performed by Busch[5] in order to compare data and validate test methods. The NACA 23012 IRT model features a removable leading edge that can be detached along with an ice accretion and placed in a mold box to create a mold. For each of the twelve test cases, the IRT was cooled to the desired temperature and the icing cloud formed for a specified length of time. Once the ice accretion was generated, the tunnel was stopped and documentation of the shape began. Digital photographs were first taken and then the laser scanner method described by Lee et al.[28] was performed. The ice was first sprayed with a titanium-dioxide, highly reflective white paint that gives the laser scanner an opaque surface to scan, rather than the transparent and refractive ice. The chosen Romer Absolute arm-based 3-D laser scanner was then used to scan the ice accretion in conjunction with the GeoMagic software.[28] Once a sufficient number of data points were collected, the model's leading-edge section was removed with the ice and placed in a mold box. The mold material was poured into the mold box with the leading edge and ice accretion and left to cure overnight in a refrigerated environment. After curing, the mold was returned to room temperature, the ice melted, and the mold removed from the mold box. All twelve molds were then shipped to the UIUC Aerospace Engineering Research Machine Shop for casting production. During an identical run, the same ice shapes were generated in order for a 2-D tracing of the shape near the center of the model span to be made. The tracing method is one of the IRT's standard methods of recording two dimensional ice shapes. A heated metal plate with a NACA 23012 cutout is used to melt a small section of ice. The plate is removed and replaced with cardboard with the same NACA 23012 geometry cutout. A pencil is then carefully moved around the ice accretion to record its important features on the cardboard.

2.1.2 Casting Production

The mold material used in the IRT to create the original molds must be able to cure at colder temperatures to ensure that the ice does not melt during pouring and curing. These colder temperatures are typically not within the design temperature range of most molding materials. The specific mold material used in this step of the process was chosen because it

is able to cure at cold temperatures. A consequence of using this material is that the resulting mold is extremely stiff and breaks easily when removing a casting. Therefore, the molds needed to be remade of a more durable and flexible material. To do this, master castings of all twelve ice shapes were made using Freeman 1080 Slow Polyurethane Elastomer that was tinted green for visibility. From the twelve master castings, six were chosen to be used in the aerodynamic performance tests. These six master castings are pictured in Figure 2.1. This choice was based on shape uniformity over the span of the casting and so that each classification of ice shape was represented. The digital scans from the 3-D laser scanner were also used in the selection process to ensure that the scanner had successfully captured the features of the ice shape selected. The chosen six master castings were used to create new molds with GT 5092 High Strength Silicone RTV that are more durable than the original molds and are able to be used repeatedly.

Each new mold was used to make four production castings: three test castings and one sacrificial casting. The sacrificial casting was cut at the spanwise location of the pressure taps and traced. This was done in order to obtain a general outline of the ice shape at the tap location and to assist in determining individual tap placement. Each trace was digitized and imported into a CAD program, where the coordinates and orientations of the tap holes were chosen and applied based on the trace geometry. Each of the three test castings were machined to a length of 11 3/16 inches at the spanwise extent chosen earlier and drilled for mounting holes. All three castings were mounted simultaneously on the leading edge of the UIUC NACA 23012 model as shown in Figure 2.2. The edge locations on the test castings were chosen to minimize the discontinuities between adjacent shapes and so the ice was as uniform as possible over the span. One of the three test castings was instrumented with 20 pressure taps at the locations and orientations determined in conjunction with the CAD drawing of the two-dimensional trace. One of the instrumented castings can be viewed close-up in Figure 2.3 and all six sets of completed test castings can be seen in Figure 2.4. The entire casting method is described in more detail in Appendix C.

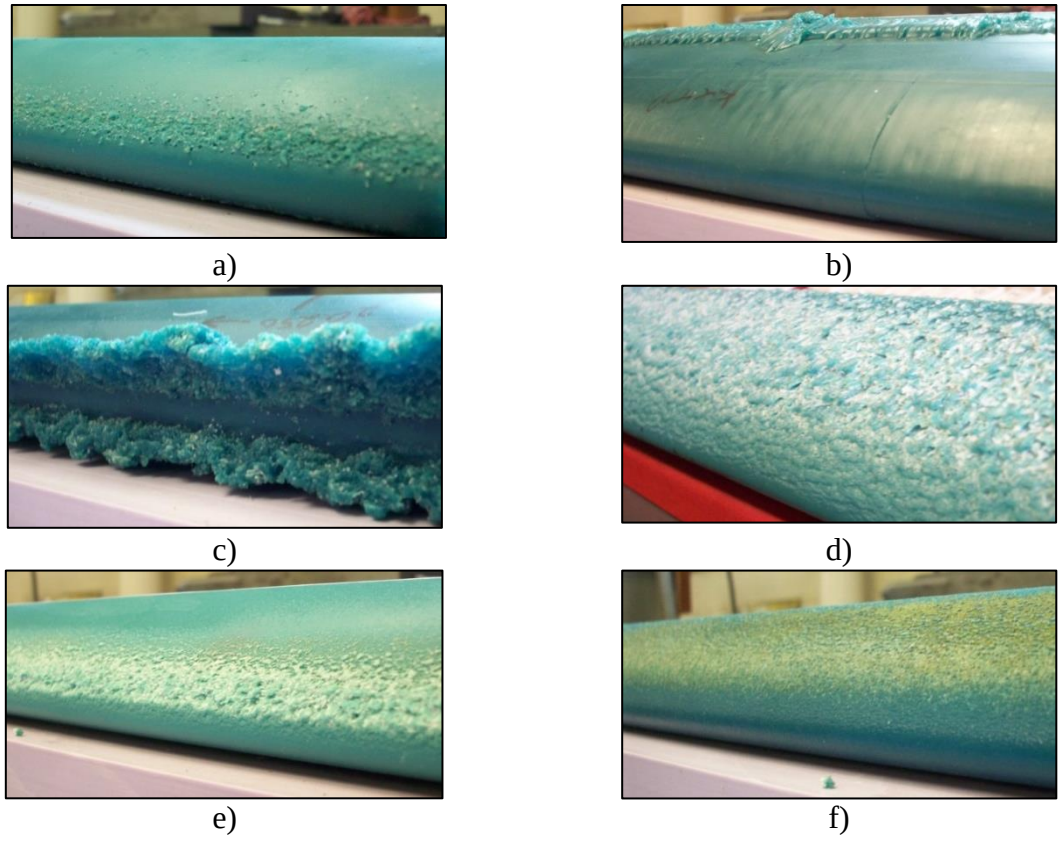

Figure 2.1: Master castings of tested ice shapes, a) ED1974 roughness, b) ED1967 runback (spanwise-ridge), c) ED1978 horn, d) ED1977 streamwise, e) ED1966 streamwise, f) ED1983 roughness.

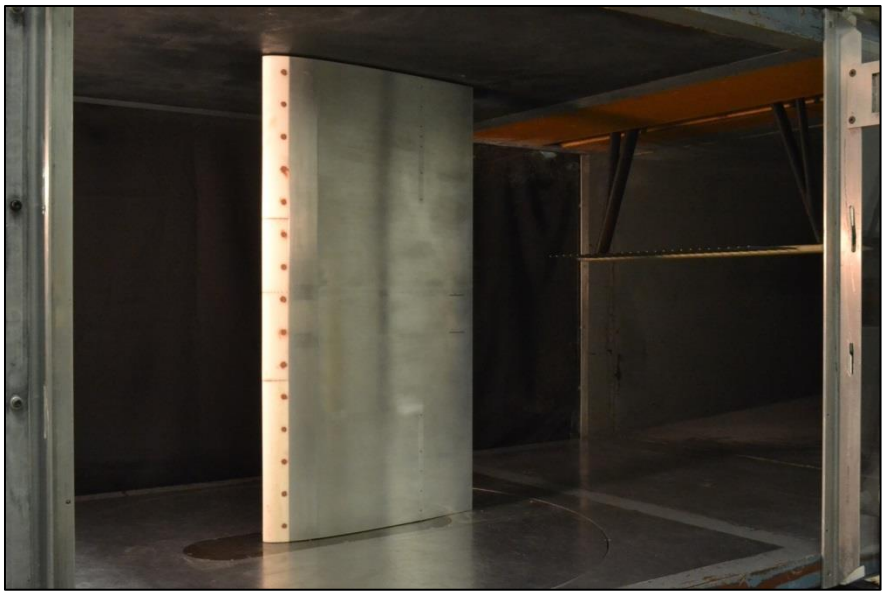

Figure 2.2: Three test castings (ED1983 roughness) installed on the NACA 23012 model in the tunnel test section.

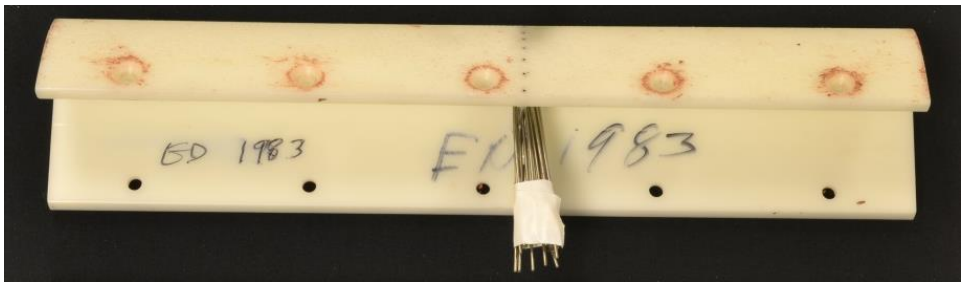

Figure 2.3: Instrumented test casting (ED1983 roughness).

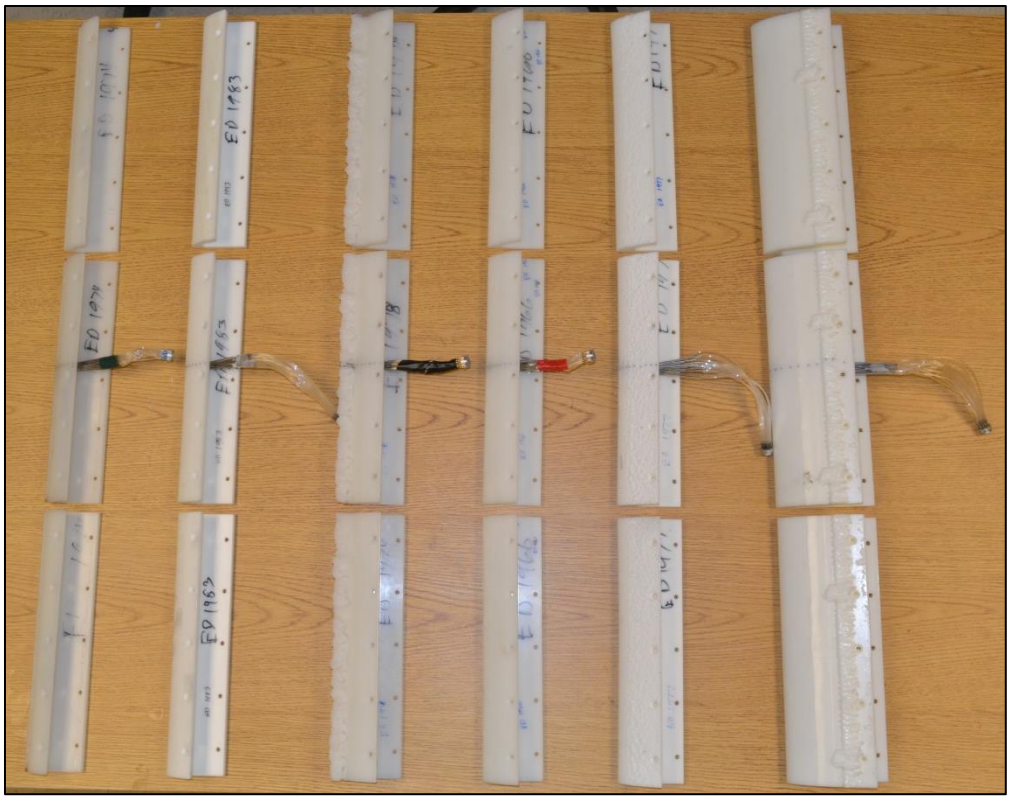

Figure 2.4: All Test Casting Ice Shapes. From left to right: ED1974 roughness, ED1983 roughness, ED1978 horn, ED1966 streamwise, ED1977 streamwise, and ED1967 runback.

2.1.3 Rapid-Prototype Shape Production

The digital scans acquired by the laser scanner were post-processed by NASA using the method outlined in Lee et al.[28] Any holes in the data were filled using the GeoMagic software. The geometry of the UIUC NACA 23012 leading edge and the mounting hole pattern were used with the scans of the ice accretions to create files that could be used with the rapid-prototype processes. Five of the shapes were fabricated using only a

stereolithography (SLA) process, while the sixth shape was fabricated using both sterolithography and Polyjet processes. Both stereolithoraphy and Polyjet techniques are rapid-prototype methods. The two different materials and processes were chosen to test the aerodynamic effects of the methods' differing resolutions. Stereolithography involves building parts in a vat of resin. A laser beam is used to cure the resin in the shape of the part layer by layer. Polyjet involves a jetting head dispensing resin on a building plate layer by layer. The resin is cured immediately using UV light.[29] Three identical rapid-prototype segments were made for each shape. These correspond to the same 11 3/16 inches spanwise segment chosen for the castings. The pressure tap locations were chosen prior to fabrication and the holes made as a part of the rapid-prototype process in one of the segments. The final seven sets of rapid-prototype shapes are presented in Figure 2.5.

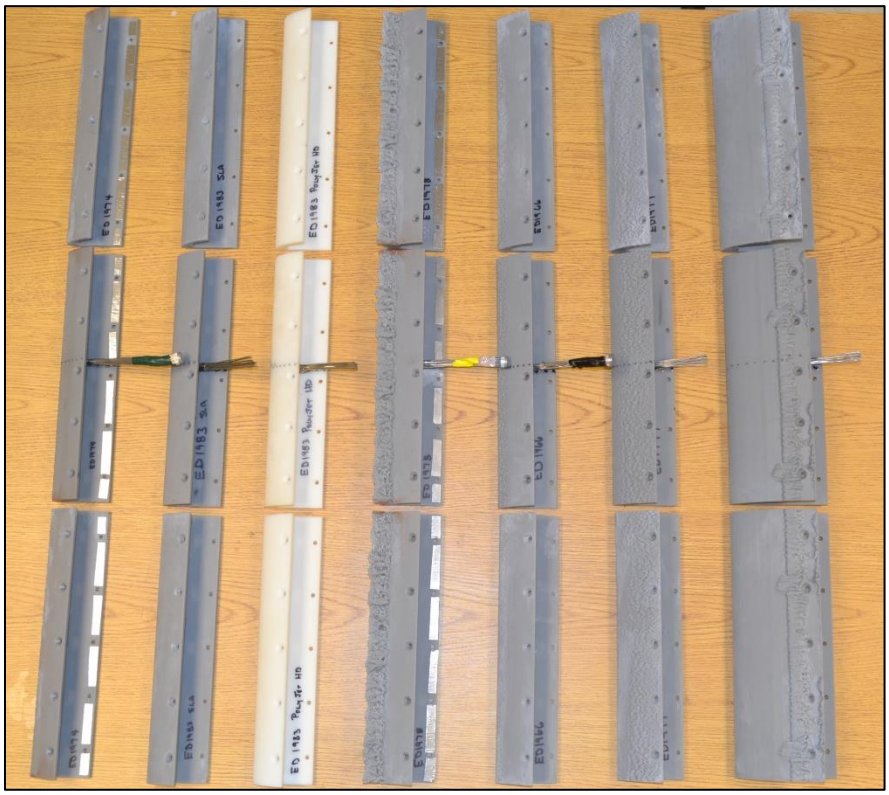

Figure 2.5: All Test RPM Ice Shapes. From left to right: ED1974 roughness, ED1983 roughness (SLA), ED1983 roughness (PJ), ED1978 horn, ED1966 streamwise, ED1977 streamwise, and ED1967 runback.

2.2 Aerodynamic Testing

2.2.1 UIUC Aerodynamics Research Lab Wind Tunnel Facility

The dry-air, aerodynamic wind tunnel testing for the 3-D laser scanner validation was performed at the UIUC subsonic wind tunnel in the Aerodynamics Research Lab. The tunnel is an open-return type with a rectangular 2.8ft by 4ft by 8ft test section. The width and height of the test section increase by 0.5 inches from beginning of the test section to the end in order to account for the growth of the floor boundary layer. The contraction ratio between the inlet and the test section is 7.5:1. The turbulence intensity is kept to below 0.1% at all operating speeds through the presence of flow straighteners, 4 inch honeycomb and four screens, at the tunnel inlet. The tunnel fan can reach rotational speeds of 1200 rpm, which corresponds to about 165 mph or 242 ft/s. The 5-bladed fan is driven by a 125 hp AC motor which is regulated by a variable frequency drive (ABB ACS 800 Low voltage AC drive) and controlled by a Labview code on a personal computer. A schematic of this facility is shown in Figure 2.6.[30,31]

The test section velocity (U_{ts}) is determined from the measurement of the pressure difference between the test section and the settling section ($P_{ss} - P_{ts}$) using Bernoulli's equation. There are four pressure taps each at the tunnel inlet and the beginning of the test section, one on each of the four sides of the tunnel, to measure static pressure. The static pressure taps are pneumatically averaged at each location and the difference measured by both a Setra 239 differential pressure transducer and an Electronically Scanned Pressure (ESP) module. The ESP system will be described in a later section. Using the combination of Bernoulli's equation in Eq. 2.1 and the conservation of mass for incompressible flow in Eq. 2.2, the velocity in the test section is calculated in Eq. 2.3. In the equations below, ρ_{amb} is the ambient density. A_{ss}, U_{ss}, and P_{ss} are the settling section cross-sectional area, velocity, and static pressure respectively. A_{ts}, U_{ts}, and P_{ts} are the test section cross-sectional area, velocity, and static pressure respectively.

$$\frac{1}{2}\rho_{amb}U_{ss}^2 + P_{ss} = \frac{1}{2}\rho_{amb}U_{ts}^2 + P_{ts} \tag{2.1}$$

$$A_{ss}U_{ss} = A_{ts}U_{ts} \tag{2.2}$$

$$U_{ts} = \sqrt{\frac{2(P_{ss}-P_{ts})}{\rho_{amb}\left(1-\left(\frac{A_{ts}}{A_{ss}}\right)^2\right)}} \tag{2.3}$$

The ambient density, ρ_{amb}, is calculated through the ideal gas law in Eq. 2.4, where *R* is the specific gas constant for air. The ambient temperature (T_{amb}) is measured using an Omega thermocouple, which is situated next to the tunnel. The ambient pressure (P_{amb}) is measured using a Setra 270 absolute pressure transducer open to the ambient air around the tunnel.

$$\rho_{amb} = \frac{P_{amb}}{RT_{amb}} \tag{2.4}$$

The dynamic pressure in the test section (q_∞) is calculated from Eqs. 2.1 and 2.2. Rearranging those two equations and using the definition of dynamic pressure, $q_\infty = \frac{1}{2}\rho_{amb}{U_{ts}}^2$, the dynamic pressure can be expressed as shown in Eq. 2.5. The pressure coefficient can then be calculated using the calculated dynamic pressure value. This equation is stated in Eq. 2.6.

$$q_\infty = \frac{1}{2}\rho_{amb}{U_{ts}}^2 = \frac{P_{ss}-P_{ts}}{1-\left(\frac{A_{ts}}{A_{ss}}\right)^2} \tag{2.5}$$

$$C_p = \frac{P-P_\infty}{q_\infty} = \frac{P-P_{ts}}{P_{ss}-P_{ts}}\left[1-\left(\frac{A_{ts}}{A_{ss}}\right)^2\right] \tag{2.6}$$

The Reynolds number based on the model chord (*Re*) is calculated using Eq. 2.7. Here, the freestream velocity is the test section velocity (U_∞) and the density is the ambient density (ρ_{amb}). The viscosity constant is calculated using Sutherland's law in Eq. 2.8. The reference viscosity coefficient and the reference temperature in Eq. 2.8 are the values for air at freezing conditions, where $\mu_0 = 3.58404\ x\ 10^{-7}\ lb\cdot s/ft^2$ and $T_0 = 491.6°\ R$. Using the ambient temperature measured by the thermocouple (T_{amb}) in Sutherland's Law, the viscosity coefficient is calculated. The tunnel Labview code held the Reynolds number to within 0.5% of the specified value. The maximum tunnel Reynolds number is 1.5 x 10^6/ft.

$$Re = \frac{\rho_{amb}U_\infty c}{\mu} \tag{2.7}$$

$$\mu = \frac{1}{\mu_0}\left[\left(\frac{T_{amb}}{T_0}\right)^{3/2}\frac{T_0+199.8}{T_{amb}+199.8}\right] \tag{2.8}$$

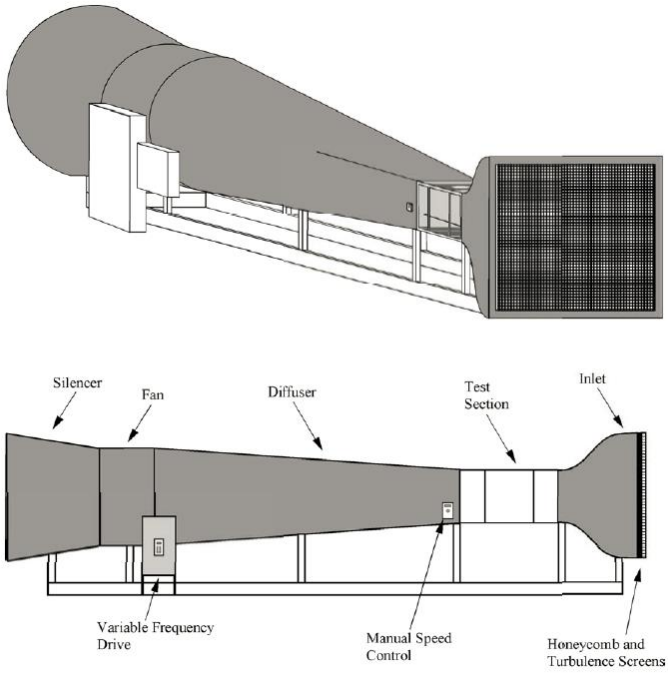

Figure 2.6: ARL 3ft by 4ft Subsonic Tunnel.[32]

2.2.2 Model

The model used for this testing is an aluminum NACA 23012 airfoil model with an 18 inch chord and 33.563 inch span. This particular model was chosen for this study to compare results with previous work by Busch[5] and to be used in conjunction with the IRT model of the same airfoil and chord. There are three interchangeable leading-edge pieces for this model: one clean leading edge and two leading edges used to mount ice shapes. These are shown in Figure 2.7. The model installed in the tunnel with the clean leading edge is pictured in Figure 2.8. The "Appendix C" leading edge is used to mount ice shapes that are representative of accretions formed in the conditions specified in Appendix C to Part 25 of the FAA Federal Aviation Regulations (FARs). The "Super-Cooled Liquid Droplet (SLD)" leading edge is used to mount ice shapes representing accretions formed in SLD conditions or on wings that use leading-edge heating devices, where ice forms further along the chord than in the Appendix C conditions. The seams between the mounted leading edges and the main body of the model are at x/c = 0.30 on the lower surface and x/c = 0.20 on the upper surface. The Appendix C leading edge has the geometry of the clean NACA 23012 airfoil from x/c = 0.13 to x/c = 0.30 on its lower surface and from x/c = 0.08 to x/c = 0.20 on its

upper surface. The remainder of the Appendix C leading edge is the mounting location for the interchangeable ice shapes. The SLD leading edge has the clean airfoil coordinates only on the lower surface, from x/c = 0.236 to x/c = 0.30. Cross-sections of both leading edges are shown in Figure 2.9. The cast and rapid-prototype ice shapes were mounted to the Appendix C and SLD leading edges as demonstrated in Figure 2.2.

The model was instrumented with surface pressure taps to obtain the 2-D streamwise pressure distribution over the airfoil. The primary row of 43 taps was located at z/b = 0.515. There was a secondary row with 22 taps at z/b = 0.417 span to compare the pressure distribution at another spanwise location to the primary row. The percent span is measured from the bottom of the model when mounted in the tunnel. A third spanwise row of 12 taps is located at x/c = 0.70 to detect any three dimensional and wall effects. Each ice shape is instrumented with 20 taps in line with the main row of pressure taps.

The model was installed vertically in the test section using eye bolts and an overhead crane. The upper surface faced the control room. It was mounted to the tunnel turntable and force balance with two struts extruding from the model that were clamped to the balance using L brackets. The model was installed so that there was an offset between the balance center and the model quarter-chord point of -0.25 in the x-direction (streamwise) and -0.3 in the y-direction (spanwise). A gap of about 0.02 inches was set by using metal spacers between the bottom of the model and the tunnel floor to minimize gap effects but to also ensure only the model remained metric. Care was taken to ensure the model was level in the test section. The gap between the model and the ceiling was set to about 0.125 inches, measured before the tunnel was started. This gap size varied slightly during testing as the suction at the leading edge increased with angle of attack which pulled the ceiling towards the model. Any cracks or gaps between the inside and outside of the test section, except the holes where the model struts passed through, were covered with Scotch book tape.

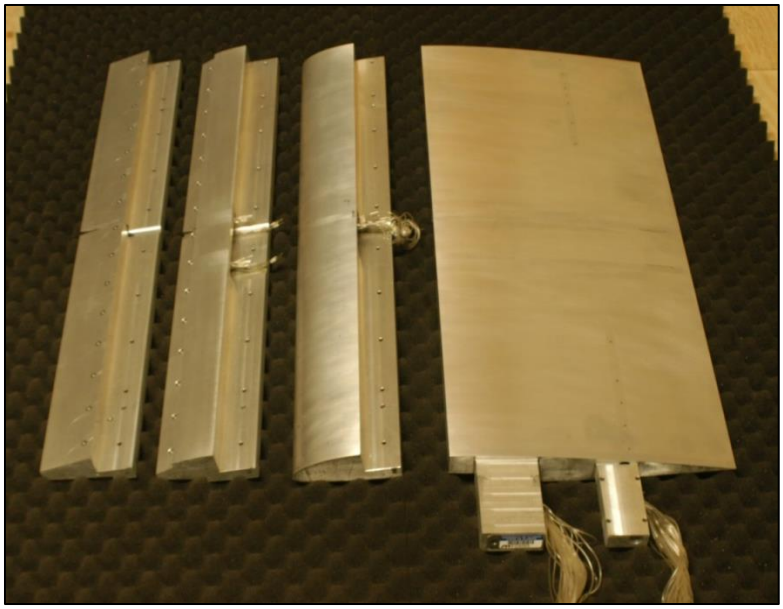

Figure 2.7: NACA 23012 model with three interchangeable leading edges. From left to right: SLD leading edge, Appendix C leading edge, clean leading edge, and main body.

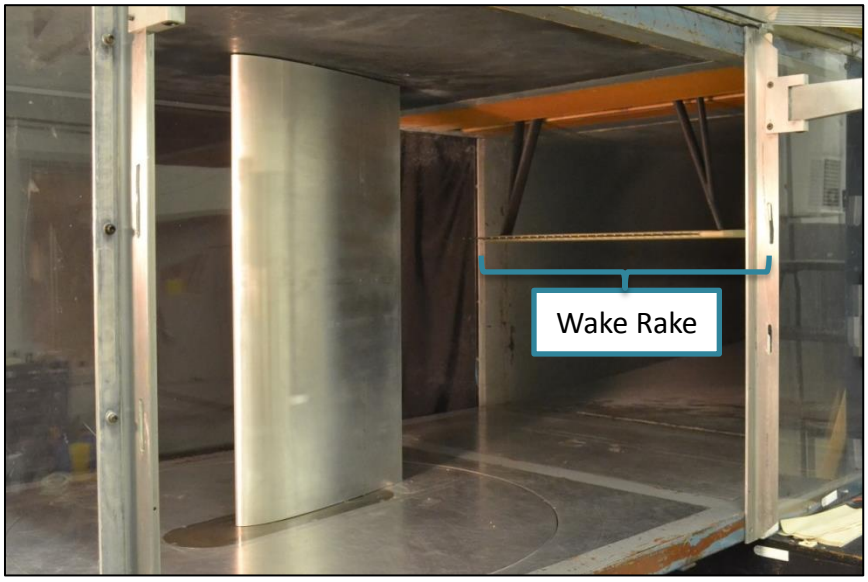

Figure 2.8: Clean NACA 23012 model installed in tunnel test section with wake rake.

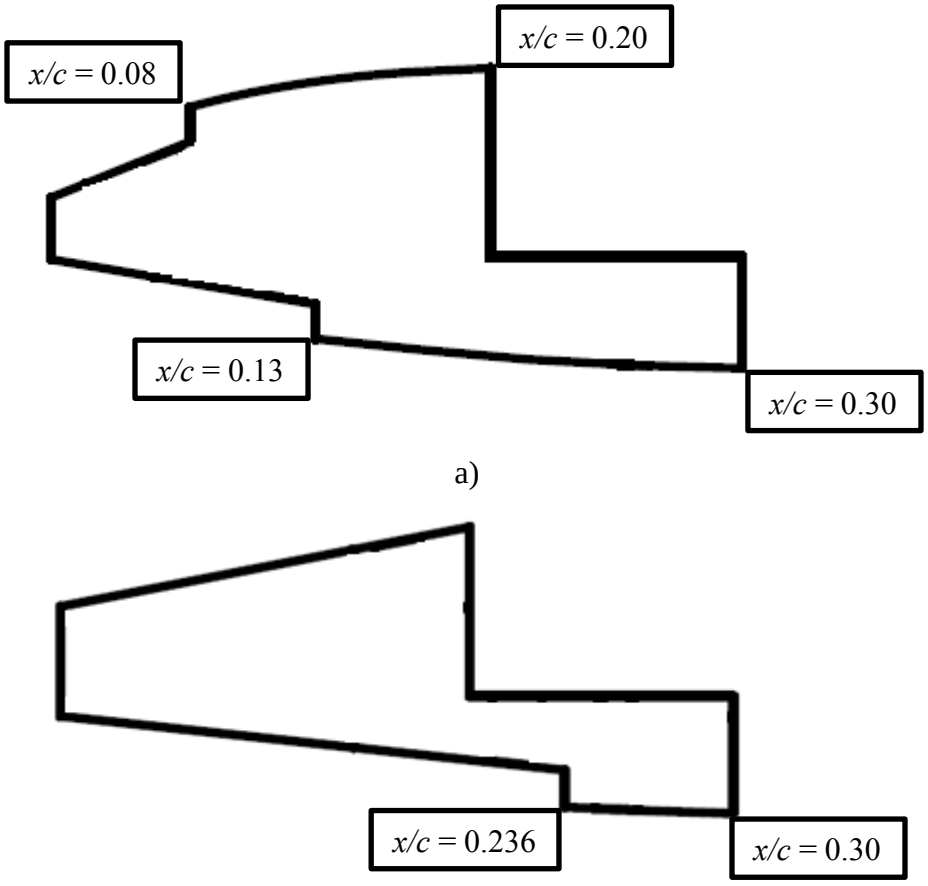

Figure 2.9: Model leading-edge cross-sections for ice shape mounting for a) Appendix C and b) SLD leading edges.

2.2.3 Wind Tunnel Data Acquisition System and Equipment

The data acquired for this study were obtained using a number of techniques that utilized different configurations and various pieces of instrumentation. Aerodynamic performance data were obtained through the use of the tunnel force balance, pressure tap system, and wake pressure survey system. Additional flow visualization was obtained using a surface oil flow visualization set-up. Pressure-sensitive paint data were acquired with optical equipment. Most data were recorded on the lab data acquisition computer using LABVIEW code to control the tunnel and save results. This computer was a Dell Precision T3400 with an Intel Core™ Quad CPU with 4GB RAM, run with the Windows XP 32-bit operating system. The PSP data were recorded on another lab computer. This computer has an Intel Core Duo CPU with 4GB RAM, and is run with Windows 7. The surface oil flow

visualization results were captured using a Nikon Model D3100 digital camera with an AF-S NIKKOR 18-55 mm 1:3.5-5.6G lens.

2.2.3.1 Force Balance

A three-component force balance is used to measure normal and axial forces and pitching moment. The balance was manufactured by Aerotech ATE Limited. Models are mounted through the tunnel floor to the force balance. The balance is connected to a turntable which is capable of setting the model angle of attack to within 0.1°. Measurements are obtained with three load cells: one for the axial measurement and two for the normal. The moment is calculated from the difference between the two normal load cells. The balance is set to measure loads in one of three ranges: low, medium, and high. The high range was chosen for these tests to be able to measure the loads on a large, heavy model tested at full tunnel speed. Table 2.1 shows the loads for the three ranges.

Table 2.1: Force balance ranges for high, medium, and low settings.

	High Range	Medium Range	Low Range
Normal Force	±450 lbf	±225 lbf	±90 lbf
Axial Force	±90 lbf	±55 lbf	±18 lbf
Pitching Moment	±45 ft-lbf	± 30 ft-lbf	± 15 ft-lbf

The voltage signals output by the load cells are within ±20 mV and are filtered through a 1 Hz low-pass filter. The signals are then amplified to a full-scale voltage of ±5V by the balance signal conditioner. To obtain a data point, 200 samples are taken at 100 Hz and averaged for the normal force, axial force, and pitching moment.

To account for loads present on the force balance from the weight of the model, balance tares were acquired over the entire angle of attack range tested. Tares were taken at the start of each day of testing as well as whenever ice shapes and leading edges were changed. The tare voltages were subtracted from the output voltages obtained during testing. The difference between the output voltage and the tare voltage was multiplied by a range ratio specific to the load range in order to obtain a scaled voltage. The range ratios for each load range are specified in Table 2.2.

Table 2.2: Force balance range ratios for high, medium, and low settings.

	High Range	Medium Range	Low Range
Normal Force	1	0.4944	0.2046
Axial Force	1	0.6278	0.2173
Pitching Moment	1	0.6755	0.3413

These scaled voltages (V_N, V_A, and V_M) are then input into a calibration matrix specific to this force balance to calculate the normal force, axial force, and pitching moment about the center of the balance. This calibration matrix is shown in Eq. 2.9.

$$\begin{Bmatrix} F_N \\ F_A \\ M \end{Bmatrix} = \begin{bmatrix} 37.7 & 0.01359 & -0.2095 & 0.01094 & 0 & -0.000865 \\ -0.1607 & 8.3125 & -0.01638 & 0.007084 & 0 & 0.007660 \\ -0.01299 & -0.005521 & 1.247 & -0.002122 & 0 & 0.00014978 \end{bmatrix} \begin{Bmatrix} V_N \\ V_A \\ V_M \\ V_N^2 \\ V_A^2 \\ V_M^2 \end{Bmatrix} \quad (2.9)$$

The lift and drag forces and the pitching moment about the quarter-chord of the airfoil model were then calculated in the tunnel LABVIEW code using the following equations, Eqs. 2.10, 2.11, and 2.12.

$$L = F_N \cos(\alpha) - F_A \sin(\alpha) \quad (2.10)$$

$$D = F_N \sin(\alpha) + F_A \cos(\alpha) \quad (2.11)$$

$$M_{c/4} = M + x_{offset} F_N + y_{offset} F_A \quad (2.12)$$

The non-dimensional aerodynamic coefficients are then calculated from the following equations:

$$C_L = \frac{L}{q_\infty S} \quad (2.13)$$

$$C_D = \frac{D}{q_\infty S} \quad (2.14)$$

$$C_M = \frac{M_{c/4}}{q_\infty S c} \quad (2.15)$$

2.2.3.2 Pressure Measurement

Measurements from the model static pressure taps were read using a Pressure System DTC Initium and Miniature Electronically Scanned Pressure (ESP) modules. Each ESP module contains 32 ports that connect via vinyl and steel tubing to the taps on the model surface. The modules are referenced to the tunnel static pressure. The modules are

connected to the Initium with PSCB cables and the Initium is connected to the tunnel data acquisition computer with an Ethernet cable. The Initium scans the modules at a rate of 650 Hz/channel and is calibrated to convert the voltages from the modules to pressure differences. Since the Initium is temperature compensated, its initial calibration is sufficient for all subsequent uses. The system does however need to be zeroed each time it is started. A burst of compressed nitrogen through a pressure line, which is connected to each module, moves a manifold inside each module. This signals the output voltages to be set to zero. A second burst of compressed nitrogen returns the manifolds to their original position.

Three types of ESP modules were used during this testing, corresponding to the range and resolution of pressure differences in psi (psid) that could be read. One ±5 psid module was used to measure the pressure differences at the leading edge of the model, where these values were higher than further downstream on the model. Two ±1 psid modules were used for a majority of the rest of the pressure taps and one ±0.35 psid module was used for the remaining taps.

The pressure coefficient measurements obtained at each pressure tap in the main tap row were used to calculate the airfoil lift and pitching moment following the method outlined by Busch.[5] The normal and axial pressure force coefficients on each small segment between taps were measured and calculated using the following two equations, Eqs. 2.16 and 2.17.

$$\Delta c_{N_i'} = \frac{Cp_i + Cp_{i+1}}{2}\left(x/c_{i+1} - x/c_i\right) \tag{2.16}$$

$$\Delta c_{A_i'} = -\frac{Cp_i + Cp_{i+1}}{2}\left(y/c_{i+1} - y/c_i\right) \tag{2.17}$$

To obtain the net normal and axial pressure forces, the sums of the forces over each segment were found using Eqs. 2.18 and 2.19.

$$c_{N'} = \sum_{i=1}^{n-1} \Delta c_{N_i'} \tag{2.18}$$

$$c_{A'} = \sum_{i=1}^{n-1} \Delta c_{A_i'} \tag{2.19}$$

Lift is determined with the following relation:

$$c_L' = c_{N'} \cos\alpha - c_{A'} \sin\alpha \tag{2.20}$$

The moment about the quarter-chord point for each segment is calculated using the following:

$$\Delta C_m = \frac{Cp_{i+1}\left(x/c_{i+1} - x/c_{c/4}\right) + Cp_i\left(x/c_i - x/c_{c/4}\right)}{2}\left(x/c_{i+1} - x/c_i\right) + \frac{Cp_{i+1}(y/c_{i+1}) + Cp_i(y/c_i)}{2}(y/c_{i+1} - y/c_i) \quad (2.21)$$

The net moment is found from summing the moment over the whole chord using Eq. 2.22:

$$c_{M'_{i_{c/4}}} = \sum_{i=1}^{n-1} \Delta\, c_{M'_{i_{c/4}}} \quad (2.22)$$

2.2.3.3 Wake Surveys

Wake pressures were acquired by total pressure probes on a wake rake to calculate the drag using momentum deficit theory. The wake rake had a span of 2ft between the centers of the first and last probes and was comprised of 25 probes equally spaced at 1 inch part. The tips of the probes were chamfered. Two ±0.35 psid ESP modules, which are referenced to the ambient pressure outside the tunnel, were used to measure pressure differential. Each probe was connected to a port on one of the two modules. The modules were zeroed at the same time as the modules used for measuring the model surface pressures. The specific rake used here has a large span in order to efficiently capture the edges of the large wakes that result from some of the ice shapes tested. The rake is connected to two Lintech traverses which are controlled by an IDC S6962 Stepper Motor Drive through the tunnel code. The traverses are situated within a sealed pressure box on top of the tunnel to reduce pressure leaks in the tunnel. The two-dimensional drag on the airfoil model is calculated more accurately using the wake survey method than the force balance drag measurement, since the drag from the force balance includes an induced drag component generated from the gap at the tunnel walls. Obtaining the wake pressures near the center of the model ensures that model end effects do not add an induced component to drag.

The tunnel code first finds the location of the wake and obtains pressure measurements at various intervals within the wake before calculating the profile drag. The code begins by searching for the wake center and moves the wake rake so that the center probe is located at that position. It then finds the wake edges, which were defined to be where the wake slope was less than the threshold value of 0.01 multiplied by the ratio of the test dynamic pressure to the maximum dynamic pressure ($q_{\infty,max} = 0.34$). The width of the

wake was calculated and used to determine the number of steps taken to obtain data. Table 2.3 tabulates this information.

Table 2.3: Wake rake step number and resolution

Wake width (in)	Number of Steps to Take	Resolution (in)
w > 16.5	2	0.5
14.5 < w < 16.5	3	0.333
12.5 < w < 14.5	5	0.2
10.5 < w < 12.5	7	0.143
w < 10.5	9	0.111

The airfoil drag is calculated from the model wake using the momentum-deficit method described by Jones.[33] This method defines two planes perpendicular to the freestream flow direction: the first plane (denoted by "1") sufficiently far downstream of the model that the static pressure in the wake is equal to the freestream static pressure, and the second plane (denoted by "w") located close to the model. The wake rake is positioned at this second plane. At the first plane, the drag per unit span is found from Eq. 2.23:

$$D' = \rho \int u_1(U_\infty - u_1)dy_1 \tag{2.23}$$

Following a streamtube from the second plane to the first plane, the conservation of mass can be applied as Eq. 2.24:

$$u_1 dy_1 = u_w dy \tag{2.24}$$

Solving the conservation of mass equation for u_1 and substituting into the previous equation, yields Eq. 2.25:

$$D' = \rho \int u_w(U_\infty - u_1)dy \tag{2.25}$$

The total pressures in the freestream (denoted by "∞"), at the wake rake plane, and at the downstream plane are expressed as Eqs. 2.26, 2.27, and 2.28 respectively:

$$P_\infty + \tfrac{1}{2}\rho U_\infty^2 = P_{o,\infty} \tag{2.26}$$

$$P_w + \tfrac{1}{2}\rho u_w^2 = P_{o,w} \tag{2.27}$$

$$P_\infty + \tfrac{1}{2}\rho u_1^2 = P_{o,1} \tag{2.28}$$

These three pressure equations are solved for the velocities at each location, U_∞, u_w, and u_1. It is assumed that the total pressure between the wake rake plane and the downstream plane is constant ($P_{o,1} = P_{o,w}$). Substituting the velocity values into the drag equation yields an expression (Eq. 2.29) for drag in terms of pressure differentials.

$$D' = 2\int \sqrt{P_{o,w} - P_w}\left(\sqrt{P_{o,\infty} - P_\infty} - \sqrt{P_{o,w} - P_\infty}\right)dy \tag{2.29}$$

Lee[32] suggested that the above equation be rearranged in terms of wake dynamic pressure. Assuming the freestream and wake static pressures are equal ($P_\infty = P_w$) and substituting Eq. 2.30 for the wake dynamic pressure, an expression for drag in terms of quantities measured directly by the wake rake is determined in Eq. 2.31.

$$q_w = q_\infty - \left(P_{o,\infty} - P_{o,w}\right) \tag{2.30}$$

$$D' = 2\int\left[\sqrt{q_\infty - (P_{o,\infty} - P_{o,w})}\left(\sqrt{q_\infty} - \sqrt{q_\infty - (P_{o,\infty} - P_{o,w})}\right)\right]dy \tag{2.31}$$

The pressure difference, $P_{o,\infty} - P_{o,w}$, can be determined through two measurements obtained by the wake rake. The ESP modules connected to the total pressure probes are referenced to atmospheric pressure. Therefore, the wake measures the difference between the wake total pressure and atmospheric pressure ($P_{o,w} - P_{amb}$). At the edges of the wake, the total pressure is equal to the total freestream pressure. Therefore, at the wake edges, the rake measures the difference between the freestream total pressure and atmospheric pressure ($P_{o,\infty} - P_{amb}$). These two measurements can be combined to find the difference between the freestream total pressure and the wake total pressure ($P_{o,\infty} - P_{o,w}$), as shown in Eq. 2.32.

$$P_{o,\infty} - P_{o,w} = \left(P_{o,\infty} - P_{amb}\right) - \left(P_{o,w} - P_{amb}\right) \tag{2.32}$$

The integral equation for drag is determined through the use of the trapezoidal rule. The incremental drag between each measurement point in the wake is calculated using Eq. 2.33. Each increment is summed over the entire wake to obtain the total profile drag in Eq. 2.34. Here, *K* is the total number of measurement points located within the wake. The drag coefficient is calculated using Eq. 2.35.

$$\begin{aligned}\Delta D_i' = [&\sqrt{q_\infty - (P_{o,\infty} - P_{o,w_i})} * \left(\sqrt{q_\infty} - \sqrt{q_\infty - (P_{o,\infty} - P_{o,w_i})}\right) \\ &+ \sqrt{q_\infty - (P_{o,\infty} - P_{o,w_{i+1}})}\left(\sqrt{q_\infty} - \sqrt{q_\infty - (P_{o,\infty} - P_{o,w_{i+1}})}\right)] \\ &* (y_{i+1} - y_i)\end{aligned} \tag{2.33}$$

$$D' = \sum_{i=1}^{K} \Delta D_i' \tag{2.34}$$

$$C_d = \frac{D'}{q_\infty c} \tag{2.35}$$

2.2.3.4 Surface Oil Flow Visualization

Surface oil flow visualization allows information about the surface stress over the entirety of the model to be seen and photographed in order to better understand the behavior of the flow. From this technique, information about transition, separation, and stall can be acquired. The model was covered with black contact paper to protect the pressure taps and provide good contrast with the dye without reflections. The model was cleaned between cases with window cleaner. A base layer of 10W-30 motor oil was applied to the model in order to provide an even surface for the fluorescent dye to move on. A mixture of the fluorescent dye (Dry Lite All in One Leak Detector Dye) and heavy viscosity mineral oil was applied using an airbrush to the area between about z/b = 0.2 and z/b = 0.8 on the model. While the tunnel was run for a short period of time, the oil sheared across the model surface. The tunnel was stopped and window opened, before two ultra-violet (UV) lamps were used to excite the dye. Images were taken using a Nikon Model D3100 digital camera with an AF-S NIKKOR 18-55 mm 1:3.5-5.6G lens. The experimental set-up for the flow visualization tests is shown in Figure 2.10.

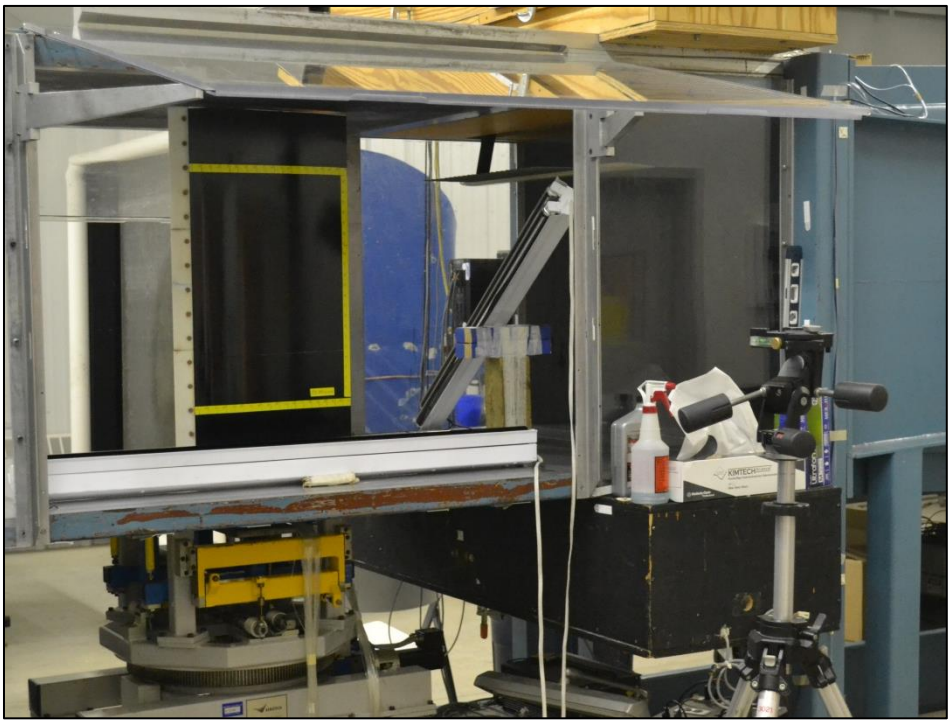

Figure 2.10: Surface Oil Flow Visualization Experimental Set-Up.

2.2.3.5 Pressure Sensitive Paint

The pressure-sensitive paint used with this test was the Innovative Scientific Solutions, Inc. (ISSI) UniFIB Pressure-Sensitive Paint. It contains a signal luminophore that fluoresces when excited by light in the UV/violet range (380nm-520nm, centered at 400nm) and emits photons in the red wavelength range (620nm-750nm, centered at ~650nm). The upper surface of the model was prepared for PSP testing with acetone so that no dirt, debris, or oil was present on the surface. The pressure taps were protected by the small tips of wooden toothpicks inserted into the holes to prevent buildup of paint inside the taps. A base coat of Krylon Indoor/Outdoor White Primer was applied. This base coat allows the PSP to adhere to a smooth, uniform surface. It also reduces reflections from the aluminum model because of its opaque quality, and increases the signal from the paint because all light is reflected from the white surface. The base coat was left to dry for between 45 minutes and an hour. The PSP was then applied using an airbrush connected to a nitrogen tank releasing gas at about 20 psi. For the UniFIB paint, about 7-9 light coats were needed, where a coat consists of painting down and up the model. In certain cases, more paint was added for a stronger signal. Only the upper surface was painted in this experiment, since the goal was to observe any differences in flow features between the rapid-prototype and casting shapes. This could be adequately done by looking at the upper surface. The model was painted while inside the tunnel test section. To move the vapors away from the painter, the tunnel fan was set to 30 rpm. Additionally, the painter wore a half mask respirator with OV/P100 filters while painting with the PSP. The lab garage doors were also opened in order to increase the air circulation in the lab. The PSP was allowed to cure at room temperature for at least 2 hours. Once the paint had dried, small registration marks were added around the edges of the painted area using a thin permanent marker spaced about 1 inch apart. These marks are used to align the wind-on image with the wind-off image to account for any model movement during the test due to aerodynamic loads and vibrations. Further painting details can be found in Appendix A.

The PSP data acquisition system included an illumination source, a charge-coupled device (CCD) camera, and software. An ISSI LM2X-DM air-cooled LED lamp was used to illuminate the PSP at wavelengths centered at 400 nm. An Andor iKon-M CCD camera with a Nikon Nikkor 28mm lens and high pass filter with a cutoff wavelength of 600 ±10 nm was

used to capture data. The filter allowed only light from the wavelengths emitted by the paint to reach the camera's CCD array. The CCD array contained pixels in a 1024 pixel by 1024 pixel arrangement. The lamp and camera were connected using a SMB-to-BNC cable that allowed the lamp to be operated in pulse mode. Whenever the camera's shutter was open a signal was sent to the lamp to turn on. This reduced the amount of time the PSP was subjected to light, and thus reduced PSP degradation due to light over time. The entire test section and the area adjacent to the tunnel containing the optical equipment were covered with blackout material to remove ambient light from the images. This reduced any errors due to background light and increased the signal-to-noise ratio. The software used for image acquisition was Andor's Solis camera software. Exposure time, number of images acquired, and other camera settings were specified using this program. The PSP experimental set-up is shown in Figure 2.11 and Figure 2.12. The excitation lamp is off in Figure 2.11 and is on in Figure 2.12 to show the emitted light from the paint.

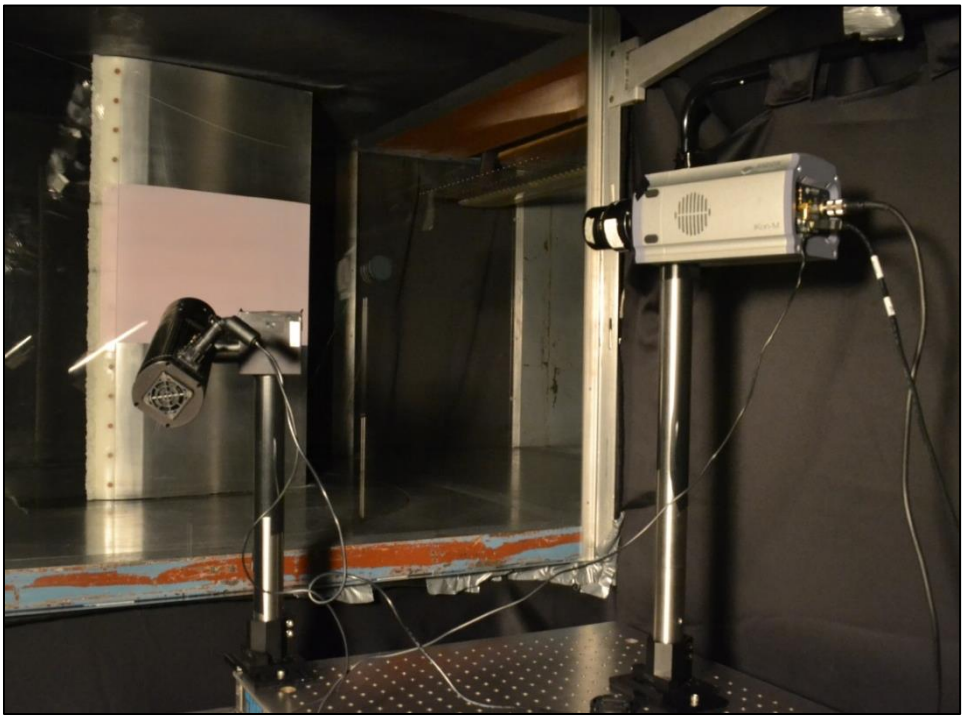

Figure 2.11: PSP Experimental Set-Up with visible light on.

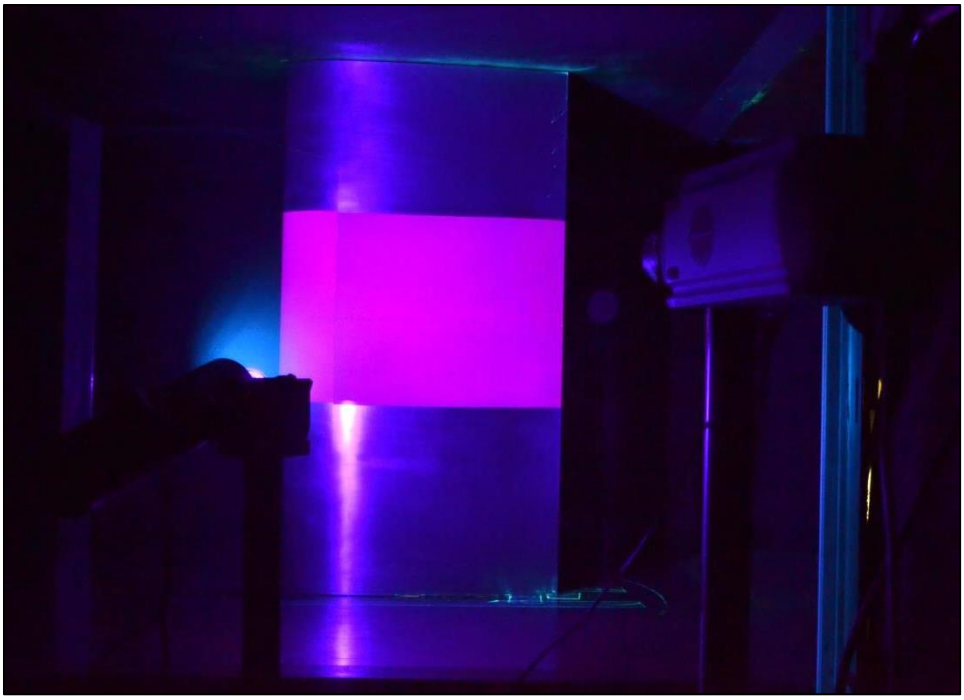

Figure 2.12: PSP Experimental Set-Up with Excitation Lamp On.

2.2.4 Test Procedure

The general procedure followed for each portion of the test is described in the following section.

2.2.4.1 Aerodynamic Testing

Once the model was properly installed and all equipment set up, the aerodynamic tests were performed. The wake rake was set to an initial position 20.875 inches from the tunnel floor and centered between the tunnel walls. This position was chosen so that wake measurements could be made near the center of the tunnel far from the floor and ceiling, and at a spanwise location free of pressure taps or other possible surface obstructions. The Labview tunnel code was started and the Initium initialized and re-zeroed. The Initium was initialized each time the tunnel code was opened and re-zeroed for each run. Before the first run of a day and after switching leading edges and ice shapes, balance tares were acquired over an angle of attack range from one degree less than the lowest angle in the test matrix to one degree more than the highest angle in one degree increments. Once the balance tare was completed, the tunnel was started and set to the desired Reynolds number of 1 million or 1.8 million. Data for each shape were obtained at both Reynolds numbers in order to compare

results to previous work by Busch.[5] The code moved the model to the first specified angle of attack. The pressures at all surface pressure taps were acquired, the balance measurements obtained, and the wake pressures measured. Wake measurements were only performed at one spanwise location. The model was moved to the next angle of attack and the data acquisition was repeated.

2.2.4.2 Surface Oil Flow Visualization

The surface oil flow visualization method was used to observe surface flow features for the horn (ED1978) case, a roughness case (ED1983), and the clean NACA 23012 at a Reynolds number of 1.8 million. Black contact paper was first applied to the model. For the horn cases, the contact paper extended upstream past the seam between the ice shape and Appendix C leading edge until directly behind the upper surface horn. This allowed a greater amount of the surface to be studied. The contact paper for the roughness cases covered the upper-surface main body and Appendix C leading edge. Yellow electrical tape with tic marks was used to mark spanwise and chordwise distances on the model. The contact paper was cleaned using Kimwipes or shop towels with window cleaner, with care taken to wipe all debris and oil from the surface which could potentially disrupt the flow. Motor oil was next applied to the model in order to create a uniform surface over the grooved texture of the contact paper. The motor oil also allows the fluorescent dye to shear more easily. All excess motor oil was removed using the Kimwipes or shop towels in straight, streamwise motions to not bias the surface flow. Next, the mixture of fluorescent dye and mineral oil was sprayed on the model until sufficiently covered in the region of interest using an airbrush set to about 30 psi. The tunnel fan was set to 30 rpm to serve as an exhaust away from the test section. The tunnel test section was closed and the fan set to about 1200 rpm, which corresponds roughly to the desired Reynolds number, and run for about 1 minute. The Reynolds number was not specified exactly since by the time the tunnel would have set Re to within 0.5%, much of the oil would have sheared away from important areas on the model. Therefore, an rpm value was specified close to known values that would result in the desired Re. Two UV lamps were placed in the tunnel, all ambient lights turned off, and pictures of the model acquired using the digital camera.

2.2.4.3 Pressure-Sensitive Paint

Three sets of images were acquired for the PSP portion of the test: background, wind-off, and wind-on. Each set included 25 images. These images were taken at a camera location that enabled the entire chord to be in the field of view. An exposure of 0.4 seconds and an f-number (f#) of 2.8 was used to acquire each individual image. The f# was set using the dial on the Nikon Nikkor 28mm lens and the exposure time was set in the Andor camera image acquisition software, Solis. Through Solis, the temperature at which to cool the camera's CCD array was specified as -20°C and the time to open and close the shutter was set to 20 ms each. The exposure time and number of images taken were also specified in this program. Image acquisition began with obtaining the background image. A background image was needed for each shape, camera location, and angle of attack in order to remove camera noise and ambient light effects. All ambient lights were turned off, blackout curtains secured, and excitation lamp turned off for this set of images. Next, the excitation lamp was set to pulse and the tunnel set to about 1200 rpm, which corresponded approximately to a Reynolds number of about 1.8 million. The tunnel was run for about 15 minutes in order for the model surface temperature to stabilize before taking the wind-on image set with all ambient light turned off and blocked. The tunnel was turned off and, after the fan reached 0 rpm, the wind-off images were immediately taken to minimize temperature differences between the two image sets. During some tests, the background images were acquired after the wind-off images, rather than before the wind-on images.

Using ImageJ, a "public domain Java image processing program,"[34] each of the three image sets (background, wind-on, and wind-off) were averaged to find the average intensity value at each pixel in the images. The averaged images were imported into OMS Lite, one of ISSI's processing software packages. Within OMS Lite, a dark threshold value was set for each case to remove the non-signal areas of the image. The dark threshold was set to between 800 and 3000 depending on the case. The dark threshold values for each case are tabulated in Appendix A. Next, registration marks were digitally added to both the averaged wind-on and wind-off images at the locations of the physical registration marks on the model surface and the pressure tap orifices. It was ensured that the numbered order of the marks were the same in both images. The program used a centroid finding algorithm to calculate the center of each tap. Next, the background image was subtracted from both the wind-on

and wind-off images in order to remove any light present from sources other than the excitation lamp and paint. OMS Lite then aligned the wind-on image to the wind-off one by fitting the respective marks to each other using a spatial transform with an order of fit of either 0 or 2, depending on marker placement. The box size and first marker to fit were left at the respective default values of 24 pixels and 0. The box size is the size of the pixel area to search for the corresponding marker in the other image. OMS Lite has the option of applying a spatial filter to the resulting image, but this feature was disabled during this part of the post-processing, since filtering was performed at a later step. Additionally, the edges of the signal were thinned by 2 pixels to remove the effects of alignment at the edges. Once all alignment and filtering settings were chosen, the program then calculated the intensity ratio of the wind-off to the wind-on intensities. These intensity ratio values and pixel coordinates were output to a .dat file and imported into a MATLAB code to perform the pressure calibration and obtain continuous c_p data over the model surface. The aligned marker locations were also saved to be used in the MATLAB code for pressure tap placement information.

The MATLAB code uses the .dat file output from OMS Lite for the intensity ratio values at each pixel location, and an input file containing information about the test conditions, pressure tap coordinates in both image and model coordinates, and pressure tap c_p data. The input file contains values from the aerodynamic performance tests performed previously. An assumption made was that the tunnel and ambient conditions were constant between the aerodynamic and pressure sensitive paint tests. It should be noted that this assumption could be responsible for some error in the PSP data. The condition data include the ambient pressure and dynamic pressure in the test section. The input file also contains the pixel coordinates of the pressure taps from the final marker location file from OMS Lite, the model coordinates of the pressure taps from the original model design, and the c_p data at those taps from the aerodynamic tests.

Once the two input files were imported into the MATLAB code, any remaining background signal and extremely erroneous intensity ratio data were removed by setting the intensity ratio to NaN at any pixel where the ratio was less than 0.85 or greater than 1.05. Since the pressure over the model will never reach a value above the ambient pressure, the maximum

ratio value is 1. Any false intensity values ahead of the edge of the paint area were set to NaN also. Next, a median filter with a 9x5 kernel and a Savitzy-Golay filter with a frame size of 47 were applied to further filter the data. As was previously stated, the ambient conditions recorded during aerodynamic performance testing were not the same as the conditions during pressure-sensitive paint testing. Since the conditions were only measured during the aerodynamic tests, the ambient pressure (p_{amb}) value recorded then was used in the PSP data processing. The recorded ambient pressure was then taken to equal the static pressure (and total pressure) in the test section during wind-off conditions that serves as the reference pressure in the PSP method ($p_{ref} = p_{amb}$). The wind-on freestream static pressure (p_∞) was also needed to calculate the pressure ratio from the pressure coefficients. Since total pressure is the sum of both static and dynamic pressures (Eq.2.36), the freestream static pressure in the tunnel can be found from subtracting the measured dynamic pressure from the total pressure. The total pressure was found using the total pressure probes in the wake rake described above to measure the total pressure outside of the wake. Using the static pressure found from this relation, the pressure ratio at each tap can be calculated using Eq. 2.37.

$$p_{total} = p_\infty + q_\infty \tag{2.36}$$

$$\frac{p}{p_{ref}} = \frac{c_p q_\infty + p_\infty}{p_{ref}} \tag{2.37}$$

Before the calibration was performed, the intensity ratio values at each pressure tap must be found. The code obtains an average intensity ratio value for each tap by finding the mean of a rectangular block of 7 pixels in the *x* direction and 13 pixels in the *y* direction. The center of this box is 10 pixels above the pressure tap *y*-pixel location and at the same tap *x*-pixel location. The averaging box was offset slightly to avoid inaccurate intensity ratio values directly surrounding the tap due to imperfect alignment and reduced signal. The reduced signal is most likely due to the fact that the toothpicks blocked some paint from adhering to the model surface while they were protecting the taps. Next, a linear fit between the tap intensity ratio and pressure ratio data was found by fitting the intensity ratio data to the pressure ratio data in a least squares manner. The resulting coefficients, *A* and *B*, are the coefficients of the Stern-Volmer equation described in Chapter 1. The equation was inverted to find a relation for pressure in terms of intensity in Eq. 2.38, before solving for the pressure

coefficient (c_p) in Eq. 2.39. These two equations were used to find the pressure ratio, pressure, and pressure coefficient data at each pixel in the image.

$$p = \frac{\left(\frac{I_{ref}}{I} - A\right)}{B} p_{ref} \tag{2.38}$$

$$c_p = \frac{p - p_\infty}{q_\infty} \tag{2.39}$$

2.2.5 Wind Tunnel Corrections

The flow over a model in a wind tunnel does not behave in the same way as the flow over the same model in free air due to the presence of the tunnel walls. To account for the tunnel walls, corrections were calculated and applied to the angle of attack, lift coefficient, drag coefficient, moment coefficient, and pressure coefficient following the method outlined in Barlow, Rae, and Pope.[35]

Three tunnel effects: solid blockage, wake blockage, and streamline curvature alteration, were significant enough for corrections to be calculated and applied to the original data. Solid blockage is an increase in flow velocity due to a reduction in the effective test section cross-sectional area due to the presence of the model. Its effects increase with greater model frontal area. With this smaller test section area, the flow velocity increases to satisfy the conservation of mass. Solid blockage effects increase for large angles of attack and for thick models. The solid-blockage velocity correction is calculated from Eq. 2.40. The area of the test section (C), model volume, and K_1 constant are needed for this calculation. The constant, K_1, is 0.52 for a model that spans the height of a tunnel of 7ft by 10ft test section proportions. Since the test section dimensions of the ARL subsonic tunnel are proportional to a 7ft x 10ft tunnel, this value can be used in the following equation. The model volume is determined with Eq. 2.41 using the dimensional maximum thickness of the airfoil (t), the model span (b), and the model chord (c).[36]

$$\epsilon_{sb} = \frac{K_1 (model\ volume)}{C^{3/2}} \tag{2.40}$$

$$model\ volume = 0.75tbc \tag{2.41}$$

The wake causes an increase in velocity over the model similar to solid blockage. The flow velocity inside the wake is less than the freestream velocity. For the conservation of mass, the velocity outside the wake must then be greater than the freestream velocity. The wake-

blockage velocity correction is determined using Eq. 2.42. The model chord (c), test section height (h), and uncorrected drag coefficient (C_{d_u}) were needed to calculated the effect of wake blockage. The total correction for velocity due to both solid blockage and wake blockage is the sum of the two corrections in Eq. 2.43.

$$\varepsilon_{wb} = \frac{1}{2}\frac{c}{h}C_{d_u} \tag{2.42}$$

$$\varepsilon = \epsilon_{sb} + \varepsilon_{wb} \tag{2.43}$$

The third correction addresses the modification of the streamlines around the model in comparison to their curvature in free flight. The tunnel walls increase the effective camber of the model, which increases the lift and pitching moment. The change in streamline curvature was accounted for in Eq. 2.44, where both the model chord (c) and test section height (h) were used.

$$\sigma = \frac{\pi^2}{48}\left(\frac{c}{h}\right)^2 \tag{2.44}$$

The two values, σ and ε, were applied to the uncorrected angle of attack (α) in Eq. 2.43, lift coefficient (c_ℓ) in Eq. 2.46, drag coefficient (c_d) in Eq. 2.47, moment coefficient (c_m) in Eq. 2.48, and pressure coefficient (c_p) in Eq. 2.49.

$$\alpha_{cor} = \alpha_u + \frac{57.3\sigma}{2\pi}\left(C_{\ell_u} + 4C_{m_u}\right) \tag{2.45}$$

$$C_{\ell_{cor}} = C_{\ell_u}(1 - \sigma - 2\epsilon) \tag{2.46}$$

$$C_{d_{cor}} = C_{d_u}(1 - 3\epsilon_{sb} - 3\varepsilon_{wb}) \tag{2.47}$$

$$C_{m_{cor}} = C_{m_u}(1 - 2\epsilon) + \frac{1}{4}\sigma C_{\ell_u} \tag{2.48}$$

$$C_{p_{cor}} = \frac{C_{p_u}}{(1+\varepsilon_{sb}+\varepsilon_{wb})^2} \tag{2.49}$$

The wind tunnel corrections decrease the absolute value of c_ℓ, c_d, and c_p results for this case. The corrections result in an increase from the uncorrected absolute value for α. The c_m uncorrected data are increased for angles of attack when the lift coefficient is negative and are decreased when the lift coefficient is positive.

2.2.6 Uncertainty Analysis Results

Sample uncertainty calculations were performed for the horn casting case at a Reynolds number of 1.8 million and an angle of attack of α = 7°. The uncorrected

aerodynamic coefficients and angle of attack uncertainties are reported here. The uncertainty results are for the flow, balance, and pressure parameters are presented in Table 2.4, Table 2.5, and Table 2.6, respectively. Details of the method followed to obtain these values are included in Appendix C.

A traditional uncertainty analysis on the PSP data was not performed for this test due to the number of contributing parameters that were unmeasurable during testing. For this reason, an error analysis was performed instead. Sample percent errors are reported in Figure 2.13 for the clean NACA 23012 model at an angle of attack of $\alpha = 12°$. These error values are the average of the standard deviation divided by the tap pressure coefficient value at a certain chordwise position. The vertical axis in the figure is the calculated percent error between the PSP and pressure tap pressure coefficient results. The red line marks the results for PSP data taken near the tap row in span, which is the location of the most accurate calibration. This is comparison to the analysis presented by the blue line. The blue line marks the results obtained over the entire span of the painted area, not just over a limited number of rows near the main tap row, plotted against chordwise position. The average percent errors calculated near the pressure tap row and over the entire span of the painted area are reported in Table 2.7. The average calculation did not include any data past *x/c* = 0.7 because the taps located further downstream were not included in the PSP calibration due to the large amount of noise in the PSP data close to the trailing edge of the model. For the smallest percent error obtained in the whole-span case, an error of 4% at *x/c* = 0.06 corresponds to a pressure deviation of 0.046 psi. Further details are included in Appendix C.

Table 2.4: Uncertainties in Flow Parameters for horn casting at Re 1.8 million and $\alpha = 7°$.

Flow Parameter	Reference Value	Absolute Uncertainty	Relative Uncertainty (%)
c	18 in.	±0.01 in.	±0.0556
b	33.563 in.	±0.02 in.	±0.0596
q_∞	0.317 psi	±0.00143 psi	±0.4505
T_{amb}	71.63° F	±1° F	±1.40
P_{amb}	14.347 psi	±0.008 psi	±0.0558
ρ_{amb}	0.00227 $\frac{slugs}{ft^3}$	±4.45x10^{-6} $\frac{slugs}{ft^3}$	±0.1963
μ	3.81x10^{-7} $\frac{lb \cdot s}{ft^2}$	±5.54x10^{-10} $\frac{lb \cdot s}{ft^2}$	±0.1454
U_∞	201.71 $\frac{ft}{s}$	±0.452 $\frac{ft}{s}$	±0.2242
Re	1800865	±5458	±0.3031

Table 2.5: Uncertainties in Balance Parameters for horn casting at Re 1.8 million and α = 7°.

Balance Parameter	Reference Value	Absolute Uncertainty	Relative Uncertainty (%)
α	6.998°	±0.02°	±0.2858
F_N	-66.504 lb	±0.09 lb	±0.1353
F_A	0.0058 lb	±0.027 lb	±5.30
M	-1.1339 $lb \cdot ft$	±0.0675 $lb \cdot ft$	±5.95
C_ℓ	0.7595	±0.00295	±0.389
C_d	0.0935	±0.00407	±0.4518

Table 2.6: Uncertainties in Pressure Parameters for horn casting at Re 1.8 million and α = 7°.

Pressure Parameter	Reference Value	Absolute Uncertainty	Relative Uncertainty (%)
C_ℓ	0.7560	±0.002239	±0.2962
C_d	0.0901	±0.00079	±0.00878

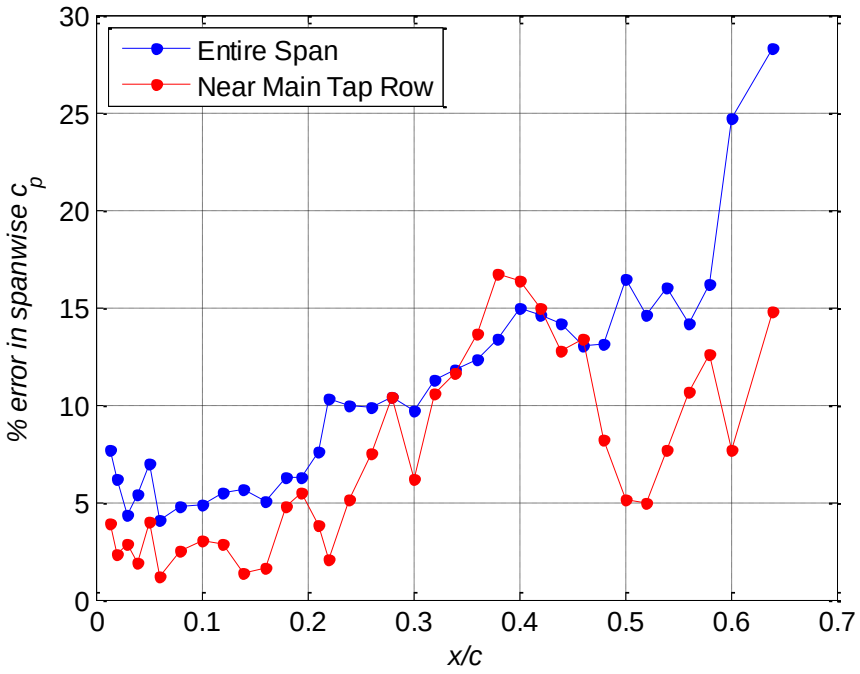

Figure 2.13: Percent error in spanwise PSP c_p data over the span of the painted area (blue) and only near the main tap row (red).

Table 2.7: Average Percent Errors in PSP at Re 1.8 million and α = 12°.

PSP Data Location	Average Percent Error Over Chord
Near Main Tap Row	7.3%
Over Span of Painted Area	10.8%

PSP tests in similar velocity ranges were performed by Bell[21] and errors between the PSP and pressure tap data reported. Bell performed a series of tests on a small swept wing with constant chord using both binary and single-luminophore PSPs. At a Mach number of M = 0.1, a pressure error of 0.01 psi was recorded using a single luminophore paint. At a lower Mach number of M = 0.05 after improving the experimental method, a pressure error of 0.006 psi was obtained. Both of these errors in pressure are significantly smaller than 0.046 psi pressure error calculated for the current test. For both test conditions, Bell tested in a tunnel with some temperature control and was therefore able to reduce temperature variation errors. Additionally, the camera used had a pixel well depth of 350,000 electrons in comparison to the well depth of 100,000 electrons for the Andor iKon camera used in the present study. Variations in gain from pixel to pixel were also accounted for through the acquisition of a flat-field image, which decreased bias errors when the intensity images were divided by the flat-field. Certain improvements were made for the lower Mach number test at M = 0.05. Bell allowed the tunnel to run for an hour before acquiring the wind-on data and averaged 65 exposures for each image. This is in comparison to the 15 minutes the tunnel was run for and the 25 exposures averaged for each image in the current investigation. The operational and instrumentation differences between the current experiment and the work by Bell[21] mostly account for the additional errors in the PSP data for this work. Recommendations to improve the accuracy in future PSP experiments are included in Chapter 4.

Chapter 3

Results and Discussion

This chapter presents the data obtained during the course of this work and the analysis performed on those results. For the purposes of this study, only the horn ice shape and one of the roughness ice shapes were tested with PSP and analyzed in the this section. These cases were chosen for more in-depth discussion because testing revealed some differences in aerodynamic performance between the rapid-prototype and casting shapes. First, the clean NACA 23012 data are discussed to provide a comparison for the iced data. This includes the aerodynamic performance validation of the experimental set-up and methodologies with respect to previous testing performed on the same model and at the same test conditions.[5] The remainder of this section is split between the discussion of the results from the horn ice shapes and the results from the roughness ice shapes. For each of the two ice shape classifications focused on in this research, the aerodynamic and pressure-sensitive paint (PSP) data are compared and analyzed for the casting and rapid-prototype (RPM) cases. The data are also discussed in relation to the clean model results. Special attention is given to any additional results found from the PSP data beyond those obtained from the traditional pressure taps. The ability of the PSP data to reproduce the pressure tap results is discussed. Reasons for differences and discrepancies between the casting and rapid-prototype shapes are posed and analyzed. The focus of this study was to jointly validate the newly developed ice shape replication method with the use of the PSP method. A more in-depth aerodynamic performance analysis between the rapid-prototype shapes and castings will be performed by Broeren et al.[37]

Since the PSP test did not occur at the same time as the aerodynamic tests, there were a few inconsistencies between the test conditions for the two experiments. The first, as discussed in the previous chapter, the ambient pressure differed between the two tests, and

was only measured during the aerodynamic performance tests. Since the ambient pressure was the reference pressure used in the PSP calibration, inaccuracies in the PSP data were introduced from using the ambient pressure value at the previously recorded time. The second point is the angles of attack values specified during this analysis were the geometric angles of attack for the PSP data and the corrected angles of attack based on tunnel corrections for the aerodynamic data. This is mostly a nomenclature issue for the purposes of this discussion.

3.1 Clean NACA 23012

3.1.1 Aerodynamic Performance

The c_ℓ-α curve for the clean NACA 23012 is shown in Figure 3.1. The maximum lift coefficient calculated from the force balance measurement was $c_{\ell,max}$ = 1.47 and occurred at an angle of attack of α_{stall}= 14.40°. The abrupt stall with a significant loss of lift after α_{stall} is characteristic of leading-edge type stall, which was expected for the NACA 23012 model at the tested Reynolds numbers. Negative stall occurred at α_{stall} = -8.20° with a lift coefficient of c_ℓ = -0.68 as measured by the balance. Both the pressure and balance data were plotted in Figure 3.1 to show the agreement between the c_ℓ results from the balance measurements and from the pressure integration. To quantify the agreement between the two lift curves, the root mean square (RMS) of the difference between the two at each angle of attack was calculated. The RMS difference in the pressure and balance data between negative and positive stall was 0.057, which shows good agreement and provides a check for the accuracy of both methods. There was a slight deviation at higher angles of attack, with the absolute c_ℓ difference between the two at the stall angle of attack of 0.02. In addition to the difference in $c_{\ell,max}$, there was a slight difference in lift slope ($c_{\ell,\alpha}$) between the pressure and balance data. In the linear region from α = -7.18° to α = 10.29°, the pressure lift curve had a higher slope of $c_{\ell,\alpha}$ = 0.1102 per degree while the balance lift curve had a slope of $c_{\ell,\alpha}$ = 0.1028 per degree. The lift slope was determined by fitting a linear curve to the c_ℓ-α data in the linear region. The difference in lift slope and $c_{\ell,max}$ was most likely due to model end effects near the tunnel walls and the airfoil-wall gap. While an airfoil model that spans the height of a tunnel theoretically is infinite, the real model ends have effects. The ends of the

model near the tunnel walls and the gaps between the model and tunnel cause the airfoil to behave as if it has a finite aspect ratio, thus reducing the lift slope. In the same way that there is no lift is produced at the tips of a finite wing, so too is the lift at the ends of the airfoil model in the tunnel zero. The pressure measurements were only obtained near midspan, and were therefore relatively free from end effects and were not affected by the reduction in lift at the model ends.

The lift coefficient (c_ℓ) versus drag coefficient (c_d) and drag coefficient (c_d) versus angle of attack (α) are shown in Figures 3.2 and 3.3. The drag measurement from the force balance differed significantly from the drag calculated from the wake pressure at positive angles of attack. This was due to the induced drag component included in the balance measurement that was the result of tip vortices formed due to the gaps between the model and tunnel walls. For this reason, the drag calculated from the wake pressures more accurately represented the profile drag and was exclusively used in this analysis. There was one condition where the balance and pressure drag coefficients match. This occurred when the lift coefficient (c_ℓ) was equal to zero, where there was no induced drag component. As Figures 3.2 and 3.3 show, the drag coefficient (c_d) values for both methods agreed near c_ℓ = 0. There were significant increases in drag at the negative and positive stall angles of attack of α_{stall} = -8.20° and 14.40° which resulted from the sudden increase in pressure drag after leading-edge type stall.

Figures 3.4 through 3.6 show Reynolds number effects on the clean model performance measured using the balance data. Tests were conducted at Reynolds numbers of 1 million and 1.8 million. Figure 3.4 shows the $c_{\ell,max}$ difference between the two cases was 0.14, where $c_{\ell,max}$ was 1.33 when the Reynolds number was 1 million. There was also a difference in lift slope between the two Reynolds number cases, where the 1.8 million case had a higher lift slope of 0.1028 per degree calculated between α = -7.18° and α = 10.29° and the 1 million case had a lift slope of $c_{\ell,\alpha}$ = 0.0981 per degree calculated between α = -6.15° and α = 9.27°. The decreased lift slope for the lower Reynolds number resulted from the greater influence of viscous effects. While the separation bubble near the leading edge dominates the stall behavior at the tested Reynolds number, trailing-edge separation may also have been present. Trailing-edge separation occurs when the flow separates at a point where

the momentum of the flow can no longer overcome the adverse pressure gradient and does not reattach downstream. The separation point can gradually move upstream with increasing angle of attack and decreasing Reynolds number. At Re 1 million, separation could have occurred further upstream for a given angle of attack in comparison to the 1.8 million case. The greater region of separated flow could have had a decambering effect on the airfoil performance resulting in the observed reduction in lift slope. Additionally, the greater extent of unattached flow could have produced less lift and more drag in comparison to the Re 1.8 million case. Figure 3.5 shows lesser values for the drag coefficient (c_d) for the higher Reynolds number case over most of the angle of attack range. The significant increases in drag at stall were seen about a degree earlier for the Re 1 million test in Figure 3.6 at α = -7.17° and α = 13.36°. As the Reynolds number increased, the separation point near the trailing edge of the airfoil may have moved downstream. This would have resulted in a smaller region of separated flow at the higher Reynolds number with less pressure drag and delayed stall in comparison to the lower Reynolds number test.

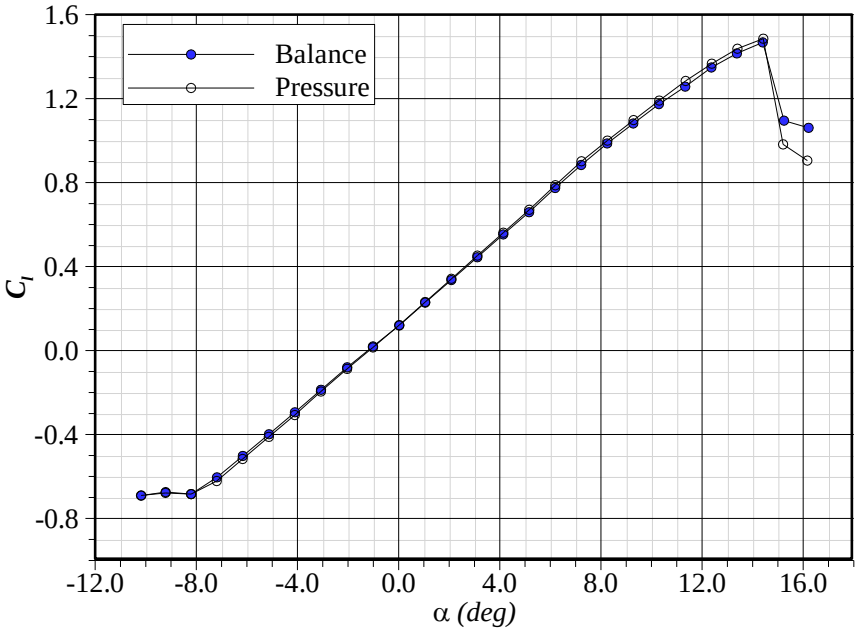

Figure 3.1: Clean NACA 23012, balance and integrated pressure data comparison c_ℓ-α curves, Re 1.8 million.

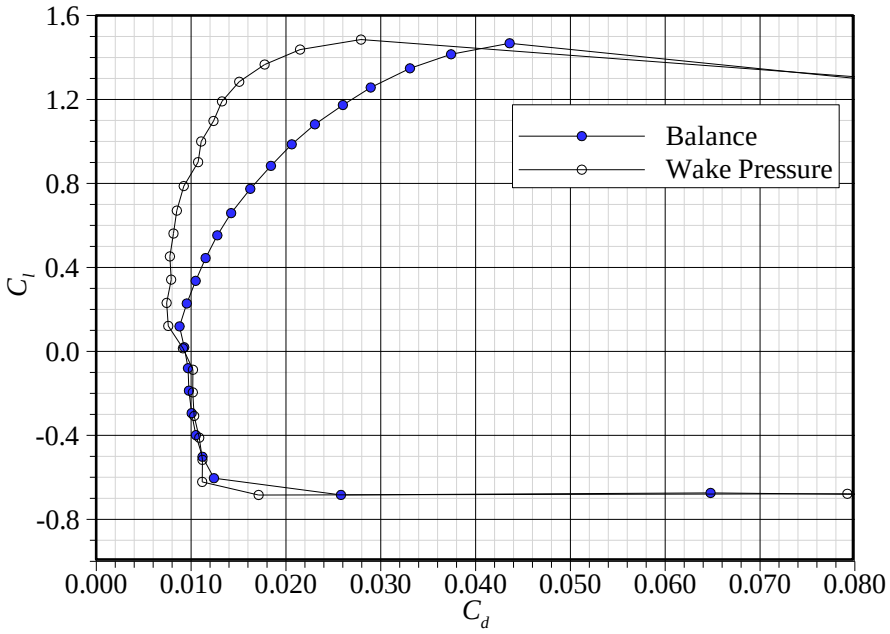

Figure 3.2: Clean NACA 23012, balance and pressure comparison drag polar, Re 1.8 million.

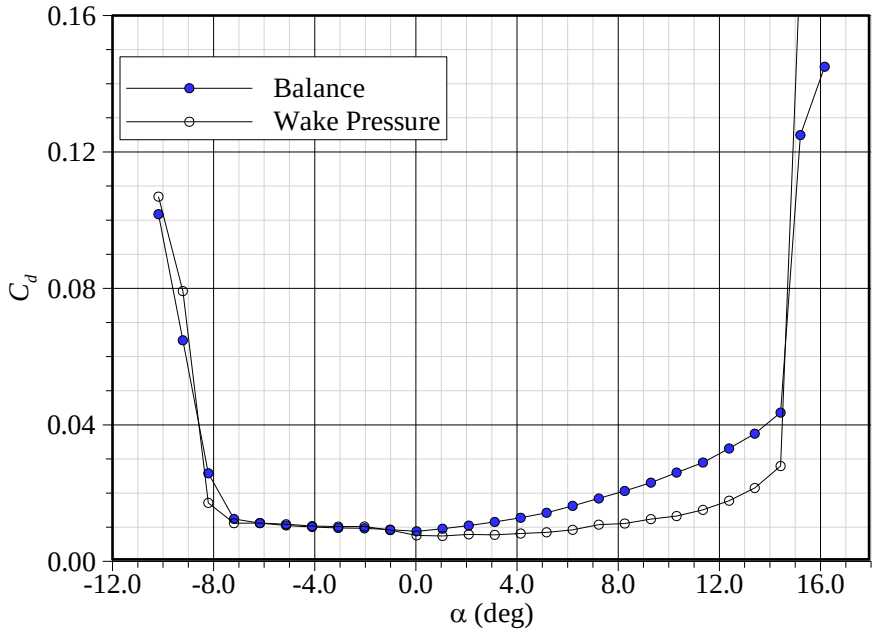

Figure 3.3: Clean NACA 23012, balance and pressure comparison c_d-α curves, Re 1.8 million.

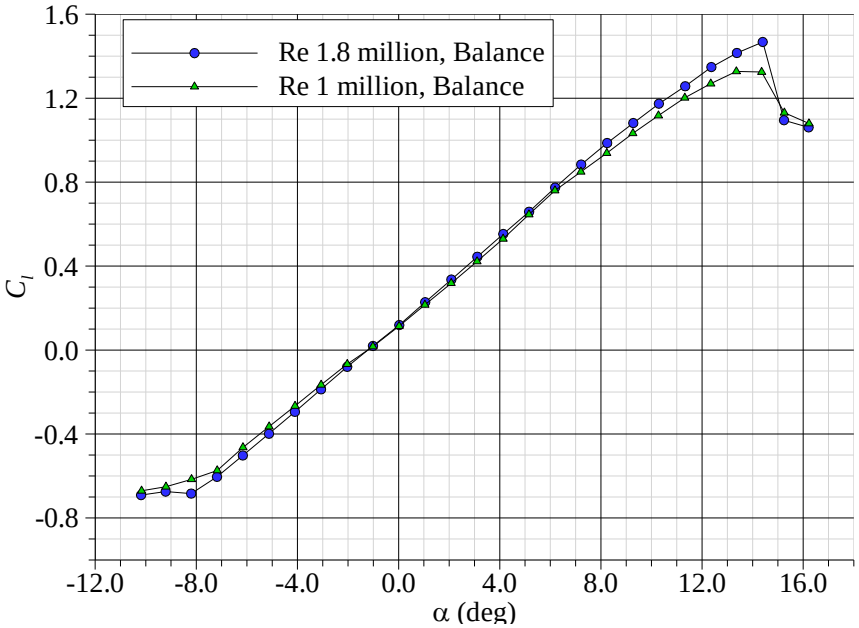

Figure 3.4: Clean NACA 23012, Reynolds number balance c_ℓ-α comparison, Re 1.8 million and 1 million.

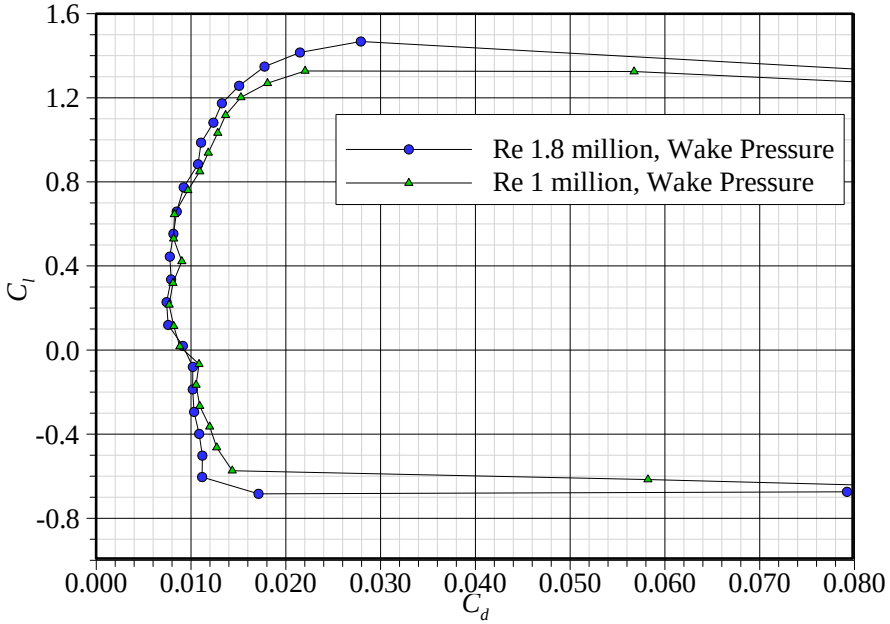

Figure 3.5: Clean NACA 23012, Reynolds number comparison wake drag polar, Re 1.8 million and 1 million.

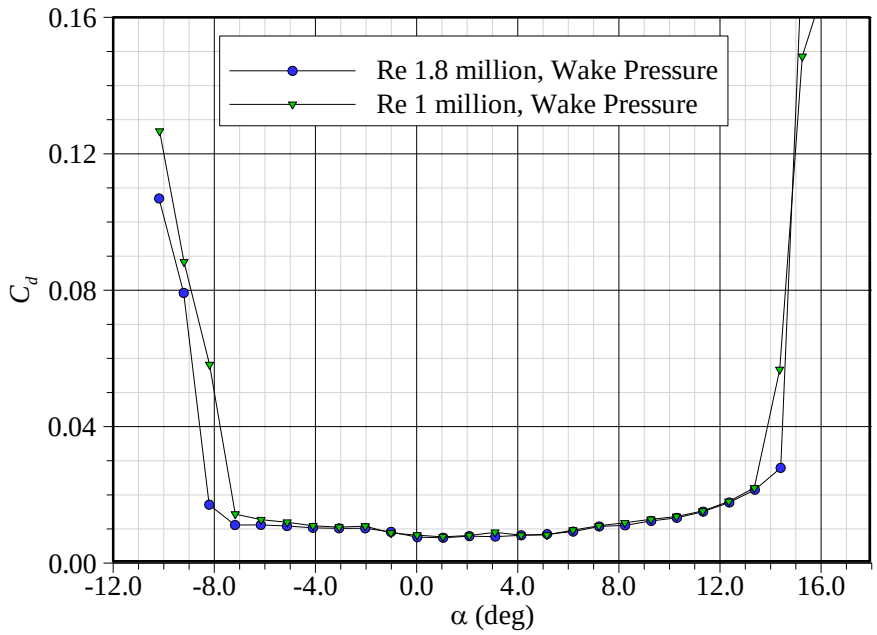

Figure 3.6: Clean NACA 23012, Reynolds number comparison c_d-α, Re 1.8 million and 1 million.

3.1.2 Validation with Previous Work

Since much of the overall project was associated with the previous research performed by Busch[5] using the same NACA 23012 model tested in the present study, the current data were validated against the data from that work. Figures 3.7 through 3.10 show the comparisons between the past and the current data to check the experimental set-up, procedure, and repeatability. Overall, there was good agreement between the two tests. The c_ℓ-α curve validation in Figure 3.7 shows small differences in $c_{\ell,max}$ of 0.01 and in c_ℓ at negative stall of 0.03. The lift curve slope calculated in the linear region between angles of attack of about α = -7° and α = 10° was $c_{\ell,\alpha}$ = 0.1027 per degree from the previous data and $c_{\ell,\alpha}$ = 0.1028 per degree for the current, which shows the lift curve slopes agreed very well. The RMS difference between the two data sets was only 0.008, showing good agreement also. Figures 3.8 and 3.9 present the drag coefficient (c_d) comparison plots and show overall repeatability in drag behavior. The c_d values from the current test were greater than the values from the past test for most of the angle of attack range. The width of the drag bucket for the previous data was slightly larger with lower c_d values. These behaviors were most likely due to surface quality changes between the tests which possibly led to earlier

transition. The comparison c_p curves are shown in Figure 3.10. Qualitatively, there was good overall agreement, especially at higher angles of attack. Figure 3.10.a shows variations in the pressure data for the lower-surface taps from the leading edge to about *x/c* = 0.3 for an angle of attack of about α = -4°. The c_p results for α = 4° in Figure 3.10.b show a slight disagreement between the upper-surface taps from the leading edge to about *x/c* = 0.2. The variations could be from surface quality differences from the seams and mounting screw holes or from slight differences in angle of attack between the compared cases. The differences in the c_p curves did not seem to have an effect on the c_ℓ-α comparison in Figure 3.7. Some data points were not present in both data sets due to taps at those locations giving incorrect measurements from leaking or blockages and thus were removed from the data set. The curves at higher angles of attack show only minor differences. This comparison shows that the current test replicated the past test well, and that results between the two could be compared.

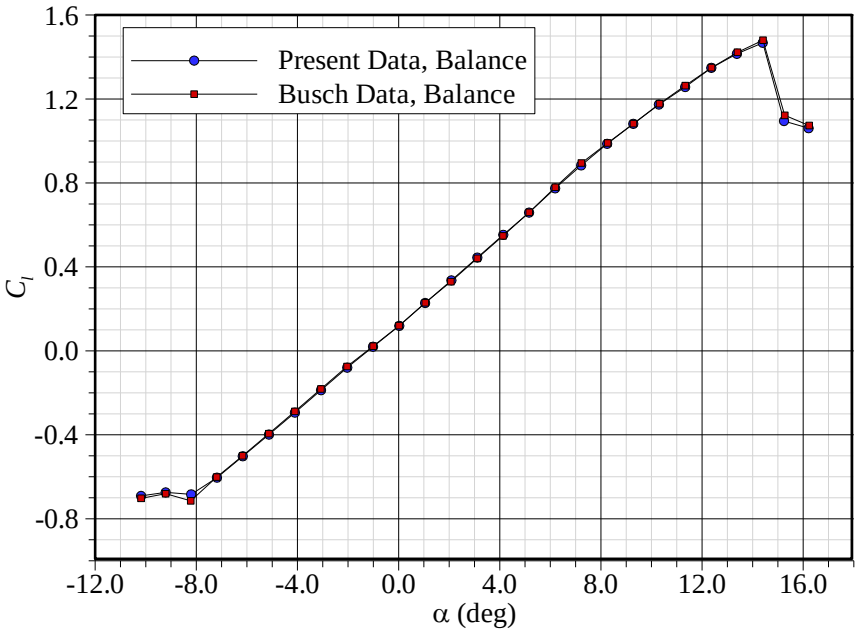

Figure 3.7: Clean NACA 23012, validation with previous data c_ℓ-α, Re 1.8 million.

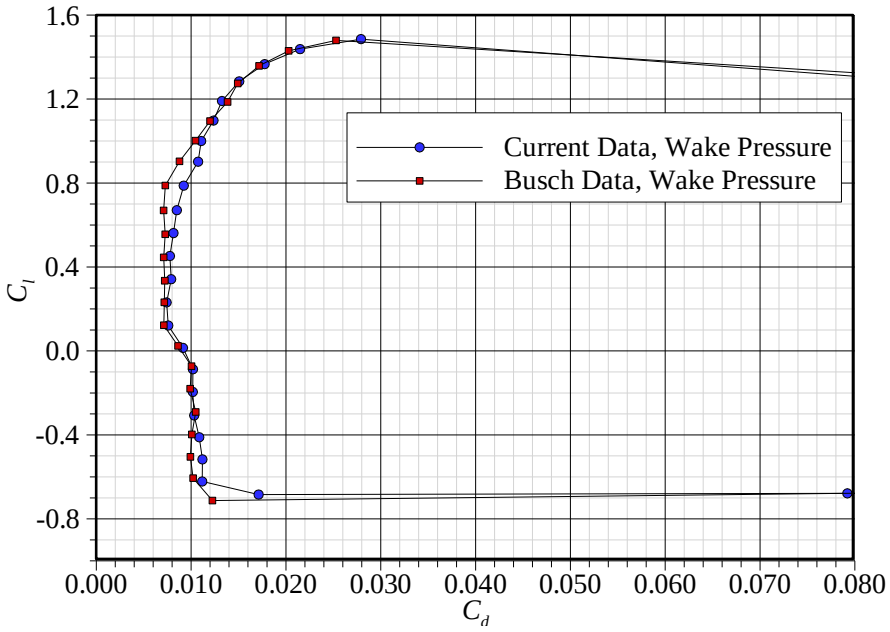

Figure 3.8: Clean NACA 23012, validation with previous data drag polar, Re 1.8 million.

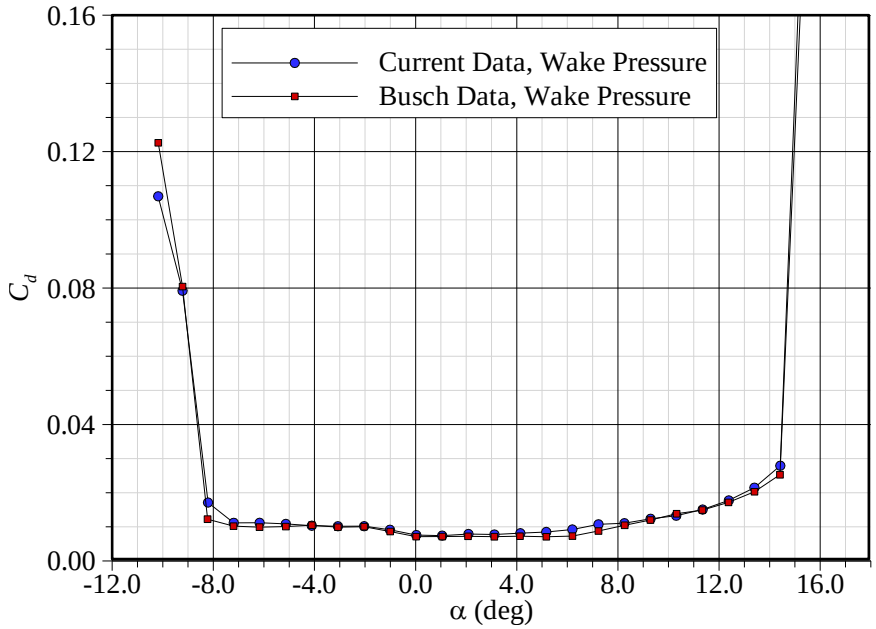

Figure 3.9: Clean NACA 23012, validation with previous data c_d-α, Re 1.8 million.

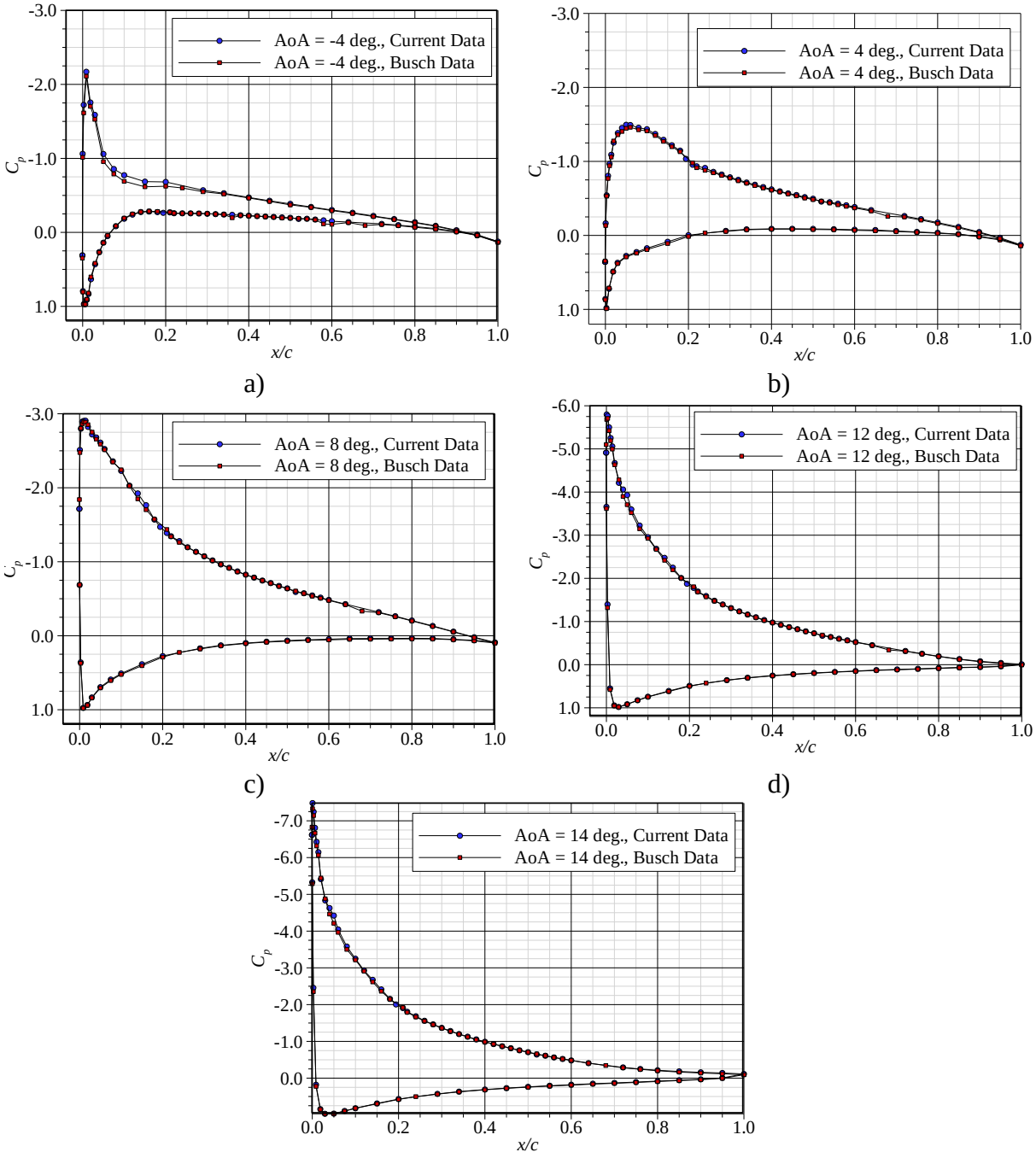

Figure 3.10: Clean NACA 23012, validation with previous data c_p curves, Re 1.8 million.

3.1.3 PSP Comparison

The PSP data are next discussed in conjunction with the aerodynamic data. The entire upper surface of the clean model was painted from about $x/c = 0$ to $x/c = 1$. Angles of attack of $\alpha = 12°$ and $\alpha = 14°$ were chosen to compare to the iced cases that will be discussed

later. If any major differences in the flowfield between the casting and RPM shapes for the horn and roughness were present, they should have been observed near stall. For this reason, a clean comparison was obtained near stall.

3.1.3.1 Calibration Procedure

The calibration relationship between intensity and pressure was determined with a linear fit to the intensity ratio values measured with PSP at the taps and the measured pressure ratio values. The linear curve fit was the Sten-Volmer equation for each test case. It should be noted that the clean leading-edge piece was painted separately from the airfoil body. Theoretically the intensity ratio (I_{ref}/I) should not be affected by two different paint applications on the two model segments because paint thickness and luminophore concentration effects should be removed during the intensity ratio calculation. To see if painting the clean leading edge separately from the main airfoil body had an effect, two methods of calibration were compared for an angle of attack of $\alpha = 14°$. The first employed a single calibration using data from both the leading-edge and main airfoil taps. The second utilized two separate calibrations: one determined from the leading-edge taps and applied only to the leading edge, and the second found from the main airfoil taps and applied only to that portion of the model.

Figure 3.11 shows the c_p contours for both calibration cases at a geometric angle of attack of $\alpha = 14°$. Qualitatively, no major difference between the results from the two calibrations could be seen from the c_p contour figures. Since not many differences could be observed, a closer examination of the calibration curves and two-dimensional c_p curves was therefore useful. The calibration and the PSP-tap comparison plots were compared and are presented in Figures 3.12 through 3.15. To provide a means of describing the goodness-of-fit for each calibration curve, the norm of the residuals was calculated as the square root of the sum of the residuals between the linear fit and the intensity ratio data points for each tap. Better goodness-of-fits correspond to lower values for the norm of the residuals. The norm of the residuals for the single calibration was 0.0138 and the norms of the residuals for the separate calibrations were 0.0075 for the leading-edge and 0.0111 for the main body data points. In order to compare with the double calibration, the norms of the residuals for the leading-edge and main body data points were also calculated for the single calibration case.

With using the single calibration, the norm of the residuals for the leading-edge is 0.0076 and for the main-body was 0.0115. These values are tabulated in Table 3.1. These numbers show that the single calibration yielded better results for the main body and the double calibration yielded better results for the leading edge, though slightly. Figures 3.13, 3.14, and 3.15 show the agreement between the pressure tap data and the PSP data. Both calibrations yielded similar trends and peaks in the data. All plots show that there was not much difference between using the single or the double calibration method, and that the PSP method yielded good results for both calibration schemes when compared to the pressure taps, despite the noise that was present. Therefore, it was reasonably concluded that if different paint applications on different model segments of the same material were used, then paint effects on the intensity ratio (I_{ref}/I) were small and one calibration could be used for the entire model. For all calibrations, taps downstream of x/c = 0.7 were not included. This was to avoid using taps near where the PSP data had high signal-to-noise ratios that could have contaminated the calibration.

Table 3.1: Clean NACA 23012, Norms of Residuals for Different Calibration Schemes

Case	Norm of the Residuals
Single Calibration	0.0138
Double Calibration-Leading-Edge Data	0.0075
Double Calibration-Main Body Data	0.0111
Single Calibration-Leading-Edge Data	0.0076
Single Calibration-Main Body Data	0.0115

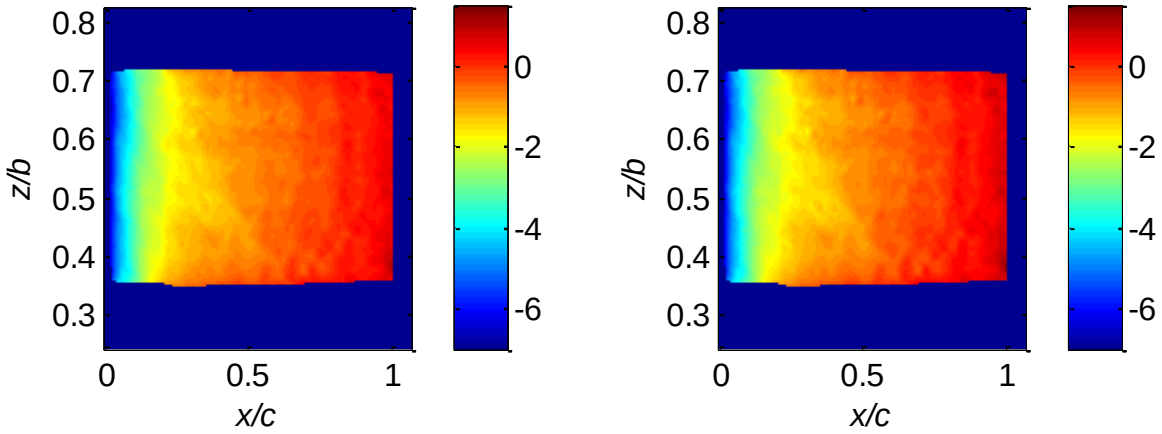

Figure 3.11: Clean NACA 23012, PSP c_p contour comparison, α = 14°, using a) one calibration and b) two calibrations.

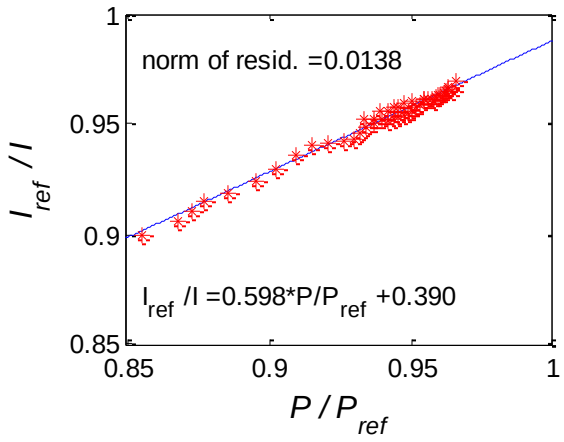

a)

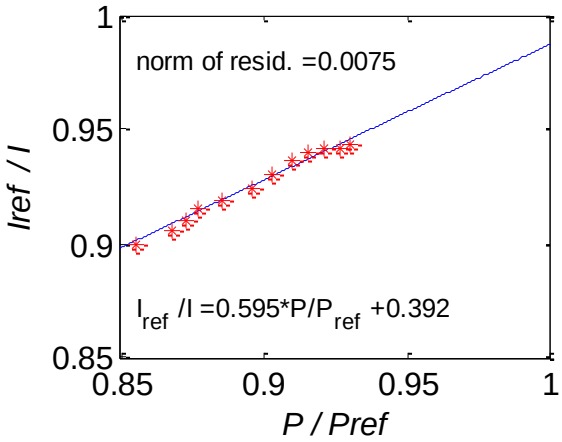

b)

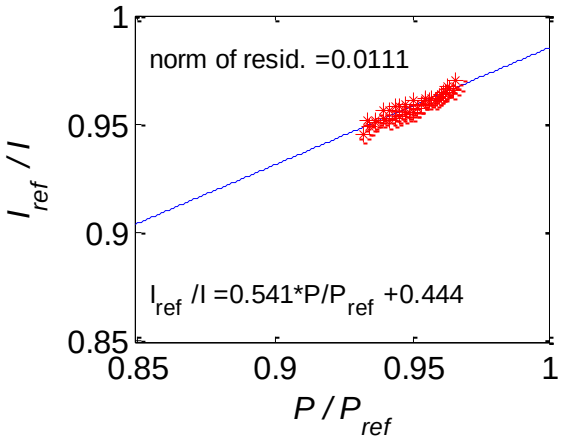

c)

Figure 3.12: Clean NACA 23012, PSP calibration, α = 14°, using a) single calibration, b) leading-edge calibration, and c) main-airfoil calibration. (Trailing-edge taps not used in calibration.)

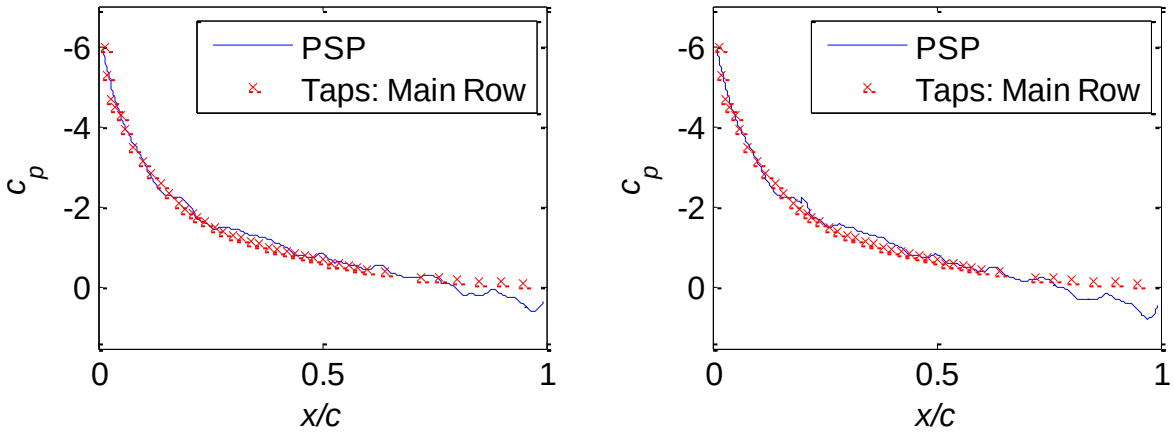

a) b)

Figure 3.13: Clean NACA 23012, PSP chordwise c_p comparison between PSP and tap data at main tap row, α = 14°, using a) one calibration and b) two calibrations. (Trailing-edge taps not used in calibration.)

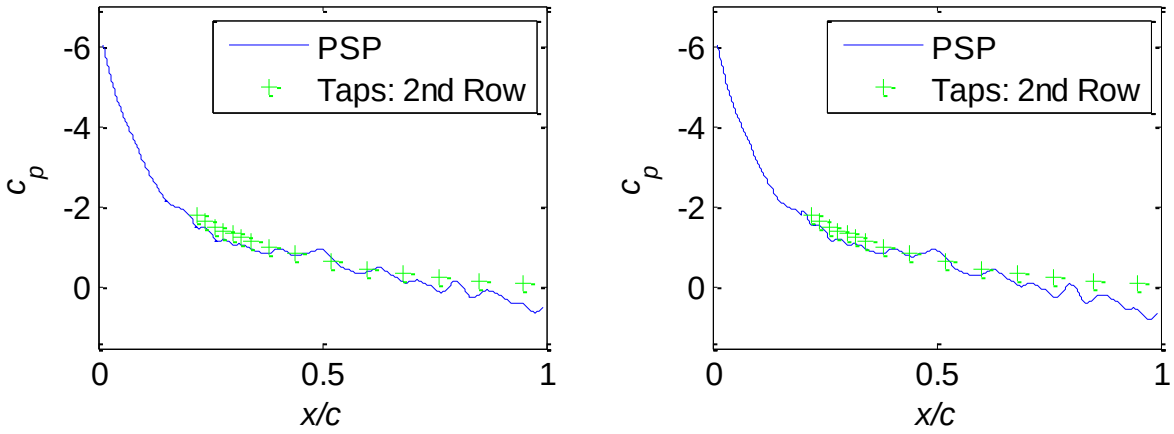

a) b)

Figure 3.14: Clean NACA 23012, PSP chordwise c_p comparison between PSP and tap data at secondary tap row, α = 14°, using a) one calibration and b) two calibrations. (Trailing-edge taps not used in calibration.)

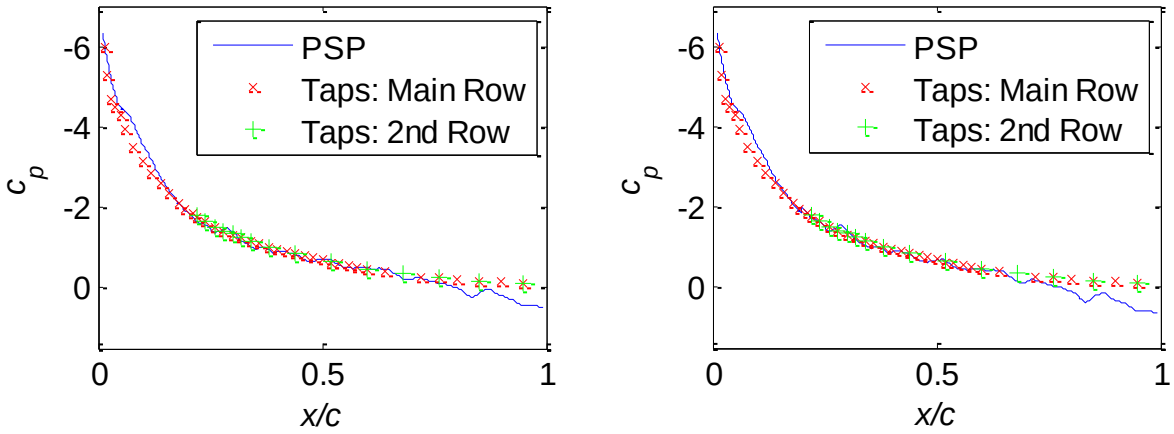

a) b)

Figure 3.15: Clean NACA 23012, PSP chordwise c_p comparison between PSP and tap data at z/b = 0.6, α = 14°, using a) one calibration and b) two calibrations. (Trailing-edge taps not used in calibration.)

3.1.3.2 Results for α = 14°

Qualitatively from Figure 3.11.a, there were few spanwise variations in pressure coefficient (c_p) for α = 14°, especially near the midspan. This was expected for a clean airfoil model, though there were some three-dimensional variations worth mentioning. The first was a gradual increase in pressure coefficient near the spanwise extremes of the painted area at $z/b \approx 0.35$ and $z/b \approx 0.7$. The curvature of the c_p contours along the span was not expected and was thought to be a result of the PSP implementation. Figure 3.16 is a plot of the c_p distributions across the span at various chordwise locations for the single calibration case and more clearly reveal this curving behavior. Near the edges of the painted area, the pressure coefficient increased along the entirety of the chord. These increases were more pronounced closer to the leading edge and were reduced further downstream. As the aerodynamic loads on the cantilevered model increased, the model deformed by bending towards the upper surface in the direction of the camera. This deformation may have caused the excitation illumination intensity at each point to change as the model moved through the intensity field of the excitation lamp. The differences in illumination between the wind-off and wind-on image at each point on the model caused the dependence on illumination to be unable to be removed from the intensity ratio. Therefore, there were errors due to model deformation and illumination variation, especially further from the center of the excitation light. It was possible the increased pressure coefficient values near the edges of the images

were due to the model deformation. A brief analysis was performed to calculate the distance a point on the model surface would have to move in order to yield the observed differences in intensity ratios. Assuming that the most accurate data was obtained at the main pressure tap row where the calibration data was taken, the reference intensity values at each point were calculated in order to produce a constant intensity ratio distribution across the span. The calculated reference intensity values were within about ±1% of the measured reference intensity values. A 1% difference corresponded to about a 0.12 in deformation. While such a deflection at the model tip could be understood, this amount of deformation closer to the constrained end of the model seemed too large. This simplified approach did not take into account the spread and distribution of the excitation light from the lamp, the more complex motion of the model, and the angle of the model movement through the excitation intensity field. These other effects could have possibly increased the intensity difference. For this reason, it was concluded that the possibility of model deformations less than 0.12 inch could have caused the increased c_p values at the spanwise extents of the painted area. In addition to this behavior, there were also a number of smaller features that consist of an area of higher c_p adjacent to an area of lower c_p than the surrounding data. These smaller features were most likely the result of an imperfect alignment and were not indicative of real flow behavior. All the above discussed effects could also have been functions of spatial and temporal temperature changes.

Figure 3.17 shows the pressure distribution at specified locations along the span. This figure exemplifies the increase in data that could be obtained with the PSP technique. In general there were no large variations along the span, though there was substantial noise closer to the trailing edge. To visualize the pressure distribution along the span at specified locations along the chord Figure 3.16 is useful. As mentioned previously, the increase in pressure at the edges of the painted area for all locations was possibly due to illumination and deformation errors. While the general behavior of the curves did not vary a great deal at midspan, the variations that were present are thought to possibly be due to the unstable flowfield near stall. The PSP data in this case were taken at $\alpha = 14°$, which was the same geometric stall angle of attack found in the aerodynamic performance tests.

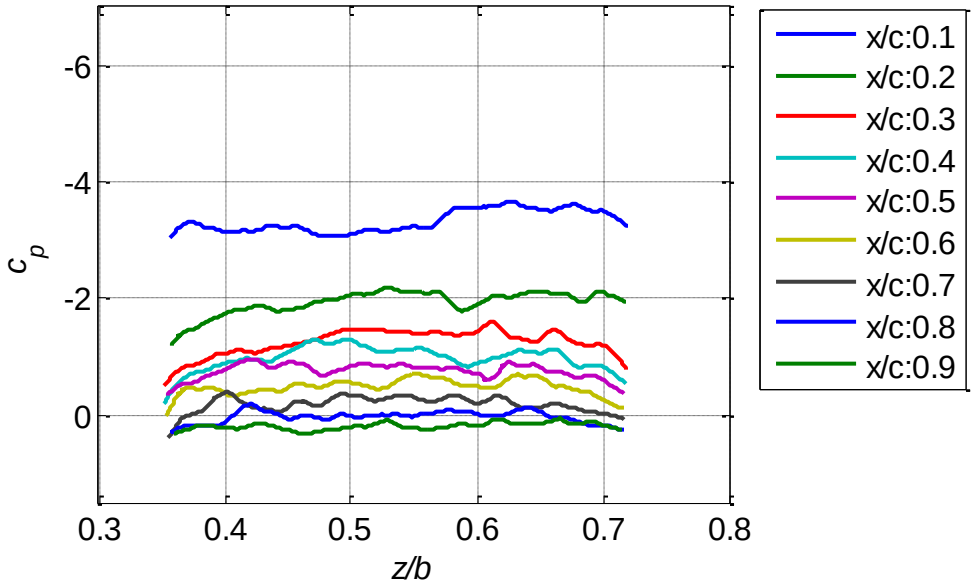

Figure 3.16: Clean NACA 23012, PSP spanwise *cp* curves at various *x/c* locations, α = 14°.

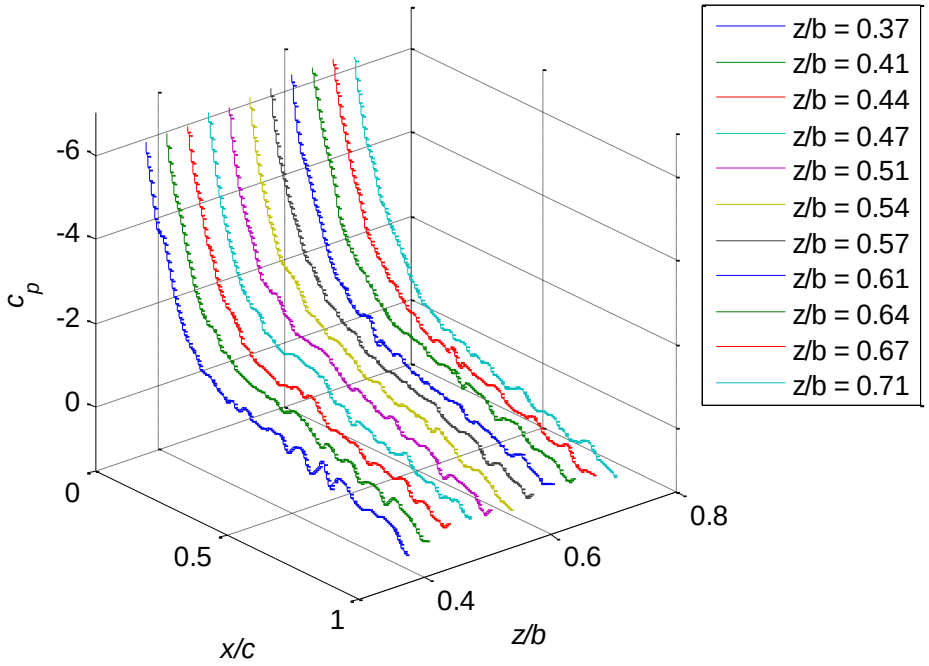

Figure 3.17: Clean NACA 23012, PSP chordwise *cp* curves at various *z/b* locations, α = 14°.

3.1.3.3 C_p Comparison at Different Angles of Attack

A comparison of the pressure coefficients for the clean case at α = 12° and α = 14° is presented in Figure 3.18. Figure 3.18 contains the pressure coefficient contours for both angles. The increased suction with the increase in angle of attack was clearly seen in the enlargement of the bluer area in this figure for the α = 14° case. The c_p data at the lower angle of attack had less spanwise variation than the data at the stall angle of attack at α = 14°. This decrease in variation could be seen in Figure 3.22, where the spanwise pressure distributions were plotted at a number of chordwise locations. Comparing this figure to the same plot for α = 14° in Figure 3.16 shows how the variations seen at the stall angle of attack were not present at the lower angle. This was due most likely to the increased aerodynamic loading on the model at the higher angle of attack. This would have caused a greater amount of model deformation and movement through the illumination field, causing greater errors at the edges of the painted area. The chordwise pressure distributions at three spanwise locations are shown in Figures 3.19, 3.20, and 3.21. Here the larger suction peak for the greater angle of attack at α = 14° was clearly observed. It could also be seen how the lower angle of attack data at α = 12° had less variation than the higher angle. This could be due to the proximity to stall of the α = 14° case.

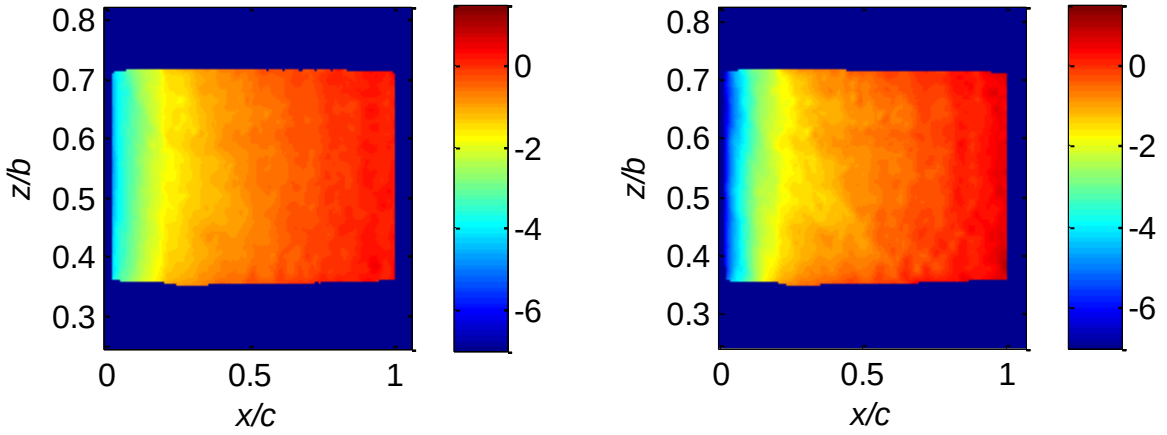

Figure 3.18: Clean NACA 23012, PSP c_p contour comparison at a) α = 12° and b) α = 14°.

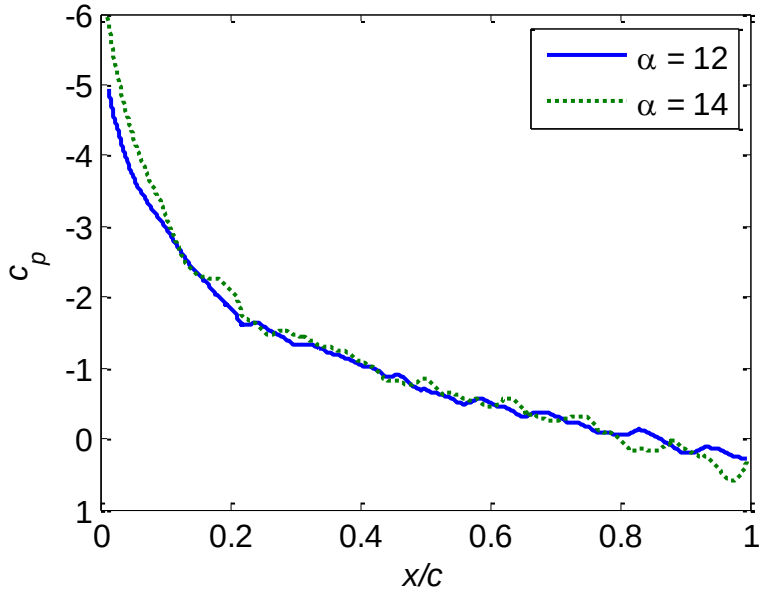

Figure 3.19: Clean NACA 23012, PSP c_p comparison between α = 12° and α = 14° at main tap row, z/b = 0.515.

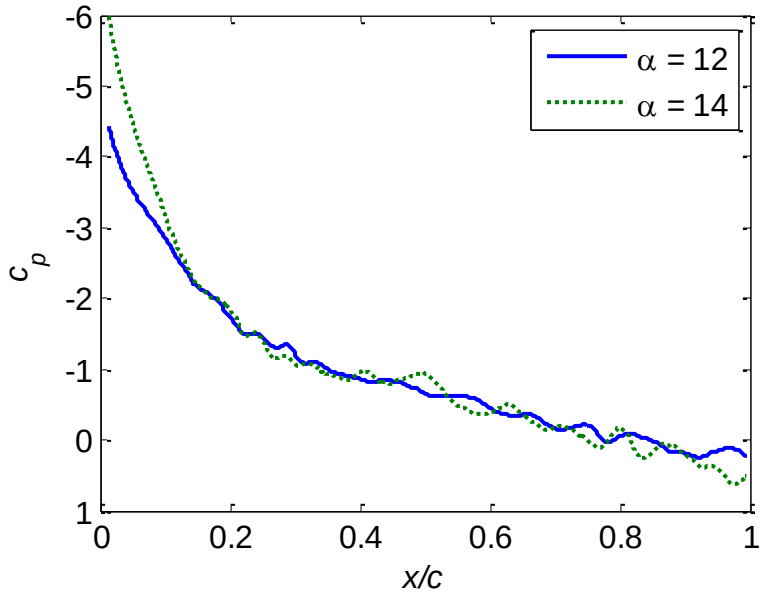

Figure 3.20: Clean NACA 23012, PSP chordwise c_p comparison between α = 12° and α = 14 at secondary tap row, z/b = 0.417.

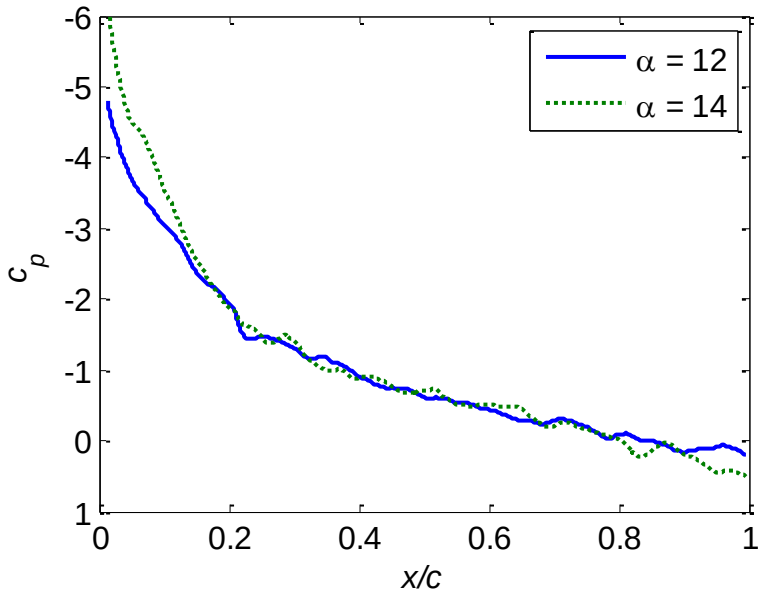

Figure 3.21: Clean NACA 23012, PSP chordwise c_p comparison between α = 12° and α = 14 at z/b = 0.6.

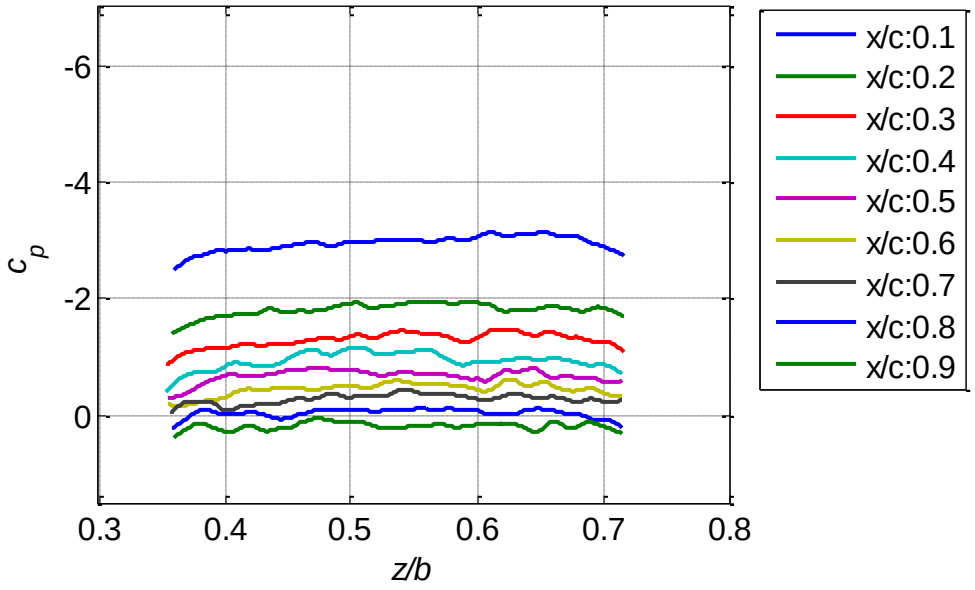

Figure 3.22: Clean NACA 23012, PSP spanwise c_p curves for various x/c locations, α = 12°.

3.2 Horn Ice Shape Comparison

3.2.1 Geometric Comparison

The horn ice shapes generated from the casting and the rapid-prototype (RPM) methods had a number of geometric differences. This was interesting because both were recorded from the same original ice accretion in the IRT, so it was expected that the larger features would be replicated similarly. Using two-dimensional traces, the horn location (*s/c*), angle (θ), and height (*k/c*) for both shapes at the main tap row span location were calculated. The location of the upper horn on the casting shape was at 0.00950 *s/c* with an angle of θ = 34.29° and height *k/c* = 0.0387 at the tap row. The rapid-prototype shape's upper horn was located closer to the leading edge at 0.00892 *s/c* with a lower angle of θ = 32.20° and greater height of *k/c* = 0.0408 at the same spanwise location as the casting trace. The lower horn on the casting shape was at 0.01178 *s/c* and θ = -42.54° with a height of *k/c* = 0.0232, while the lower horn on the rapid-prototype shape was further from the leading edge at 0.01251 *s/c* and has a greater angle of θ = -45.19° with a greater height of *k/c* = 0.0238. These values were determined from the outlines of the two shapes at the main tap row. The casting outline was found by cutting a casting of the shape at the spanwise location of the taps, which was done as part of the process of determining the location and orientation of the tap holes and is described in the Experimental Methodology chapter. The ice shape was then traced onto cardboard with a cutout of the NACA 23012 geometry (the same process as was performed in the IRT to two-dimensionally record ice shapes) and digitized. The outline of the shape for the rapid-prototype model was determined from the software used to record and process the digital scan. Figure 3.23 shows the outlines of both shapes. Lee et al.[28] concluded that initial comparisons performed during the development of the 3-D methodology agreed. However, there were differences for this test that should be noted. The tip of the upper horn for the casting was more rounded and was at a higher angle to the chordline than the RPM horn. A large feature was also present on the upper horn of the rapid-prototype shape just before the ice/airfoil junction that was not present in the casting trace. These were indicative of differences that are present along the span. Figure 3.24 shows both leading edges with the upper- and lower-surface horns outlined. There were a number of features that differ between the two that were more easily seen in the overlay of the two shapes in Figure 3.25.

While this was a coarse comparison, the tendency of the 3-D laser scanner/rapid-prototype method to produce ice shapes with larger features than the mold and casting method was apparent across the span. In some instances there were features present on the RPM shape which did not exist on the casting. This could be due to the processing of the laser scans, where holes in the data could have been filled so that artificial features were created that differed from the original ice accretion geometry. It was also possible that some features broke off the ice accretion or melted during the molding process or during the course of the casting creation. However, it was unlikely that enough ice would have broken off to cause the RPM shape to consistently possess larger features due to the care taken during ice shape acquisition in the IRT. Other potential causes for the smaller casting geometry could be due to air pockets between the mold and the casting material or the mold pressing against the casting material during curing. Either of these possibilities would yield a smaller casting than RPM shape. It was currently unknown what the exact cause of the differing geometries was, though further work is being performed by Lee et al. to address this issue.[38]

Table 3.2: Geometric horn parameter comparison for the casting and rapid-prototype shapes.

Horn Parameter	Casting	Rapid-Prototype Shape
k/c (upper-surface horn)	0.0387	0.0408
k/c (lower-surface horn)	0.0232	0.0238
s/c (upper-surface horn)	0.0095	0.00892
s/c (upper-surface horn)	0.01178	0.01251
θ (upper-surface horn)	34.29°	32.20°
θ (lower-surface horn)	-42.54°	-45.19°

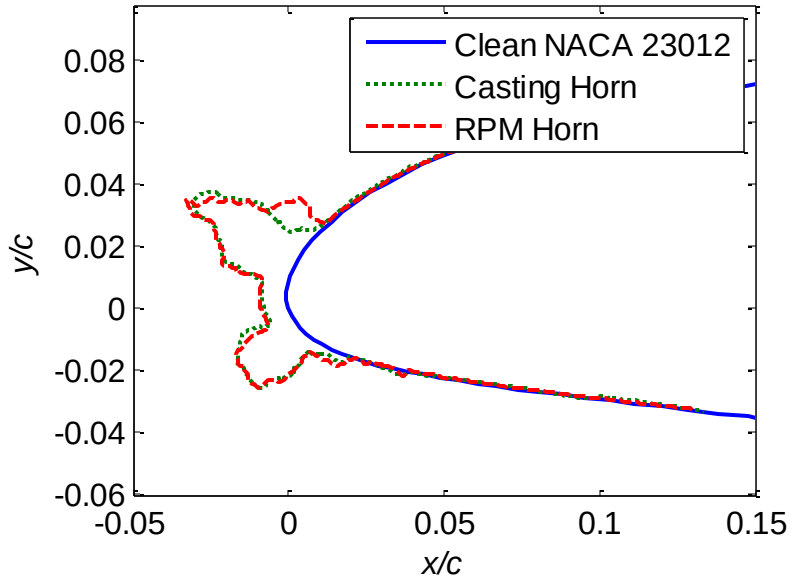

Figure 3.23: Horn ice shapes, 2-D trace comparison between casting and RPM shapes at main tap row, z/b = 0.515.

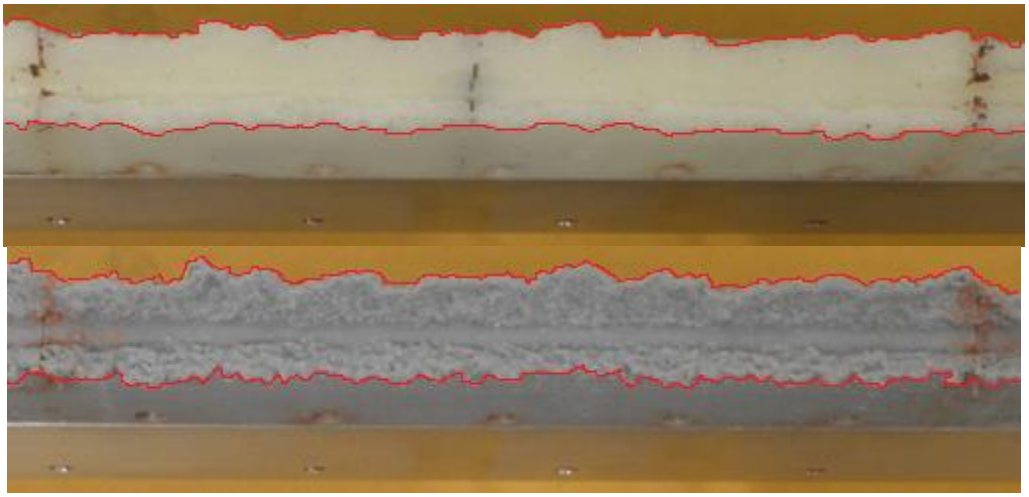

Figure 3.24: Horn ice shapes, casting (top) and RPM shape (bottom) viewed from leading edge with rough location of tips outlined in red.

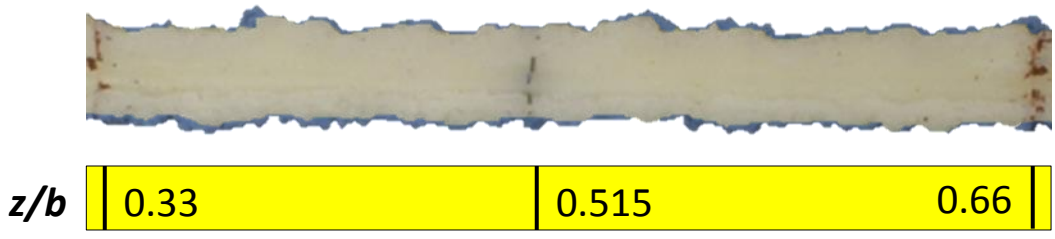

Figure 3.25: Horn ice shape, overlay comparison between casting (white) and RPM shape (blue) viewed from leading edge.

3.2.2 Aerodynamic Comparison

Figures 3.26 through 3.33 show the aerodynamic performance of both horn shapes in comparison to the clean model. Only the force balance data were presented here because of the reduced effectiveness of the pressure taps to provide good enough spatial resolution for accurate pressure integration. Both casting and rapid-prototype shapes caused the typical severe reduction in the maximum lift coefficient ($c_{\ell,max}$), as well as in the stall angle of attack (α_{stall}), associated with horn ice accretions and can be seen in Figure 3.26. There was a 0.77 drop in $c_{\ell,max}$ for the casting horn shape, which was a 52.3 % loss. Similarly, there was a 0.79 drop in $c_{\ell,max}$ for the rapid-prototype horn shape, which was a 53.9 % loss.

Additionally, the stall behavior changed with the presence of the ice shapes. The clean airfoil exhibited leading-edge type stall as could be observed in the c_ℓ-α curve. From the gradual stalling behavior seen in Figure 3.26 and the large separation bubble observed from the oil flow for both the horn shapes, the horn case seemed to exhibit thin-airfoil stall. The flow had a fixed separation point at the horn tip due to the large adverse pressure gradient at that location, similar to that at the leading edge of a flat plate. The flow reattached further downstream, forming a separation bubble behind the horn. As this recirculation region grew with increased angle of attack, the lift deviated further from the clean case value. Stall occurred when the shear layer failed to reattach downstream. This type of stall was seen in the flow visualization data taken for the horn shapes. Figure 3.27 is the surface oil flow visualization for both horn shapes at α = 4°, Figure 3.28 for α = 6°, and Figure 3.29 at α = 7°. The recirculation region, where its downstream extent was denoted by the yellow reattachment line, clearly increased with angle of attack, and would eventually encompass the entire chord at stall. The reattachment line was not drawn in Figure 3.29 because it was more difficult to determine its location so close to stall. The red line marked the secondary separation of the recirculated flow within the bubble.

The rapid-prototype shape stalled first, though this was difficult to determine since data were taken only once every degree in angle of attack. The casting horn $c_{\ell,max}$ was 0.7, in comparison to the lower value of 0.68 for the rapid-prototype horn. The flow visualization images in Figures 3.27, 3.28, and 3.29 show differences in the lengths of the separation bubbles for each shape. In Figure 3.27 at α = 4°, the reattachment location, represented by

the yellow line, for the casting was at about *x/c* = 0.1 while the reattachment location was further downstream at about *x/c* = 0.15 for the RPM shape. At α = 6° these reattachment lines moved further downstream to about *x/c* = 0.2 for the casting and *x/c* = 0.275 for the RPM shape. The reattachment line for α = 7° was not marked in Figure 3.29 since it cannot clearly be seen in the oil flow. Results similar to those seen at positive stall occurred at negative stall as well. The lower-surface horn modified the flow in a similar way as the upper-surface horn. This was evident in the less negative α_{stall} values for both horn shapes when compared to the clean airfoil, as well as the gradual stall behavior. While both ice shapes showed similar negative effects in c_ℓ, the magnitudes of these effects differed slightly.

These differing results for the casting and rapid-prototype shapes were unexpected considering aerodynamic penalties from a horn shape are dependent on the geometric characteristics of the horn: height, location, and angle, and not small scale roughness.[3] Since both shapes were created from the same initial ice accretion, it was expected that the major geometric features would be comparable. The geometric variations between the two shapes made from the two methods could be significant enough to cause these discrepancies. More work is being done to find the cause of this, perhaps in the way the scanning software processes the shape.[38]

Similar trends could be seen in the other horn shape performance plots. The drag polar and c_d-α plots in Figures 3.30 and 3.31, show the significant increase in drag that was associated with the horn ice shapes' presence. These show a 306% increase in minimum drag coefficient (c_d) for the casting shape and a 315% increase for the rapid-prototype shape. At positive angles of attack the drag for the RPM shape was greater than the drag for the casting case, though this was not the case at negative angles of attack. At angles of attack less α = 1°, where the lower horn dominated the aerodynamics, good agreement is observed between the two horn ice shapes. This implied that both shapes could have similar lower-surface horn geometries, or that the differing geometries had similar effects. The geometric features that caused differences in the aerodynamic performance were then more prevalent on the upper-surface horns.

Figure 3.32 shows the c_p comparison curves for both horn shapes and the clean model at α = 4°, α = 6°, α = 7°, α = 9°, and α = 10°. All angles show the change in leading-edge

suction peak behavior for both shapes in comparison to the clean case. The plateau-like behavior of the iced c_p curves near the leading edge was indicative of a separation bubble, and was present at all angles of attack for both ice shapes. There was also a significant decrease in suction peak as seen at higher angles of attack. At lower angles, such as $\alpha = 4°$, the suction peak for the iced cases exceeded the clean model suction peak. However, the presence of the lower-surface horn and the steep adverse pressure gradient behind the horn yielded no benefit in the integrated pressure calculation for lift. Throughout the angle of attack range presented here, the casting horn consistently had greater suction near the leading-edge upper surface, which resulted in greater integrated pressure values for lift than was observed for the RPM shape. At some point downstream of the leading edge, the upper-surface portions of each iced-c_p curve intersected. This intersection point was a useful reference point that was used to compare the PSP data discussed later to the aerodynamic data. This point occurred at about $x/c = 0.15$ for $\alpha = 4°$ and $x/c = 0.2$ for $\alpha = 7°$. The pressure distributions for the two shapes followed the same general behavior, leading to the conclusion that both stalled at about the same angle of attack, though the aerodynamics prior to stall differed in magnitude. By $\alpha = 9°$ both distributions had stalled over most of the upper surface, as indicated by the flattened c_p curves. Stall seemed to be complete by $\alpha = 10°$.

The wakes for the two horn shapes and the clean model at $\alpha = 7°$ are shown in Figure 3.33, which is a plot of the measured pressure difference between the wake stagnation pressure and atmospheric pressure in a plane normal to the freestream direction. The wakes for the two horn shapes had a significantly larger width and much larger pressure differences than the clean model. The rapid-prototype horn shape had a larger wake than the casting horn ice shape at the same angle of attack, especially from the upper surface. These wake differences most likely stemmed from the geometric differences between the two horn shapes. The overall greater upper-surface horn height for the RPM shape probably caused a greater disruption to the flow, less pressure recovery, and greater momentum loss for this case. This resulted in greater drag values for that shape than for the casting shape.

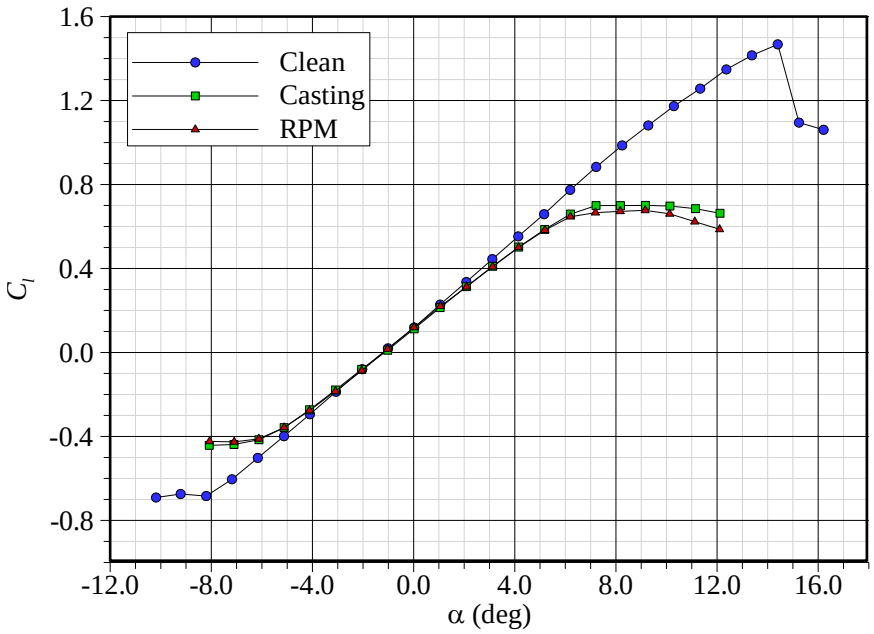

Figure 3.26: Horn ice shapes, c_ℓ-α curve comparison, Re 1.8 million.

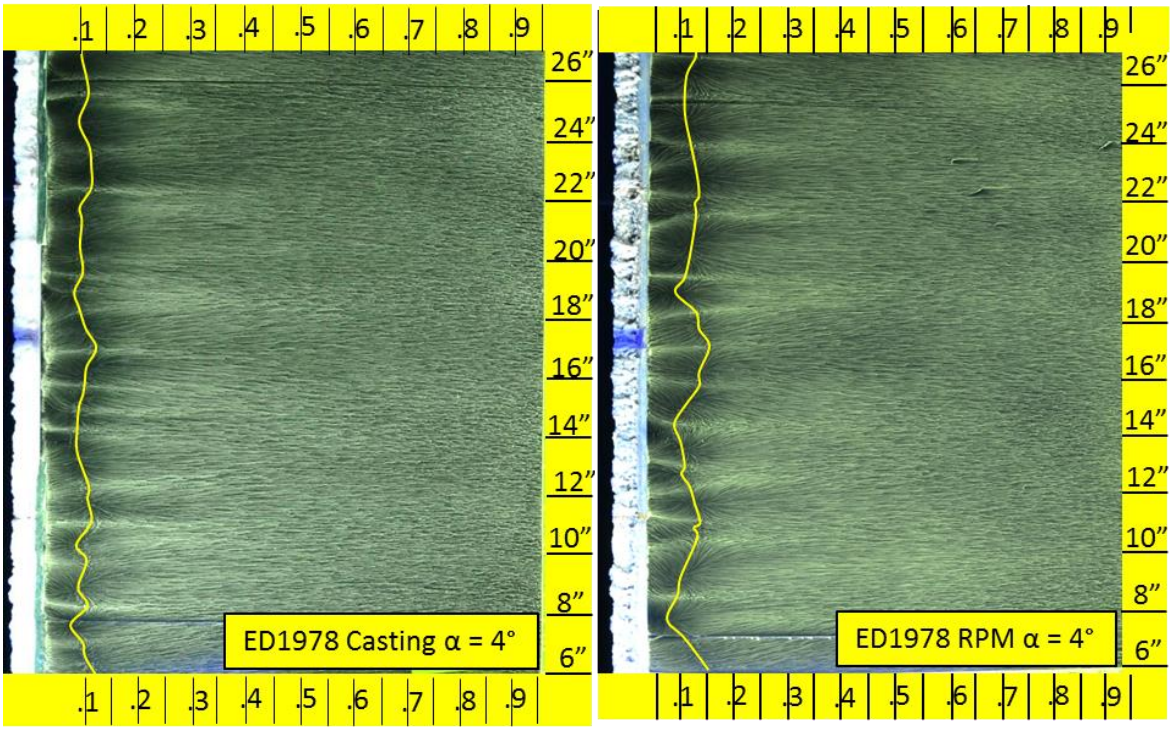

a) b)

Figure 3.27: Horn ice shapes, surface oil flow visualization comparisons at α = 4° for the a) casting and b) RPM shapes. Yellow line denotes reattachment line. Horizontal scales mark *x/c* locations and vertical scales mark height from tunnel floor. All locations are approximate.

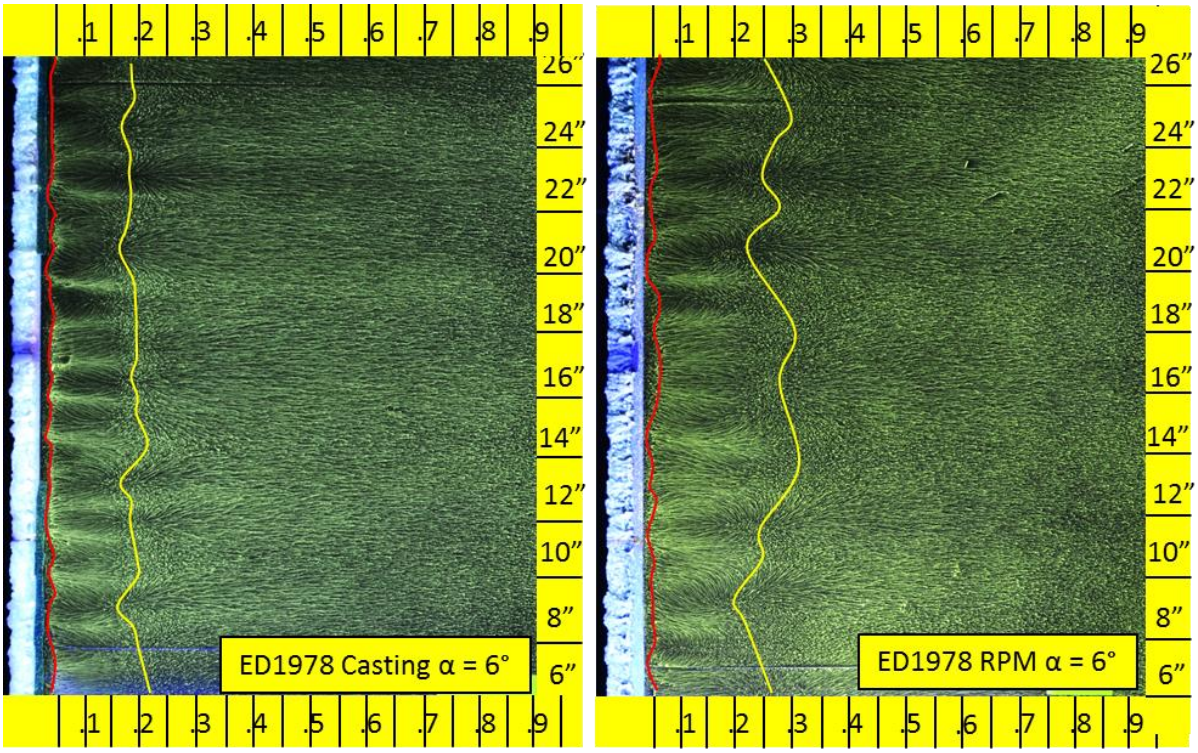

a) b)

Figure 3.28: Horn ice shapes, surface oil flow visualization comparisons at α = 6° for the a) casting and b) RPM shapes. Yellow line denotes the reattachment line and red line denotes the secondary reattachment line. Horizontal scales mark *x/c* locations and vertical scales mark height from tunnel floor. All locations are approximate.

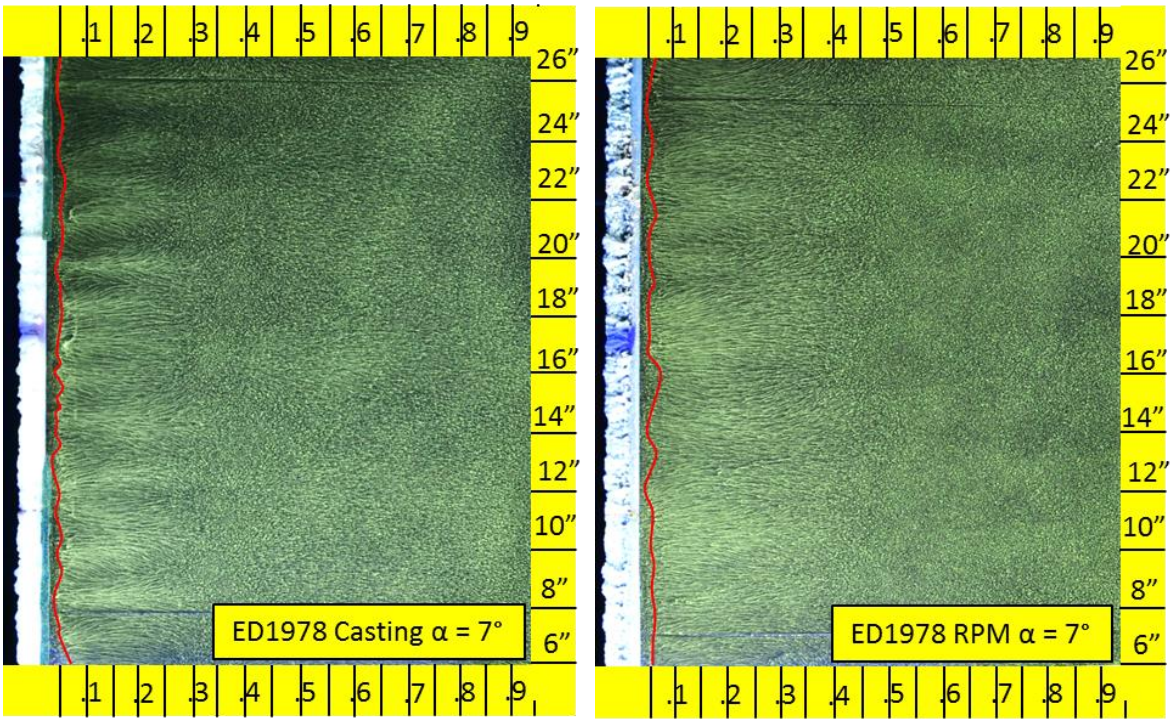

a) b)

Figure 3.29: Horn ice shapes, surface oil flow visualization comparisons at α = 7° for the a) casting and b) RPM shapes. Red line denotes the secondary reattachment line. Horizontal scales mark *x/c* locations and vertical scales mark height from tunnel floor. All locations are approximate.

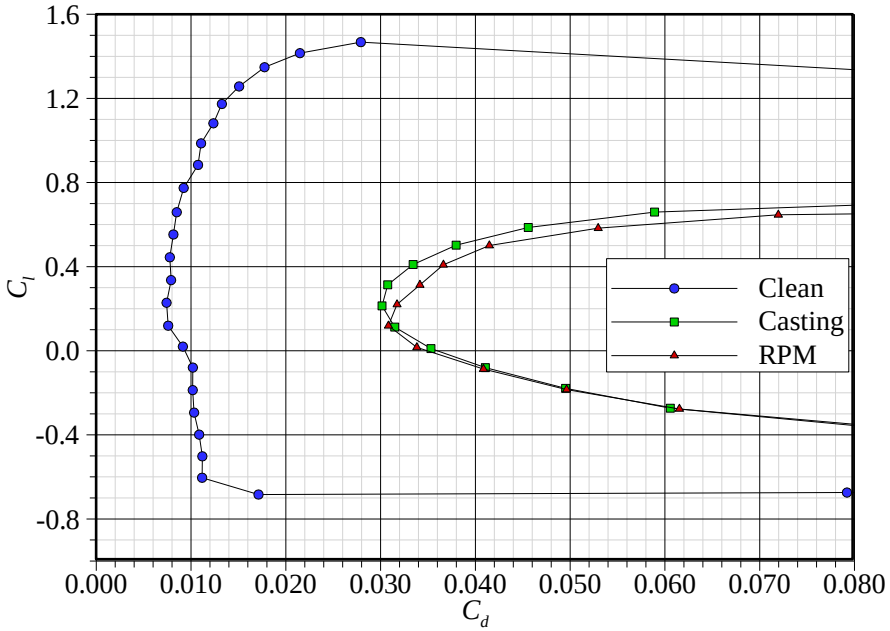

Figure 3.30: Horn ice shapes, drag polar comparison, Re 1.8 million.

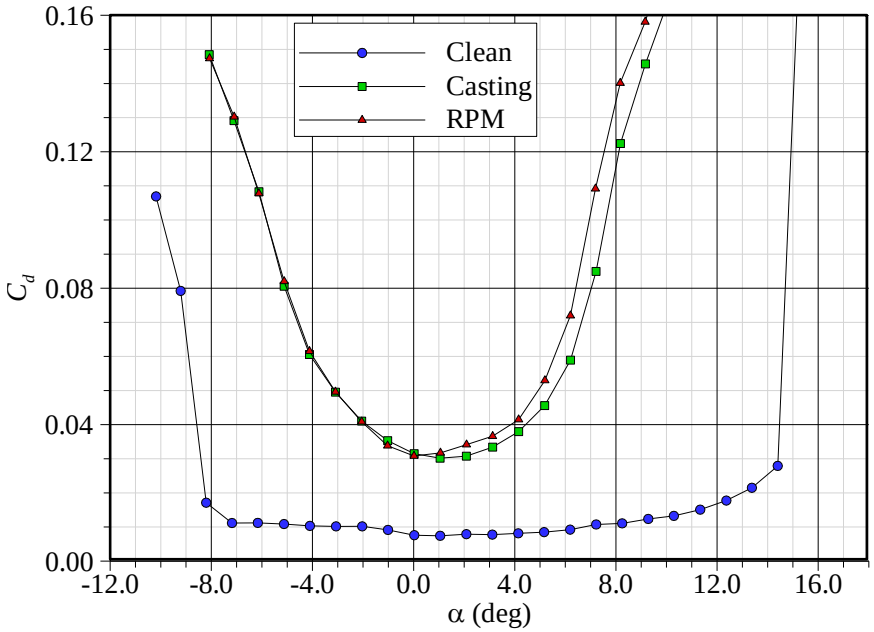

Figure 3.31: Horn ice shapes, c_d-α curve comparison, Re 1.8 million.

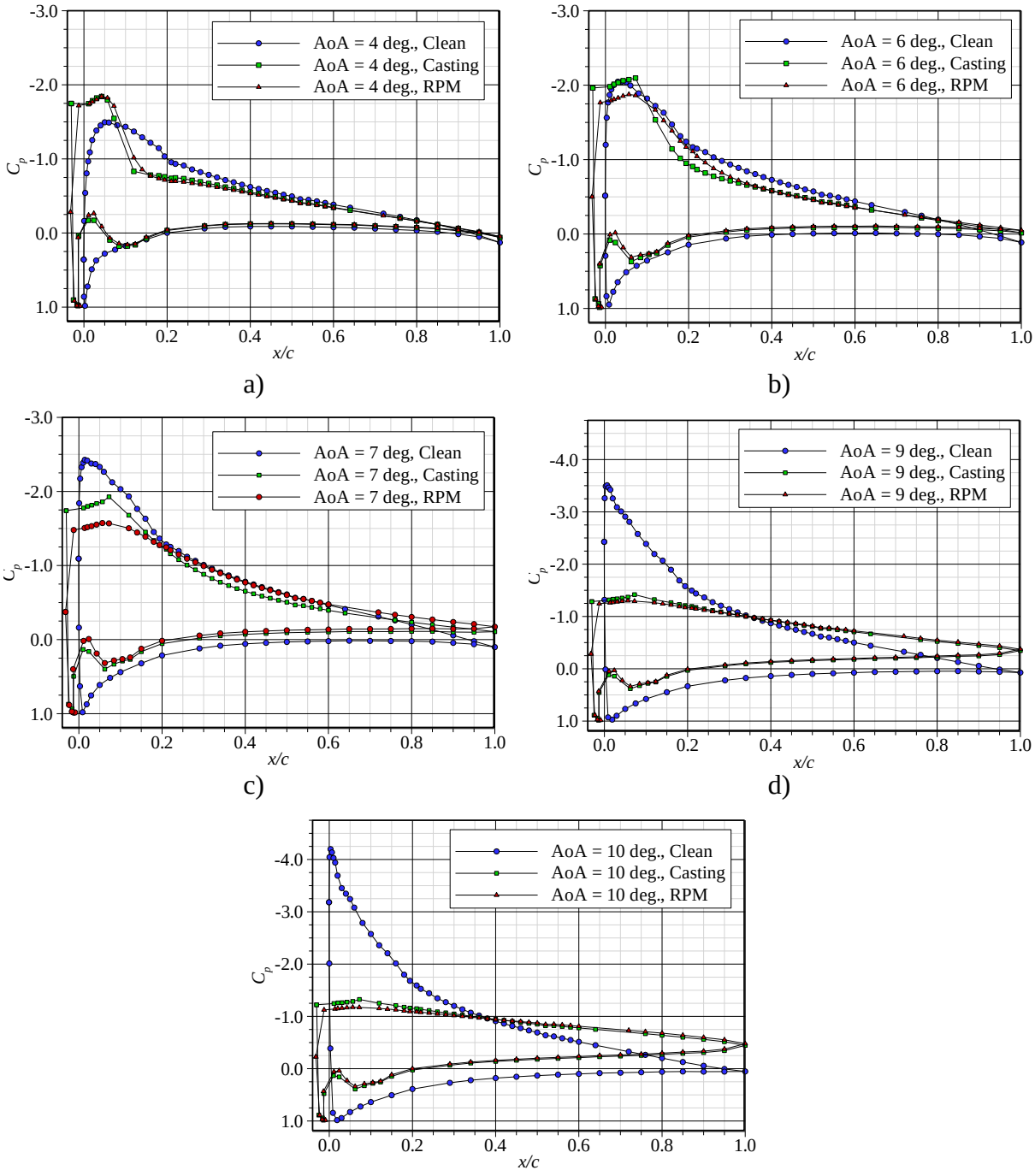

Figure 3.32: Horn ice shapes, c_p curve comparisons at a) α = 4°, b) α = 6°, c) α = 7°, d) α = 9°, and e) α = 10°.

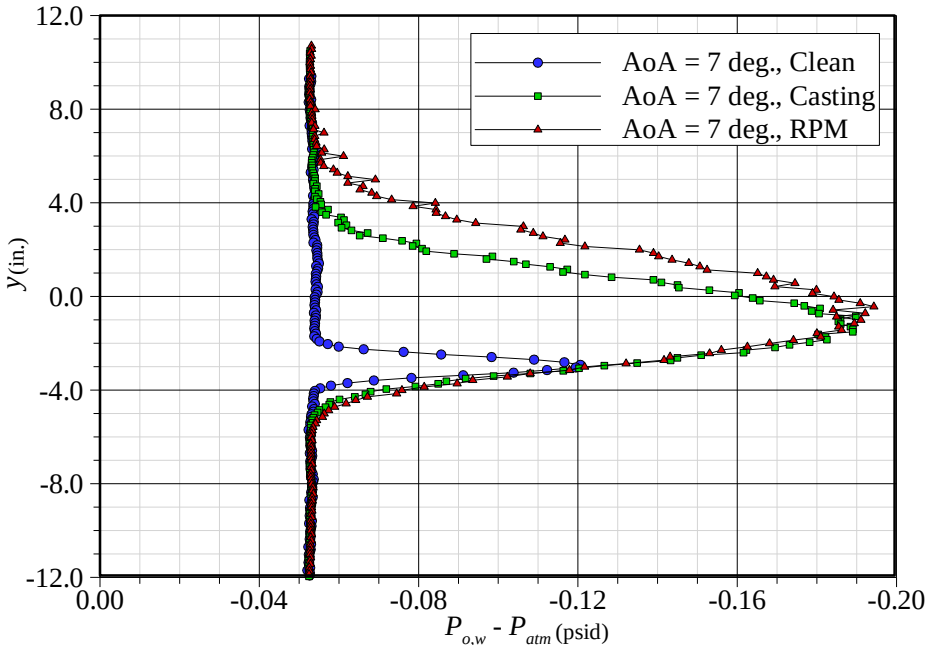

Figure 3.33: Horn ice shapes, wake comparisons at α = 7°.

3.2.3 PSP Comparison

The PSP data for the horn shapes were compared to the pressure tap c_p distributions for angles of attack of α = 6° and α = 7°. Through the use of the PSP method, c_p data over the entire painted section were able to be obtained. The painted area extended from directly behind the upper-surface horn to the trailing edge. PSP could not be applied to the horn itself because the roughness features would cause self-illumination errors in the data. Self-illumination occurs when emitted light from the paint is reflected off of other areas of the model. The intensity at the reflection point is the sum of the reflection due to self-illumination and the emission from luminophore excitation at that location. Painting a large portion of the model allowed a greater three-dimensional analysis to occur than is possible solely with pressure taps.

The calibrations for the horn cases are presented in Figure 3.34. Two slightly different calibration techniques were used for the casting and RPM shapes. Two separate calibrations were applied to the RPM data: one for the leading-edge portion of the model, and a second for the remainder of the airfoil body. Only one calibration was applied to the casting data. This was decided because a single calibration for the rapid-prototype shape revealed two distinct groups of data: one for the leading-edge ice shape taps and the other for the

Appendix C leading edge and main body taps. A possible reason for this difference could stem from the different materials of those surfaces. The rapid-prototype leading-edge ice shape was formed from SLA material, while the body of the airfoil was made from aluminum. The different optical and thermal properties of these materials may have affected the emitted intensities in those regions. To quantify the goodness-of-fit of the calibrations, the norm of the residuals for each calibration was calculated. Using the single calibration method, the norm of the residual for the rapid-prototype shape was calculated as 0.0119. Using the two calibration method, the two norms of residuals for the leading-edge and body calibrations were 0.0015 and 0.0078, respectively. The leading-edge data from the casting ice shape, on the other hand, fit well with the data on the rest of the model with a norm of the residuals of 0.0089. For this reason, only one calibration was used for the casting horn ice shape. These values for the norms of the residuals are tabulated in Table 3.3. Whether this was because the optical and thermal properties of the casting resin were similar enough to the aluminum or because there were differences in the base coat or PSP application between the casting and RPM shapes remains to be determined. The calibration analysis performed on the clean model and discussed previously showed how one calibration could be used for the data from the separately painted leading-edge piece and main body both made from aluminum. This seemed to support that differing materials have more of an effect on PSP results than paint application.

To validate the method for this case, pressure tap and PSP data were plotted together to compare results at the same spanwise locations for an angle of attack of $\alpha = 7°$. It was observed from Figures 3.35 through 3.37 that the pressure tap data agreed well with the PSP data. Since an in-situ calibration was used, the agreement at the two pressure tap row locations was expected to be good. Therefore, to show the agreement elsewhere, another location for comparison was chosen ($z/b = 0.6$), far from the tap rows. Here, the PSP data were taken at $z/b = 0.6$ while the tap data was taken from both the main and secondary tap rows. Figures 3.35, 3.36, and 3.37 show that for both the casting and rapid-prototype horn cases, PSP could be used to successfully yield the same information as traditional pressure taps. One drawback to the PSP data set was the noise. While care was taken to eliminate as much noise as possible in this work, further work can and is being performed to reduce it. The pressure differences resolved here are very small by the nature of the particular model

and facility used in this study. In larger tunnels with higher test dynamic pressures, the pressure range is significantly greater. This would produce a larger signal-to-noise ratio and more accurate calibration.

The c_p plots over the entire painted area are presented in Figure 3.38. The greatest difference between the casting and RPM horn shapes was the longer length of the lower pressure region for the RPM shape. This was seen in the greater extent of blue and green in the RPM case. Additionally, it was observed that the suction peak was higher for the casting than the RPM. To more clearly visualize the differences, two-dimensional cuts of the data in both the chordwise and spanwise directions were analyzed. Figure 3.39 shows the pressure distributions along the chord at a number of spanwise locations. No significant changes were visible in this figure along the span, though there was increased noise from about *x/c* = 0.5 to the trailing edge.

Comparisons of the chordwise pressure coefficients for the two shapes plotted together at each of three spanwise locations are shown in Figures 3.40, 3.41, and 3.42. The casting consistently had lower pressure values directly behind the horn, which agreed with the pressure tap data previously discussed and corresponded to a shorter upper-surface horn height. At about *x/c* = 0.2, it was observed that the c_p curves for the two horn shapes intersected. After this point the RPM pressure was generally lower than that for the casting, and agreed with the observations seen in the pressure tap data.

The spanwise c_p distributions in Figures 3.43 and 3.44 show the evolution of the spanwise behavior over the chord. The casting horn in Figure 3.43 had higher c_p values at lower *x/c* locations and more variations in magnitude. The specific *x/c* locations were compared in Figures 3.45 through 3.50. In general, both shapes had similar features in the comparison plots but with slight offsets. Figure 3.45 shows how each peak and valley in the casting data was mimicked in the RPM shape data at *x/c* = 0.05, with an offset between the two. At this location, the casting had lower pressure over most of the span. At x/c ≈ 0.2, the c_p curves crossed. This was evident in Figure 3.47, where both c_p distributions were about equal along the span. After this point, the RPM shape had lower pressure until the trailing edge. These results agreed with those seen from the two-dimensional pressure tap data.

Table 3.3: Horn ice shapes, Norms of Residuals for Different Calibration Schemes

Case	Norm of the Residuals
Single Calibration: RPM	0.0119
Double Calibration-Leading-Edge Data: RPM	0.0015
Double Calibration-Main Body Data: RPM	0.0078
Single Calibration: Casting	0.0089

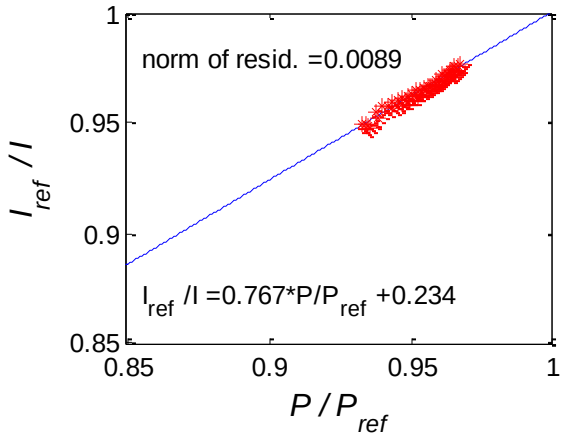

a)

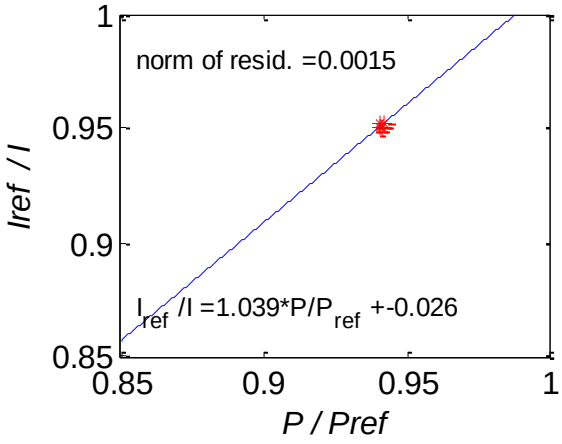

b)

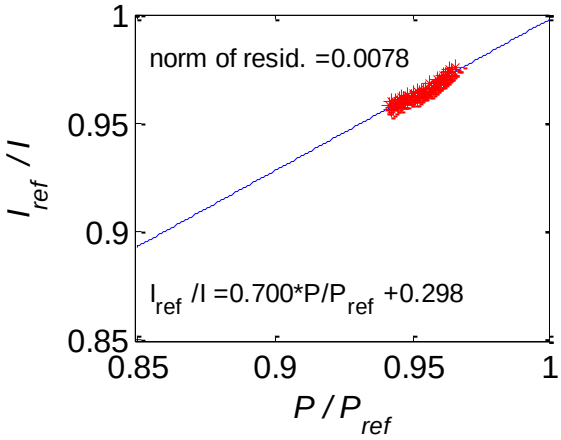

c)

Figure 3.34: Horn ice shapes, PSP calibrations, α = 7°, a) casting, b) RPM leading edge, and c) RPM body calibrations.

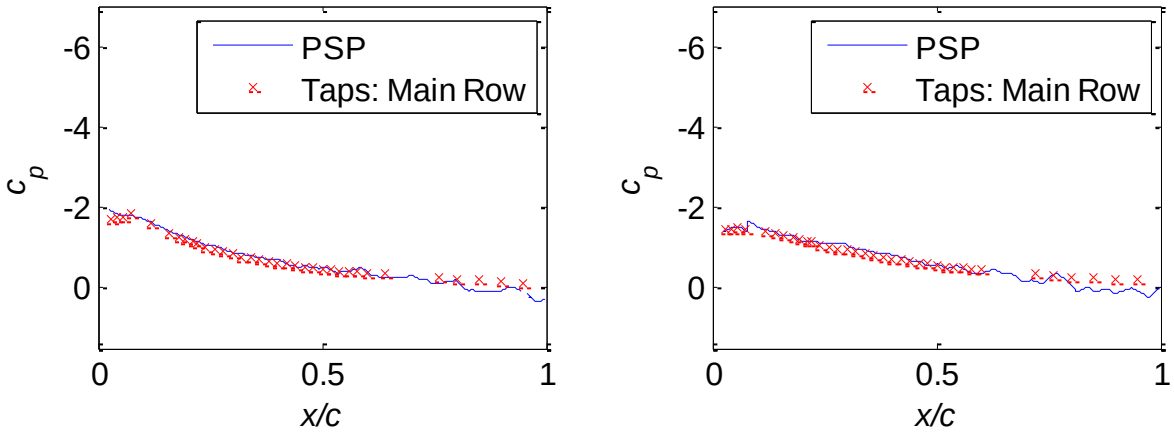

a) b)

Figure 3.35: Horn ice shapes, PSP chordwise c_p comparison between PSP and tap data at main tap row, z/b = 0.515, at α = 7°, a) casting and b) RPM shape. (Trailing-edge taps not included in calibration.)

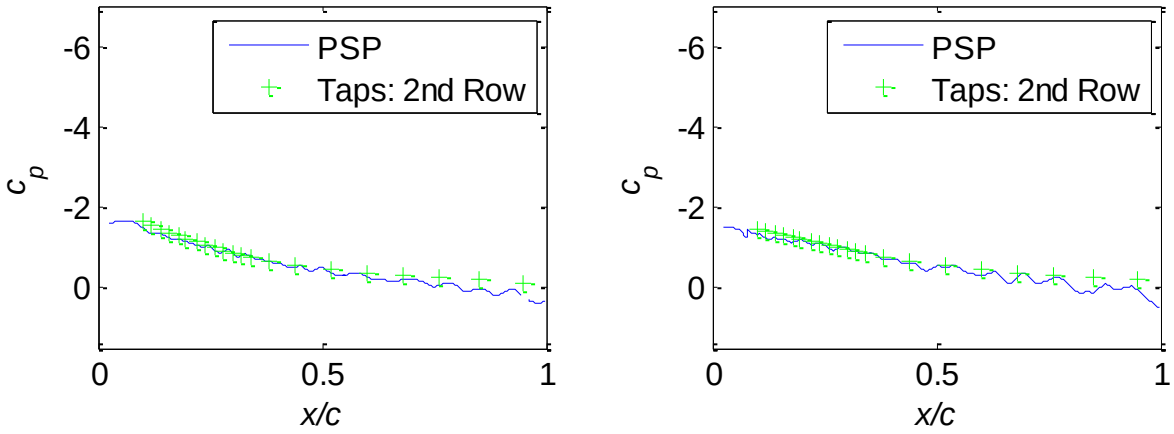

a) b)

Figure 3.36: Horn ice shapes, PSP chordwise c_p comparison between PSP and tap data at secondary tap row, z/b = 0.417, at α = 7° a) casting and b) RPM shape. (Trailing-edge taps not included in calibration.)

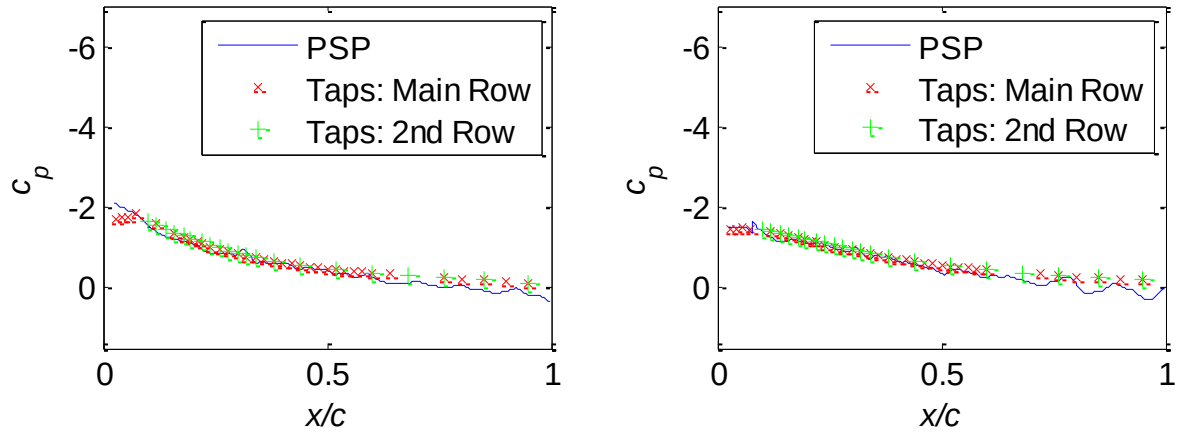

a) b)

Figure 3.37: Horn ice shapes, PSP chordwise c_p comparison between PSP and tap data at *z/b* = 0.6, at α = 7°, a) casting and b) RPM shape. (Trailing-edge taps not included in calibration.)

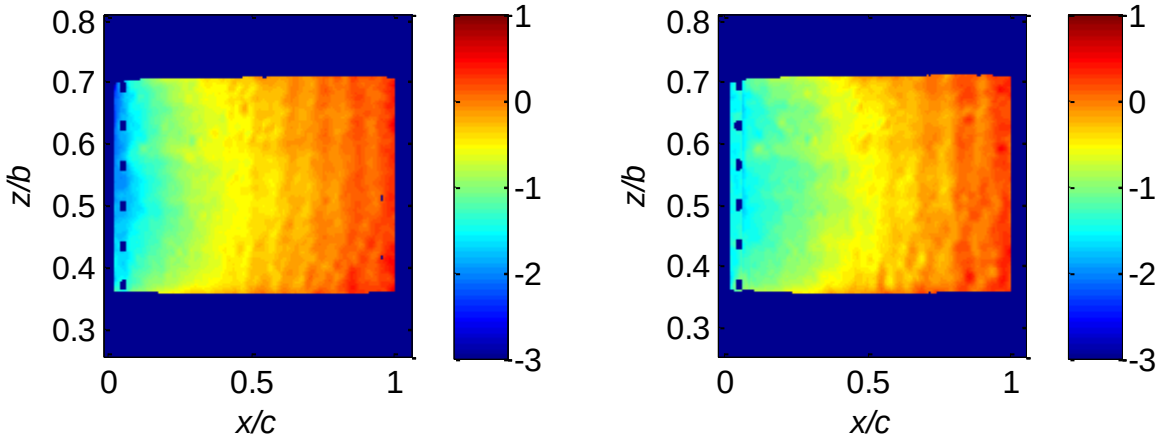

a) b)

Figure 3.38: Horn ice shapes, PSP c_p contour comparisons, α = 7° for a) casting and b) RPM shape.

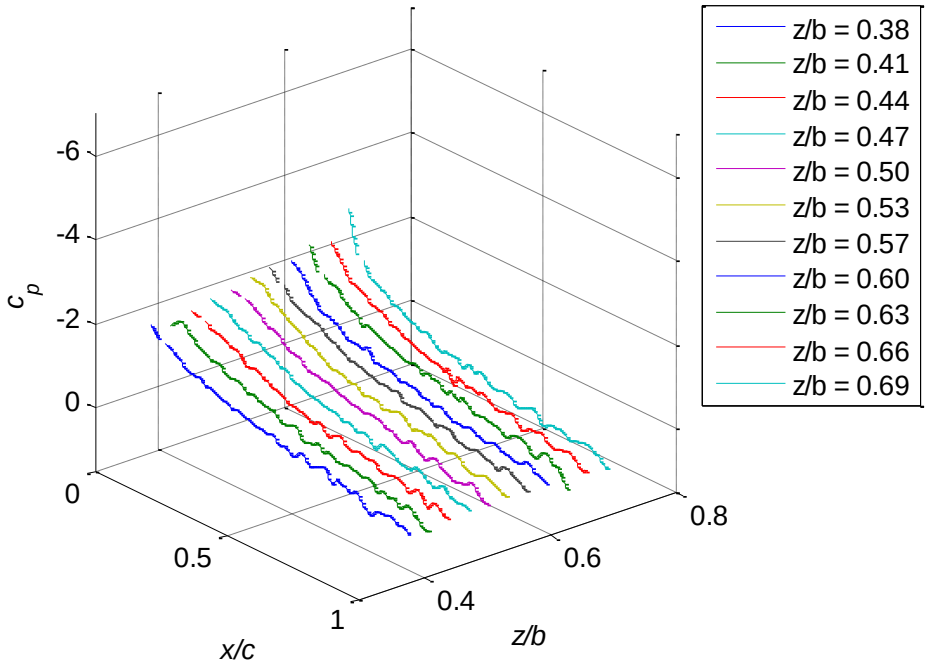

a)

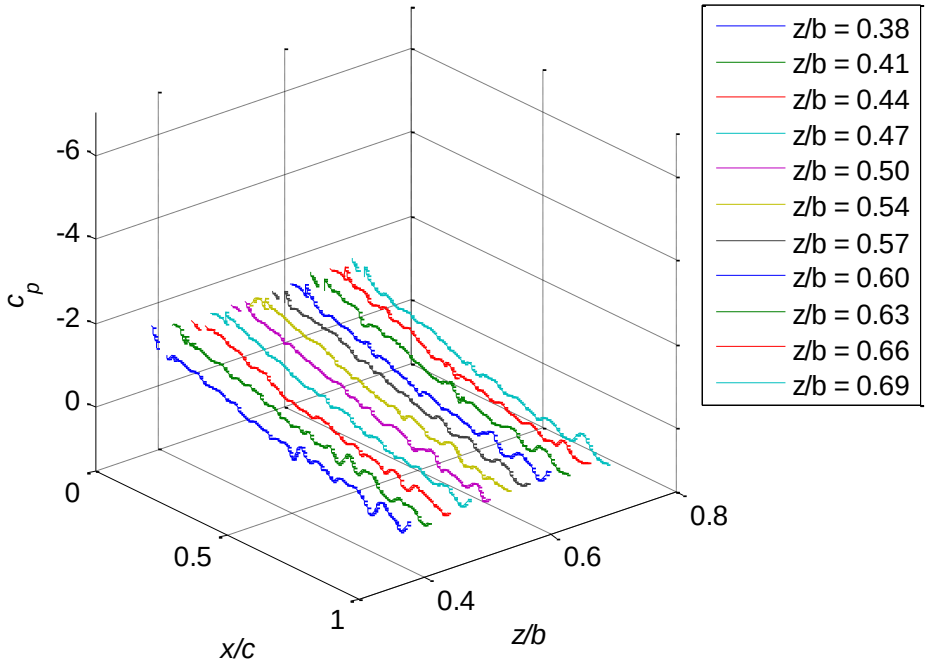

b)

Figure 3.39: Horn ice shapes, PSP chordwise *cp* curves at various *z/b* locations, α = 7°, a) casting and b) RPM shape.

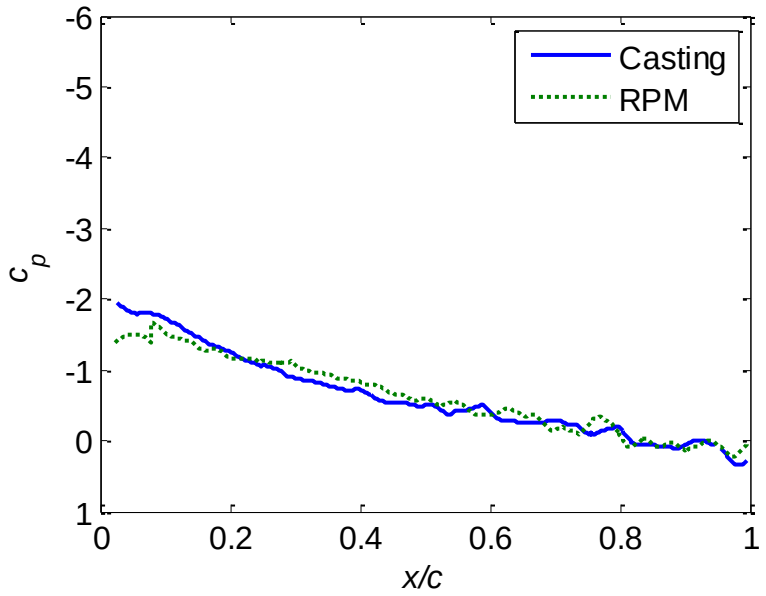

Figure 3.40: Horn ice shapes, PSP chordwise c_p comparison at main tap row, z/b = 0.515, α = 7°, a) casting and b) RPM shape.

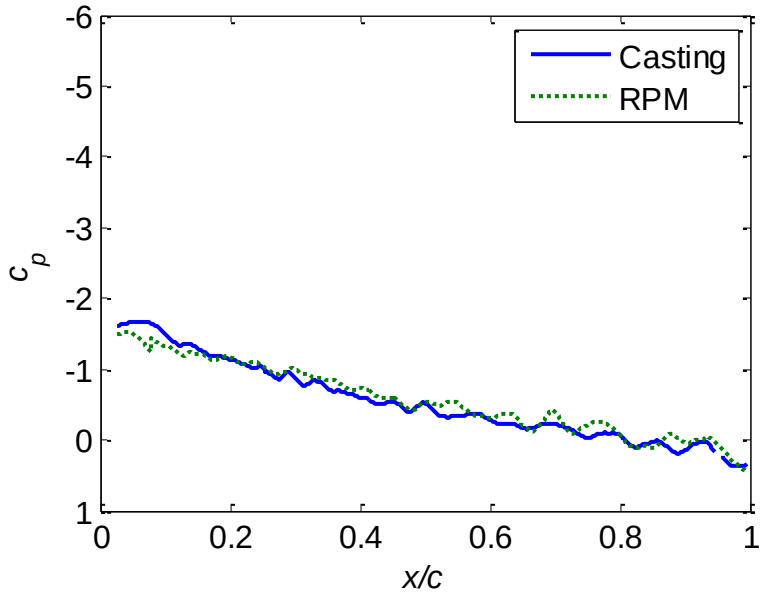

Figure 3.41: Horn ice shapes, PSP chordwise c_p comparison at secondary tap row, z/b = 0.417, α = 7°, a) casting and b) RPM shape.

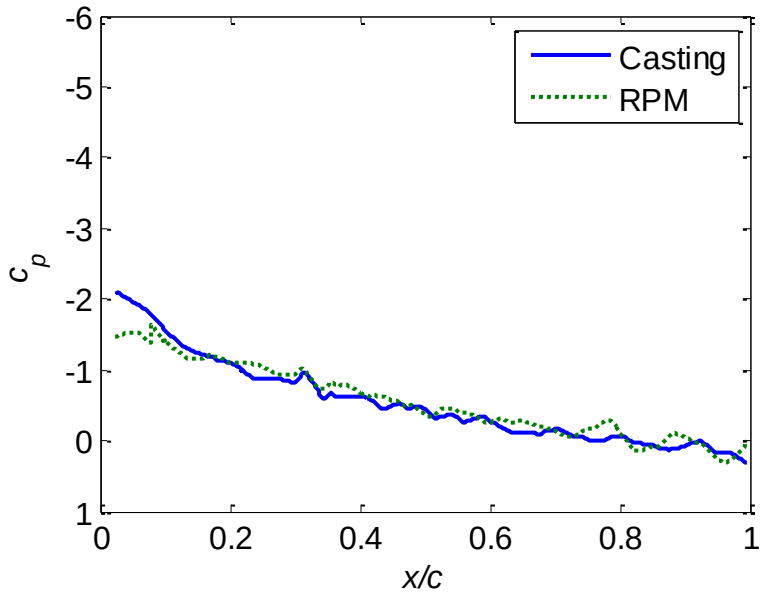

Figure 3.42: Horn ice shapes, PSP chordwise c_p comparison at z/b = 0.6, α = 7°, a) casting and b) RPM shape.

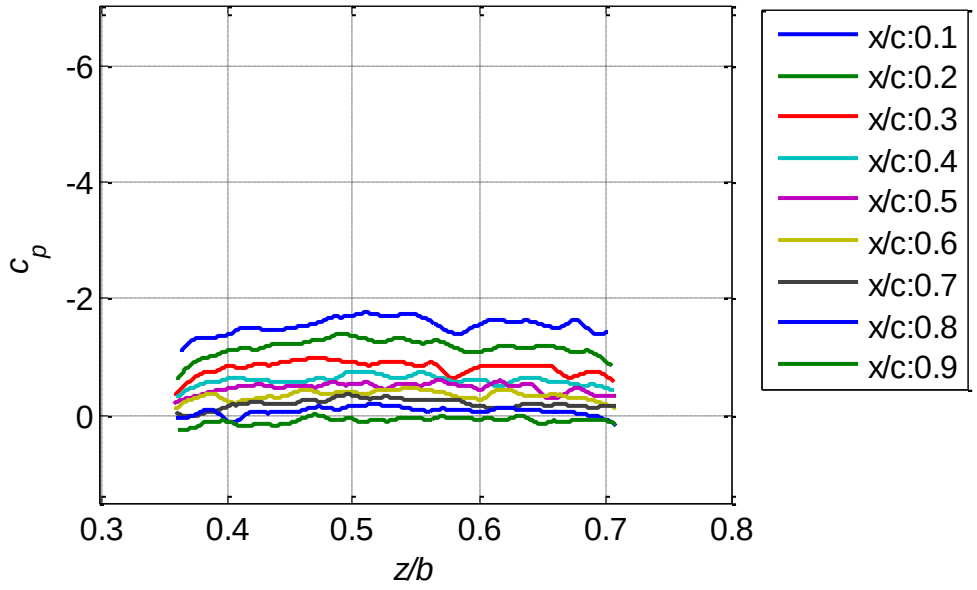

Figure 3.43: Horn casting, PSP spanwise c_p curves at various x/c locations, α = 7°.

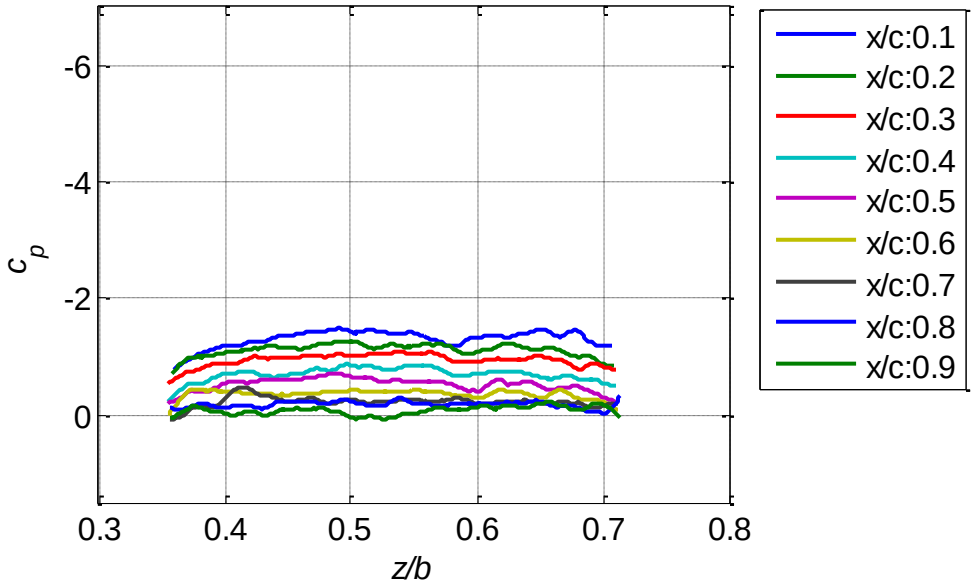

Figure 3.44: Horn RPM shape, PSP spanwise c_p curves at various x/c locations, $\alpha = 7°$.

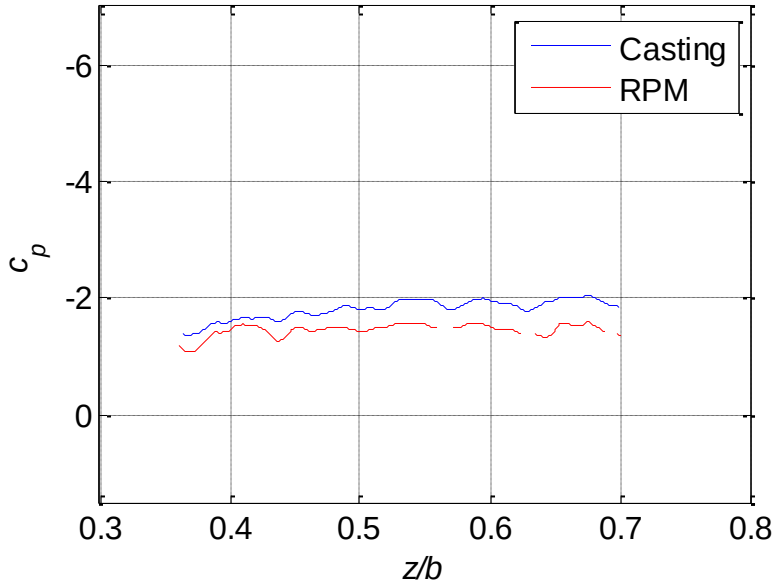

Figure 3.45: Horn ice shapes, PSP spanwise c_p comparison, $\alpha = 7°$, $x/c = 0.05$.

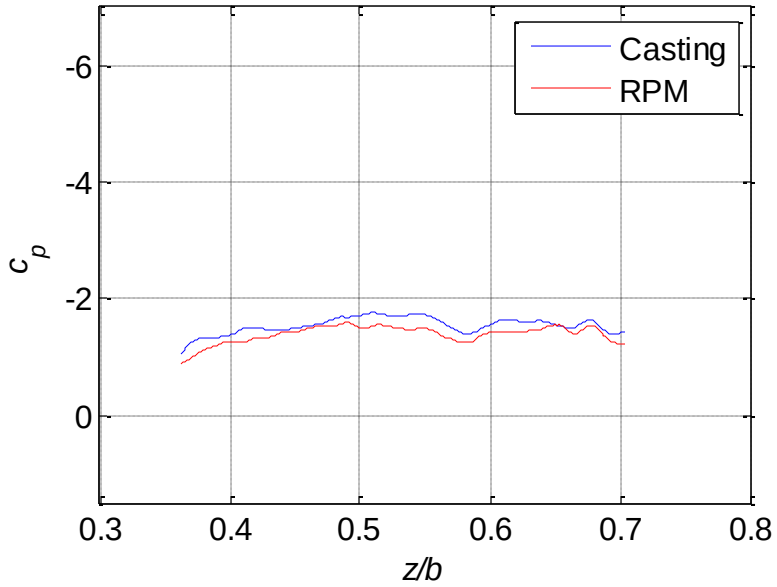

Figure 3.46: Horn ice shapes, PSP spanwise c_p comparison, α = 7°, *x/c* = 0.1.

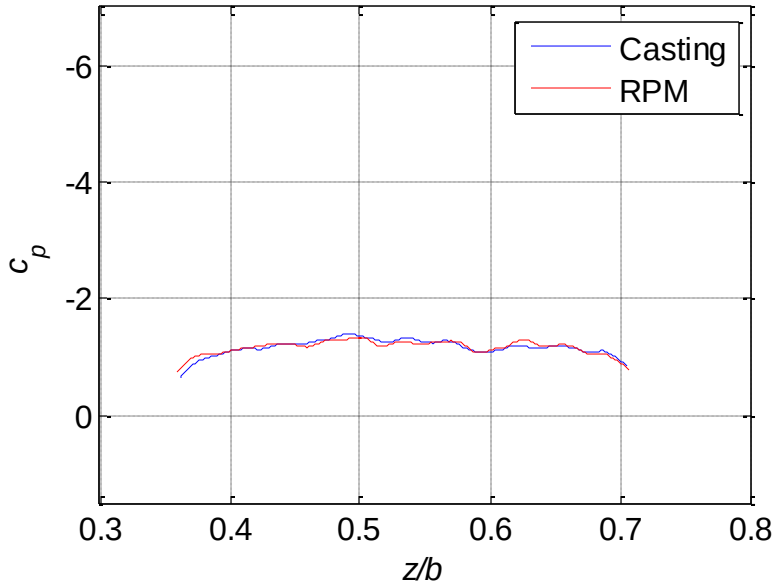

Figure 3.47: Horn ice shapes, PSP spanwise c_p comparison, α = 7°, *x/c* = 0.2.

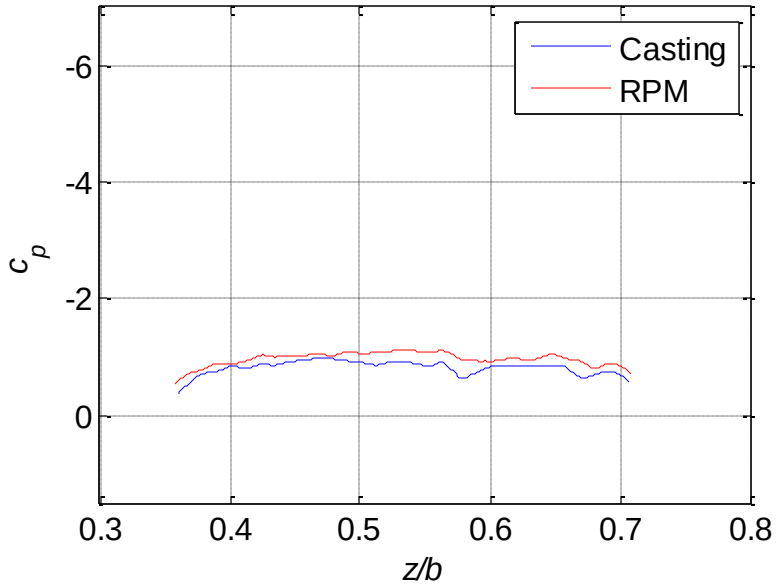

Figure 3.48: Horn ice shapes, PSP spanwise c_p comparison, α = 7°, *x/c* = 0.3.

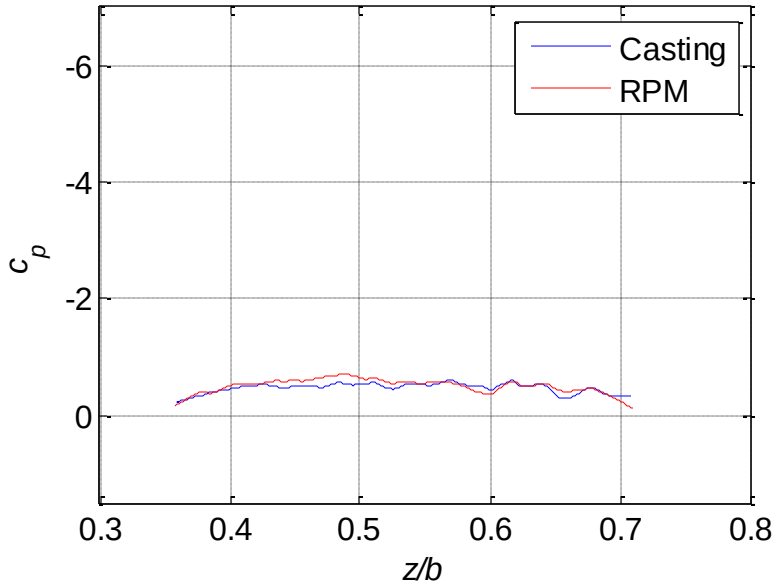

Figure 3.49: Horn ice shapes, PSP spanwise c_p comparison, α = 7°, *x/c* = 0.5.

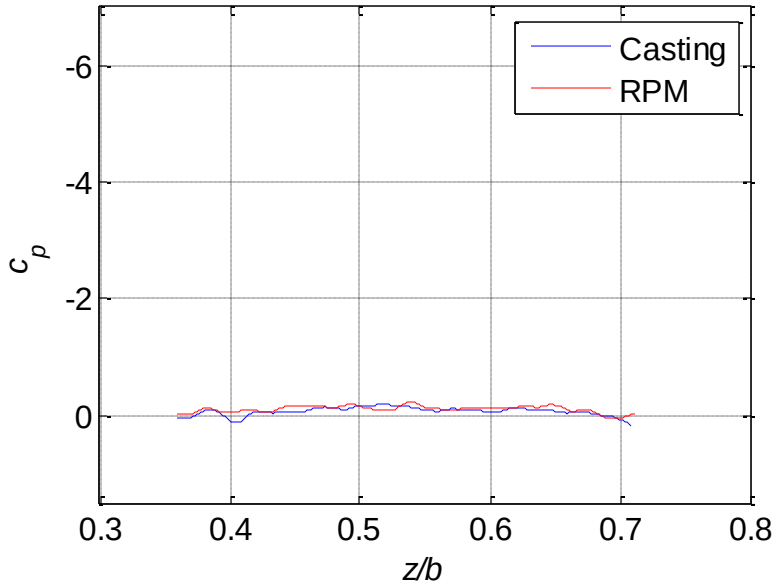

Figure 3.50: Horn ice shapes, PSP spanwise c_p comparison, α = 7°, *x/c* = 0.8.

PSP data at α = 6° were also obtained during this work, and similar results were found at this lower angle. The c_p contours are presented in Figure 3.51, where the same trends seen at the higher angle of attack were present. The chordwise c_p distribution comparisons for both shapes at the different angles of attack are shown in Figure 3.52 and Figure 3.53. These show the pressure rise with increasing angle of attack as the separation bubble grew. Along the span the same trends were seen as were observed in these chordwise pressure distributions. Figures 3.54, 3.55, and 3.56 are the spanwise c_p comparisons with angle of attack for the horn casting. At *x/c* = 0.5 in Figure 3.54 the distribution at α = 6° had lower pressure across the span than the distribution at α = 7°. At about *x/c* = 0.1, as seen in Figure 3.55, the pressure values for both angles were about equal. This agreed with the point of intersection between the two angle of attack distributions for the casting shape at the two angles of attack. Downstream of this point, the α = 7° distribution shows lower pressure, as exemplified by Figure 3.56. A similar trend is seen in Figures 3.57, 3.58, and 3.59 for the RPM shape. However, the crossing point between the distributions at the different angles of attack occurred further downstream at about *x/c* = 0.2, as shown in Figure 3.58.

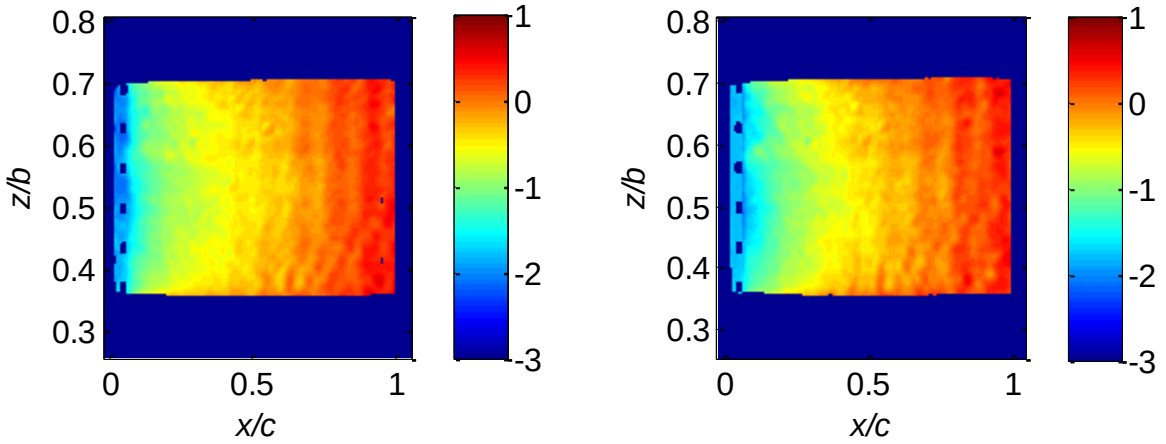

Figure 3.51: Horn ice shapes, PSP c_p contour comparison, α = 6°, a) casting and b) RPM shape.

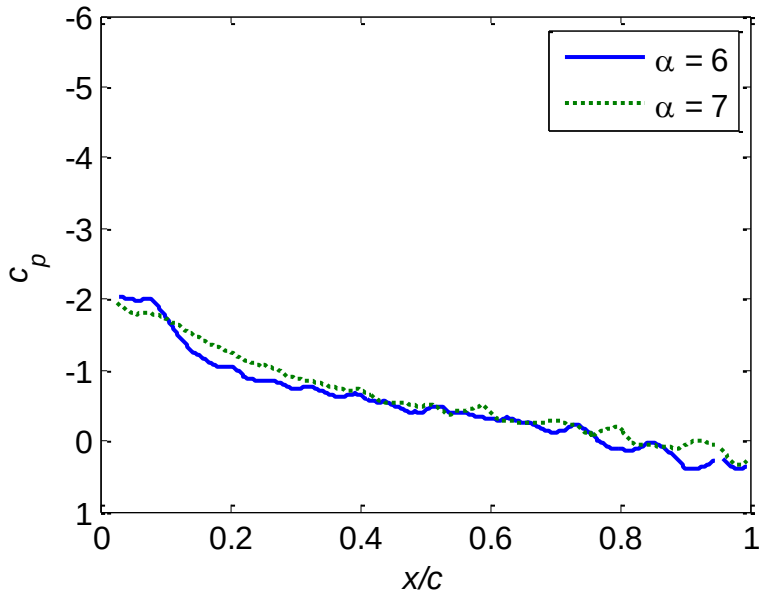

Figure 3.52: Horn casting, PSP chordwise c_p comparison for α = 6° and α = 7° at main tap row, z/b = 0.515.

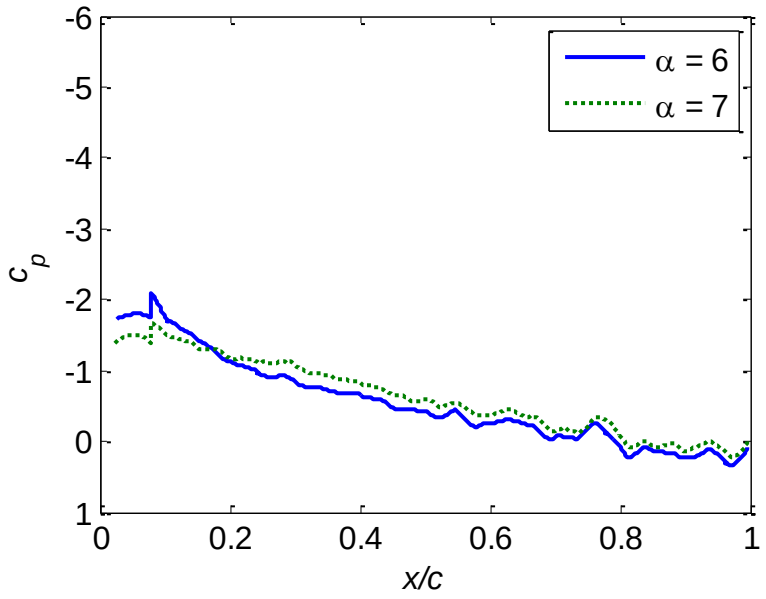

Figure 3.53: Horn RPM, PSP chordwise c_p comparison for α = 6° and α = 7° at main tap row, z/b = 0.515.

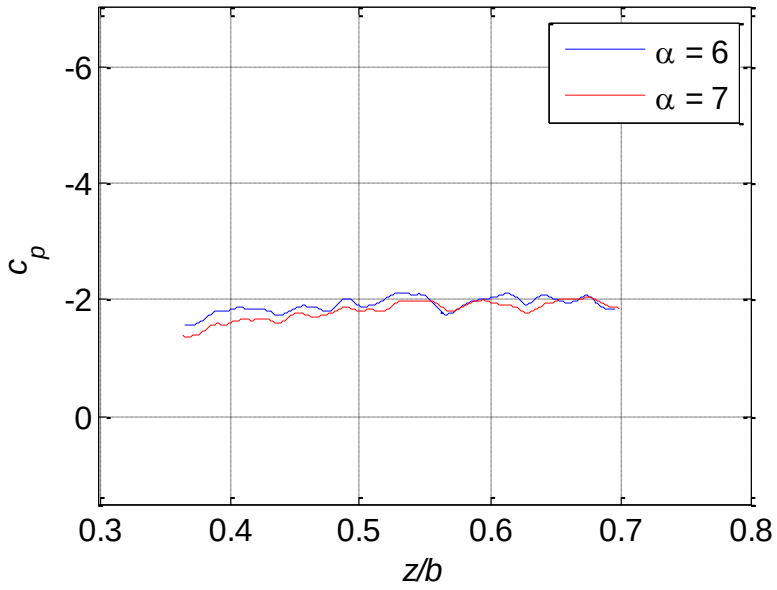

Figure 3.54: Horn casting, PSP spanwise c_p comparison for α = 6° and α = 7° at x/c = 0.05.

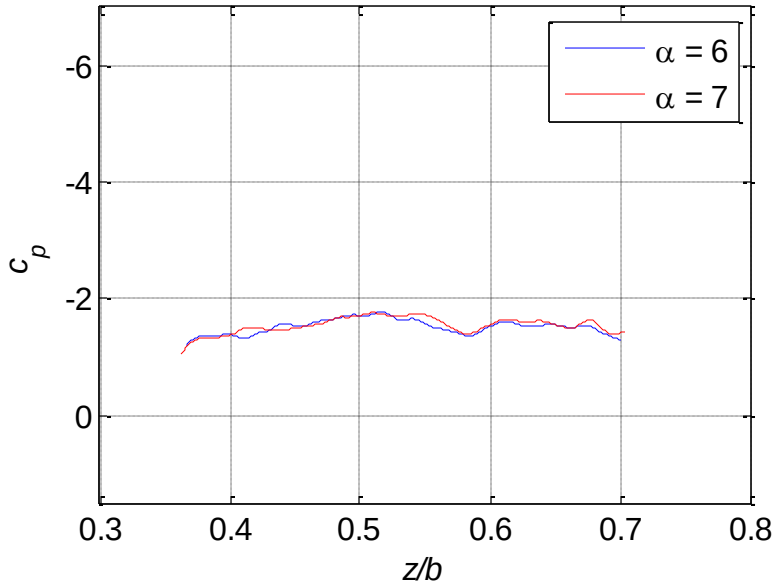

Figure 3.55: Horn casting, PSP spanwise c_p comparison for α = 6° and α = 7° at x/c = 0.1.

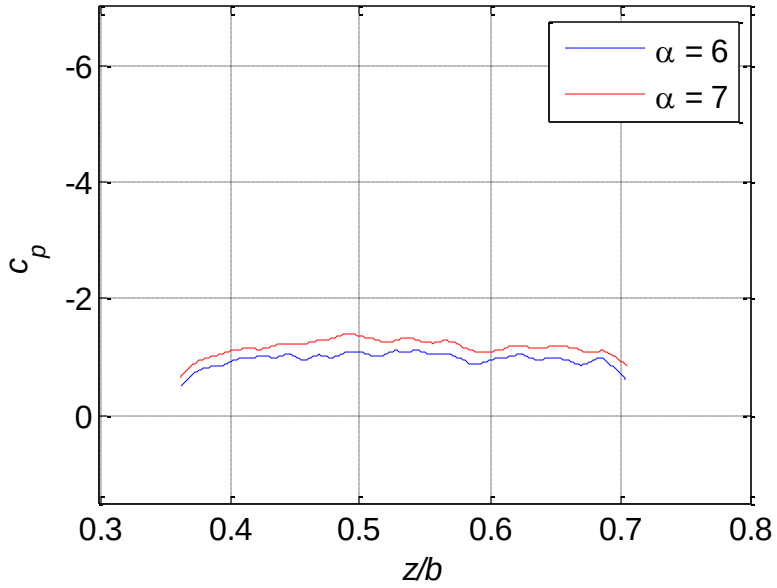

Figure 3.56: Horn casting, PSP spanwise c_p comparison for α = 6° and α = 7° at x/c = 0.2.

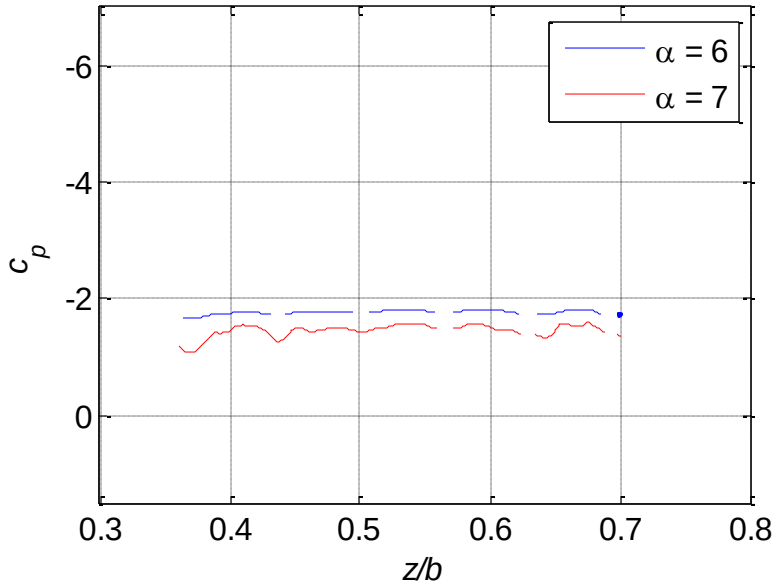

Figure 3.57: Horn RPM shape, PSP spanwise c_p comparison for α = 6° and α = 7° at x/c = 0.05.

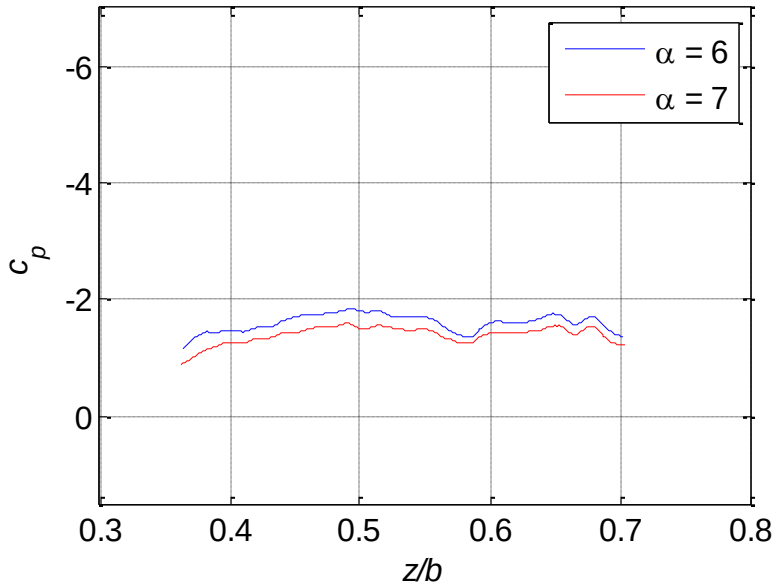

Figure 3.58: Horn RPM shape, PSP spanwise c_p comparison for α = 6° and α = 7° at x/c = 0.2.

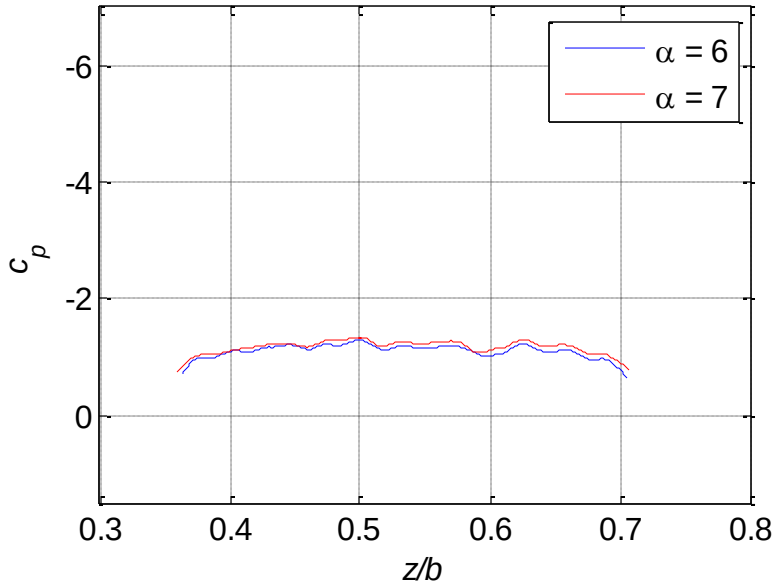

Figure 3.59: Horn RPM shape, PSP spanwise c_p comparison for α = 6° and α = 7° at *x/c* = 0.3.

3.3 Roughness Ice Shape Comparison

3.3.1 Aerodynamic Comparison

The aerodynamic performance of the roughness ice shapes is shown in Figure 3.60 through Figure 3.64. They were plotted with the clean data for comparison. Overall, the three roughness ice shapes: casting, SLA, and Polyjet, exhibited behavior expected with the presence of roughness features. The roughness present at the leading edge caused an earlier transition to turbulent flow. Further downstream, separation occurred earlier due the boundary layer losing the momentum needed to overcome the adverse pressure gradient. All three reduced the $c_{\ell,max}$, α_{stall}, and lift curve slope ($c_{\ell\alpha}$) from the clean case. The casting shape stalled first at an angle of attack of 11.3°. Both of the rapid-prototype shapes stalled at a similar angle of attack of 12.33° for the SLA shape and 12.34° for the Polyjet shape. It was reasonable to state that the SLA and Polyjet shapes stalled at the same angle of attack due to the resolution of the test matrix. The three shapes had varying $c_{\ell,max}$ values in addition to their differing α_{stall} values. The Polyjet shape had the highest $c_{\ell,max}$ at 1.24. The SLA had a middle value of $c_{\ell,max}$ = 1.19, and the casting shape had the lowest maximum lift coefficient with $c_{\ell,max}$ = 1.12. The Polyjet shape had the highest lift slope of the roughness

cases with $c_{\ell,\alpha}$ = 0.1002 per degree and the casting had the lowest with $c_{\ell,\alpha}$ = 0.0979 per degree. The SLA shape had a lift slope of $c_{\ell,\alpha}$ = 0.0998 per degree. The lift slope was determined over the linear region of the c_l-α curve from α = -7° to α = 8°. As trailing-edge separation possibly increased in chordwise extent with increasing angle of attack, there was a de-cambering effect that reduced the lift slope close to stall. The differences in lift slope that exist at low angle of attacks far from stall were exaggerated as the angle of attack increased.

Figures 3.61 and 3.62 show the drag coefficient (c_d) effects from the roughness ice shapes. All three increased the c_d significantly, though much less so than the horn shape discussed earlier. The casting had the highest drag with a minimum drag coefficient ($c_{d,min}$) of 0.0138. The SLA had the lowest minimum drag coefficient ($c_{d,min}$) of 0.0120, while the Polyjet shape had a minimum drag coefficient of ($c_{d,min}$) of 0.01226. The SLA and Polyjet curves intersected a number of times so that the shape that yielded the lowest c_d varied with angle of attack. It was clear from the drag plots that the two rapid-prototype shapes stalled at the same angle of attack since both had a drastic increase in drag at the same angle of α = 12.33° for the SLA and α = 12.34° for the Polyjet. The casting shape stalled about a degree earlier at α = 11.30°. Overall, the presence of roughness reduced the drag performance from that of clean model. These characteristics further supported how the casting results have the greatest aerodynamic penalty and the Polyjet ice shape the least.

The overall shapes of the pressure coefficient (c_p) curves for the roughness cases did not change as drastically as for the horn case previously discussed, as can be seen in Figure 3.63. Strong suction peaks were still evident at the leading edge, though at lesser values than for the clean case. As would be expected from the casting shape effect on $c_{l,max}$ and the c_l-α curve, the c_p distribution for the casting ice shape had the lowest pressure peak over the angle of attack range. The Polyjet shape had the highest peak and most closely followed the distribution of the clean model. All three pressure distributions flattened slightly behind the suction peak for a short extent over the chord. This could be due to a small separation bubble present in the flowfields of the roughness ice shapes. These separation bubbles could not be seen in oil flow visualization pictures since they exist upstream of the seam between the ice shape and the airfoil body.

The wakes for the three roughness shapes were plotted in Figure 3.64 along with the clean model wake. It was clear that the increase in wake size was small when compared to the horn shapes' effect in Figure 3.33 but was still significant. The casting roughness shape had the largest wake, followed by the SLA case, and then the Polyjet case with the smallest wake. These results were in line with the observation that the casting and Polyjet had the greatest and least effect on the flowfield and aerodynamics, respectively. The differences between the cases were probably due to differences in the roughness resolution. The casting had the sharpest and largest roughness features, while the Polyjet shape had the smoothest features. Without the original ice accretion for reference, it was unknown which of the three shapes replicated the ice roughness best. Due to the limited resolution of the rapid-prototype methods, it was most likely that the true roughness features are coarser than the RPM shapes and smoother than the casting. These differences in the roughness features caused variations in the boundary layers for the three shapes, affecting the aerodynamics. While the effects were distinct for each case, the general behaviors were similar.

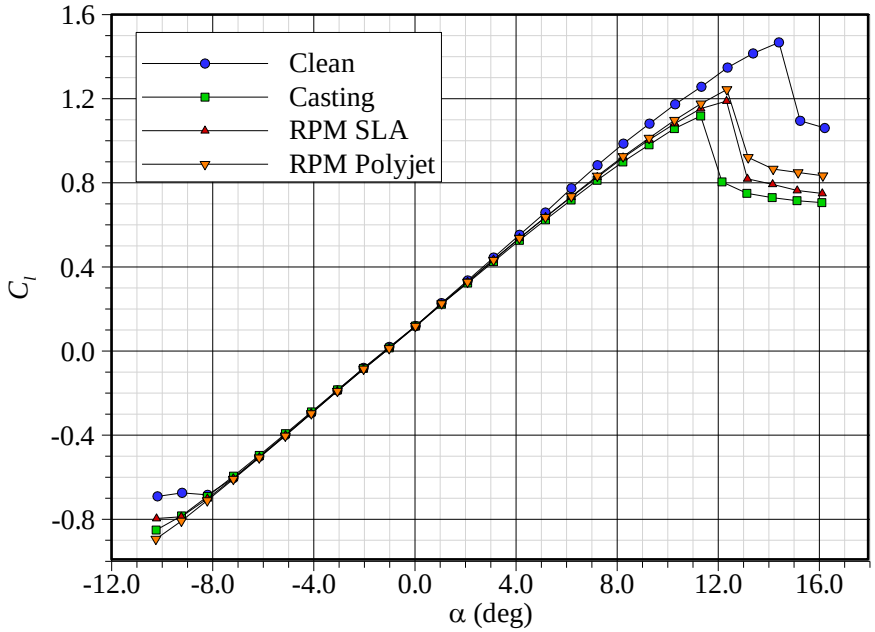

Figure 3.60: Roughness ice shapes, c_ℓ-α curve comparison, Re 1.8 million.

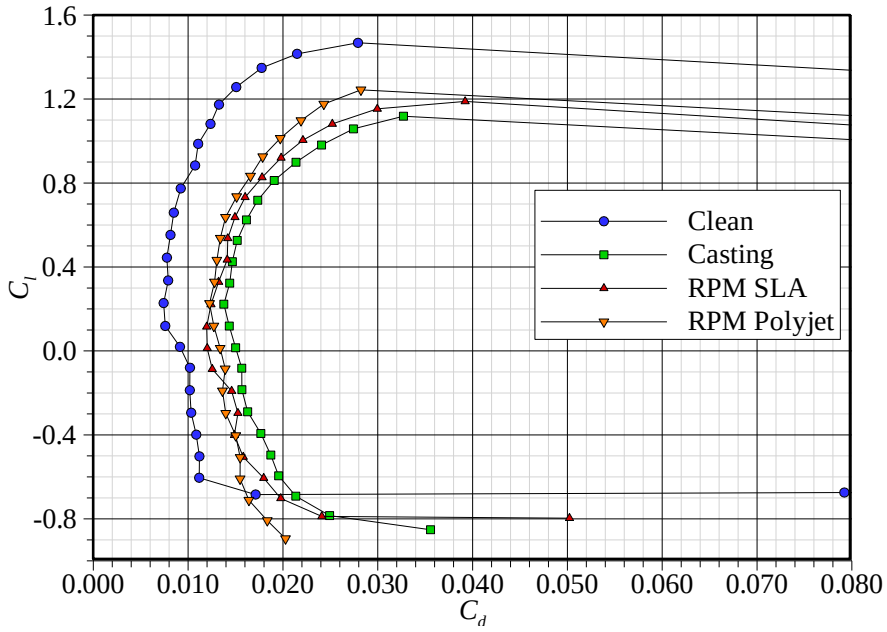

Figure 3.61: Roughness ice shapes, drag polar comparison, Re 1.8 million.

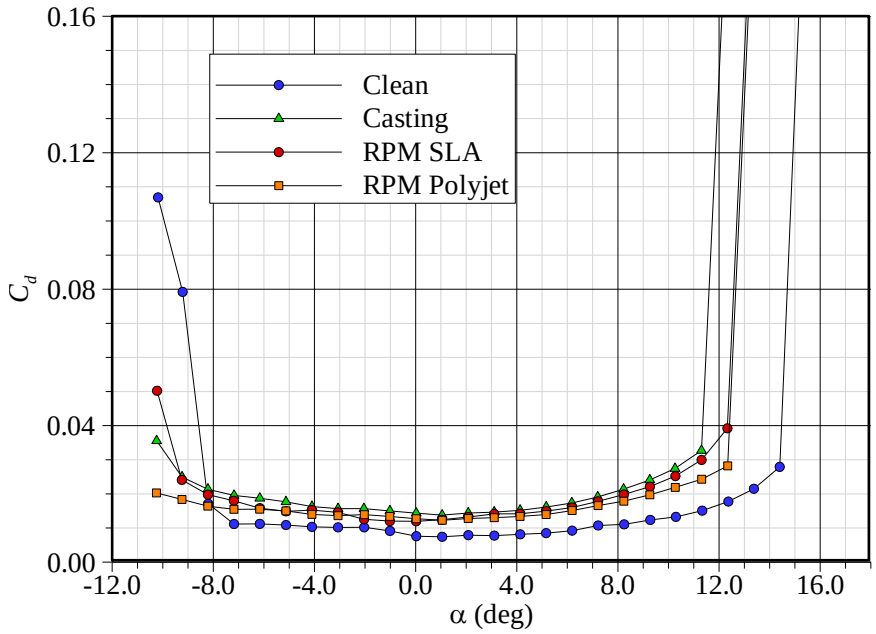

Figure 3.62: Roughness ice shapes, c_d-α curve comparison, Re 1.8 million.

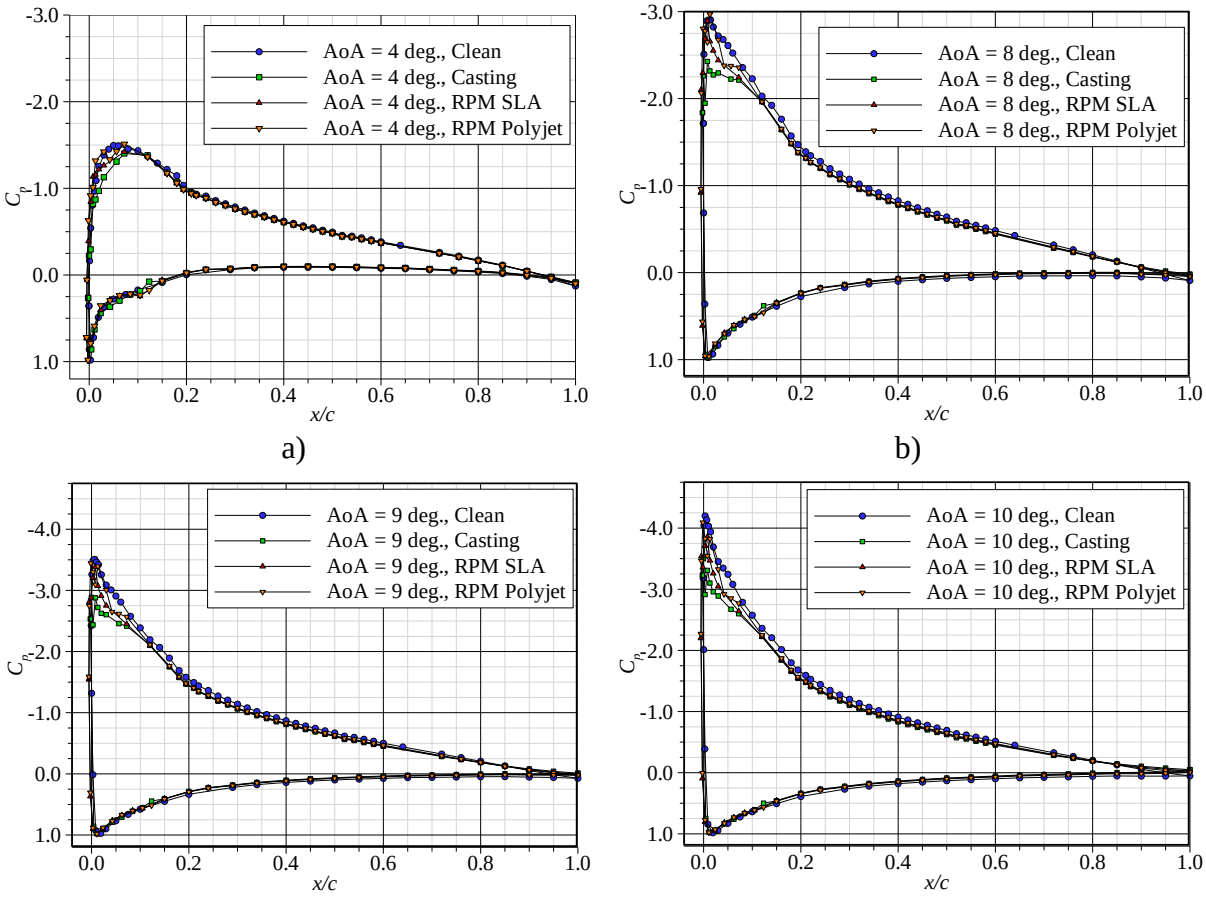

Figure 3.63: Roughness ice shapes, c_p curve comparisons at a) α = 4°, b) α = 8°, c) α = 9°, and d) α = 10°.

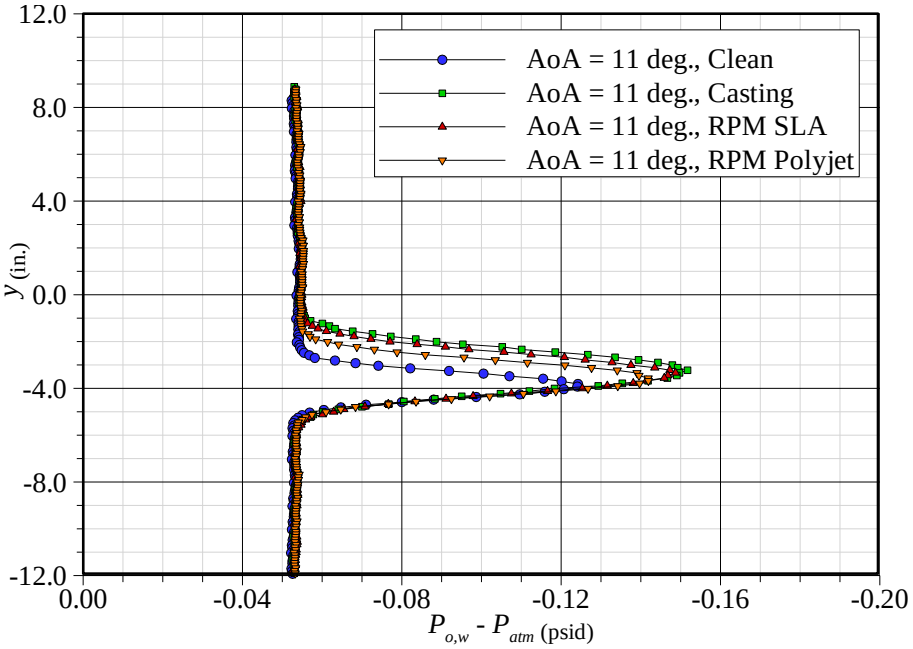

Figure 3.64: Roughness ice shapes, wake comparison, α = 11°.

3.3.2 PSP Comparison

For the roughness cases, PSP was only applied to the airfoil main body. The small roughness features on the ice shapes covered the whole leading-edge piece and, if painted, would cause self-illumination errors. The roughness PSP results are presented in Figures 3.65 through 3.72. Overall, the three plots for the three variations of the same ice shape had similar c_p contours (Figure 3.65), indicating the flows over the three shapes were similar on a large scale. This agreed with what was observed from the performance tests, where the overall effects of the roughness shapes were similar, yet distinct. These plots revealed the same gradual increase in pressure at the paint edges that were hypothesized to be caused by the model deformation through the intensity field from aerodynamic loading. The more subtle differences between the three could be discovered by examining the other plots.

The three calibrations in Figure 3.66 had similar slopes and intercepts. The casting, SLA, and Polyjet shapes had calibration slopes of 0.658, 0.655, 0.713 and intercepts of 0.336, 0.338, and 0.283, respectively. This showed that the differences between the three cases were slight. Figures 3.67 through 3.69 show the PSP and pressure tap comparisons. The agreement for all three cases was good over most of the chord, though not excellent. The trailing-edge taps at chordwise locations greater than x/c = 0.7 were not included in the

calibrations due to the increased signal-to-noise ratio near the trailing edge. The variations in the c_p curves are more clearly seen in Figures 3.70, 3.71, and 3.72, which plot the PSP data from all three roughness shapes on the same plot at the main tap row, secondary tap row, and z/b = 0.6 respectively. For most of the painted area, the Polyjet ice shape seemed to have slightly more negative c_p values than the SLA or casting shapes. Directly behind the ice shape, the casting had the more negative values at the two tap rows and the Polyjet shape had the least negative values. There was an intersection point at about x/c = 0.15 for all three spanwise locations. This agreed with the pressure tap data, where the pressure curves from the three shapes came together just past x/c = 0.1. Over the remainder of these curves past the intersection point, it was difficult to determine any trends in the PSP data.

The chordwise c_p distributions along the span in Figure 3.73 show the ability of the PSP method to provide an increased amount of data over the pressure tap method. More information on the spanwise characteristics of each roughness shape could be obtained from Figures 3.74, 3.75, and 3.76, where the spanwise distributions at a number of chord locations were plotted together. Possible features along the span of each shape could be seen in these figures. The plots for the casting roughness shape in Figure 3.74 show two dips in c_p at about z/b = 0.58 and z/b = 0.67 that were present at most x/c locations. There was also a peak in the spanwise distribution at about z/b = 0.5 for most x/c locations. Figure 3.75 was the same plot for the RPM SLA ice shape. Here a similar dip in c_p was observed beginning at about z/b = 0.57 and propagating to z/b = 0.65 further downstream. Figure 3.76 shows this same dip for the RPM Polyjet shape from about z/b = 0.57 to z/b = 0.6. It was possible that there was also a dip at about z/b = 0.67. The data for all three sets possessed at least one feature in common: the dip at about z/b = 0.6. This could possibly have been from a common geometric trait that was accurately replicated in all three shapes. Specific comparisons between all three shapes at the same x/c locations were made in Figures 3.77 through 3.82. The comparison at x/c = 0.1 in Figure 3.77 supported the observation of two similar dips in the data from all three shapes at about z/b = 0.57 and z/b = 0.67. Over the part of the model closer to the tunnel floor where z/b < 0.57, the casting had the lowest pressure, followed by the SLA shape, and then the Polyjet shape with the highest pressure. At spanwise locations greater than z/b = 0.57 this trend varied. At x/c = 0.2 in Figure 3.78 the Polyjet shape had the lowest pressure over the span. The dip was still present for the Polyjet shape and casting,

though not for the SLA shape. Figure 3.79 shows much spanwise variation between the three shapes at x/c = 0.3 while Figure 3.80 shows similar behaviors for the three shapes at *x/c* = 0.5. Over most of the span at *x/c* = 0.7 in Figure 3.81, the SLA shape had the lowest pressure, followed by the Polyjet shape, and lastly the casting. This trend was not seen at *x/c* = 0.9, where the casting had the highest pressure, and the Polyjet the lowest. It should be noted that due to the larger signal-to-noise ratio present near the trailing edge and the fact that the trailing edge taps were not included in the calibrations, meant that the results downstream of *x/c* = 0.7 may not be as accurate as the upstream results.

The variations in pressure over the model surface for each roughness case were small, and trends were difficult to see in the two-dimensional c_p curves and the c_p contours. For this reason, another technique was employed to compare the three roughness ice shapes. The surface integral of the pressure coefficient c_p over the entire model's painted area was computed for each shape and compared. The surface integral mimicked the pressure integration calculation for lift performed conventionally with pressure taps. If PSP data were collected over the entire model, not just the upper surface behind the ice shape, the lift and pitching moment could be calculated. However, since PSP was only applied to a portion of the model, the pressure coefficient integral was solely a representation of the lift behavior. The integral equaled 0.1830 for the casting, 0.2008 for the Polyjet rapid-prototype shape, and 0.1903 for the SLA rapid-prototype shape. These values were a component of the lift coefficient (c_ℓ) and are tabulated in Table 3.4. The more positive the integral value, the greater the corresponding lift coefficient (c_ℓ). These results showed that the Polyjet shape yielded the most positive integral value, and therefore the highest corresponding lift coefficient. The casting result was smallest, which corresponded to the least lift coefficient value. The SLA shape had values between those of the other two shapes. Similarly, the c_ℓ-α curves in Figure 3.60 demonstrate how the Polyjet roughness shape had the highest $c_{\ell,max}$ and the casting roughness shape the lowest, as discussed previously. The PSP data expressed this same trend in the discrete surface integral values, which showed the PSP method supports the force balance results. With improved PSP techniques, the lift force and pitching moment could be calculated from PSP. This would yield valuable information about the lift distribution along the span, which cannot be measured using the force balance.

Table 3.4: Roughness ice shapes, integrated pressure value comparison.

Roughness Shape	Integrated Pressure Value
Casting	0.1830
RPM SLA	0.1903
RPM Polyjet	0.2008

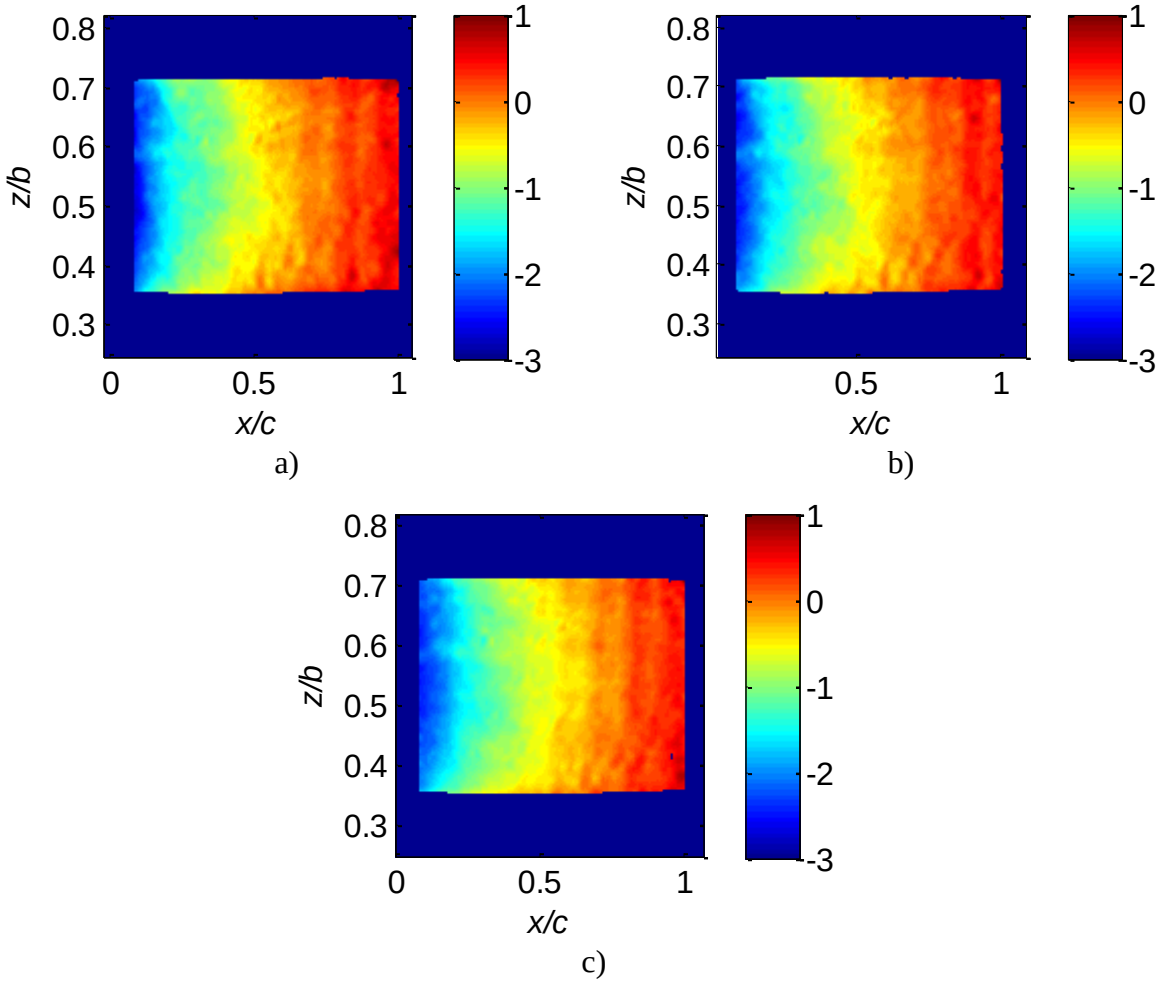

Figure 3.65: Roughness ice shapes, PSP c_p contour comparison, $\alpha = 11°$ for a) casting, b) RPM SLA, and c) RPM Polyjet.

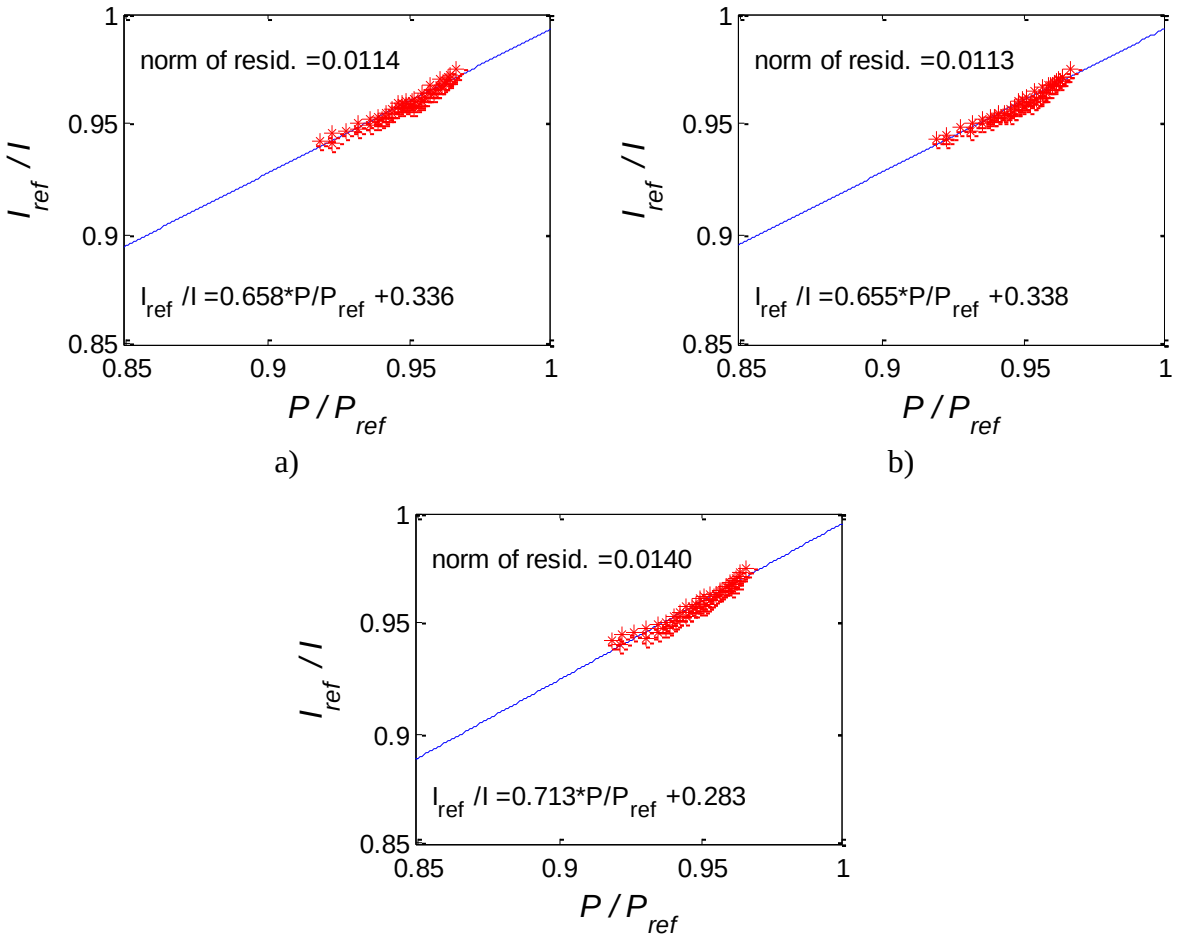

Figure 3.66: Roughness ice shapes, PSP calibrations, α = 11°, a) casting, b) RPM SLA, and c) RPM Polyjet.

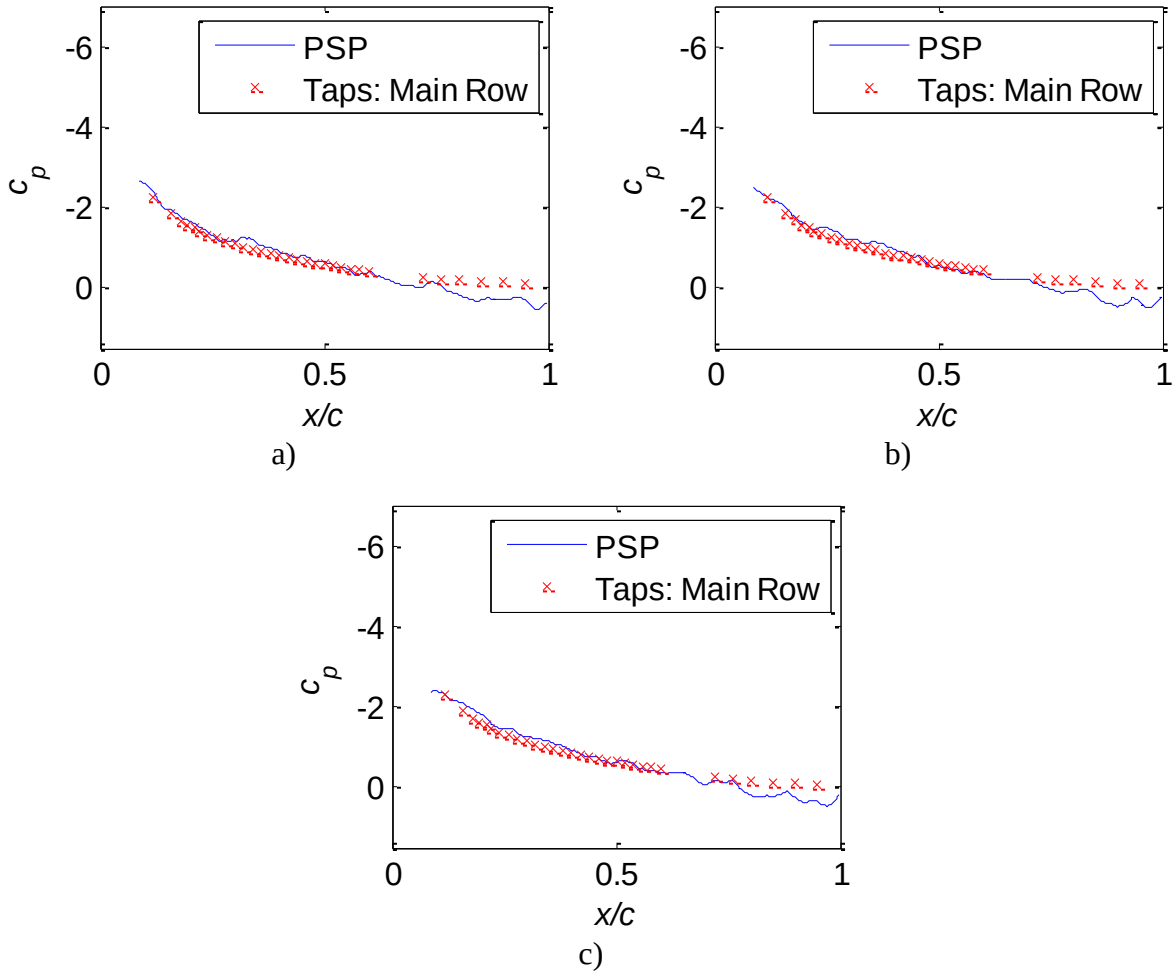

Figure 3.67: Roughness ice shapes, PSP chordwise c_p comparison between PSP and tap data at main tap row, z/b = 0.515, at α = 11°, a) casting, b) RPM SLA, and c) RPM Polyjet. (Trailing-edge taps not included in calibration.)

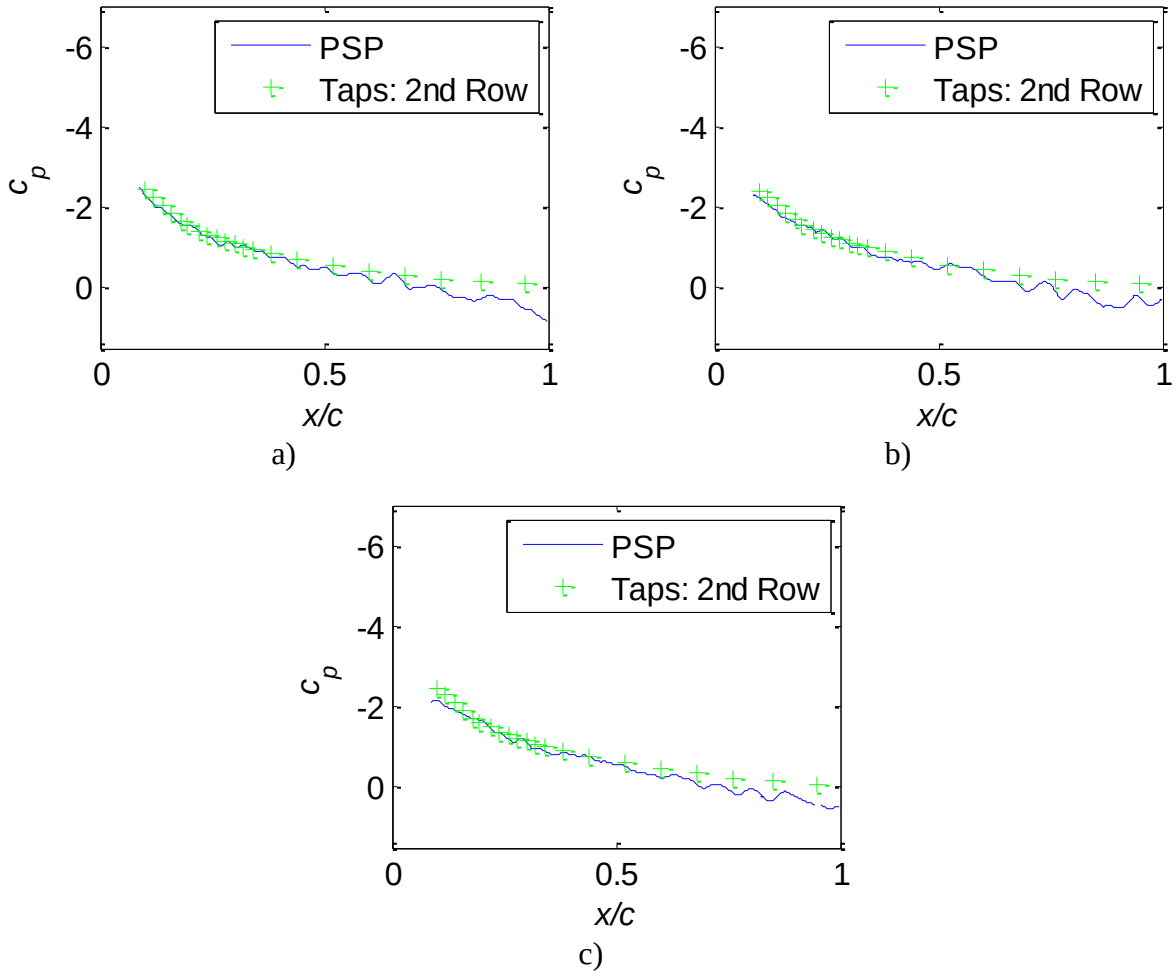

Figure 3.68: Roughness ice shapes, PSP chordwise c_p comparison between PSP and tap data at secondary tap row, z/b = 0.417, for α = 11°, a) casting, b) RPM SLA, and c) RPM Polyjet. (Trailing-edge taps not included in calibration.)

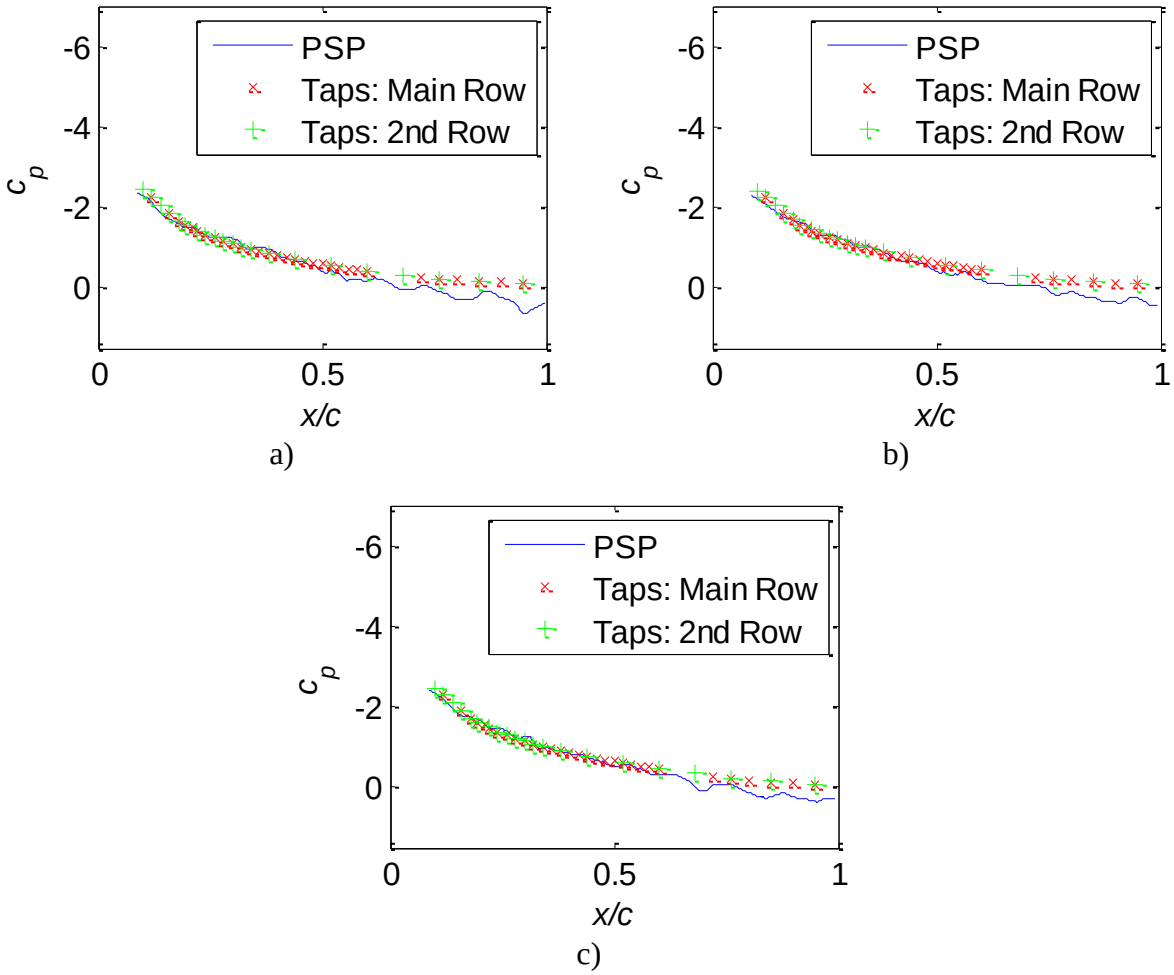

Figure 3.69: Roughness ice shapes, PSP chordwise c_p comparison between PSP and tap data at $z/b = 0.6$, $\alpha = 11°$, a) casting, b) RPM SLA, and c) RPM Polyjet. (Trailing-edge taps not included in calibration.)

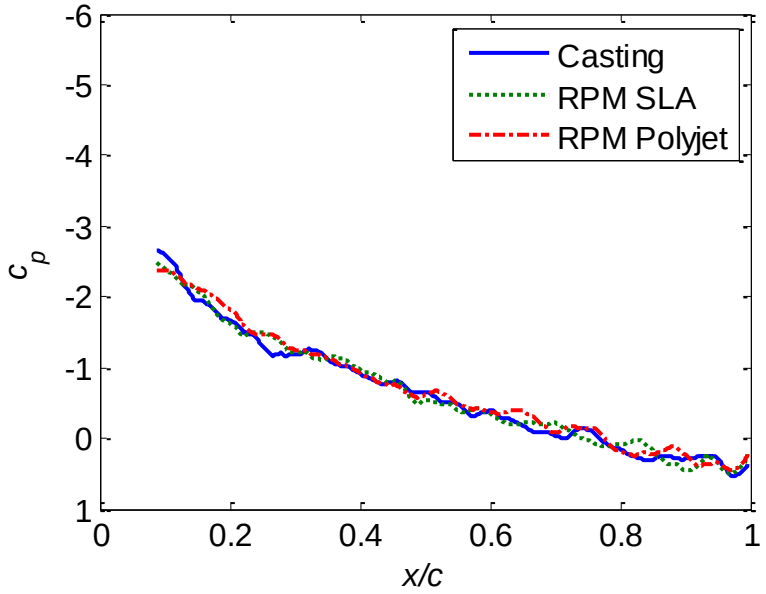

Figure 3.70: Roughness ice shapes, PSP chordwise c_p comparison at main tap row, z/b = 0.515,α = 11°, a) casting, b) RPM SLA, and c) RPM Polyjet.

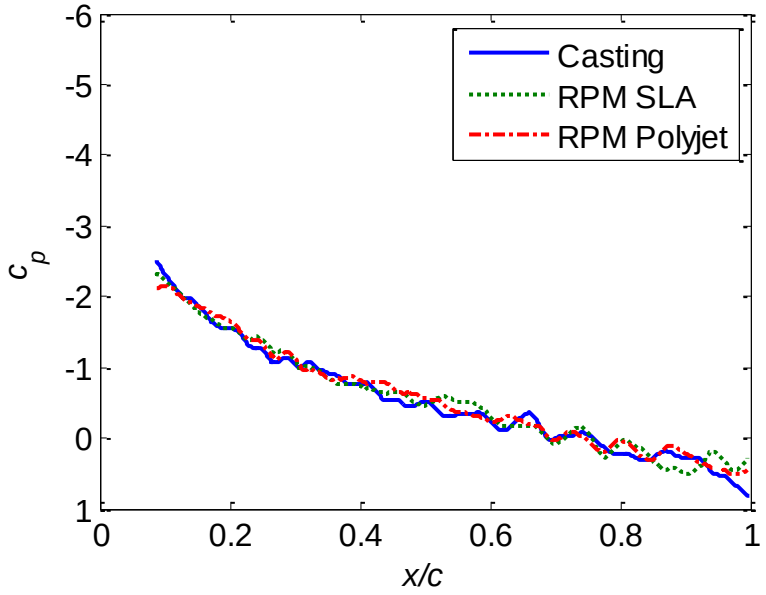

Figure 3.71: Roughness ice shapes, PSP chordwise c_p comparison at secondary tap row, z/b = 0.417, α = 11°, a) casting, b) RPM SLA, and c) RPM Polyjet.

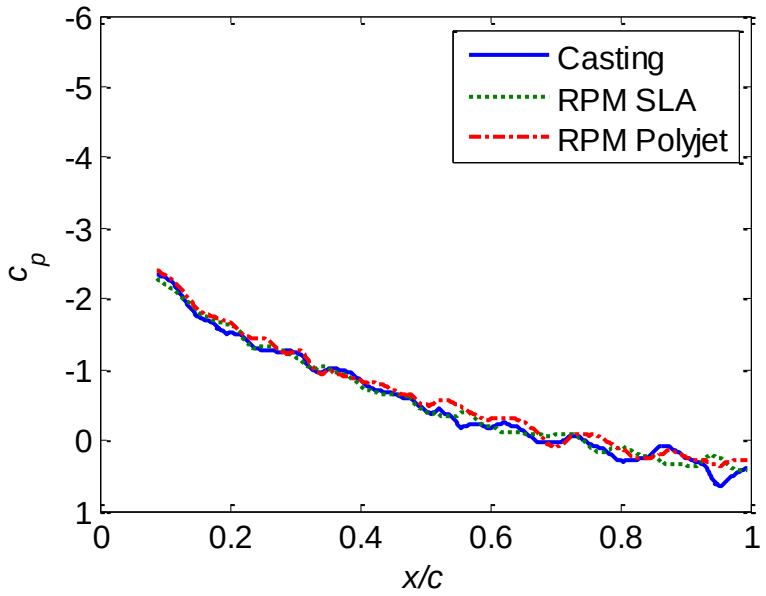

Figure 3.72: Roughness ice shapes, PSP chordwise c_p comparison at z/b = 0.6, α = 11°, a) casting, b) RPM SLA, and c) RPM Polyjet.

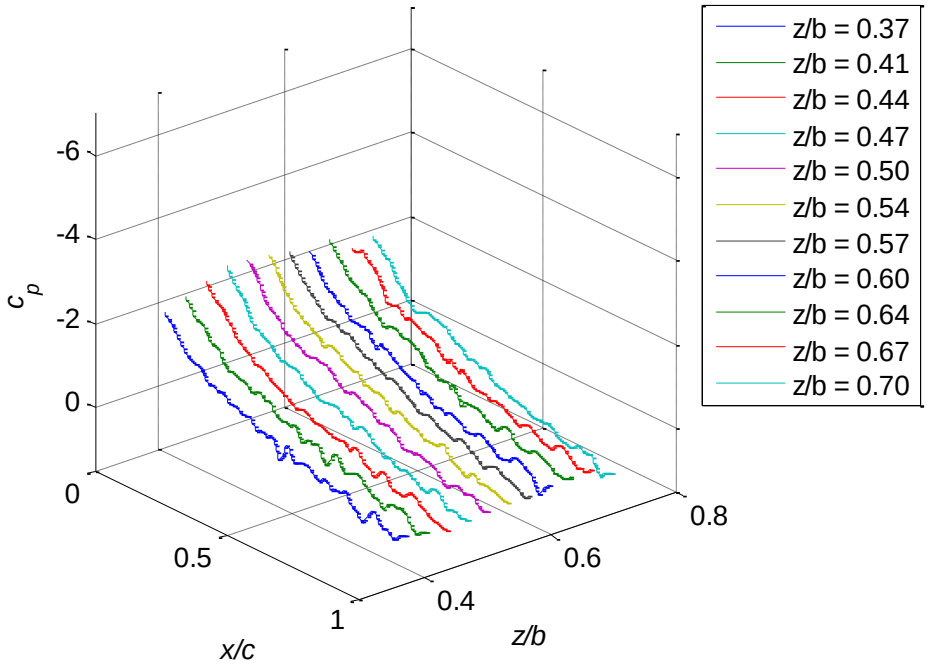

a)

Figure 3.73: Roughness ice shapes, PSP chordwise c_p curves at various z/b locations, α = 11°, a) casting, b) RPM SLA, and c) RPM Polyjet.

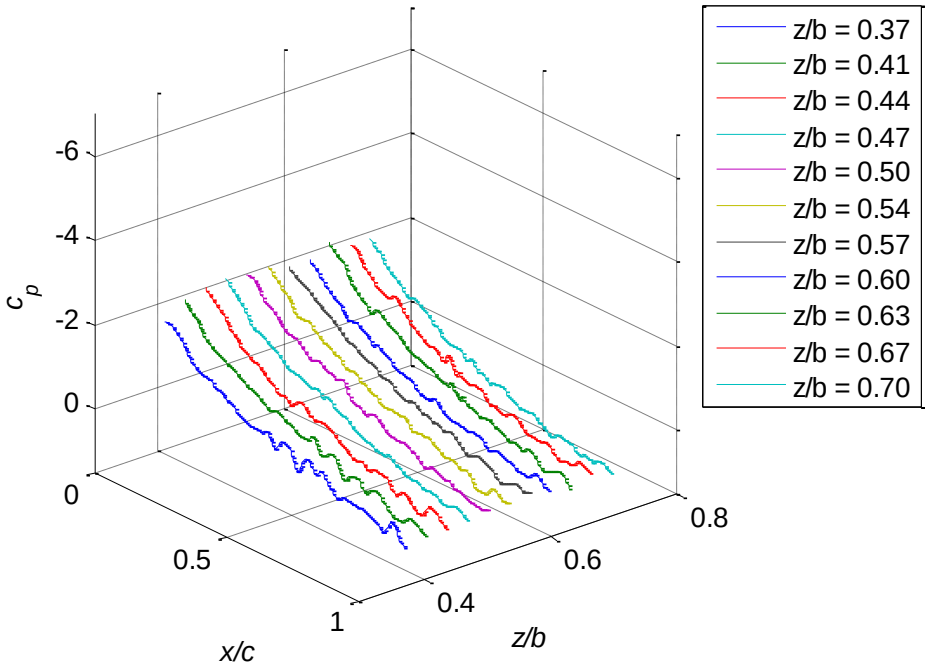

b)

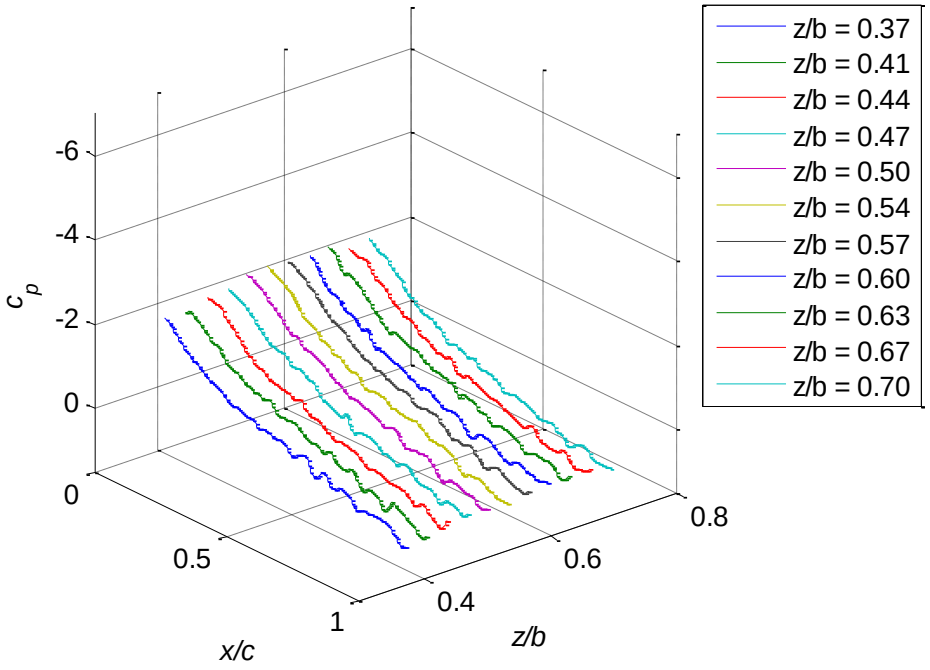

c)

Figure 3.73: Roughness ice shapes, PSP chordwise cp curves at various z/*b* locations, α = *11*°, a) casting, b) RPM SLA, and c) RPM Polyjet.

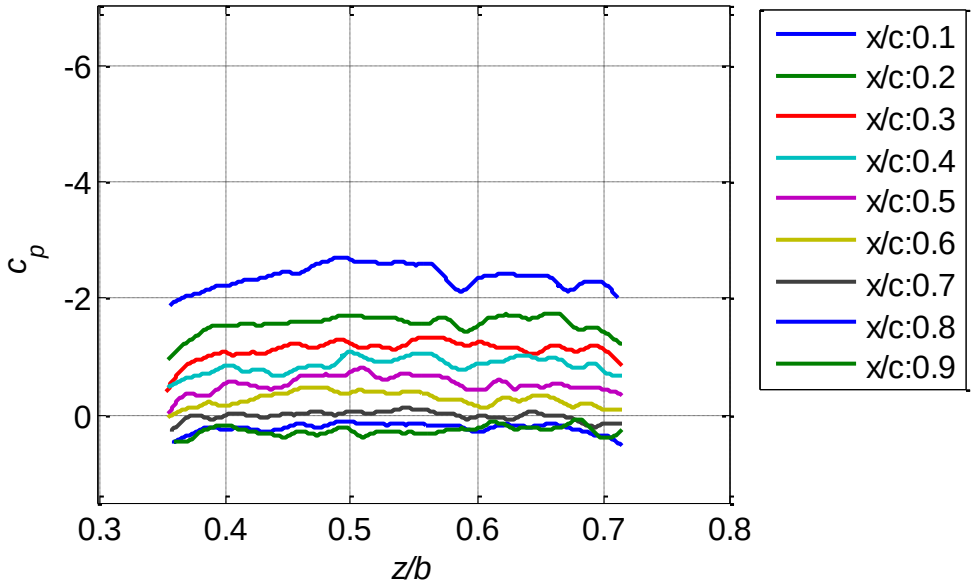

Figure 3.74: Roughness casting, PSP spanwise c_p curves at various *x/c* locations, α = 11°.

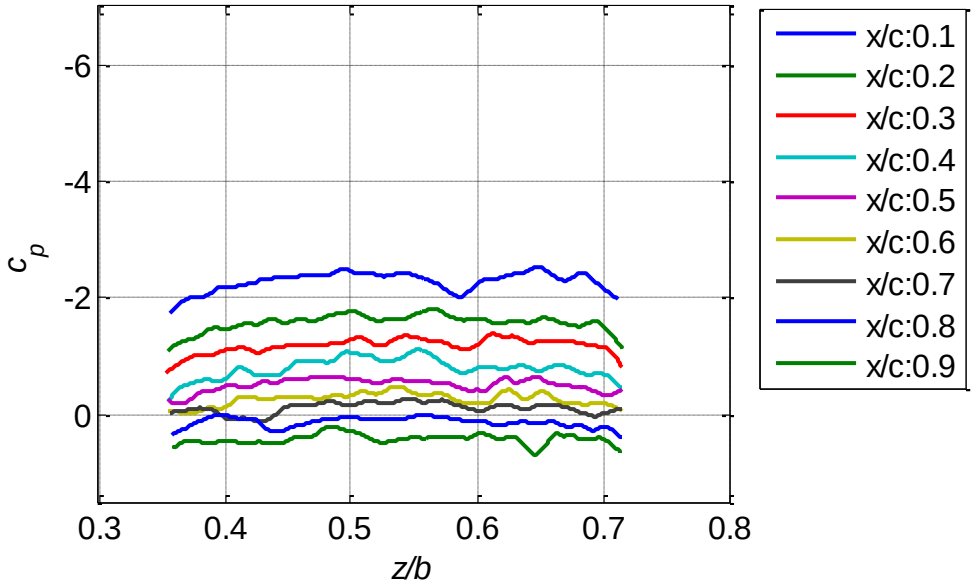

Figure 3.75: Roughness RPM SLA shape, PSP spanwise c_p curves at various *x/c* locations, α = 11°.

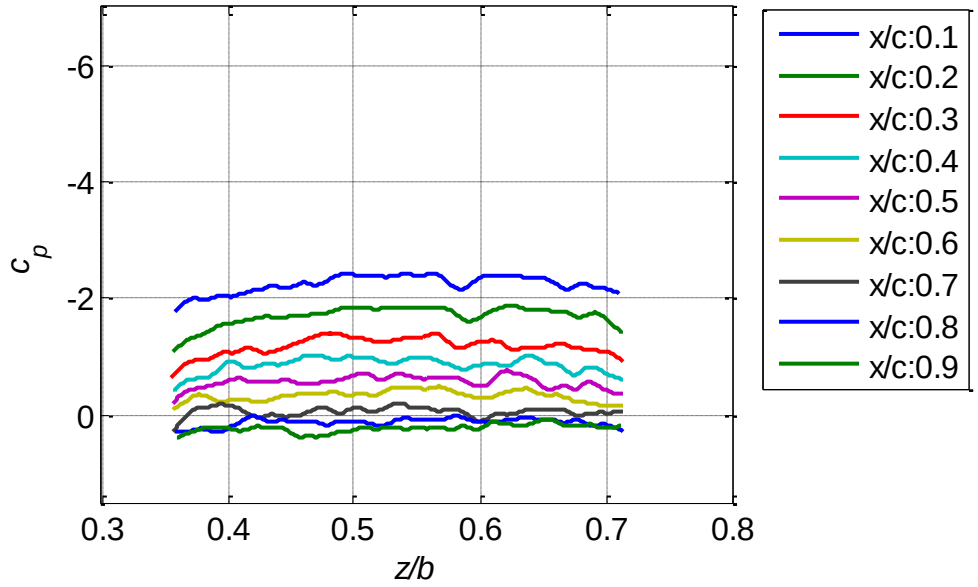

Figure 3.76: Roughness RPM Polyjet shape, PSP spanwise c_p curves at various *x/c* locations, $\alpha = 11°$.

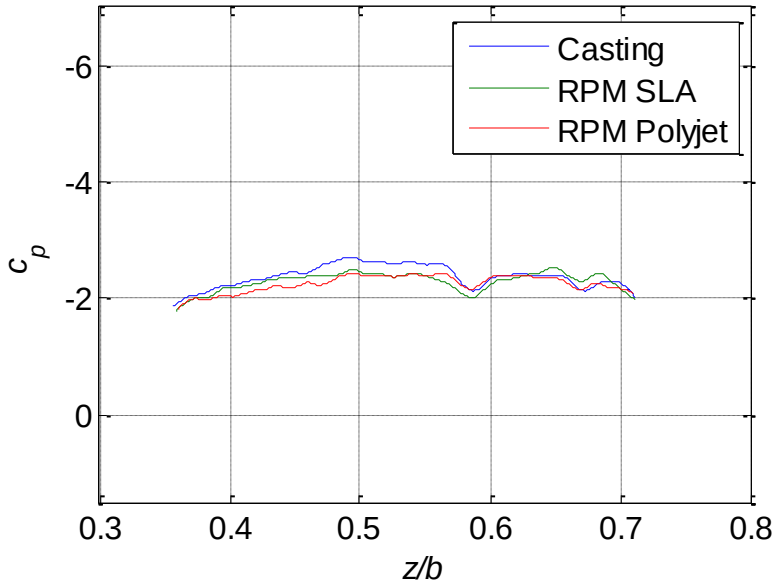

Figure 3.77: Roughness ice shapes, PSP spanwise c_p comparison, $\alpha = 11°$, *x/c* = 0.1.

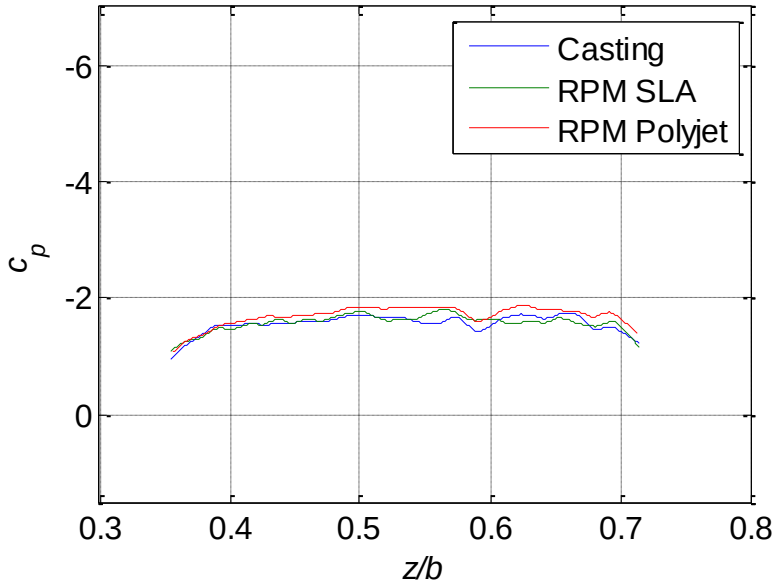

Figure 3.78: Roughness ice shapes, PSP spanwise c_p comparison, α = 11°, *x/c* = 0.2.

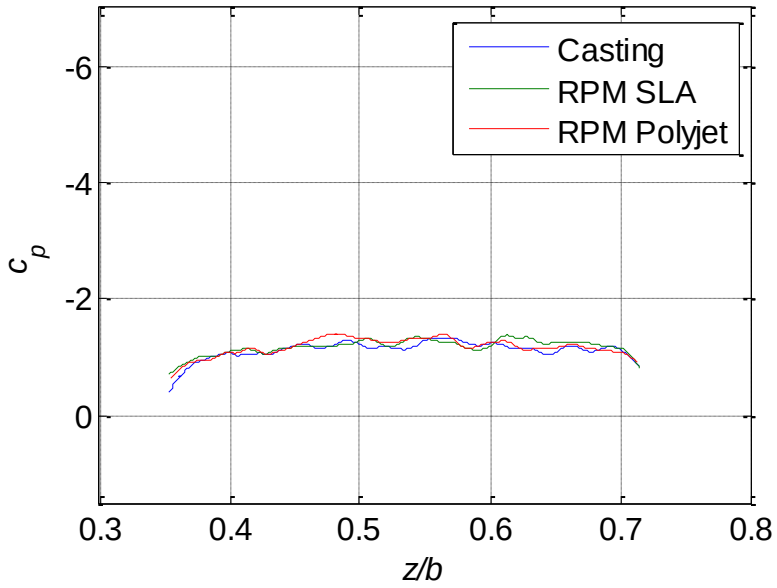

Figure 3.79: Roughness ice shapes, PSP spanwise c_p comparison, α = 11°, *x/c* = 0.3.

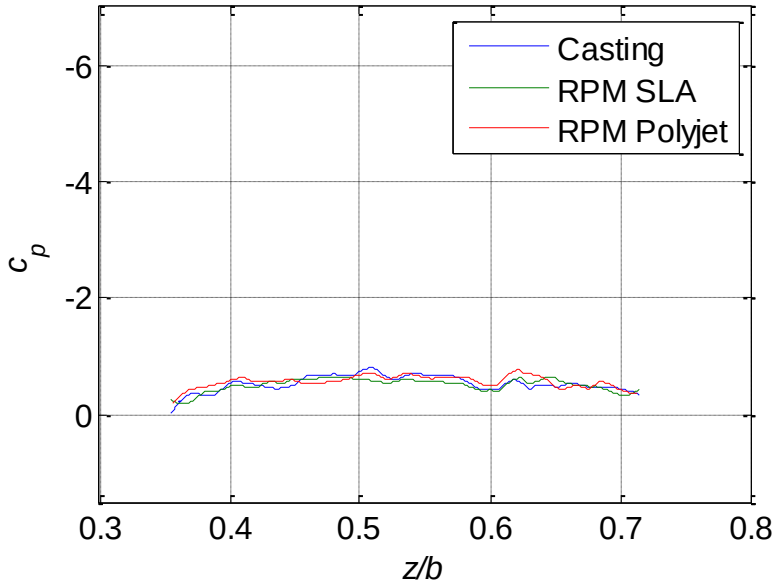

Figure 3.80: Roughness ice shapes, PSP spanwise c_p comparison, α = 11°, x/c = 0.5.

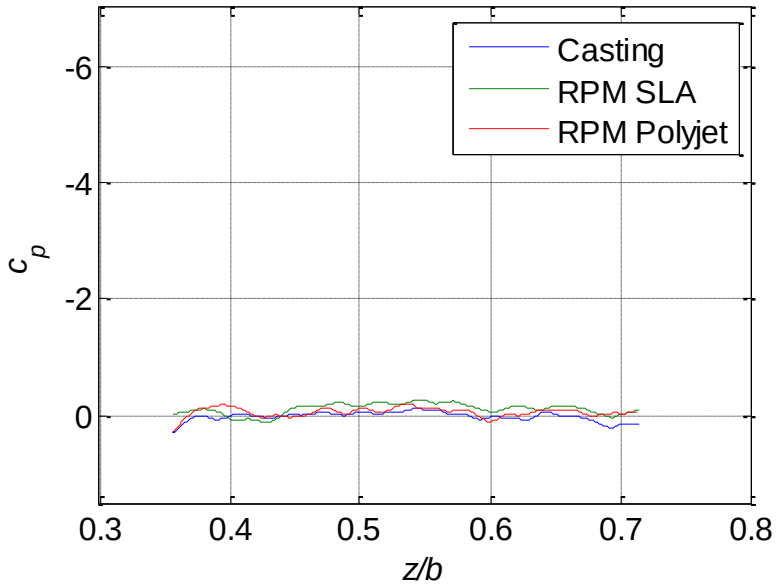

Figure 3.81: Roughness ice shapes, PSP spanwise c_p comparison, α = 11°, x/c = 0.7.

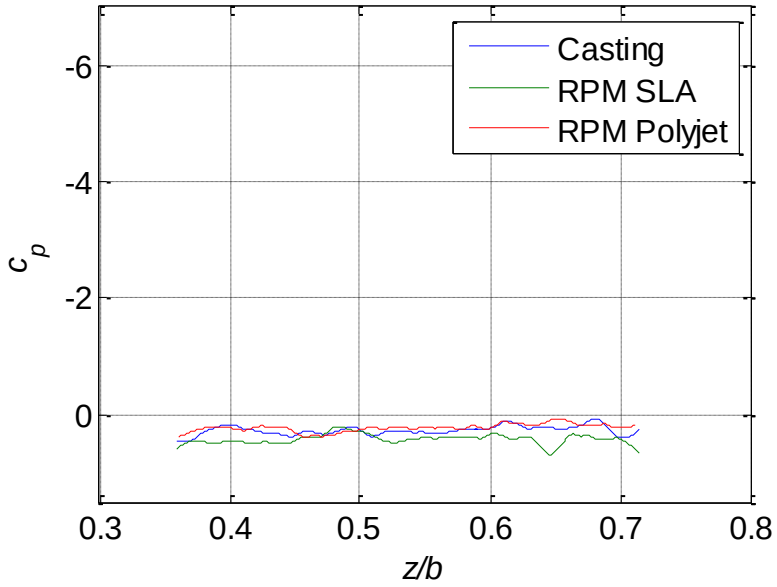

Figure 3.82: Roughness ice shapes, PSP spanwise c_p comparison, α = 11°, *x/c* = 0.9.

Chapter 4

Summary, Conclusions, and Recommendations

4.1 Summary

This study sought to experimentally validate the recently developed 3-D ice accretion measurement methodology through a comparison wind tunnel test program utilizing various experimental techniques. Ice shapes generated from the new method were aerodynamically compared to ice shapes created from the currently-used mold and casting method. The new method used a laser scanner to record an ice accretion in an icing tunnel. The acquired scan was then be used to produce a rapid-prototype ice shape replica. Benefits of this procedure over the mold and casting method include the ability to scale ice shapes and to obtain a digital record of original ice accretions. Before the new method could be fully implemented, agreement with the accepted method first had to be achieved.

For the purposes of this investigation, two ice shape classifications were chosen to be studied in depth: a horn shape and a roughness shape. The two methods reproduced ice shape features with varying degrees of accuracy and resolution, so the choice of these two shapes allowed aerodynamic differences due to both large-scale and small-scale ice feature variations to be observed. Shapes were made using a stereolithography (SLA) rapid-prototype method and were compared to the castings. The roughness case included an additional rapid-prototype shape made using the Polyjet process. This provided additional information on the roughness resolution necessary to replicate the iced aerodynamics of the original ice accretion.

The validation tests included aerodynamic performance comparisons using force balance, integrated pressure tap results, and total pressure probe wake surveys. The performance results were supplemented with pressure-sensitive paint (PSP) data, which

provided additional information about the pressure distribution along the span. The PSP results were compared to the pressure tap and performance results to assess the accuracy and value of the PSP method as implemented in the UIUC 3ft by 4ft subsonic wind tunnel.

The overall results showed reasonable agreement between the casting and rapid-prototype shapes, with some noticeable differences. The horn casting had less of an aerodynamic penalty than the rapid-prototype shape. The horn casting had a higher maximum lift coefficient ($c_{\ell,max}$) by 0.02 and smaller drag coefficients (c_d) over the tested angle of attack range. A geometric comparison between the two horn shapes showed a general trend where the rapid-prototype shape had larger ice features. This general geometric difference most likely caused the observed aerodynamic differences. The PSP data corroborated this observation by showing a pressure distribution with more upper-surface suction for the casting. The roughness shapes had more subtle differences. The rapid-prototype Polyjet roughness shape had the least effect on the aerodynamics when compared to the clean NACA 23012 case. The rapid-prototype SLA shape had more of an aerodynamic effect, and the casting had the most effect. This trend was observed in the highest maximum lift coefficient value of 1.24 for the Polyjet and the lowest for the casting with a value of 1.12. The drag coefficient for the casting was highest with a minimum drag coefficient of $c_{d,min}$ = 0.0138 and lowest for the Polyjet was with a minimum drag coefficient of $c_{d,min}$ = 0.01226. The PSP data showed the greatest suction peak for the Polyjet case, thus supporting this observation. The PSP pressure coefficient (c_p) results were compared to the pressure tap data and found to follow the trends observed in the pressure and force balance data. The PSP results for the cases tested during these experiments showed good agreement at the pressure tap locations with a calculated average percent error of 7.3%. The agreement along the entire span was less good, with an average percent error of 10.8%.

4.2 Conclusions

1. The overall aerodynamic agreement between the rapid-prototype and casting shapes appeared to be good. The differences between the shapes made from the two methods were slight compared to the differences between the clean and iced cases.

2. The pressure-sensitive paint (PSP) data supported the trends observed in the aerodynamic performance, pressure tap, and wake survey data.
3. The aerodynamic differences are most likely consequences of geometric variations between the rapid-prototype and casting shapes. The geometric differences could result from the varying resolution capabilities of the replication methods. Errors in the two methods, such as the laser scanner software's capability to interpolate between scan data points or the accuracy of the mold and casting method, could contribute to these variations also. In general, the rapid-prototype SLA and Polyjet shapes had smoother features than the castings.
4. Spanwise pressure coefficient (c_p) data were obtained using PSP over a greater model area than was evaluated using the pressure taps.
5. Careful experimental set-up and control of errors are necessary to obtain quantitative PSP results.
6. PSP data showed that the flowfields were mostly two-dimensional for both ice shapes in that the same trends generally exist over the entire span.
7. The new method for documenting and replicating three-dimensional ice shapes through the use of a laser scanner and rapid-prototyping methods was reasonably validated.

4.3 Recommendations

During the course of this experiment and subsequent analysis, ideas concerning future extensions of this research were formed and developed. These pertain to improved implementation of the experimental methods and next steps in the overall project.

1. The source of the geometric differences between the horn ice shapes produced from the two methods should be investigated. This could include testing the accuracy of each method and could be accomplished by scanning the casting with the 3-D laser scanner and creating another rapid-prototype shape. This rapid-prototype shape made from the casting could be compared in the scanning software to the original rapid-prototype shape to quantify the geometric variations. Aerodynamic testing could be performed on this shape as well. Agreement between the original casting and the scanned/rapid-prototype casting would show the mold and casting method is accurate,

while disagreement between the two would reveal inaccuracies in that process. Aerodynamic agreement between the original rapid-prototype shape and the rapid-prototype shape made from the casting would expose errors in the newly developed 3-D ice accretion measurement methodology. A similar study could be performed by making a casting of the original rapid-prototype shape.

2. Improvements to PSP implementation were determined based on experiences with the PSP process currently used in the UIUC 3ft by 4ft subsonic wind tunnel. Errors in PSP data could be reduced significantly by applying the modifications listed below. Further work should include:
    a. Acquisition of PSP and pressure tap data at the same conditions is necessary to obtain quantitative results. These include Reynolds number and atmospheric pressure.
    b. Reduction of, or correction for, model motion is important. This could be accomplished through more robust model design or physically constraining the model during PSP testing. The use of binary paint could also reduce some of the effects from model motion, as could a more accurate alignment process. Further research into these motion correction schemes would therefore be worthwhile.
    c. Temperature effects are significant in PSP work. Measurement of the temperature values and gradients during testing through the use of binary paint, infrared cameras, or thermocouples at the model surface could help account for temperature errors.
    d. Increasing the signal to noise ratio in the PSP data could be accomplished by increasing the intensity of the excitation light.
    e. Performing PSP experiments in wind tunnels capable of testing at higher dynamic pressures than are obtained at UIUC would improve the ability of the method to resolve pressure differences over the model surface.

References

[1] Broeren, A.P., Potapczuk, M.G., Riley, J.T., Villedieu, P., Moens, F., and Bragg, M.B., "Swept-Wing Ice Accretion Characterization and Aerodynamics," AIAA Paper 2013-2824, 2013.

[2] Diebold, J.M., Broeren, A.P., and Bragg, M.B., "Aerodynamic Classification of Swept-Wing Ice Accretion," AIAA Paper 2013-2825.

[3] Bragg, M.B., Broeren, A.P., and Blumenthal, L.A., "Iced-Airfoil aerodynamics." *Progress in Aerospace Sciences*, Vol. 41, No. 5, July 2005, pp. 323-418.

[4] Anderson, D.N., and Shin, J., "Characterization of ice roughness from simulated icing encounters," AIAA Paper 1997-0052, 1997.

[5] Busch, G.T., "Ice Accretion Aerodynamic Simulation on a Subscale Model," MS Thesis, Dept. of Aerospace Engineering, UIUC, Urbana, IL, 2004.

[6] Tani, I., "Low-Speed Flows Involving Bubble Separations," *Progress in Aerospace Sciences*. Vol. 5, 1964, pp. 70-103.

[7] Anderson, J.D., Jr., *Fundamentals of Aerodynamics*, McGraw-Hill, 4rd ed., USA, 2005.

[8] Jacobs, J.J. and Bragg, M.B., "Particle Image Velocimetry Measurements of the Separation Bubble on an Iced Airfoil," AIAA Paper 2006-3646, 2006.

[9] Blumenthal, L., "Surface Pressure Measurement on a Three-Dimensional Ice Shape," MS Thesis, Dept. of Aerospace Engineering, UIUC, Urbana, IL, 2003.

[10] "Supercooled Large Droplets (SLD)," Federal Aviation Administration, Washington, D.C. [https://www.faasafety.gov/gslac/ALC/course_content.aspx?cID=33&sID=155&preview=true. Accessed 11/14/13.]

[11] Broeren, A.P., Bragg, M.B., Addy, H.E., Jr., Lee, S., Moens, F., Guffond, D., "Effect of High-Fidelity Ice-Accretion Simulations on Full-Scale Airfoil Performance," *Journal of Aircraft*, Vol. 47, No. 1, Jan.-Feb. 2010, pp. 240-254.

[12] Reehorst, A.L. and Richter, G.P., "New Methods and Materials for Molding and Casting Ice Formations," NASA TM-100126, 1987.

[13] Callister, W.D. and Rethwisch, D.G., *Fundamentals of Materials Science and Engineering: An Integrated Approach*, 3rd ed., John Wiley & Sons, Inc, US, 2008.

[14] Liu, T. and Sullivan, J.P., *Pressure and Temperature Sensitive Paints*, Springer-Verlag, Germany, 2005.

[15] Kautsky, H. and Hirsch, H., "Detection of minutest amounts of oxygen by extinction of phosphorescence" (in German). *Z Anorg allg Chem*, 1935, pp 222-216.

[16] Peterson, J.I. and Fitzgerald, R.V., "New technique of surface flow visualization based on oxygen quenching of fluorescence," *Rev Sci Instrum*, Vol. 51, 1980, pp. 670-671.

[17] Pulkin, E., Carlson, B., Gouin, S., Costin, C., Green, E., Ponomarev, S., Tanji, H., and Gouterman, M. "Ideality of Pressure-Sensitive Paint. I. Platinum Tetra(pentafluorophenyl)porphine in Fluoroacrylic Polymer," Journal of Applied Polymer Science, Vol. 77, No. 13, Sept. 2000, pp. 2795-2804.

[18] Bell, J.H., "Accuracy Limitations of Lifetime-Based Pressure-Sensitive Paint (PSP) Measurements," *Instrumentation in Aerospace Simulation Facilities, 2001. 19th Congress on iciasf.*, Aug 2001, pp. 5-16.

[19] Crafton, J.W., Fonov, S.D., Goss, L.P., Jones, E.G., and Reeder, M.W. "Comparison of Radiometric and Lifetime based Pressure-Sensitive Paints for Low Speed Measurements." AIAA Paper 2006-1041, 2006.

[20] Juliano, T.J., Peng, D., Jensen, C., Gregory, J., Liu, T., Montefort, J., Palluconi, S., Crafton, J., and Fonov., S., "PSP Measurements on an Oscillating NACA 0012 Airfoil in Compressible Flow." AIAA Paper 2011-3728, 2011.

[21] Bell, J.H. "Applications of Pressure-Sensitive Paint to Testing at Very Low Flow Speeds." AIAA Paper 2004-878,2004.

[22] Crafton, J., Fonov, S., Forlines, R., and Palluconi, S., "Development of Pressure-Sensitive Paint Systems for Low Speed Flows and Large Wind Tunnels." AIAA Paper 2013-0482, 2013.

[23] Bencic, T.J., "Application of Pressure-Sensitive Paint to Ice Accreted Wind Tunnel Models." AIAA Paper 2000-16674, 2000.

[24] Ferrigno, F., Guille, M., Auletta, A., and Palazzo, S. "Low Speed PSP Measurements on an Ice Accretion Shaped Model." AIAA Paper 2003-744, 2003.
[25] Diebold, J.M., Monastero, M.C., and Bragg, M.B., "Aerodynamics of a Swept Wing with Ice Accretion at Low Reynolds Number." AIAA Paper 2012-2795, 2012.
[26] Vassberg, J.C., DeHaan, M.A., Rivers, S.M., and Wahls, R.A., "Development of a Common Research Model for Applied CFD Validation Studies," AIAA Paper 2008-6919, 2008.
[27] "Icing Research Tunnel," NASA. [http://facilities.grc.nasa.gov/irt/index.html. Accessed 12/13/13.]
[28] Lee, S., Broeren, A.P., Addy, Jr., H.E., Sills, R., and Pifer, E.M., "Development of 3D Ice Accretion Measurement Method." AIAA Paper 2012-2938, 2012.
[29] Chua, C.K., Leong, K.F., and Lim, C.S. *Rapid Prototyping: Principles and Applications.* 3rd ed., World Scientific, Singapore, 2010.
[30] Diebold, J.M., "Aerodynamics of a Swept Wing with Leading-Edge Ice at Low Reynolds Number," MS Thesis, Dept. of Aerospace Engineering, UIUC, Urbana, IL, 2012.
[31] Ansell "Flight Envelope Protection Using Flap Hinge Moment Measurement," MS Thesis, Dept. of Aerospace Engineering, UIUC, Urbana, IL, 2010.
[32] Lee, S. "Effects of Supercooled Large-Droplet Icing on Airfoil Aerodynamics," Ph.D. Dissertation, Dept. of Aerospace Engineering, UIUC, Urbana, IL, 2001.
[33] Jones, B.M., "The Measurement of Profile Drag by Pitot Traverse Method," Rech. Rep. 1688, British Aeronautical Research Council Reports & Memoranda, 1936.
[34] "ImageJ," ImageJ. [http://rsbweb.nih.gov/ij/index.html. Accessed 12/13/13.]
[35] Barlow, J.B., Rae, W.H., Jr., and Pope, A. *Low Speed Wind Tunnel Testing*. 3nd ed, John Wiley & Sons, Inc, USA, 1999.
[36] Rae, W.H., Jr. and Pope, A. *Low Speed Wind Tunnel Testing*. 2nd ed, John Wiley & Sons, Inc, USA, 1984.
[37] Broeren, A.P., Addy, H.E., Jr., Lee, S., and Monastero, M.C. "Validation of 3-D Ice Accretion Measurement Methodology for Experimental Aerodynamic Simulation," Extended Abstract Submitted to the 6th AIAA Atmospheric and Space Environments Conference, June 2014.
[38] Lee, S., Broeren, A.P., Kreeger, R.E., Poptapczuk, M.G., and Utt, L., "Implementation and Validation of 3-D Ice Accretion Measurement Methodology," Extended Abstract Submitted to the 6th AIAA Atmospheric and Space Environments Conference, June 2014.
[39] Weaver, W.L, Jordan, J.D., Dale, G.A., and Navarra, K.R., "Data Analysis Methods for the Development and Deployment of Pressure-Sensitive Paints," AIAA Paper 99-0565, 1999.
[40] Kline, S. and McClintock, F.A., "Describing Uncertainty in Single-Sample Experiments," *Mechanical Engineering*, Vol. 75, 1953, pp.3-8.
[41] Liu, T., Guille, M., and Sullivan, J.P., "Accuracy of Pressure-Sensitive Paint," *AIAA Journal*, Vol. 39, No. 1, Jan. 2001, pp. 103-112.
[42] Crafton, J.W., "The Impingement of Sonic and Sub-Sonic Jets Onto a Flat Plate at Inclines Angles," Ph.D. Dissertation, School of Aeronautics and Astronautics, Purdue University, West Lafayette, IN, 2004.
[43] Liu, T., Guille, M., and Sullivan, J.P., "Accuracy of Pressure-Sensitive Paint," AIAA Paper 99-3785, 1999.

Appendix A

Pressure Sensitive Paint Method

A.1 Method employed in ARL

The current pressure-sensitive paint method implemented in the Aerodynamic Research Lab as of the completion of the test discussed in this thesis is outlined below. For this work, the single-channel radiometric PSP method was used.

A.1.1 Experimental Set-Up

As described in Chapter 2, the PSP experiment was set up in the UIUC 3ft x 4ft subsonic tunnel. An acrylic window used specifically for optical experiments was installed to provide optical access for the excitation lamp to shine through and the camera to record data with minimal interference from scratches and smudges. Initial PSP experiments with the usual tunnel window showed the importance of using a window with few scratches and surface impurities. Any dirt, oil, or scratches can interfere with the signal, as can be seen from the results in Figure A.1a where the old tunnel window was installed. This data is from a previous test using a swept-wing model. The old window has numerous scratches, oil, and dirt that disrupted the excitation light from the lamp and the emitted light from the paint. Installing a new window resulted in the results in Figure A.1b, which are much cleaner without the reflections and errors seen in Figure A.1a. The circular feature in the center of the image is due to poor camera positioning so that reflections from the camera lens interfered with the data. All further PSP experiments were performed with the new window.

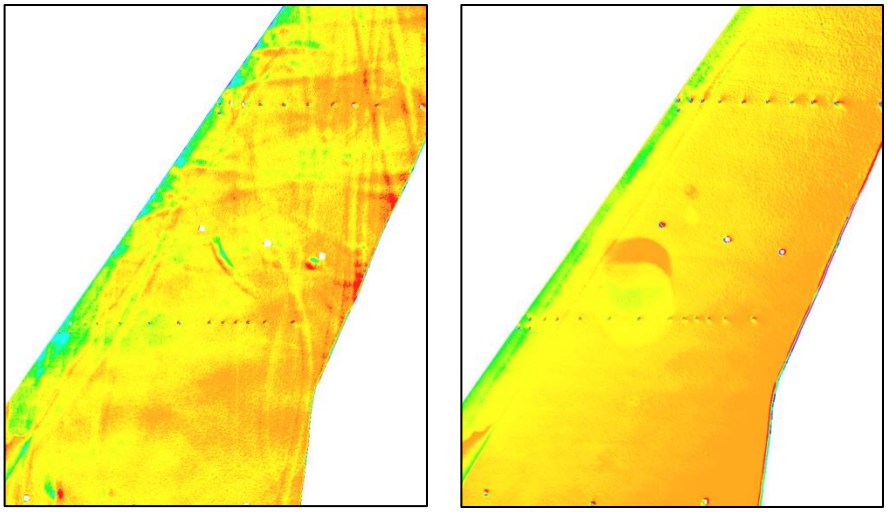

a) b)

Figure A.1: Effect of wind tunnel window condition on intensity ratio results for a swept-wing model with a a) scratched window and b) new window.

Once the aluminum model was installed and cleaned with acetone, the surface section to be painted was edged with tape, and the rest of the model and tunnel were covered in drop cloths. For plastic models, such as the swept-wing model made of stereolithography (SLA) material in Figure A.1, the surface was covered in contact paper. This protected the model surface from being exposed to large amounts of acetone during cleaning. Figure A.2 shows the model installed in the tunnel and prepared for painting. The pressure taps were covered with toothpick tips to prevent the paint from clogging the orifices and tubes, as shown in Figure A.3. First, the white base coat of Krylon Indoor/Outdoor Primer was applied and allowed to dry completely for between 45 minutes to an hour. The base coat was thick enough to provide a uniform coating that was optically opaque. The PSP (here, ISSI's UniFIB PSP) was next applied using an airbrush as seen in Figure A.4 following the application instructions provided with the paint. This image was acquired during painting of the swept-wing, but the method is the same for the airfoil model. Between 7 and 9 coats were applied, though additional paint was added if needed. A coat counts as moving down the entire section and up the entire section in side-to-side passes with the airbrush. During all painting the tunnel was set to 30 rpm and the garage door opened to provide adequate ventilation. Additionally, the painter wore a half-mask respirator with OV/P100 filters to protect against organic vapors. The PSP was allowed to dry for at least 2 hours. A completed PSP application can be seen in Figure A.5 for the horn casting used in this test.

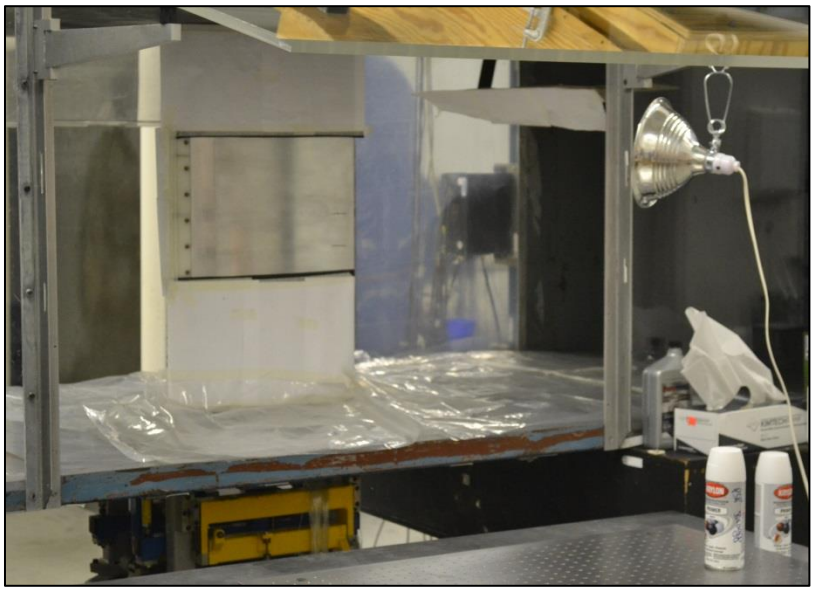

Figure A.2: Model installed in tunnel and prepared for painting.

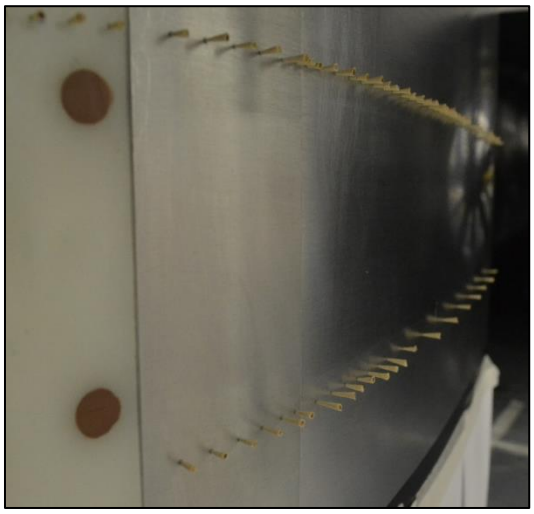

Figure A.3: Toothpick ends in the pressure taps. Close up viewed from near leading edge towards the trailing edge.

Figure A.4: Painting of the swept-wing model using an airbrush in the tunnel test section.

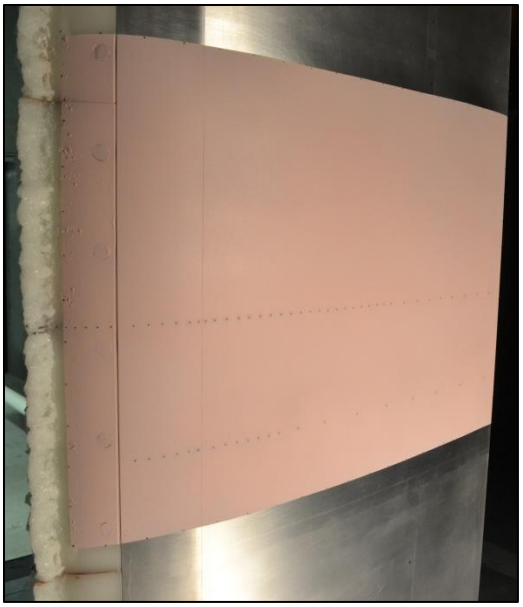

Figure A.5: Completed PSP application for the horn casting.

An optical table and optical mounting equipment were used to set up the camera and excitation lamp. See Chapter 2 for details on the lamp and the CCD camera. The entire test section and adjacent area with the test equipment were enclosed in blackout material in order to remove contaminating ambient light as shown in Figure A.6.

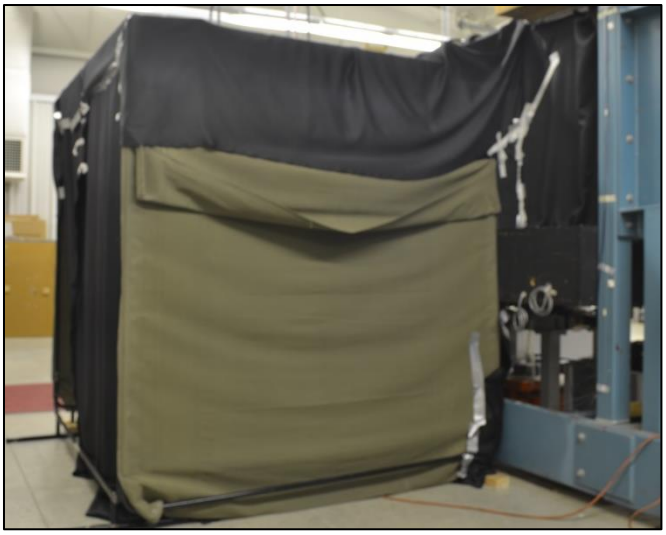

Figure A.6: Black-out curtains surrounding test section and optical equipment.

A.1.2 Image Acquisition

PSP data were acquired using the method described in Chapter 2. Three sets of images were taken during testing. The wind-on image set was obtained after the tunnel had been running for at least 15 minutes to help ensure that the model was close to thermal equilibrium. A reference image set at the wind-off condition was obtained to remove illumination, paint thickness, and luminophore concentration effects from the data. A third image set was also acquired with the excitation lamp off to account for any ambient light or CCD array effects. The image acquisition software from Andor, Solis, was used to obtain and save the images.

A.1.3 Processing

The three sets of images for the background, wind-on, and wind-off images were first averaged using ImageJ, a public domain image processing software. The groups of 25 images are each called a "stack," where all 25 images are in one file. Each of the three stacks were opened in ImageJ and averaged at each pixel. The menus for this are *Image>Stacks>Z Projection* as exhibited in Figure A.7.

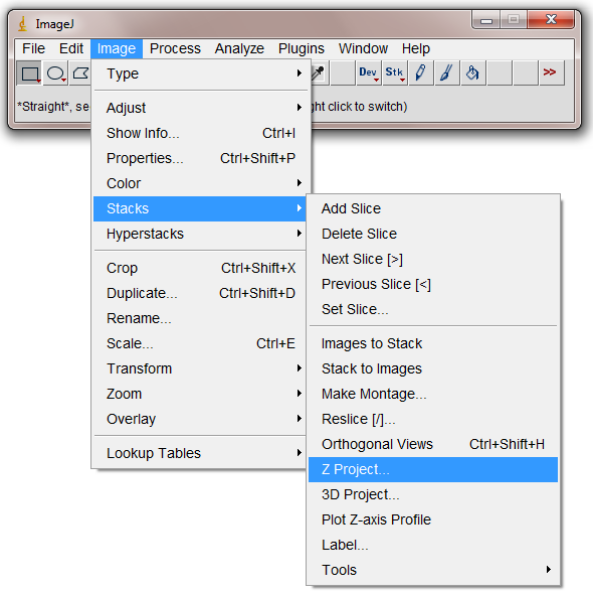

Figure A.7: Z-Projection Menu.

Using the "Z Projection" window displayed in Figure A.8, the average intensity at each pixel in all 25 images is performed by choosing "Average Intensity" from the drop-down "Projection Type" menu and ensuring that all images, or "slices", are included. The resulting averaged image was saved as a .tiff for use with the next program.

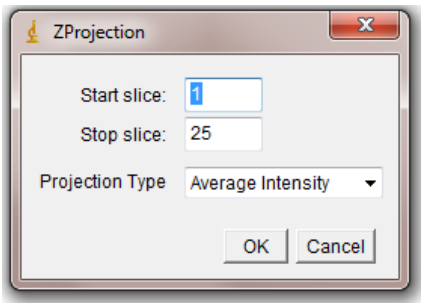

Figure A.8: Z-Projection Average Intensity Window.

The next step is to calculate the intensity ratio from the three averaged images for the wind-on, wind-off, and background intensity. OMS Lite, ISSI's PSP processing software, is used to remove non-painted areas from the data, place markers, align the wind-off and wind-on images, and calculate the intensity ratio. (OMS Lite can also perform the pressure calibration, though this is done in a separate MATLAB code in this method.) For this test the "PSP Single Channel" option was selected, though the "PSP Binary Channel" would be

selected if using binary PSP. The averaged TIFF background, wind-on, and wind-off images were imported and the dark threshold value set using the OMS Lite main window show in Figure A.9. The dark threshold value removes intensities below the chosen value from the wind-on and wind-off images in order to remove a large portion of the non-painted signal from the image. The dark threshold values used in this test are tabulated in Table A.1.

Table A.1: Dark Threshold Values.

Leading Edge	Dark Threshold Value
ED1983 Cast	800
ED1983 RPM SLA	800
ED1983 RPM PJ	900
ED1978 Cast	900
ED1978 RPM	900
Clean	850
ED1978 RPM same paint	800

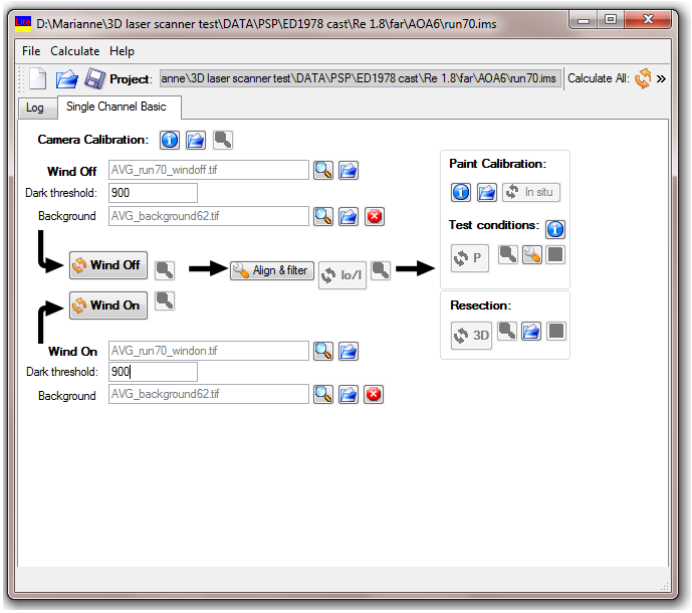

Figure A.9: OMS Lite Main Window

Markers, used for the alignment of the wind-on image to the wind-off image, were placed virtually in both images in the same sequential order using the "Add Marker" button. The OMS Lite button "Revise Markers" uses a centroid finder to place each marker at the center of the pressure tap. The wind-off and wind-on intensity images with added markers are shown in Figures A.10 and A.11, respectively.

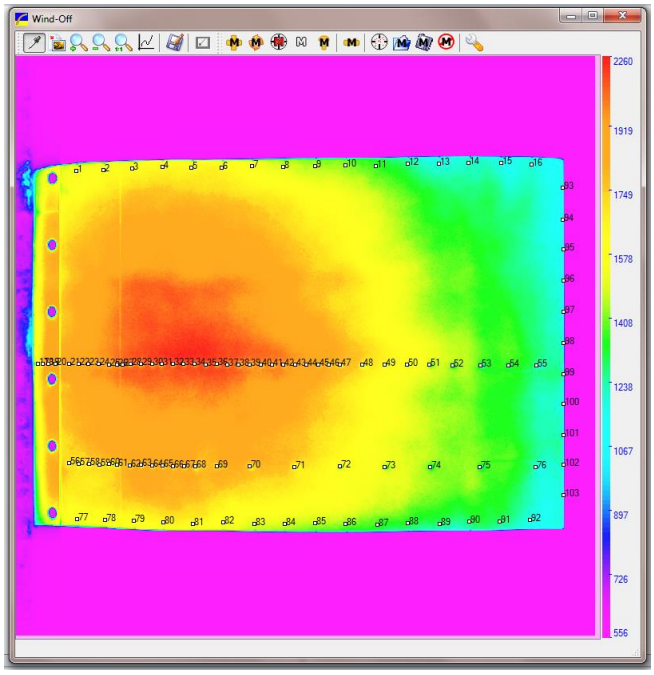

Figure A.10: Wind-off image with markers.

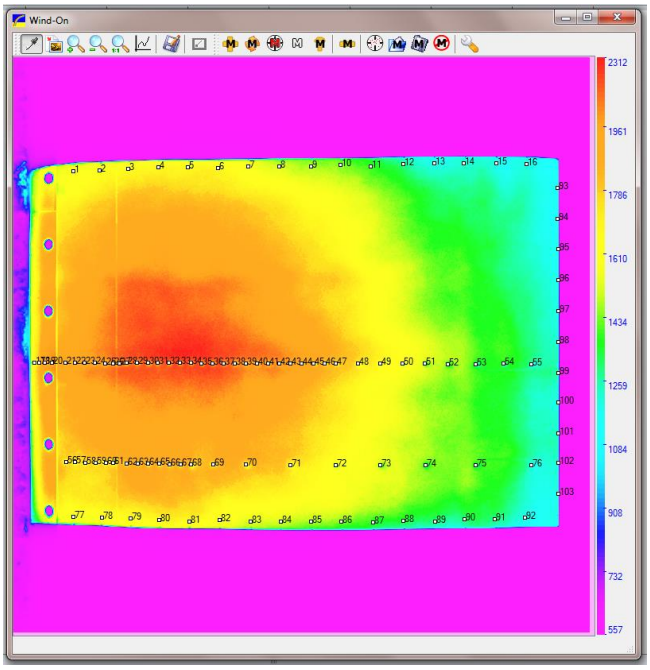

Figure A.11: Wind-on image with markers.

The “Wind On” and “Wind Off” buttons were pressed in the main window to subtract the background image from both the wind-on and wind-off images and to apply the dark

threshold value. Figures A.12 and A.13 show the resulting images in their respective windows.

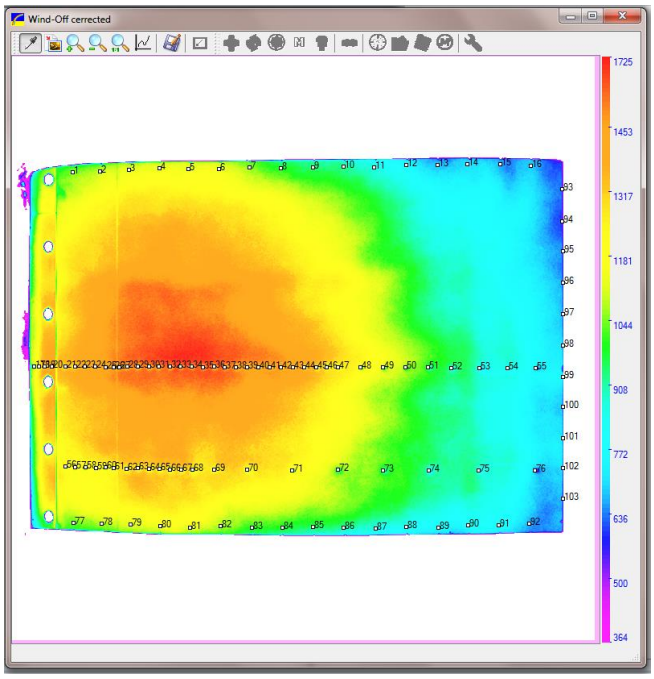

Figure A.12: Wind-off image with background subtracted.

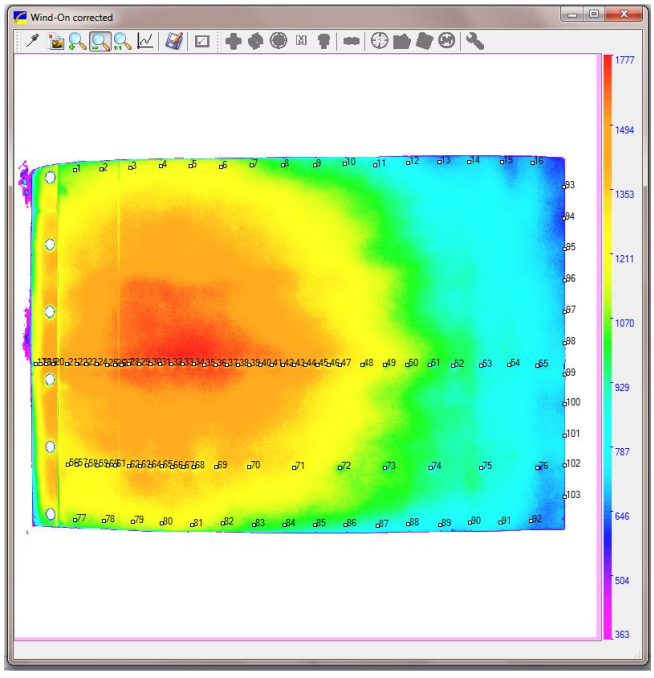

Figure A.13: Wind-on image with background subtracted.

Next, the alignment and filtering options are chosen in the "Align and Filter" window. The Figure A.14 below shows the values of all the settings typically used. For most cases, markers were used for alignment, with a box size of 24, order of fit of 2, and fitting marker 0 first. No filters were applied in OMS Lite for the current test. Thinning was also applied with a border of 2 pixels. The QPED correlation alignment and threshold features were not used. For the ED1978 RPM same paint case, no alignment markers were applied at the top and bottom of the painted area. For this reason, an order of fit of 2 could not accurately be used, and an order of 0 was used instead. The alignment of the wind-on image to the wind-off image was needed to account for potential model motion between the two conditions using the image registration technique outlined in Weaver et al.[39]

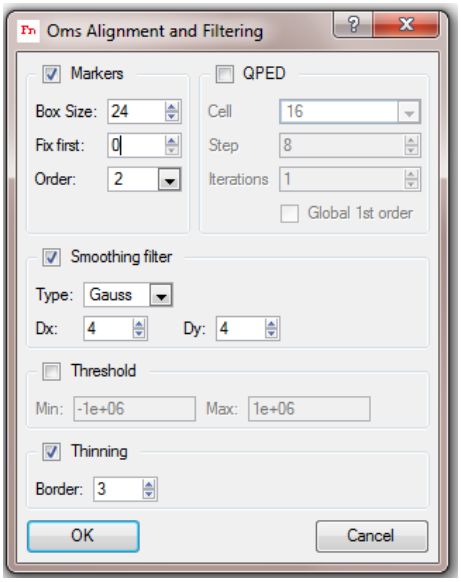

Figure A.14: Alignment and Filtering Options Window.

Once the alignment and filtering settings were chosen, the intensity ratio was calculated. During that process, the program filters (if a filter is specified), aligns, and ratios the images. The final image, presented in Figure A.15, was saved as a .dat Tecplot file to be used with the MATLAB processing code. The final aligned marker locations were also saved to be used in the input file for the MATLAB code.

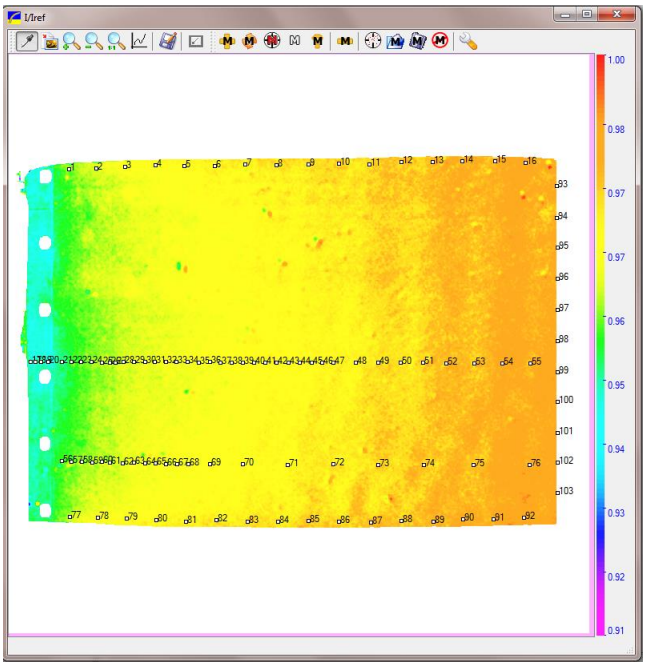

Figure A.15: Intensity ratio (I_{ref}/I) image.

Within the MATLAB code, the intensity ratio values of the pixels surrounding each pressure tap are averaged and plotted against the pressure ratio measured at that tap. The pressure ratio is the measured surface pressure over the tunnel static pressure. The linear fit through the data points from each tap is the relationship between intensity ratio and pressure ratio and is called the Stern-Volmer equation. It is used to convert the intensity ratio data in the entire image to pressures.

The processing code first imports the .dat intensity ratio file and the input file (containing test condition data, pressure tap pixel and model coordinates, and pressure coefficient data). As described in Chapter 2, any background signal or extremely erroneous intensity image data is set to NaN if the ratio is less than 0.85 or greater than 1.05. Additionally, the code calculated the approximate pixel location of the beginning of the painted surface. All pixels located at x-pixel values less than that location were set to NaNs. This ensured that any erroneous signals from paint splotches or reflections from the ice shapes did not interfere with the analysis. A median filter with a kernel of 9x5 is applied to the data. The pressure ratios of the taps are calculated from the pressure coefficients. The average intensity ratios at each tap are found by finding the mean of a 7x13 rectangle of pixels centered at an offset of (0,+10 pixels) from the center of each tap. Since the PSP data

downstream of about *x/c* = 0.7 has a low signal-to-noise ratio, those taps were removed from the calibration calculation. The calibration was performed to find the coefficients of the Stern-Volmer ratio equation, as described earlier, and is plotted in Figure A.16 for the horn casting at Re 1.8 million, α = 7°. The coefficients of the linear fit between the two data sets were found by fitting the intensity ratio data to the pressure ratio data in a least squares manner and are reported as the slope and intercept of the equation stated in Figure A.16. The relation for pressure in terms of intensity was found by inverting the resulting linear fit. The axes for all figures were chosen to provide a uniform standard of comparing between all cases. A separate code was used to perform the calibrations and processing for cases, such as the rapid-prototype horn, where the leading edge data points differed significantly from the main body data points. For these cases separate calibrations were performed for the ice shape and the main body.

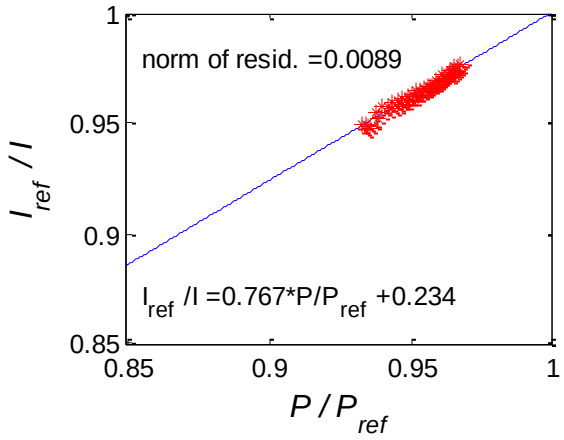

Figure A.16: PSP calibration curve for the horn casting at α = 7°.

In order to quantify the agreement between the data points and calibration curve, a goodness-of-fit test was performed on each calibration. This was accomplished through the calculation of the norm of the residuals between the data points and linear curve fit. The lower the value of the norm of the residuals, the better the fit is. Next, the intensity ratio data, along with the pressure tap marker locations, were plotted as in Figure A.17.

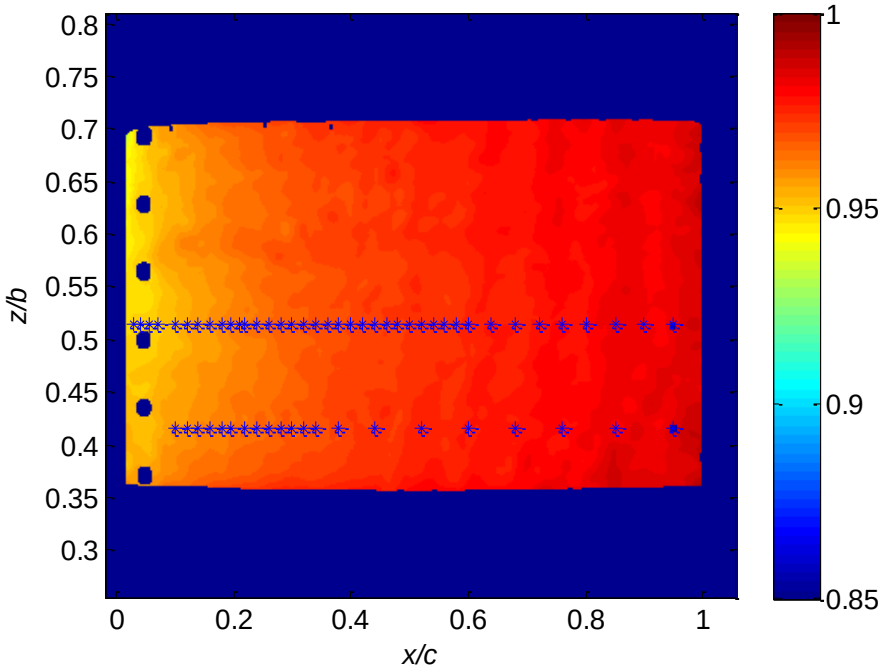

Figure A.17: PSP intensity ratio image for the horn casting at α = 7°.

This intensity ratio data was put through the calibration to find the pressure ratio data, shown in Figure A.18. The pressure was then calculated and plotted in Figure A.19.

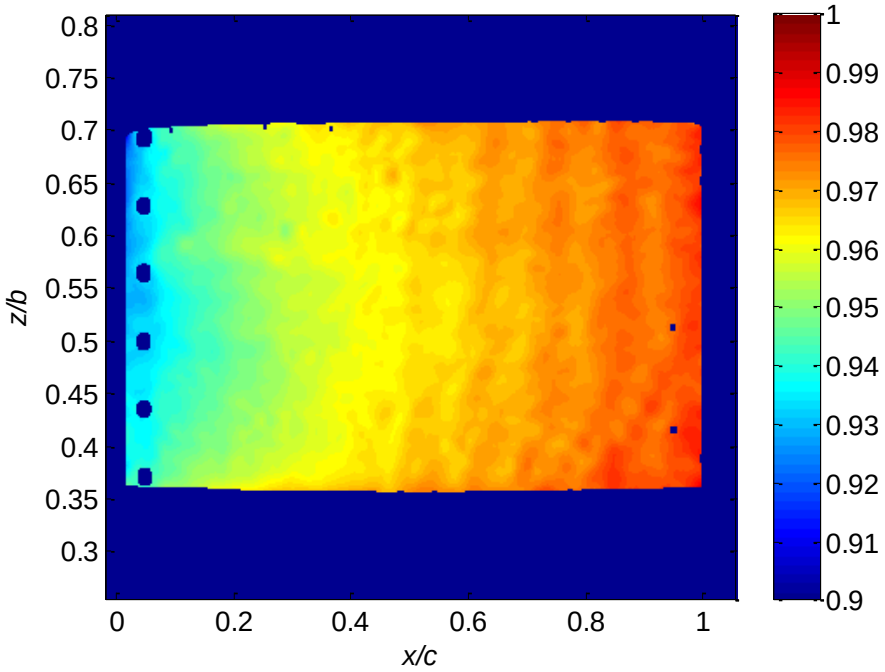

Figure A.18: PSP pressure ratio image for the horn casting at α = 7°.

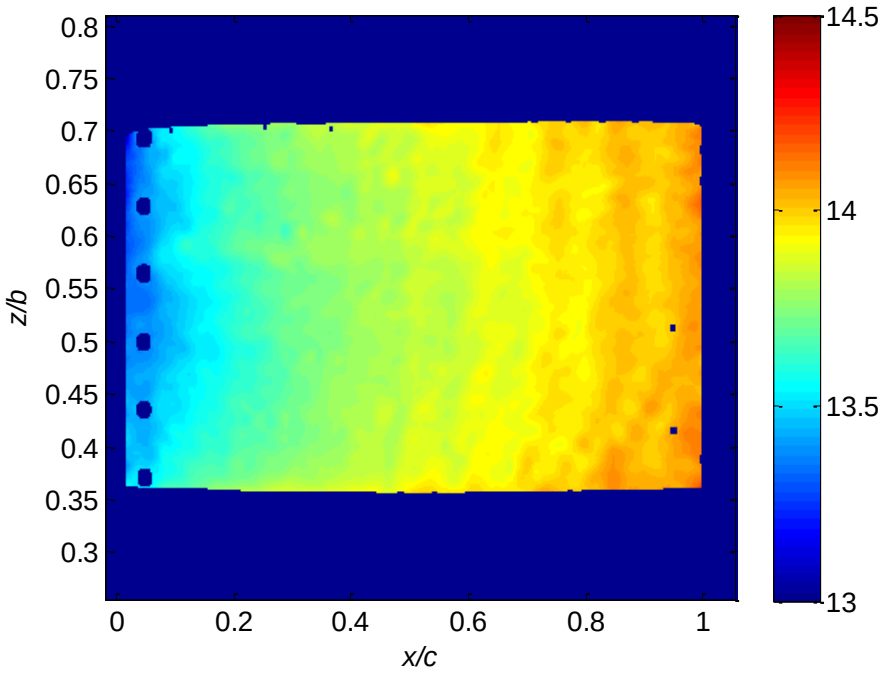

Figure A.19: PSP pressure image for the horn casting at α = 7°.

The pressure coefficient could then be found for the entire painted surface (Figure A.20).

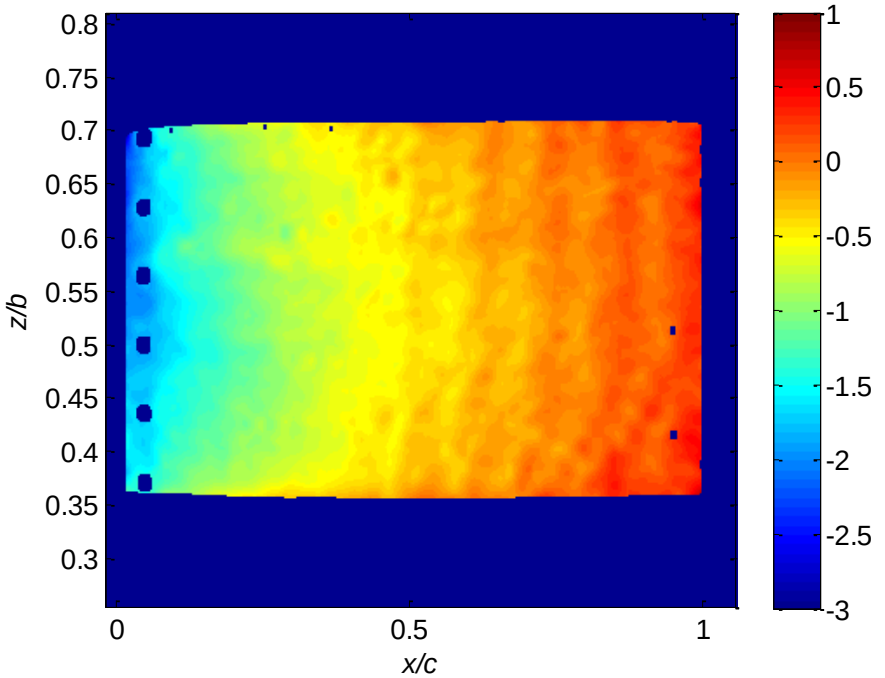

Figure A.20: PSP pressure coefficient (c_p) image for the horn casting at α = 7°.

All plots used model coordinates of *x/c* and *z/b*. The images were acquired in pixel coordinates and a transform applied to switch to model coordinates. The transform linearly interpolates the model coordinates of each pixel between every two taps. Equation A.1 is the equation for the transform in the x-direction. The transform is similar for the y-direction.

$$x/c_{pixel} = x/c_{tap\ (i)} + \frac{\left(x/c_{tap\ (i+1)} - x/c_{tap\ (i)}\right)}{\left(xpixel_{tap\ (i+1)} - xpixel_{tap\ (i)}\right)} * \left(xpixel_{tap(i+1)} - xpixel_{pixel}\right) \quad \text{(A.1)}$$

For the image area ahead of the first tap and behind the last tap, the transform for the closest segment was applied. For example, at the leading edge and upstream of the first visible tap, the transform values found for the segment between the first and second visible taps was applied. The same was performed at the trailing edge in the *x*-direction and in the *y*-direction above the main tap row and below the secondary tap row.

A number of plots were generated by the code to visualize and analyze the pressure distribution over the surface of the painted area. Figure A.21 shows the pressure coefficient plots at various spanwise locations.

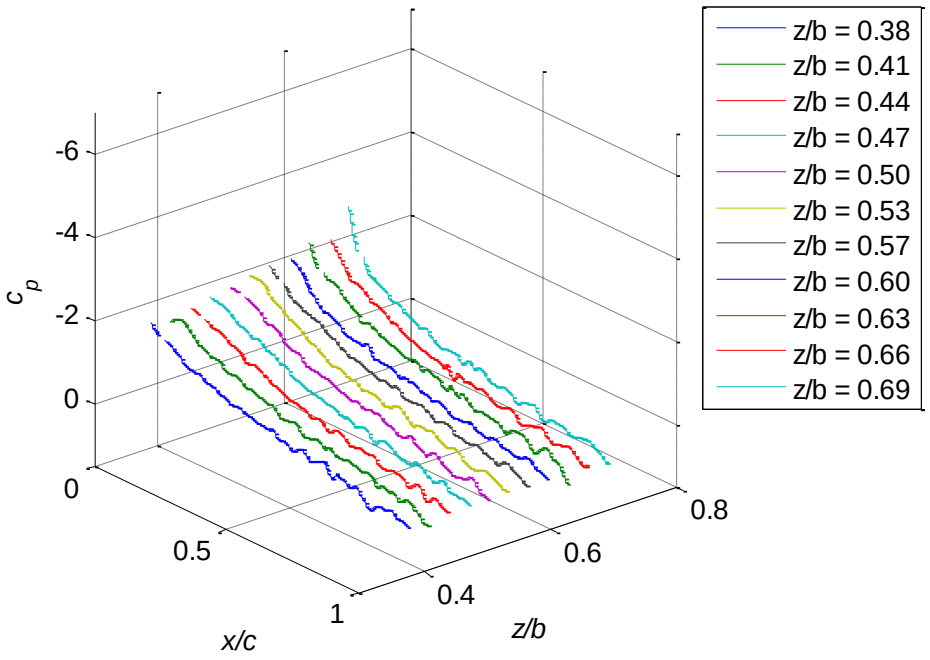

Figure A.21: PSP chordwise c_p curves at various *z/b* locations for the horn casting at α = 7°.

To visualize the comparison between the pressure tap data and the pressure sensitive paint data, three c_p curves were plotted with both data sets at three spanwise locations. The

first c_p curve was taken at the main tap row (z/b = 0.515). The PSP data was obtained from the average of the c_p values over 11 pixel rows (from 5 pixels below the tap row to 5 pixels above). The tap data plotted in Figure A.22 was obtained at the main tap row.

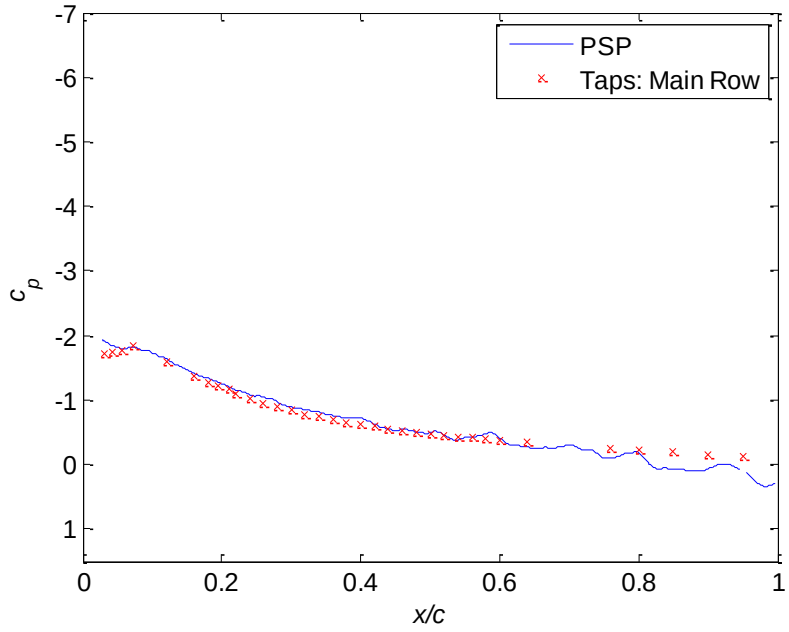

Figure A.22: PSP c_p comparison between PSP and tap data at main tap row, z/b = 0.515, for the horn casting at α = 7°.

Similarly a plot was obtained for the pressure coefficient data at the secondary tap row (z/b = 0.417) and is shown in Figure A.23.

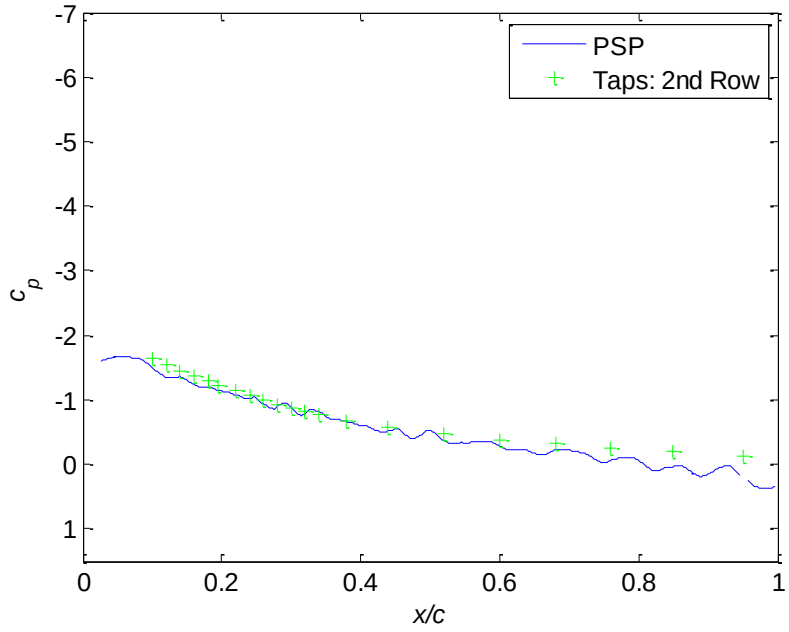

Figure A.23: PSP c_p comparison between PSP and tap data at secondary tap row, z/b = 0.417, for the horn casting at α = 7°.

A third comparison plot took the PSP data far from either tap row at z/b = 0.6 and plotted it with tap data from both main and secondary rows. This comparison is shown in Figure A.24.

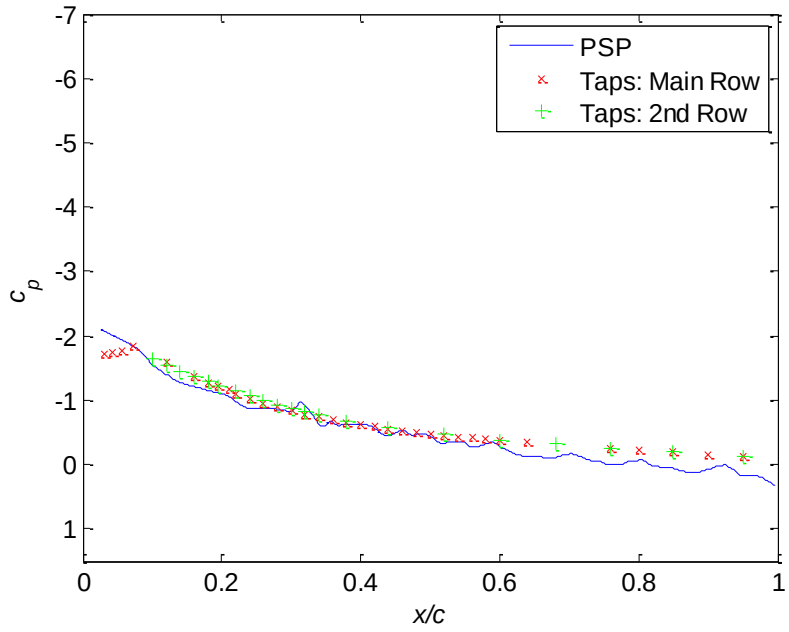

Figure A.24: PSP c_p comparison between PSP and tap data at z/b = 0.6, for the horn casting at α = 7°.

Once the final pressure coefficient (c_p) was computed, comparisons could be made between different shapes. These comparisons could be visualized along the span or along the chord for multiple ice shape cases.

Appendix B

Mold and Casting Method

The following section describes in a step-by-step manner the mold and casting method as implemented at UIUC. It begins with the arrival of the original molds from NASA. These original molds are made from the original ice accretions in the NASA Glenn Icing Research Tunnel (IRT). Since they are extremely stiff and break after making one casting, more durable molds must be made. This necessitates the making of a master casting from the original white mold to make the production molds. These production molds are purple and are used to make the castings used in wind tunnel testing.

First, the mold boxes used to make the molds and castings are prepared. These mold boxes are rectangular boxes that contain the same geometry of the wind tunnel leading edge, as seen in Figure B.1. This figure shows the original white mold inside the mold box and ready for the casting material to be poured into the negative space between the original mold and the leading edge geometry piece.

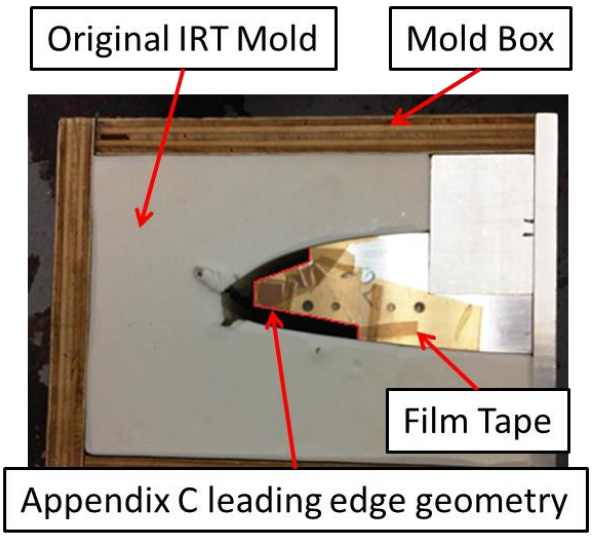

Figure B.1: Original mold for horn ice shape, inside a mold box and prepared to make a master casting.

Mold box preparation involves lining the entire inside of the box and the entire outline of the airfoil geometry piece with film tape as exemplified in Figures B.2. The tape used in this study was 2 in. wide and 3.8 mil thick 3M PTFE Film Tape 3580. The tape allows the mold and casting material to more easily be removed from the box. To aid in the mold and casting removal from the box, mold release spray is also used. It was applied to the inside of the mold box and the inside of the mold as seen in Figure B.3.

Figure B.2: Application of film tape to leading-edge template.

Figure B.3: Preparation of original molds with mold release spray.

After the mold has been sprayed with the mold release spray, the mold is placed inside the mold box and the sides sealed with caulk to prevent leaks. Figure B.4 shows the application of the caulk and Figure B.5 shows the base of the mold box being installed.

Figure B.4: Application of caulk.

Figure B.5: Placement of mold box bottom.

Next the proper amount of casting resin and hardener are mixed along with green dye. The green dye enhanced the visual difference between the casting and the mold material. The mixture was then mixed in a bucket with a drill and stirrer. These steps are illustrated in Figures B.6 though B.9. Figure B.6 shows the combination of the resin and hardener is the proper proportions. Figures B.7 and B.8 show the addition of the green dye. Figure B.9 shows the stirring method to mix the components of the casting material.

Figure B.6: Measurement of casting resin and hardener materials.

Figure B.7: Addition of green dye.

Figure B.8: Typical amount of dye used for each master casting.

Figure B.9: Mixing of casting materials.

Next, all air bubbles were removed from the mixture through the use of a vacuum pump. The bucket of casting material was placed inside the pump as shown in Figure B.10. The pump was turned on, and all remaining air was removed. The material bubbled as seen in Figure B.11. Care was taken to complete this portion of the work in a timely manner before the casting began to harden.

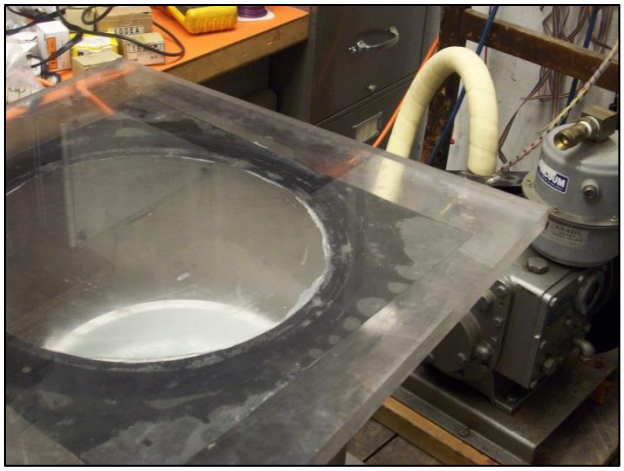

Figure B.10: Casting material inside vacuum pump chamber.

Figure B.11: Removal of air bubbles in casting material in vacuum pump chamber.

The casting mixture was then poured into the negative space between the original white mold and the airfoil geometry piece as can be seen in Figure B.12. The casting was allowed to set until hardened (Figure B.13).

Figure B.12: Pouring of casting material into negative space between mold and leading-edge template to create master casting.

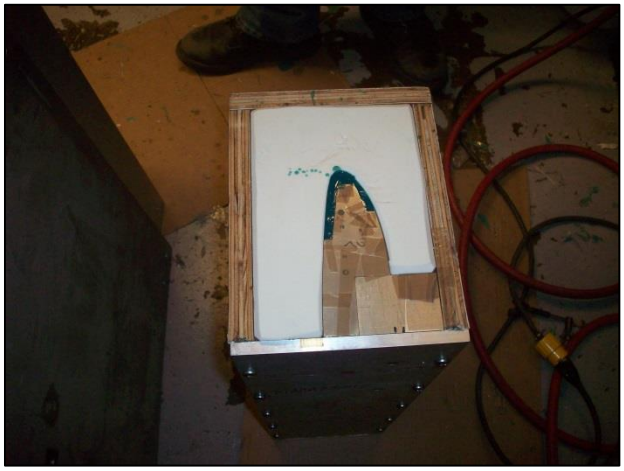

FigureB.13: The casting material left to cure.

Once the casting hardened, the mold box was opened and the mold removed (Figure B.14). The mold with the casting still inside is shown in Figure B.15. To remove the casting from the stiff mold, the mold was destroyed as shown in Figure B.16. The master casting for the horn case removed completely from the mold is presented in Figure B.17. This process left small pieces of mold material in the small crevices of the master casting. A number of sharp dental tools and picks were used to remove as much of this material as possible.

Figure B.14: Removal of master casting from mold and mold box.

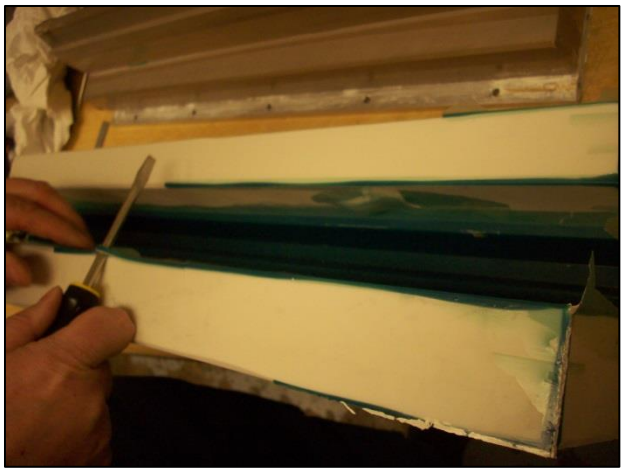

Figure B.15: Removal of master casting from mold.

a) b)

Figure B.16: Destruction of original mold to remove master casting.

Figure B.17: Master casting.

After a master casting was obtained, the production mold could be created. The production molds were made from GT 5092 High Strength Silicone RTV and are purple in color. The mold box was reassembled with the master casting mounted inside (Figure B.18). The master casting was held to the airfoil geometry piece with adhesive.

Figure B.18: Master casting in mold box and prepared to make production mold.

The mold material was mixed similarly to the casting material and placed inside the vacuum pump (Figures B.19 through B.21). Figure B.19 shows the measurement of the mold material components in the correct proportions and Figure B.20 shows the mixing of mold material. This mold material expanded significantly during degassing as can be seen in Figure B.21a. Care was taken to ensure that the material did not spill over the side of the bucket by opening a valve on the pump. After most of the air was removed, the material "fell" as can be seen in Figure B.21b. At this point, the degassing process was just about complete.

Figure B.19: Measurement of mold material components.

Figure B.20: Mixing of mold material.

a) b)

Figure B.21: Degassing of mold material, a) air is removed from material as it expands and b) most of the air is removed once the material "falls."

The mold material was then poured into the mold box (Figure B.22) and allowed to cure (Figure B.23). The completed mold is pictured in Figure B.24 and is significantly more durable and flexible than the original white mold.

Figure B.22: Pouring of mold material into mold box around master casting.

Figure B.23: Mold left to cure.

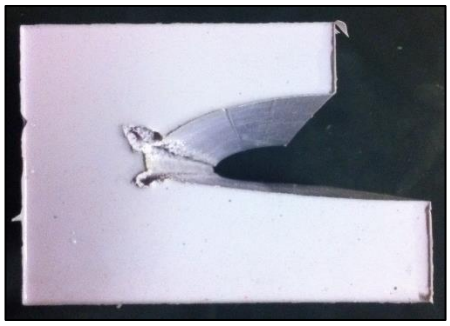

a) b)

Figure B.24: Completed production mold for horn ice shape.

To make the castings used in testing, the above process for the master casting creation is repeated, though without the addition of the green dye. Four separate castings were created for each ice shape. The spanwise extent of the casting to be used in testing was determined as was the location of the pressure tap row. To begin the pressure tap instrumentation process, the locations and orientations of the desired number of taps needed to be determined. This was accomplished by cutting one of the four castings at the same chosen location where the holes for the pressure taps will be drilled. The ice shape at this cut was then traced using the method outlined in Chapter 2 and used extensively in the NASA Glenn Icing Research Tunnel (IRT). This trace was digitized using the GetData Graph Digitizer software and was then imported into the Unigraphics NX CAD program. The pressure tap hole locations and orientations were chosen based on the 2-D tracing within

CAD. The determined coordinates and angles were used to drill the tap holes on a vertical miller in a machine shop. The final instrumented casting is shown in Figure B.25.

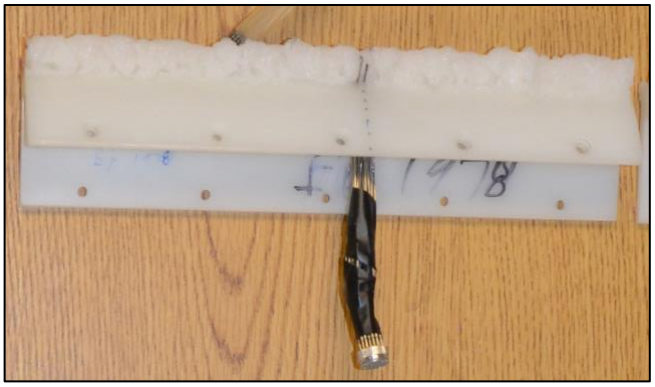

Figure B.25: Horn casting instrumented with pressure taps.

Appendix C

Calculation of Uncertainties

Uncertainties are inherent factors in any experimental methodology. The uncertainty analysis for the 3-D laser scanner validation test performed in the UIUC 3ft by 4ft subsonic wind tunnel are described in this appendix. The following sections include the equations used to calculate the uncertainties in the flow condition, force balance, pressure system, and PSP results. Sample uncertainties for a specific test conditions are then stated. The analysis follows the method described by Kline and McClintock.[40] The PSP uncertainty analysis followed the method outlined in Liu et al[41] and Crafton.[42] The analysis performed by Busch in previous work was referred to throughout the section.[5]

If R is a calculated result that is a function of a number of measurements, $x_1, x_2, \ldots, x_3$, the uncertainty in the result can be calculated using Eq. C.1 and the root-sum-square of the component uncertainties multiplied by the derivatives of the result with respect to the component values. These derivatives are a measure of the sensitivity of the final result to each component measurement.

$$U_R = \sqrt{\left(\frac{\partial R}{\partial x_1} U_{x_1}\right)^2 + \left(\frac{\partial R}{\partial x_2} U_{x_2}\right)^2 + \cdots + \left(\frac{\partial R}{\partial x_3} U_{x_3}\right)^3} \tag{C.1}$$

C.1 Flow Conditions Uncertainty

C.1.1 Dynamic Pressure

The dynamic pressure was calculated using Eq. 2.5 and is a function of the pressure difference between the settling and test sections and the inlet contraction ratio. Since the contraction ratio is known to be 7.5:1 the uncertainty in that value is neglected. The uncertainty in dynamic pressure is therefore calculated using Eq. C.2 and the partial derivative of the dynamic pressure with respect to the pressure difference between the

settling and test sections is found using Eq. C.3. The uncertainty in the 1 psid ESP module used to measure the differential pressure difference is ±0.0014, as stated by the manufacturer.

$$U_{q_\infty} = \sqrt{\left(\frac{\partial q_\infty}{\partial(P_{ss}-P_{ts})} U_{P_{ss}-P_{ts}}\right)^2} \tag{C.2}$$

$$\frac{\partial q_\infty}{\partial(P_{ss}-P_{ts})} = \frac{1}{1-\left(\frac{A_{ts}}{A_{ss}}\right)^2} \tag{C.3}$$

C.1.2 Ambient density

The ambient density was calculated using the ideal gas law in Eq. 2.4. It is a function of the specific gas constant for air, the ambient pressure, and ambient temperature. The values for the measured ambient temperature and pressure add uncertainty to the density measurement. The uncertainty is calculated from Eq. C.4 where the partial derivatives of density with respect to ambient temperature and pressure were calculated from Eqs. C.5 and C.6, respectively. The uncertainty in the pressure measurement obtained from the Setra 270 absolute pressure transducer is stated as ±0.008 psi by the manufacturer. The uncertainty in the ambient temperature measured by the Omega thermocouple is stated as ±1°.

$$U_{\rho_{amb}} = \sqrt{\left(\frac{\partial \rho_{amb}}{\partial P_{amb}} U_{P_{amb}}\right)^2 + \left(\frac{\partial \rho_{amb}}{\partial T_{amb}} U_{T_{amb}}\right)^2} \tag{C.4}$$

$$\frac{\partial \rho_{amb}}{\partial P_{amb}} = \frac{1}{RT_{amb}} \tag{C.5}$$

$$\frac{\partial \rho_{amb}}{\partial T_{amb}} = \frac{P_{amb}}{RT_{amb}^2} \tag{C.6}$$

C.1.3 Viscosity Coefficient

The viscosity coefficient, μ, is calculated from Sutherland's Law as stated in Eq. 2.8 and is a function of the ambient temperature (T_{amb}), the viscosity coefficient at freezing (μ_0), and the temperature at freezing (T_0). Both the viscosity coefficient and temperature at freezing are constants and do not add to the uncertainty in the viscosity coefficient. The uncertainty is calculated using Eq. C.7 and the partial derivative of viscosity coefficient with respect to ambient temperature is calculated from Eq. C.8. The uncertainty in the temperature measurement is ±1° as stated by the thermocouple manufacturer.

$$U_\mu = \sqrt{\left(\frac{\partial \mu}{\partial T_{amb}} U_{T_{amb}}\right)^2} \tag{C.7}$$

$$\frac{\partial \mu}{\partial T_{amb}} = \frac{3}{2}\mu_0 \sqrt{\frac{T_{amb}}{T_0}} \frac{T_0+199.8}{T_0(T_{amb}+199.8)} - \mu_0 \left(\frac{T_{amb}}{T_0}\right)^{\frac{3}{2}} \frac{T_0+199.8}{(T_{amb}+199.8)^2} \tag{C.8}$$

C.1.4 Freestream Velocity

The freestream velocity in the tunnel test section was calculated from the pressure differential between the settling and test sections, the ambient density, and the tunnel contraction ratio in Eq. 2.3. This equation can be expressed in terms of dynamic pressure as Eq. C.9. The total uncertainty then in the freestream velocity calculation is determined from the uncertainty in the dynamic pressure calculation and ambient density measurement that were determined above. Eq. C.10 states the freestream velocity uncertainty and Eqs. C.11 and C.12 express the calculations for the partial derivatives of freestream velocity with respect to dynamic pressure and ambient density respectively.

$$U_\infty = \sqrt{\frac{2q_\infty}{\rho_{amb}}} \tag{C.9}$$

$$U_{U_\infty} = \sqrt{\left(\frac{\partial U_\infty}{\partial q_\infty} U_{q_\infty}\right)^2 + \left(\frac{\partial U_\infty}{\partial \rho_{amb}} U_{\rho_{amb}}\right)^2} \tag{C.10}$$

$$\frac{\partial U_\infty}{\partial q_\infty} = \frac{1}{\sqrt{2q_\infty \rho_{amb}}} \tag{C.11}$$

$$\frac{\partial U_\infty}{\partial \rho_{amb}} = -\frac{1}{\rho_{amb}} \sqrt{\frac{q_\infty}{2\rho_{amb}}} \tag{C.12}$$

C.1.5 Reynolds Number

The Reynolds number (*Re*) was calculated using Eq. 2.7 and is a function of ambient density (ρ_{amb}), freestream velocity (U_∞), model chord (c), and viscosity coefficient (μ). The uncertainties in freestream velocity, ambient density, and viscosity coefficient were calculated above in Eqs. C.9, C.4, and C.7, and the uncertainty in the chord measurement was estimated to be ±0.01 inches. The uncertainty in Reynolds number calculation can then be found using Eq. C.13. The partial derivatives for ρ_{amb}, U_∞, c, and μ are expressed in Eqs. C.14, C.15, C.16, and C.17.

$$U_{Re} = \sqrt{\left(\frac{\partial Re}{\partial \rho_{amb}} U_{\rho_{amb}}\right)^2 + \left(\frac{\partial Re}{\partial U_\infty} U_{U_\infty}\right)^2 + \left(\frac{\partial Re}{\partial c} U_c\right)^2 + \left(\frac{\partial Re}{\partial \mu} U_\mu\right)^2} \tag{C.13}$$

$$\frac{\partial Re}{\partial \rho_{amb}} = \frac{U_\infty c}{\mu} \tag{C.14}$$

$$\frac{\partial Re}{\partial U_\infty} = \frac{\rho_{amb} c}{\mu} \tag{C.15}$$

$$\frac{\partial Re}{\partial c} = \frac{\rho_{amb} U_\infty}{\mu} \tag{C.16}$$

$$\frac{\partial Re}{\partial \mu} = -\frac{\rho_{amb} U_\infty c}{\mu^2} \tag{C.17}$$

C.2 Force Balance Measurement Uncertainty

C.2.1 Lift Coefficient

The lift coefficient (C_L) as measured by the force balance was calculated using Eqs. 2.8 and 2.11. It is a function of normal force (F_N), axial force (F_A), angle of attack (α), dynamic pressure (q_∞), model chord (c), and model span (b). The uncertainty in the lift coefficient measured by the force balance can then be expressed using Eq. C.18. The partial derivatives of the lift coefficient with respect to each of the six measurements are stated in Eqs. C.19 through C.24. According to the manufacturer of the force balance, the uncertainty in normal force measurements is 0.02% of the full-scale value. The uncertainty is 0.03% the full-scale value for the axial force and is 0.15% for the pitching moment. The turntable was able to set the angle of attack to within ±0.02° of the specified angle. The uncertainty in the dynamic pressure equals the value calculated in Eq. C.2. The uncertainty in the chord measurement was estimated as 0.01 inches and the uncertainty in span measurement was estimated as 0.02 inches. These values for the uncertainties in the contributing measurements used to calculate the lift coefficient uncertainty apply to the following section for the drag calculation.

$$U_{C_{L_{bal}}} = \left[\left(\frac{\partial C_{L_{bal}}}{\partial \alpha} U_\alpha\right)^2 + \left(\frac{\partial C_{L_{bal}}}{\partial F_N} U_{F_N}\right)^2 + \left(\frac{\partial C_{L_{bal}}}{\partial F_A} U_{F_A}\right)^2 + \left(\frac{\partial C_{L_{bal}}}{\partial q_\infty} U_{q_\infty}\right)^2 + \left(\frac{\partial C_{L_{bal}}}{\partial c} U_c\right)^2 + \left(\frac{\partial C_{L_{bal}}}{\partial b} U_b\right)^2\right]^{\frac{1}{2}} \tag{C.18}$$

$$\frac{\partial C_{L_{bal}}}{\partial \alpha} = \frac{1}{q_\infty S}[-F_N \sin(\alpha) - F_A \cos(\alpha)] \tag{C.19}$$

$$\frac{\partial C_{L_{bal}}}{\partial F_N} = \frac{\cos(\alpha)}{q_\infty S} \tag{C.20}$$

$$\frac{\partial C_{L_{bal}}}{\partial F_A} = -\frac{\sin(\alpha)}{q_\infty S} \tag{C.21}$$

$$\frac{\partial C_{L_{bal}}}{\partial q_\infty} = \frac{1}{{q_\infty}^2 S}[F_N \cos(\alpha) - F_A \sin(\alpha)] \tag{C.22}$$

$$\frac{\partial C_{L_{bal}}}{\partial c} = \frac{1}{q_\infty b c^2}[F_N \cos(\alpha) - F_A \sin(\alpha)] \tag{C.23}$$

$$\frac{\partial C_{L_{bal}}}{\partial b} = \frac{1}{q_\infty c b^2}[F_N \cos(\alpha) - F_A \sin(\alpha)] \tag{C.24}$$

C.2.2 Drag Coefficient

The drag coefficient (C_D) as measured by the force balance was calculated using Eqs. 2.9 and 2.12. It is a function of normal force (F_N), axial force (F_A), angle of attack (α), dynamic pressure (q_∞), model chord (c), and model span (b). The uncertainty in the drag coefficient measured by the force balance can then be expressed using Eq. C.25 in a similar way to the uncertainty in the lift coefficient determined above in Eq. C.18. The partial derivatives of the drag coefficient with respect to each of the six measurements are stated in Eqs. C.26 through C.31.

$$U_{C_{D_{bal}}} = \left[\left(\frac{\partial C_{D_{bal}}}{\partial \alpha} U_\alpha\right)^2 + \left(\frac{\partial C_{D_{bal}}}{\partial F_N} U_{F_N}\right)^2 + \left(\frac{\partial C_{D_{bal}}}{\partial F_A} U_{F_A}\right)^2 + \left(\frac{\partial C_{D_{bal}}}{\partial q_\infty} U_{q_\infty}\right)^2 + \left(\frac{\partial C_{D_{bal}}}{\partial c} U_c\right)^2 + \left(\frac{\partial C_{D_{bal}}}{\partial b} U_b\right)^2\right]^{\frac{1}{2}} \tag{C.25}$$

$$\frac{\partial C_{D_{bal}}}{\partial \alpha} = \frac{1}{q_\infty S}[F_N \cos(\alpha) - F_A \sin(\alpha)] \tag{C.26}$$

$$\frac{\partial C_{D_{bal}}}{\partial F_N} = \frac{\sin(\alpha)}{q_\infty S} \tag{C.27}$$

$$\frac{\partial C_{D_{bal}}}{\partial F_A} = \frac{\cos(\alpha)}{q_\infty S} \tag{C.28}$$

$$\frac{\partial C_{D_{bal}}}{\partial q_\infty} = \frac{1}{{q_\infty}^2 S}[F_N \sin(\alpha) + F_A \cos(\alpha)] \tag{C.29}$$

$$\frac{\partial C_{D_{bal}}}{\partial c} = \frac{1}{q_\infty b c^2}[F_N \sin(\alpha) + F_A \cos(\alpha)] \tag{C.30}$$

$$\frac{\partial C_{D_{bal}}}{\partial b} = \frac{1}{q_\infty c b^2}[F_N \sin(\alpha) + F_A \cos(\alpha)] \quad \text{(C.31)}$$

C.3 Pressure System Uncertainty

The uncertainties for each pressure module as specified by the manufacturer, are summed in Table C.1.

Table C.1: ESP module uncertainties.

Module	Module Uncertainty	Calibration Uncertainty	Total Uncertainty
5 psid	±0.0035 psid	±0.0010 psid	±0.0036 psid
1 psid	±0.0010 psid	±0.0010 psid	±0.0014 psid
0.35 psid	±0.00035 psid	±0.0002 psid	±0.0004 psid

C.3.1 Pressure Coefficient

The pressure coefficient was calculated using Eq. 2.6 as a function of the difference between the static pressures at the pressure taps and test section ($P - P_{ts}$) and the difference between the static pressures between the settling section and the test section ($P_{ss} - P_{ts}$). The uncertainty is calculated using Eq. C.32. The partial derivatives of pressure coefficient with respect to both the pressure differences are stated by Eqs. C.33 and C.34. The uncertainty in both pressure differential measurements is the total uncertainty stated for the specific ESP module in Table C.1.

$$U_{C_p} = \sqrt{\left(\frac{\partial C_p}{\partial (P_{ss}-P_{ts})} U_{(P_{ss}-P_{ts})}\right)^2 + \left(\frac{\partial C_p}{\partial (P-P_{ts})} U_{(P-P_{ts})}\right)^2} \quad \text{(C.32)}$$

$$\frac{\partial C_p}{\partial (P_{ss}-P_{ts})} = -\frac{P-P_{ts}}{(P_{ss}-P_{ts})^2}\left[1 - \left(\frac{A_{ts}}{A_{ss}}\right)^2\right] \quad \text{(C.33)}$$

$$\frac{\partial C_p}{\partial (P-P_{ts})} = \frac{1}{P_{ss}-P_{ts}}\left[1 - \left(\frac{A_{ts}}{A_{ss}}\right)^2\right] \quad \text{(C.34)}$$

C.3.2 Lift Coefficient

The lift coefficient (C_l) calculated from the pressure measurements is a function of the angle of attack and the pressure coefficients at each pressure tap. It was calculated from Eqs. 2.14 through 2.18. The uncertainty in this result is expressed in Eq. C.35 and the necessary partial derivatives in Eqs. C.36 and C.37. The uncertainty of each pressure tap measurement is calculated using Eq. C.32 and the uncertainty in angle of attack is ±0.02.

$$U_{C_l} = \sqrt{\left(\frac{\partial C_l}{\partial \alpha} U_\alpha\right)^2 + \sum_{i=1}^{N} \left(\frac{\partial C_l}{\partial C_{p_i}} U_{C_{p_i}}\right)^2} \tag{C.35}$$

$$\frac{\partial C_l}{\partial \alpha} = -\sin(\alpha) \sum_{i=1}^{N} \left[\frac{C_{P_i} + C_{P_{i+1}}}{2} \left(\frac{x}{c_{i+1}} - \frac{x}{c_i}\right)\right] - \cos(\alpha) \sum_{i=1}^{N} \left[\frac{C_{P_i} + C_{P_{i+1}}}{2} \left(\frac{y}{c_{i+1}} - \frac{y}{c_i}\right)\right] \tag{C.36}$$

$$\frac{\partial C_l}{\partial C_{p_i}} = \cos(\alpha) \left(\frac{x}{c_{i+1}} - \frac{x}{c_i}\right) - \sin(\alpha) \left(\frac{y}{c_{i+1}} - \frac{y}{c_i}\right) \tag{C.37}$$

C.3.3 Drag Coefficient

The drag coefficient (C_d) determined from the wake pressures was calculated from Eqs. 2.32 and 2.33. These equations are dependent on dynamic pressure (q_∞), model chord (c), freestream total pressure ($P_{o,\infty}$), and total pressure at each total pressure probe in the wake (P_{o,w_i}). The uncertainty is found from Eq. C.38. The uncertainty in dynamic pressure was calculated using Eq. C.2, and the uncertainty in chord is estimated as ±0.01 inches. The uncertainties for both wake and freestream total pressure both equal the uncertainty in the 0.35 psid ESP module stated in Table C.1. The necessary partial derivative calculations are stated in Eqs. C.39 through C.40.

$$U_{C_d} = \sqrt{\left(\frac{\partial C_d}{\partial q_\infty} U_{q_\infty}\right)^2 + \left(\frac{\partial C_d}{\partial \mathrm{c}} U_{\mathrm{c}}\right)^2 + \left(\frac{\partial C_d}{\partial P_{o,\infty}} U_{P_{o,\infty}}\right)^2 + \sum_{i=1}^{N} \left(\frac{\partial C_d}{\partial P_{o,w_i}} U_{P_{o,w_i}}\right)^2} \tag{C.38}$$

$$\frac{\partial C_d}{\partial q_\infty} = -\frac{1}{q_\infty^2 c}\sum_{i=1}^{K}\left(\left(\sqrt{q_\infty^2 - q_\infty\left(P_{o,\infty} - P_{o,w_\mathrm{i}}\right)} + \sqrt{q_\infty^2 - q_\infty\left(P_{o,\infty} - P_{o,w_{i+1}}\right)}\right.\right.$$
$$\left.\left. - 2q_\infty + 2P_{o,\infty} - P_{o,w_\mathrm{i}} - P_{o,w_{i-1}}\right)(y_{i+1} - y_i)\right)$$
$$+ \frac{1}{q_\infty c}\sum_{i=1}^{K}\{\left(\frac{2q_\infty - \left(P_{o,\infty} - P_{o,w_\mathrm{i}}\right)}{2\sqrt{q_\infty^2 - q_\infty\left(P_{o,\infty} - P_{o,w_\mathrm{i}}\right)}}\right.$$
$$\left. + \frac{2q_\infty - \left(P_{o,\infty} - P_{o,w_{\mathrm{i}+1}}\right)}{2\sqrt{q_\infty^2 - q_\infty\left(P_{o,\infty} - P_{o,w_{\mathrm{i}+1}}\right)}} - 2\right)(y_{i+1} - y_i)\} \quad \text{(C.39)}$$

$$\frac{\partial C_d}{\partial \mathrm{c}} = -\frac{1}{q_\infty c^2}\sum_{i=1}^{K}\left(\sqrt{q_\infty^2 - q_\infty\left(P_{o,\infty} - P_{o,w_\mathrm{i}}\right)} + \sqrt{q_\infty^2 - q_\infty\left(P_{o,\infty} - P_{o,w_{\mathrm{i}+1}}\right)}\right.$$
$$\left. - 2q_\infty + 2P_{o,\infty} - P_{o,w_\mathrm{i}} - P_{o,w_{i+1}}\right)(y_{i+1} - y_i)) \quad \text{(C.40)}$$

$$\frac{\partial C_d}{\partial P_{o,\infty}} = \frac{1}{q_\infty c}\sum_{i=1}^{K}\left(\left(2 - \frac{q_\infty}{2\sqrt{q_\infty^2 - q_\infty\left(P_{o,\infty} - P_{o,w_\mathrm{i}}\right)}}\right.\right.$$
$$\left.\left. - \frac{q_\infty}{2\sqrt{q_\infty^2 - q_\infty\left(P_{o,\infty} - P_{o,w_{\mathrm{i}+1}}\right)}}\right)(y_{i+1} - y_i)\right) \quad \text{(C.41)}$$

$$\frac{\partial C_d}{\partial P_{o,w_i}} = \frac{1}{q_\infty c}\left[\frac{q_\infty}{2\sqrt{q_\infty^2 - q_\infty\left(P_{o,\infty} - P_{o,w_\mathrm{i}}\right)}} - 1\right](y_{i+1} - y_i) \quad \text{(C.42)}$$

C.4 Pressure-Sensitive Paint Uncertainty

Liu et al.[41] and Crafton[42] describe the detailed process for calculating the uncertainties for single-luminophore, radiometric PSP methods. The full PSP uncertainty analysis is complicated due to the complex nature of the PSP test set-up and the number of parameters involved. Since certain parameters were unable to be measured or estimated for the tests reported in this thesis, a calculation of the total uncertainty in the PSP test was not completed. What follows is a detailed description of the sources of error inherent in

radiometric PSP testing and the analytical formulas for each error source's pressure uncertainty. The uncertainties of the error sources were calculated or estimated where it was possible to do so.

C.4.1 PSP System Definition

According to Liu et al.,[41] the resulting pressure can be modelled by Eq. C.43. Pressure is a function of the photodetector (camera) output at the wind-on ($V(t',x')$) and wind-off ($V_{ref}(t,x)$) conditions, the reference pressure (P_{ref}), the temperature dependent Stern-Volmer constants ($A(T)$ and $B(T)$), and the factor, U_1. U_1 is defined in Eq. C.44 and combines the effects of the imaging system performance (Π_c and $\Pi_{c,ref}$), the filter parameters (Π_f and $\Pi_{f,ref}$), the paint layer thickness ($h(x')$ and $h_{ref}(x)$), the luminophore concentration ($c(x')$ and $c_{ref}(x)$), and the excitation flux at the wind-on and wind-off conditions ($q_0(t',X')$ and $q_{0,ref}(t,X)$. The primes (') denote the wind-on spatial and temporal coordinates. The lower case *x* specifies the coordinates in the image and the upper case *X* specifies the coordinates in space.

$$P = U_1 \frac{V_{ref}(t,x)}{V(t\prime,x\prime)} \frac{P_{ref}}{B(T)} - \frac{A(T)}{B(T)} P_{ref} \tag{C.43}$$

$$U_1 = \frac{\Pi_c}{\Pi_{c,ref}} \frac{\Pi_f}{\Pi_{f,ref}} \frac{h(x')}{h_{ref}(x)} \frac{c(x')}{c_{ref}(x)} \frac{q_0(t',X')}{q_{0,ref}(t,X)} \tag{C.44}$$

In order to remove the coupling between temporal and spatial variations for the photodetector output factors, the time and displacement can be represented as an initial wind-off value plus the difference between the wind-on and wind-off values ($x' = x + \Delta x$ and $t' = t + \Delta t$). In this way the ratio of the photodetector outputs can be written as Eq. C.45, where $D_t(\Delta t) = 1 - \left(\frac{\partial V}{\partial t}\right)\frac{(\Delta t)}{V}$ and $D_x(\Delta x) = 1 - (\nabla V) \cdot \frac{(\Delta x)}{V}$. The ratio of the excitation flux at the wind-off and wind-on conditions can then be represented by Eq. C.46, where $D_{q0}(\Delta t) = 1 + \left(\frac{\partial q_0}{\partial t}\right)\frac{(\Delta t)}{q_0}$.

$$\frac{V_{ref}(t,x)}{V(t\prime,x\prime)} \approx D_t(\Delta t) D_x(\Delta x) \frac{V_{ref}(t,x)}{V(t,x)} \tag{C.45}$$

$$\frac{q_0(t',X')}{q_{0,ref}(t,X)} \approx D_{q0}(\Delta t) \frac{q_0(t,X')}{q_{0,ref}(t,X)} \tag{C.46}$$

The above decompositions yield a modified version of Eq. C.43 for pressure in Eq. C.47. The factor, U_2, is defined by Eq. C.48.

$$P = U_2 \frac{V_{ref}(t,x)}{V(t,x)} \frac{P_{ref}}{B(T)} - \frac{A(T)}{B(T)} P_{ref} \tag{C.47}$$

$$U_2 = D_t(\Delta t) D_x(\Delta x) D_{q0}(\Delta t) \frac{\Pi_c}{\Pi_{c,ref}} \frac{\Pi_f}{\Pi_{f,ref}} \frac{h(x')}{h_{ref}(x)} \frac{c(x')}{c_{ref}(x)} \frac{q_0(t,X')}{q_{0,ref}(t,X)} \tag{C.48}$$

The detector output (V) is the most complex parameter affecting the PSP system. It is defined by Eq. C.49. The two parameters, Π_c and Π_f, represent the camera and filter systems, β_{λ_1} is the extinction coefficient of the PSP for the excitation light, and $\Phi(P,T)$ is the quantum yield as a function of pressure and temperature.

$$V = \Pi_c \Pi_f \beta_{\lambda_1} h q_0 \Phi(P,T) \tag{C.49}$$

The factor, Π_c, is defined in Eq. C.50 and is a function of the system gain (G), the image area (A_I), the camera lens f-number (F), and the optical magnification (M_{op}). The factor, Π_f, is the product of two values, K_1 and K_2 (Eq. C.51). K_1 describes the effect of the excitation lamp's optical filter, the excitation light scattering, and the direction of the incident excitation light. K_2 expresses the effect of the optical filter, scattering, and system response for the luminescent light. The extinction coefficient (β_{λ_1}) is defined as the product of the molar absorptivity (ε_{λ_1}) and the luminophore concentration (c). The quantum yield is defined by Eq. C.52 and is a function of the radiative rate constant (k_r), the non-radiative deactivation rate constant (k_{nr}), the quenching rate constant (k_q), and the oxygen concentration ($[Q]$).

$$\Pi_c = \frac{\pi}{4} G A_I \left[F^2 \left(1 - M_{op}\right)^2 \right]^{-1} \tag{C.50}$$

$$\Pi_f = K_1 K_2 \tag{C.51}$$

$$\Phi(P,T) = \frac{k_r}{k_r + k_{nr} + k_q[Q]} \tag{C.52}$$

The equations for the calculation of K_1 and K_2 are expressed in Eqs. C.53 and C.54. E_{λ_1} is the spectrum of incident excitation light, C_d is the coefficient representing the directional effect of the excitation light, $\rho_{\lambda_1}^{ap}$ is the reflectivity of the air-PSP interface, $\rho_{\lambda_1}^{wp}$ is the reflectivity of the PSP-wall interface, and $F_{t1}(\lambda_1)$is the filter function describing the excitation light's optical filter. In Eq. C.54, τ_{op} is the optical transmittance of the system,

τ_{atm} is the optical transmittance of the atmosphere, E_{λ_2} is the spectrum of the emitted light, $\langle M \rangle$ is the coefficient representing the effects of the both reflection and scattering of the luminescent light at the wall, $R_q(\lambda_2)$ is the detector's quantum efficiency, and $F_{t2}(\lambda_2)$ is the filter function describing the camera's optical filter. The two wavelengths, λ_1 and λ_2, denote the incident excitation light and the emitted luminescent light respectively.

$$K_1 = {\beta_{\lambda_1}}^{-1} \int_0^\infty \beta_{\lambda_1} E_{\lambda_1}(\lambda_1) C_d \left(1 - \rho_{\lambda_1}^{ap}\right)\left(1 + \rho_{\lambda_1}^{wp}\right) F_{t1}(\lambda_1) d\lambda_1 \tag{C.53}$$

$$K_2 = \int_0^\infty \tau_{op} \tau_{atm} E_{\lambda_2}(\lambda_2) \langle M \rangle R_q(\lambda_2) F_{t2}(\lambda_2) d\lambda_2 \tag{C.54}$$

The two coefficients used in the above equations, C_d and $\langle M \rangle$, are calculated using the expressions in Eqs. C.55 and C.56. In these equations, $\mu = \cos(\theta)$ and μ_{ex} is from the angle the excitation lamp makes with the model surface and μ_1 and μ_2 are the two polar angles in the solid angle of the luminescent light.

$$C_d = -\mu_{ex} \exp\left(\frac{\beta_{\lambda_1} h}{\mu_{ex}}\right) \tag{C.55}$$

$$\langle M \rangle = 0.5 + \rho_{\lambda_2}^{wp}(\mu_1 + \mu_2) \tag{C.56}$$

C.4.2 Uncertainty Calculation Method

The definition of the total uncertainty of a result using by Liu et al.[41] is slightly different from the method described by Kline and McClintock[40] and employed for the aerodynamic performance uncertainty analysis above. The total uncertainty in a result, such as pressure, is expressed as the ratio of the variance in the result to the square of the result. For a PSP system with independent parameters, the total uncertainty in pressure is expressed by Eq. C.57. M is the total number of error sources, S_i are the sensitivity coefficients for each parameter, and ζ_i is the ith parameter. The sensitivity coefficients are defined in Eq. C.58. The total uncertainty in pressure is the sum of the uncertainty in pressure due to each of the system's error sources.

$$\frac{var(P)}{P^2} = \sum_{i=1}^{M} S_i^2 \frac{var(\zeta_i)}{\zeta_i^2} \tag{C.57}$$

$$S_i = \frac{\zeta_i}{P} \frac{\partial P}{\partial \zeta_i} \tag{C.58}$$

The expressions for the sensitivity coefficients and variances for each parameter in the PSP system are summarized in Table C.2 from Liu et al.[41] Many of the sensitivity coefficients are functions of φ, which is defined by Eq. C.59.

$$\varphi = 1 + \frac{A(T)}{B(T)} \frac{P_{ref}}{P} \tag{C.59}$$

If the detector is a CCD camera, the variance of the detector output is dominated by photon shot noise. Photon shot noise is calculated in Eq. C.60 as the inverse of square root of the total number of photo-electrons collected in a pixel (n_{pe}) multiplied by the number of images acquired (N). The variance of the photodetector output used in the uncertainty calculation in Eq. C.57 is the square of the shot noise.

$$photon\ shot\ noise = \frac{1}{\sqrt{N n_{pe}}} \tag{C.60}$$

Crafton[42] further describe the method discussed by Lie et al.[41] The sensitivity coefficients for the photodetector output at the wind-on and wind-off conditions are further defined as stated in Eq. C.61.

$$S_i = \left[1 + \frac{A(T)}{B(T)} \frac{P}{P_{ref}}\right] \left[\sqrt{1 + A + B(T) \frac{P}{P_{ref}}}\right] \tag{C.61}$$

Table C.2: Sensitivity coefficients and elemental variances for PSP pressure uncertainty.

Variable ζ_i	Sensitivity coefficient S_i	Elemental variance $\mathrm{var}(\zeta_i)$	Physical origin
$D_t(\Delta t)$	$\varphi = 1 + A(T)/B(T)(P_{\mathrm{ref}}/P)$	$[(\partial V/\partial t)(\Delta t)/V]^2$	Temporal variation in luminescence due to photodegradation and surface contamination
$D_x(\Delta \boldsymbol{x})$	φ	$[(\partial V/\partial x)^2\sigma_x^2 + (\partial V/\partial y)^2\sigma_y^2]V^{-2}$	Image registration errors for correcting luminescence variation due to model motion
$D_{q0}(\Delta t)$	φ	$[(\partial q_0/\partial t)(\Delta t)/q_{0\,\mathrm{ref}}]^2$	Temporal variation in illumination
V_{ref}	φ	$V_{\mathrm{ref}} G\hbar\nu B_d$	Photodetector noise
V	$-\varphi$	$V G\hbar\nu B_d$	Photodetector noise
$\Pi_c/\Pi_{c\,\mathrm{ref}}$	φ	$[R_2/(R_1+R_2)]^2(\Delta R_1/R_1)^2$	Change in camera performance parameters due to model motion
$\Pi_f/\Pi_{f\,\mathrm{ref}}$	φ	$\mathrm{var}(\Pi_f/\Pi_{f\,\mathrm{ref}})$	Illumination spectral variability and filter spectral leakage
h/h_{ref}	φ	$[(\partial h/\partial x)^2\sigma_x^2 + (\partial h/\partial y)^2\sigma_y^2]h_{\mathrm{ref}}^{-2}$	Image registration errors for correcting thickness variation due to model motion
c/c_{ref}	φ	$[(\partial c/\partial x)^2\sigma_x^2 + (\partial c/\partial y)^2\sigma_y^2]c_{\mathrm{ref}}^{-2}$	Image registration errors for correcting concentration variation due to model motion
$q_0/q_{0\,\mathrm{ref}}$	φ	$(q_{0\,\mathrm{ref}})^{-2}\lvert(\nabla q_0)\cdot(\Delta \boldsymbol{X})\rvert^2$	Illumination variation on model surface due to model motion
P_{ref}	1	$\mathrm{var}(P)$	Error in measurement of reference pressure
T	$-[T/B(T)][B'(T) + A'(T)(P_{\mathrm{ref}}/P)]$	$\mathrm{var}(T)$	Temperature effects of PSP
A	$1-\varphi$	$\mathrm{var}(A)$	Paint calibration error
B	-1	$\mathrm{var}(B)$	Paint calibration error
Pressure mapping	1	$(\partial P/\partial x)^2\sigma_x^2 + (\partial P/\partial y)^2\sigma_y^2$ and $\lvert(\nabla P)_{\mathrm{surf}}\cdot(\boldsymbol{X})_{\mathrm{surf}}\rvert^2$	Errors in camera calibration and pressure mapping on a surface of a presumed rigid body

[a] Standard deviations of least-squares estimation in the image registration or camera calibration, are σ_x and σ_y.

[b] Total uncertainty in pressure:

$$\frac{\mathrm{var}(P)}{P^2} = \sum_{i=1}^{M} \frac{S_i^2 \mathrm{var}(\zeta_i)}{\zeta_i^2}$$

C.4.3 Simplified PSP Uncertainty Calculations

Liu et al.[41] state that the PSP uncertainty analysis can be simplified by using a first-order approximation. This approximation results in simplified estimates for a number of the parameters, so that $D_t(\Delta t) \approx 1$, $D_x(\Delta x) \approx 1$, $D_{q0}(\Delta t) \approx 1$, $\frac{\Pi_c}{\Pi_{c,ref}} \approx 1$, $\frac{\Pi_f}{\Pi_{f,ref}} \approx 1$, $\frac{h(x')}{h_{ref}(x)} \approx 1$, $\frac{c(x')}{c_{ref}(x)} \approx 1$, and $\frac{q_0(t,X')}{q_{0,ref}(t,X)} \approx 1$. Substituting these approximated values into Eq. C.48 for U_2 results in $U_2 \approx 1$. This leaves the major contributing factors to uncertainty in pressure as the detector output at both the wind-on and wind-off conditions (V and V_{ref}), the reference pressure (P_{ref}), temperature (T), the Stern-Volmer equation calibration coefficients (A and B), and mapping of the pressure image to a three-dimensional model. The PSP pressure results were not mapped onto a three-dimensional grid of the model so there are no errors resulting from pressure mapping.

The uncertainty in the reference pressure is the uncertainty in the Setra 270 pressure transducer, which is reported as ±0.008 psi by the manufacturer. The uncertainty in temperature was estimated using the relations outlined in Lie et al.[42] The temperature sensitivity (S_T) value is found using Eq. C.62. The prime denotes the derivatives of the Stern-Volmer coefficients with respect to temperature. $B'(T)$ was estimated to be negligible. $A'(T)$ was estimated using the known UniFIB PSP temperature sensitivity of 0.5% as is stated by the paint manufacturer. The variance of temperature was also estimated since no temperature measurements were obtained on the model surface. The square of the estimated difference of 0.5% from the ambient temperature was taken as a reasonable estimate.

$$S_T = -\left[\frac{T}{B(T)}\right]\left[B'(T) + A'(T)\left(\frac{P_{ref}}{P}\right)\right] \tag{C.62}$$

The error in the photodetector output can be calculated using Eqs. C.60 and C.61. An estimate for the photon shot noise can be calculated for the average of 25 images ($N = 25$) and the maximum number of photons typically collected at one pixel ($n_{pe} = 100{,}000\ electrons$) using Eq. C.60.

C.4.4 PSP Error Analysis

Many of the contributing parameters to the uncertainty in the PSP pressure results were unable to be measured during testing and are therefore unknown. This made a complete

uncertainty analysis like was outlined in the previous section impossible to perform for these tests. Therefore, another method of quantifying the error in the PSP measurements was employed. The error was defined as the standard deviation between of the difference between the measured value and the actual value. The actual value in this case was the pressure coefficient data measured using the surface pressure taps. To perform this error analysis along the span, a case with a known constant pressure distribution across the span was used. The clean model, especially at angles below the stall angle of attack, has a relatively constant pressure distribution along the span. Therefore, any observed deviations in pressure values in the spanwise direction are the result of errors in the method and not actual pressure variations. For this reason, the clean NACA 23012 model at an angle of attack of $\alpha = 12°$ was chosen for the sample error calculation.

For each main row pressure tap included in the analysis, a rectangular region was defined with edges three pixels up- and downstream from the pressure tap location. The region extended the entire span of the painted area. In order to remove tap effects due to less paint or inexact alignment methods, 6 tap rows above and below the *z/b* location of the tap were removed from the rectangular region. The standard deviation of the remaining data points were found using Eq. C.63. N is the total number of pixels in the rectangular region around the pressure tap (i) contributing to the error. $C_{P_{i,pixel}}$ is the pressure coefficient value at each pixel as measured using the PSP method. $C_{p_{tap}}$ is the pressure coefficient measured using the surface pressure tap. The error at all pressure taps within the painted region at chordwise locations less than *x/c* = 0.7 were calculated in this way. Pressure taps past *x/c* = 0.7 were not used in this analysis because they were not included in the calibration due to the large amount of noise in that region. To quantify the error over the entire model, the average percent error was calculated.

$$error = \sqrt{\sum_{i=1}^{N} \left(C_{P_{i,pixel}} - C_{p_{tap}} \right)^2} \tag{C.63}$$

This analysis was performed twice: once as described above and again using a smaller rectangular area surrounding each tap. Focusing on the PSP region close to the tap row allowed an error estimate at a single spanwise location to compare with the error estimate along the entire span of the painted section.

C.5 Sample Uncertainties

Sample uncertainty calculations were performed for the horn casting case at a Reynolds number of 1.8 million and an angle of attack of α = 7°. The uncorrected aerodynamic coefficients and angle of attack are reported here.

Table C.3: Uncertainties in Flow Parameters for horn casting at Re 1.8 million and α = 7°.

Flow Parameter	Reference Value	Absolute Uncertainty	Relative Uncertainty (%)
c	18 in.	±0.01 in.	±0.0556
b	33.563 in.	±0.02 in.	±0.0596
q_∞	0.317 psi	±0.00143 psi	±0.4505
T_{amb}	71.63° F	±1° F	±1.40
P_{amb}	14.347 psi	±0.008 psi	±0.0558
ρ_{amb}	0.00227 $\frac{slugs}{ft^3}$	±4.45x10^{-6} $\frac{slugs}{ft^3}$	±0.1963
μ	3.81x10^{-7} $\frac{lb \cdot s}{ft^2}$	±5.54x10^{-10} $\frac{lb \cdot s}{ft^2}$	±0.1454
U_∞	201.71 $\frac{ft}{s}$	±0.452 $\frac{ft}{s}$	±0.2242
Re	1800865	±5458	±0.3031

Table C.4: Uncertainties in Balance Parameters for horn casting at Re 1.8 million and α = 7°.

Balance Parameter	Reference Value	Absolute Uncertainty	Relative Uncertainty (%)
α	6.998°	±0.02°	±0.2858
F_{N}	-66.504 lb	±0.09 lb	±0.1353
F_{A}	0.0058 lb	±0.027 lb	±5.30
M	-1.1339 $lb \cdot ft$	±0.0675 $lb \cdot ft$	±5.95
C_ℓ	0.7595	±0.00295	±0.389
C_d	0.0935	±0.00407	±0.4518

Table C.5: Uncertainties in Pressure Parameters for horn casting at Re 1.8 million and α = 7°.

Pressure Parameter	Reference Value	Absolute Uncertainty	Relative Uncertainty (%)
C_ℓ	0.7560	±0.002239	±0.2962
C_d	0.0901	±0.00079	±0.8768

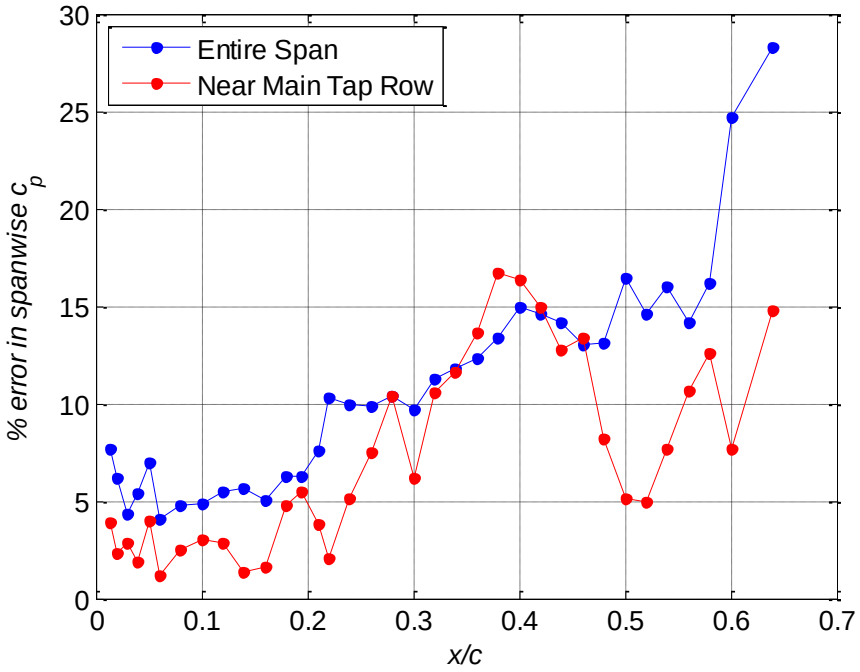

Figure C.1: Percent error in spanwise PSP data near the main tap row and over the span of the painted area.

Table C.6: Average Percent Errors in PSP at Re 1.8 million and α = 12°.

PSP Data Location	**Average Percent Error Over Chord**
Near Main Tap Row	7.3%
Over Span of Painted Area	10.8%